The optical morphologies and radio properties of HERGs with intermediate radio powers

Jonathon Cheng Shan Pierce

Department of Physics & Astronomy
The University of Sheffield

A dissertation submitted in candidature for the degree of Doctor of Philosophy at the University of Sheffield

December 2020

“ That still only counts as one! ”

– *Gimli*

Contents

List of Figures

List of Tables

Declaration

I declare that, unless otherwise stated, the work presented in this thesis is my own. No part of this thesis has been accepted or is currently being submitted for any other qualification at The University of Sheffield or elsewhere.

Much of the work presented here has already been published and can be found in:

1. Pierce et al. (2019), "*Do AGN triggering mechanisms vary with radio power? I. Optical morphologies of radio-intermediate HERGs*", published in Monthly Notices of the Royal Astronomical Society in May 2019.
2. Pierce et al. (2020), "*The radio properties of HERGs with intermediate radio powers*", published in Monthly Notices of the Royal Astronomical Society in February 2020.

Acknowledgments

This thesis would not have been possible without the continued help and support of a large number of people over the past four years.

I would firstly like to thank the many members of the astronomy group at The University of Sheffield, both past and present, whose constant friendliness and positivity created a highly enjoyable working environment throughout my PhD studies. Marvin, you were a great mentor for me in the early stages, and I owe a lot to your initial support and guidance. Katie, you were an invaluable confidant throughout the four years, and your personal advice helped me on innumerable occasions. I know you never did this for thanks, but I want you to know that it was greatly appreciated, nonetheless. Jenny, our conversations in the final few months helped me to regain the confidence and optimism I needed to get myself over the line. My special thanks, of course, also go to Clive. Your role as supervisor has extended beyond the valuable professional advice that you have always provided, and it has been very much appreciated.

I also owe particular thanks to my mother Katerina, my father Adrian, my sister Suzy, my step-father Arthur and my aunties, Marie and Rita. Your unwavering love and support has served as a constant example of the importance of family, during the high times and the low. My thanks also go to my grandmother Gwen. Our shared interest in astronomy has reminded me how fortunate I am to be in this position.

In addition, I want to thank my close friends Tom and Jed. Our experiences together on what turned out to be a life-changing trip to Southeast Asia will never be forgotten.

Finally, I would like to thank my beautiful and caring wife Tatiana. Your constant love and support through the ups and downs of the past year has helped me in more ways than you can know, and I am forever grateful. Te amo muito, amor da minha vida.

My thanks are also due to many other colleagues, friends, and family members, of whom there are too many to mention. I can assure you that you have all played key roles in the work that has led to an unprecedented thesis, written in unprecedented times.

Thesis summary

Sensitive radio surveys with broad sky coverage have revealed that the local radio AGN population is dominated by sources with lower powers than those previously studied as representative of the class. High-excitation radio galaxies (HERGs) with intermediate radio powers ($10^{22.5} < \mathrm{L}_{1.4\mathrm{GHz}} < 10^{25}$ W Hz^{-1}) represent a particularly important subset of these lower-power objects, given their strong association with kinematic disturbances in the multiphase gas of their host galaxies. Despite this, little is currently known about the properties of these radio-intermediate HERG sources.

For this thesis, deep optical imaging observations of radio-intermediate HERGs have been used to characterise their detailed morphologies for the first time. The host morphologies of powerful radio AGN and Type 2 quasars have also been studied, as well those of stellar-mass- and redshift-matched non-active control galaxies. The rate of morphological disturbance for lower-power radio-intermediate HERGs is found to be relatively low and indistinguishable from the control sample. However, when the full active galaxy sample is considered, there is clear evidence to suggest that the enhancement in the rate of disturbance relative to the controls increases strongly with the AGN power, such that objects with quasar-like [OIII]λ5007 emission line luminosities exhibit a $5\,\sigma$ excess relative to matched non-active galaxies. This strongly supports the idea that merger-based triggering is dominant for the most luminous AGN. Evidence for a transition in the dominant AGN host types from early-type galaxies at high radio powers to late-type galaxies at low radio powers is also found, which may indicate that triggering by secular, disk-based processes holds more importance for radio AGN with more moderate luminosities.

In addition, high-resolution radio observations of 16 radio-intermediate HERGs have revealed a mixture of compact and extended radio structures. Several of the latter are double-lobed/edge-brightened, consistent with the idea that such structures could be connected with the radiatively-efficient AGN accretion mode.

Chapter 1

Introduction

1.1 Chapter overview

Although the phenomenon was not known at the time, observational evidence for active galactic nuclei (AGN) was entwined with that used to identify the first galaxies beyond our Milky Way. Now, around one century later, the study of extragalactic objects has developed into an important area of modern astronomical research, and the significance of AGN in this context is well realised.

The extreme conditions associated with AGN provide us with a unique laboratory for testing the limits of complex physical theories such as general relativity. Furthermore, observations suggest that every massive galaxy hosts a central supermassive black hole that will undergo an active phase at least once during its lifetime, releasing large amounts of energy that can significantly alter the properties of the host galaxy and even its large-scale environment (e.g. Cattaneo et al., 2009; Fabian, 2012; Veilleux et al., 2020). Through these *feedback* effects, it has become clear that AGN also hold high importance in a cosmological framework, being tied to the formation and evolution of the galaxies in which they reside.

Radio AGN host powerful relativistic jets that may couple particularly efficiently with the gas in the surrounding interstellar and intergalactic media (e.g. McNamara & Nulsen, 2007; Wagner & Bicknell, 2011; Fabian, 2012; Wagner et al., 2012; Mukherjee et al., 2016, 2018a,b), and so both observational and theoretical investigation of the *triggering*, accretion, and feedback properties of this subpopulation are crucial for further advancing our understanding of galaxy evolution. Deep radio surveys with broad sky coverage have revealed that the local radio AGN population is dominated by lower-power sources (Mauch & Sadler, 2007; Best & Heckman, 2012; Sadler et al., 2014; Sabater et al., 2019), and there is evidence that the substantial subset of these objects that have strong optical emission lines and intermediate radio powers ($10^{22.5} < L_{1.4\mathrm{GHz}} < 10^{25}$ $\mathrm{W\,Hz^{-1}}$) are capable of driving strong multiphase outflows on galaxy scales (e.g. Mullaney et al., 2013; Tadhunter et al., 2014a; Harrison et al., 2015; Villar-Martín et al., 2017). Although these objects could, therefore, hold particular importance in the context of the AGN-host galaxy connection, the properties of these objects remain relatively unexplored. This is the main open issue that this thesis aims to help address.

In this chapter, I provide a general introduction to our current knowledge of AGN and their relationships with their host galaxies, with a particular focus on radio AGN, and define some of the key terms and concepts that will be referred to throughout this thesis. A brief historical introduction to galaxies and AGN is provided in §1.2. Common classifications of AGN are outlined in §1.3, where the conventional "unified model" of

AGN activity is also presented. The evidence for a link between AGN and their host galaxies is discussed in §1.4. A focused discussion on the feedback mechanisms, host galaxy properties, accretion modes, and triggering of radio AGN is provided in §1.5, where the importance of lower-power radio AGN is also presented. §1.6 then introduces the open questions that this thesis aims to help address, and outlines its general structure and the contents of the subsequent chapters.

1.2 Brief historical context

1.2.1 Galaxies

While the existence of extragalactic bodies was first postulated in the eighteenth century (Wright, 1750; Kant, 1755; Herschel, 1785), it was not until the turn of the twentieth century that supporting observational evidence began to accumulate. Spectroscopic observations of what were then referred to as "spiral nebulae" (e.g. as identified by Rosse, 1850, and later, with improved observational capabilities, by Keeler, 1899) revealed predominantly continuous/absorption line spectra that were consistent with a stellar origin (Scheiner, 1899; Huggins & Huggins, 1899; Fath, 1909), but that typically also implied large radial velocities (Slipher, 1915, 1917b). This led to suggestions that these nebulae were, in fact, "island universes" at large distances from the Milky Way.[1] The discovery of a period-luminosity relationship for Cepheid variable stars (the Leavitt Law; Leavitt, 1908; Leavitt & Pickering, 1912) allowed for the first reliable estimates of distances to nebulae that contained them (Hubble, 1925, 1926a, 1929b), which confirmed their extragalactic nature and inspired Hubble to propose the now well-known correlation between radial velocity (i.e. redshift, z) and distance, for extragalactic objects (the Hubble Law; Hubble, 1929a). It also became clear that the structure of these external galaxies was not limited to spirals, since elliptical and "irregular" shapes were also exhibited; the appearance of galaxies is still regularly classified using these broad categorisations from the basic visual scheme introduced by Hubble (1926b).

The realisation that there are vast collections of stars in the Universe of varying shapes and sizes that exist far beyond the extent of the Milky Way provided a significant paradigm shift, not just for the field of astronomy, but for human perception in general. These breakthroughs therefore paved the way for the beginning of extragalactic astronomy as a serious research discipline. Considerable technological advancements

---

[1] This idea was one of the key components of "The Great Debate" of the 1920s, regarding the true scale of the Universe and of our Galaxy within it (e.g. Shapley & Curtis, 1921).

since this period have facilitated the growing interest in investigating the properties of extragalactic phenomena from both observational and theoretical perspectives, allowing the topic to play an important role at the forefront of modern astronomical research. One modern study has now estimated that the observable universe is host to over two trillion galaxies, of which approximately 200 billion would be observable at the limits of current optical instrumentation (Conselice et al., 2016). The central goal of this area of research is to understand the formation and evolution of these galaxies, along with the cosmological importance of the interplay that they have with their large-scale environments. As will be outlined in the remainder of this introduction, each of these aspects are believed to be intimately linked with their central supermassive black holes and the *active galactic nucleus* (AGN) phenomenon that is associated with them.

1.2.2 Active galactic nuclei

While investigating the spectra of spiral nebulae, Fath (1909) had also unknowingly found the first observational evidence for AGN, noting that NGC 1068, alongside its otherwise star-like spectrum, exhibited strong emission lines akin to those found in gaseous nebulae. Subsequent observations by Slipher (1917a) and Campbell & Moore (1918) confirmed this, with the latter study also noting the presence of a comparable spectrum in the object NGC 4151. Hubble (1926b) later grouped these objects with another spiral nebula, NGC 4051, as "rare cases of apparent stellar nuclei" with the "typical planetary [nebula] spectrum". In a period where the developing interest in extragalactic objects tended to focus on their more general properties, however, these "rare" objects were typically neglected, until their systematic study by Carl K. Seyfert over a decade later.

Seyfert (1943) used spectral observations of six "emission spirals" with nuclear emission of "high-excitation" (including the aforementioned objects) to contrast the broad ($>10^3$ km s^{-1}) permitted and/or forbidden lines seen in these galaxy nuclei with the narrow line spectra of diffuse nebulae (i.e. HII regions) in the main body of irregular and spiral galaxies. This provided the first evidence that these objects comprised a class in their own right. Even though some of the galaxies Seyfert originally identified were later not included in the class (e.g. Burbidge et al., 1963b), these eventually became known as *Seyfert galaxies*. While broad emission lines were typically the deciding factor in their identification, Seyfert galaxies were also characterised by very bright nuclei in optical images and strong, and sometimes variable, non-stellar continua, with notable ultraviolet excesses (e.g. see Weedman, 1977, and references therein).

It was around this period that the discipline of radio astronomy began, and its subsequent rapid growth played a key role in launching the field of AGN research. In the 1930s, Karl G. Jansky had discovered that the Milky Way was actually a considerable radio source that caused static for transatlantic radio communications, with the strongest emission originating in its centre in the constellation of Sagittarius (Jansky, 1935). Grote Reber later investigated this "cosmic static" further and provided the first map of the radio sky (at 160 MHz), identifying several additional emission maxima in other constellations (Reber, 1944). As the capabilities of radio observations improved, it became clear that the radio sky was in fact host to many bright, discrete sources (Bolton, 1948; Ryle & Smith, 1948; Ryle et al., 1950), some of which were consistent with the positions of Reber's maxima. These advancements also allowed for more accurate positions to be derived for these radio sources, paving the way for the first identifications of their optical counterparts, of which several proved to be external galaxies (e.g. Bolton et al., 1949; Baade & Minkowski, 1954a,b; Minkowski, 1960). The early signs that at least some of these *radio galaxies* were also associated with strong emission lines (Baade & Minkowski, 1954a; Minkowski, 1960) were confirmed by later results, with a minority exhibiting Seyfert-like spectra (Schmidt, 1965a; Sandage, 1966; Burbidge, 1967). Like Seyferts, some radio galaxies also showed bright nuclei in optical images (sometimes named "N galaxies", e.g. Matthews et al., 1964) and several were seen to be variable (at optical and radio wavelengths; Kellermann & Pauliny-Toth, 1968), providing some early suggestions that the two groups might be linked.

In addition, some radio sources were found to coincide with objects that were star-like in their optical appearance but that exhibited certain unusual properties: excess ultraviolet radiation; photometric variability; broad emission lines in unexpected spectral regions. These became known as "quasi-stellar radio sources", "quasi-stellar sources", or *quasars*[2]. While initially thought to be foreground stars with irregular properties, Maarten Schmidt and his colleagues realised that key spectral features for the seminal cases 3C 273 and 3C 48 could be well explained by known Balmer or forbidden emission lines that were redshifted by $z = 0.16$ and $z = 0.37$, respectively (Schmidt, 1963; Greenstein & Matthews, 1963). High redshifts became a common feature once further identifications were made (Schmidt, 1965b), and since these were hard to reconcile with the picture of an origin in or near to the Milky Way (e.g. Greenstein & Schmidt, 1964), their interpretation as distant extragalactic sources eventually gained favour (a sum-

---

[2] From this point forward, the term "quasars" is used in this thesis to refer to quasi-stellar objects both with and without associated radio emission. This is in line with the modern usage of the term, which is often simply used to refer to very luminous AGN with bolometric luminosities ($L_{\rm bol}$, the integrated luminosity across all wavelengths) in excess of 10^{38} W (10^{45} erg s^{-1}).

mary is given by Weedman, 1976a). Soon after, it became apparent that there was a large population of quasi-stellar objects that lacked an associated radio source but still showed ultraviolet excesses, broad emission lines, and systematically high redshifts (Sandage, 1965). These also appeared to be much more numerous (Sandage & Luyten, 1967; Lynden-Bell, 1971). Quasars were hence found to be reminiscent of Seyfert galaxies, except for their typically higher luminosities and redshifts (Weedman, 1976b), which led to the now accepted idea that they were simply more distant, more extreme examples of the Seyfert phenomenon (e.g. Weedman, 1977).

Supported by the accumulation of further photometric and spectral data, it therefore became clear that Seyfert galaxies, quasars, and at least some radio galaxies shared several key properties: i) strong and/or broad emission lines in their nuclear spectra; ii) bright nuclear regions in images; iii) strong and sometimes variable continuum emission, particularly at optical/ultraviolet wavelengths. Early X-ray observations of Seyferts, quasars, and radio galaxies suggested that bright, and sometimes variable, X-ray emission was also a common feature (e.g. Elvis et al., 1978; Tananbaum et al., 1979; Zamorani et al., 1981; Fabbiano et al., 1984). The variability timescales and extreme luminosities of the nuclear emission (optical, radio and X-ray) also implied that a very compact source of high energy was common to the three groups. Through these growing bodies of evidence, the idea that they represented different manifestations of the same phenomenon gained acceptance, and so their collective categorisation as *active galactic nuclei (AGN)* began.

From early on it was realised that the extreme luminosities associated with these sources could have a significant impact on the galaxies in which they reside (Burbidge et al., 1963a), which, coupled with the mystery of their compact sizes and the physical mechanisms that might be involved, presented interesting and important problems that deserved much further investigation. This brought AGN to the forefront of extragalactic astronomical research, and laid the foundations for the vast amount of work that has been undertaken in this area since this time. Further review of the history of AGN research is beyond the scope of this thesis, and so only the aspects that are key to its main focus will be addressed in detail in the remainder of this introduction. Before moving on to more specific discussions, however, the next subsection details how the now widely-accepted model of their fuelling by supermassive black hole accretion was established.

1.2.3 Supermassive black holes

The puzzle of the energy source associated with AGN activity presented a unique and unprecedented problem in astronomical research. Short variability timescales indicated an extremely small size for the emitting region (light-days to light-months), which simultaneously had to be capable of producing the high luminosities associated with Seyfert galaxies, radio galaxies, and quasars ($L_{\rm bol} \approx 10^{35}$–$10^{40}$ W). As a consequence, a plethora of novel early theories developed to explain the phenomenon, linked to: (i) stellar collisions in a dense nuclear star cluster (Woltjer, 1964; Spitzer & Saslaw, 1966); (ii) very frequent, or possibly chain reactions of, supernovae (Burbidge, 1961; Colgate, 1967, 1968); (iii) supermassive stars (Hoyle & Fowler, 1963a,b); (iv) rapidly rotating, highly magnetised bodies of plasma (sometimes called ‘magnetoids’ or ‘spinars’; Ozernoi, 1966; Morrison, 1969; Piddington, 1970; Morrison & Cavaliere, 1971); (v) accreting supermassive black holes (SMBHs; Salpeter, 1964; Zeldovich & Novikov, 1964; Lynden-Bell, 1969).

Although diverse in their approaches, the majority of these theories required gravitational potential to provide the energy reserve for the various different types of emission observed, since the relative inefficiency of alternative processes (e.g. nuclear fusion) made them unrealistic (Lynden-Bell, 1978). Of these models, the highest energy conversion efficiencies were available via black hole accretion, particularly when the possibility of rotation was considered (Bardeen, 1970; Thorne, 1974; Blandford & Znajek, 1977; see §1.3.3). Furthermore, in the majority of the alternative scenarios, the natural end product was gravitational collapse to a supermassive black hole (e.g. Rees, 1978a, 1984). Therefore, while it was generally agreed that these preliminary stages might play a role in some forms of nuclear activity, an accreting supermassive black hole proved to be the most attractive proposition for sustaining prolonged periods of activity in an efficient manner (Rees, 1984; Begelman et al., 1984); this was crucial, for instance, when considering the large scale, continuous radio structures that emanated from the nuclei of some radio galaxies and quasars (Lynden-Bell, 1978; Rees, 1978b).

Once AGN fuelling by SMBH accretion had become accepted theoretically, the last piece of the puzzle lay in finding evidence for their existence. Given that quasar activity was seen to be most common at a redshift of $z \sim 2$, one of the key implications of the theory was that there should be many “non-active” SMBH remnants, i.e. “dead quasars”, in galaxies at lower redshifts (Lynden-Bell, 1969; Soltan, 1982). Observational searches therefore mostly focused on measuring the kinematics of the stars and gas in the nuclei of nearby galaxies, probing the regions expected to lie within the gravitational

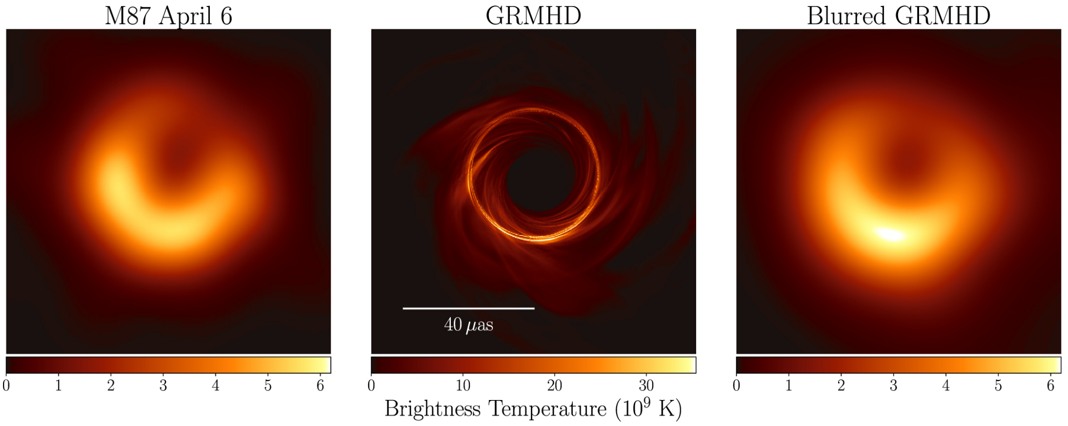

Figure 1.1: An image of the emission ring and "shadow" of the SMBH in the nearby giant elliptical galaxy M87, constructed from Event Horizon Telescope observational data (left panel). The ring has a diameter of $42 \pm 3\,\mu$as. This is accompanied by a model of the accretion flow (middle panel) and the synthetic image produced when it is smoothed to match the resolution of the observations (right panel). Brightness temperature is a measure of the relative intensity of the black body radiation produced. Figure credit: Event Horizon Telescope Collaboration et al. (2019b).

influence of the SMBHs.

While early evidence for SMBHs in some of these galaxies was obtained from ground-based spectroscopic observations (Kormendy & Richstone, 1995), the major breakthroughs in this aspect came after the launch of the *Hubble Space Telescope (HST)*. This afforded major improvements in the sensitivity and spatial resolution capabilities of both photometry and spectroscopy, and the flood of data on stellar and ionised gas dynamics that followed progressed research on black hole demographics significantly (Kormendy & Ho, 2013). Supplemented by evidence from circumnuclear water maser disks (e.g. Kuo et al., 2011), reverberation mapping (e.g. Peterson et al., 2004; Bentz et al., 2009), and the proper motions of stars around the Galactic centre (Genzel et al., 2010), this left little doubt of the existence and abundance of SMBHs with typical masses $\sim 10^6 - 10^9$ $M_\odot$ in both active and non-active galaxies. More recently, observational evidence for SMBHs has culminated in the groundbreaking results from *Event Horizon Telescope*[3] data for the nearby elliptical galaxy M87, which have provided the first ever direct images of the "shadow" that is expected to result from gravitational lensing effects near the event horizon of a black hole (see Figure 1.1; project summarised in Event Horizon Telescope Collaboration et al., 2019a).

---

[3] The Event Horizon Telescope is a very long baseline interferometer with a maximum baseline length that is close to the diameter of the Earth. Observing at its operating frequency of 1.3 mm, it can achieve a diffraction-limited resolution of $\sim 25\,\mu$as (Event Horizon Telescope Collaboration et al., 2019a).

As a consequence of the theoretical and observational evidence described here, it is now very widely accepted that SMBHs lie at the centre of at least the vast majority of massive galaxies ($M_* \approx 10^{10} - 10^{12}$ $M_\odot$), and that these galaxies undergo phases of strong SMBH accretion during which they manifest as an AGN.

1.3 AGN classifications and unification

As the field of AGN research developed, it became apparent that the phenomenon is associated with many different types of emission that span the entire electromagnetic spectrum, reflecting the variety of physical processes that can occur within them (see Padovani et al., 2017, for a recent review). This provides several routes through which they can be identified. In reality, it is often hard to detect all of these characteristic sources of electromagnetic radiation for each AGN, and so we instead rely on subsets of these indicators for their identification. Furthermore, AGN are diverse in the relative intensities of the emission they exhibit in each waveband. These factors have led to the development of several "classes" or "types" of AGN. In accordance with the focus of this thesis, I here outline some key examples of AGN classifications that are based on their optical and radio properties. Although some of the observed dissimilarities between the classes/types are thought to be caused by differing intrinsic physical properties, for example between different types of radio galaxies (see §1.5), many are interpreted to be the result of viewing the active nucleus along different lines of sight, such that there is a fundamental structure that is inherent to all AGN. This commonly accepted "unified model" is also described in this section.

1.3.1 Optical classifications

In general, the three original classes of AGN – Seyfert galaxies, quasars, and radio galaxies – are still commonly used as broad categorisations in modern day research. As mentioned in the previous section, a key recurring feature for AGN in each of these categories is strong emission line spectra at optical wavelengths, which typically include permitted hydrogen and or helium lines, and forbidden lines from other ionised atomic species (e.g. oxygen, nitrogen, sulphur, neon, iron). Once optical spectral data became more abundant, it was found that Seyfert galaxies could be divided into two main subclasses based on the relative breadth of these permitted and forbidden emission lines (e.g. Khachikian & Weedman, 1974): i) "class 1", "Type 1", or "Seyfert 1", with broad permitted lines ($\sim 10^3 - 10^4$ $\mathrm{km\,s^{-1}}$) and narrower ($\sim 10^2 - 10^3$ $\mathrm{km\,s^{-1}}$) forbidden

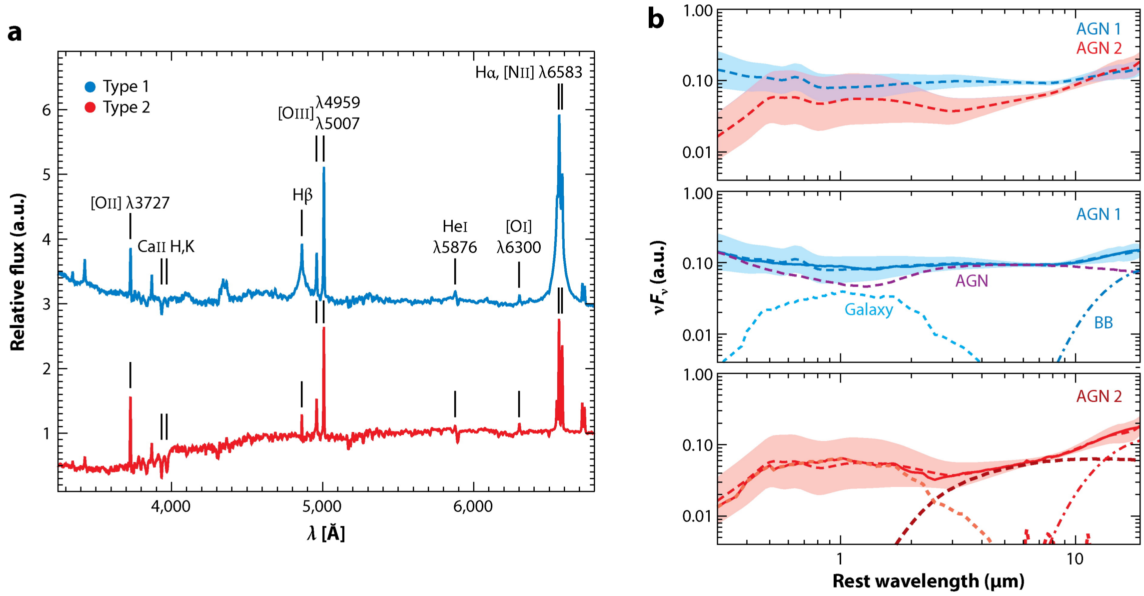

Figure 1.2: Composite SDSS optical spectra (a) and SDSS/UKIDSS/WISE optical to mid-infrared spectral energy distributions (SEDs) (b) for Type 1 and Type 2 AGN. Figure credit: Hickox & Alexander (2018).

lines; and ii) "class 2", "Type 2", or "Seyfert 2", with permitted and forbidden lines of the same width.[4] In addition, Type 1 Seyferts exhibit bright, non-stellar, point source continuum emission in many wavebands, while Type 2 Seyferts show comparatively weak or non-existent non-stellar continua. Both of these features are exhibited in Figure 1.2 (from Hickox & Alexander, 2018), which shows composite optical spectra and optical to mid-infrared spectral energy distributions (SEDs) for Type 1 and Type 2 AGN selected from the *Sloan Digital Sky Survey (SDSS)*.

While originally identified for Seyfert galaxies, similar classifications have also been defined for quasars and radio galaxies. Type 1 quasars are the traditional "quasi-stellar objects" that represent the high-luminosity counterparts of Seyfert 1s, exhibiting more intense optical/ultraviolet continuum emission and comparable characteristic strong optical emission spectra, with broad permitted lines and narrower forbidden lines. Large numbers of Type 2 quasars – high redshift, luminous counterparts of Seyfert 2s that lack the strong, point-source continuum of Type 1s – have also been identified through their optical spectral properties (e.g. Zakamska et al., 2003; Reyes et al., 2008). In these cases, Type 2 quasars are typically separated from Seyfert 2s based on the luminosity of

---

[4] While further sub-classifications have been suggested (e.g. Seyfert 1.5, 1.8, 1.9; Osterbrock, 1989), only the more commonly used general classifications of Type 1 and Type 2 AGN are considered throughout this thesis.

the [OIII]λ5007 emission line ($L_{[OIII]}$), with a canonical boundary at $L_{[OIII]} > 3 \times 10^8$ $L_\odot$ ($\sim 10^{35}$ W; Zakamska et al., 2003).

In line with the Type 1 and Type 2 divisions for Seyfert galaxies and quasars, radio galaxies with strong emission line spectra can similarly be separated into two classes based on the relative widths of their permitted and forbidden lines: broad-line radio galaxies (BLRGs, analogous to Type 1s; e.g. Osterbrock et al., 1976; Grandi & Osterbrock, 1978) and narrow-line radio galaxies (NLRGs, analogous to Type 2s; e.g. Costero & Osterbrock, 1977). Collectively, BLRGs and NLRGs can be referred to as "strong-line radio galaxies" (SLRGs; e.g. Ramos Almeida et al., 2011) or "high-excitation radio galaxies" (HERGs; based on the "high excitation galaxy" class of Laing et al., 1994; Buttiglione et al., 2010). In contrast with the other main AGN groups, however, a significant population of radio galaxies with weak optical emission lines also exists (Hine & Longair, 1979), and, in fact, appears to dominate the local radio AGN population (see Figure 1.9; Best & Heckman, 2012). To align with the SLRG/HERG classes, these are commonly referred to as "weak-line radio galaxies" (WLRGs; e.g. Tadhunter et al., 1998) or "low-excitation radio galaxies" (LERGs; again based on Laing et al., 1994; Buttiglione et al., 2010). Note that while there is significant overlap between the SLRG/WLRG and HERG/LERG classification schemes (Tadhunter, 2016), they are defined in different ways and are hence not identical – SLRGs and WLRGs are separated by a boundary in [OIII]λ5007 equivalent width (SLRGs have $EW_{[OIII]} > 10$ Å and WLRGs have $EW_{[OIII]} < 10$ Å), while HERGs and LERGs are identified through their emission line ratios (see below).

In addition to these traditional classes of "strong" AGN, one further population that has relevance for this thesis is the Low Ionization Nuclear Emission-line Region (LINER) class of active nucleus (Heckman, 1980). These objects have relatively weak optical emission lines that indicate low ionisation states in the emitting regions and appear to be much more common than strong AGN (Heckman, 1980; Ho et al., 1997). They are therefore similar to WLRGs/LERGs in both of these senses – however, note that, because the latter classification is based on emission line ratios, some LERGs still show evidence for relatively strong optical emission lines (e.g. see spectrum of 3C 84 in Buttiglione et al., 2009). While there are strong arguments that at least a proportion of LINERs could be ionised by stellar radiation fields from, for example, post asymptotic giant branch stars (e.g. Cid Fernandes et al., 2011; Singh et al., 2013), this is not yet conclusive (e.g. Coldwell et al., 2018; Frederick et al., 2019), and so they are included here as a potential class of weak AGN with implied similarity to WLRGs/LERGs, for

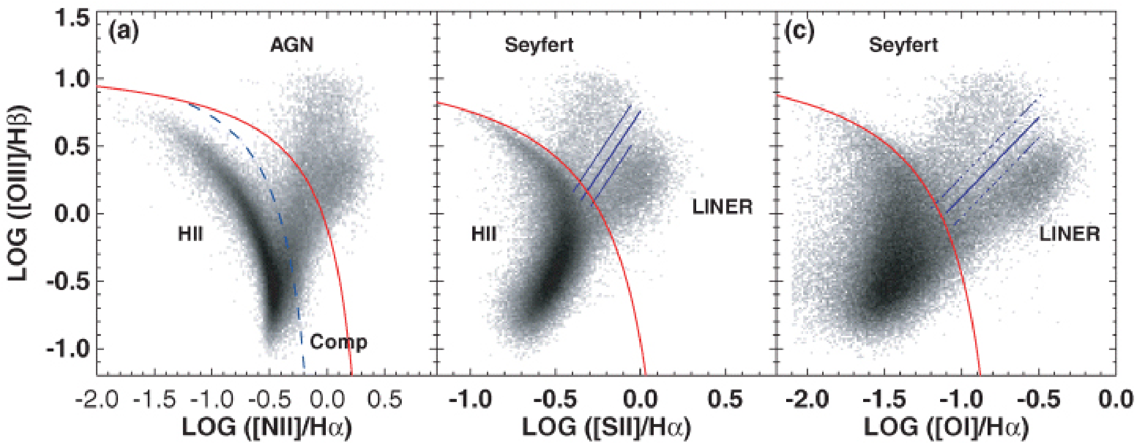

Figure 1.3: An example of diagnostic diagrams that separate "strong" AGN (such as Seyfert galaxies) from star forming galaxies (with HII regions) and "weak" LINER AGN. The curves divide AGN from galaxies with strong (dashed blue) and extreme (solid red) star formation, While the solid blue lines (centre and right-hand panels) indicate the separation between galaxies with Seyfert-like and LINER-like spectra. Figure credit: Kewley et al. (2006).

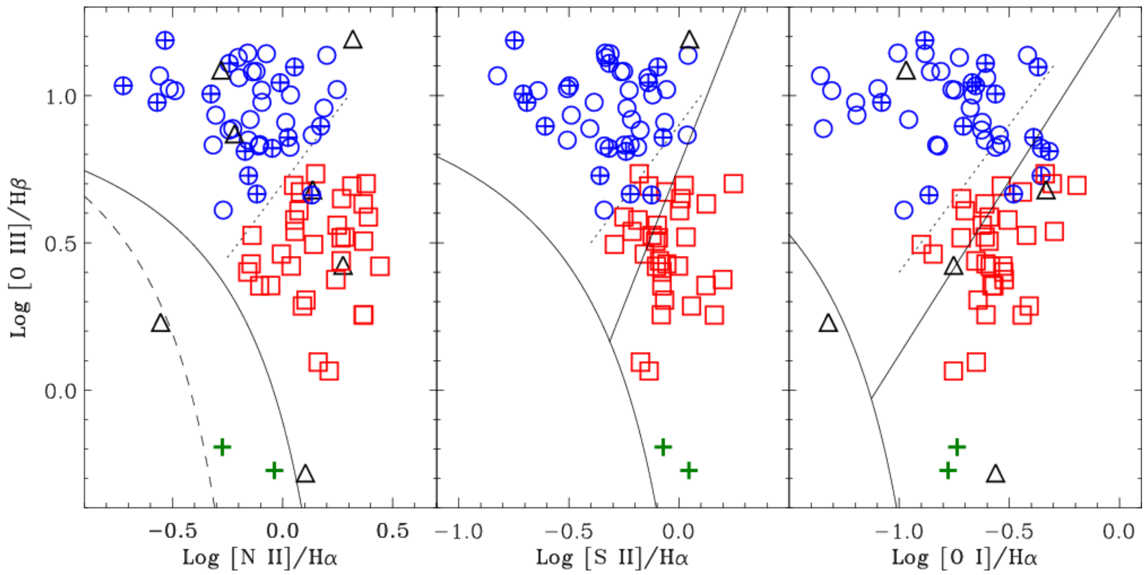

Figure 1.4: Example of diagnostic diagrams that separate high excitation radio galaxies (HERGs; blue symbols) from low excitation radio galaxies (LERGs; red symbols). The dashed line indicates the proposed separation between high-excitation and low-excitation spectra, while the solid lines represent the divisions from the scheme of Kewley et al. (2006), as shown in Figure 1.3. Figure credit: Buttiglione et al. (2010).

completeness.

So-called emission line diagnostic diagrams are often used to distinguish strong AGN

(Seyfert-like) from other galaxies with detectable emission lines: galaxies with high rates of star formation or weak, LINER-like spectra (e.g. Baldwin et al., 1981; Kewley et al., 2006). These typically utilise the intensity ratios of commonly detected permitted and forbidden emission lines (e.g. Hα, Hβ, [OI]λ 6364, [OIII]λ 5007, [NII]λ 6584, [SII]$\lambda\lambda$ 6719, 6731), which provide information on the physical properties of the emitting regions, such as ionisation and excitation level, temperature, and density. Similar plots have also been used to separate HERGs from LERGs (e.g. Buttiglione et al., 2010). Diagnostic diagrams are regularly used as a standard method for defining samples of optically selected AGN and their sub-types. Examples of these diagrams are shown in Figures 1.3 and 1.4.

1.3.2 Radio classifications

Due to the fact that radio astronomy played a crucial role in the early development of the field of AGN research, study of the radio properties of AGN has received much focused attention. As a result, alongside the optical classifications outlined above, *radio AGN*[5] have also been separated into various classes based on the continuum and spectral properties of their radio emission. Many alternative classifications to those outlined in this section exist in the literature, but these are not described here for the sake of maintaining brevity and relevance.

Once large amounts of radio interferometry observations of powerful radio galaxies had been acquired, it became clear that they typically showed extended emission structures that were double in nature, and that these could mostly be separated into two distinct morphological classes: i) edge-darkened structures, for which the brightest extended emission was concentrated within less than half of the total source size (Fanaroff-Riley Class I or FRI); ii) edge-brightened structures, for which the brightest extended emission was present at distances greater than half of the total size (Fanaroff-Riley Class II or FRII; Fanaroff & Riley, 1974). Examples of these two classifications are presented in Figure 1.5.

In addition to the difference in their morphological appearance, it originally seemed that the two classes were separated by radio power, with FRI sources being of lower radio luminosity than FRIIs (Fanaroff & Riley, 1974), in a way that appeared to be connected to the optical luminosity of the host galaxy (e.g. Owen, 1993; Ledlow & Owen, 1996). This led to suggestions that FRII sources represent those with powerful jets that remain

---

[5] Note that throughout this thesis, I will use the term “radio AGN” to refer to AGN that have a clear association with radio emission from their relativistic jets, regardless of its luminosity. This therefore includes cases from both the “radio-loud” and “radio-quiet” populations traditionally used in the literature (see §1.5.5 for discussion of these classes).

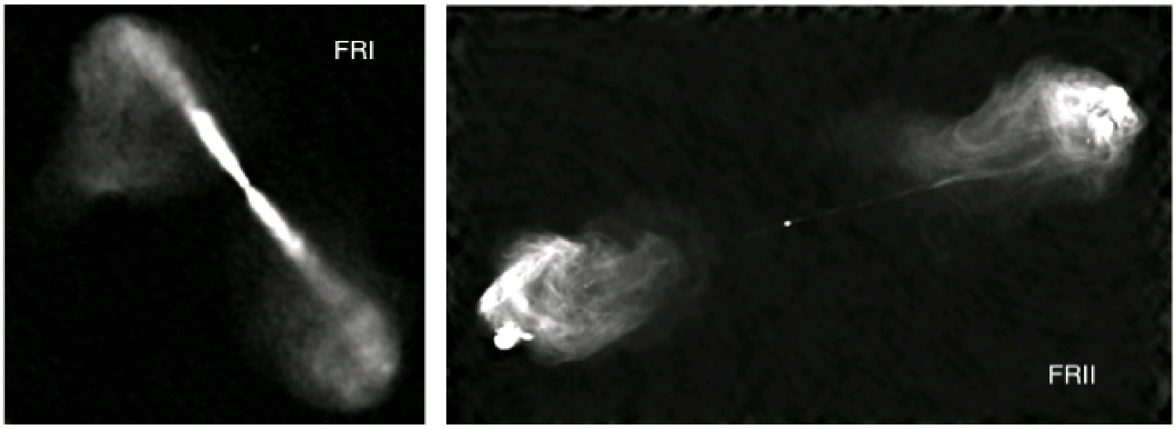

Figure 1.5: Examples of radio galaxies that exhibit the two Fanaroff & Riley (1974) classifications of extended radio structure: 3C 296, with the edge-darkened Fanaroff-Riley Class I (FRI; left); and Cygnus A (3C 405), with the edge-brightened Fanaroff-Riley Class II (FRII; right). Both images were downloaded from the NASA/IPAC Extragalactic Database (NED).

relativistic to large distances, while FRI jets are disrupted on host galaxy scales either because of their relative weakness or the influence of denser gas environments, or both (e.g. Bicknell, 1995; Kaiser & Best, 2007; Tchekhovskoy & Bromberg, 2016). However, recent work has shown that FRI/FRII divisions based on the source radio power and the luminosity of the host galaxy are not as clean as first thought (e.g. Best, 2009; Capetti et al., 2017; Mingo et al., 2019), which causes complications with these interpretations.

In addition to those exhibiting large extended radio structures, a significant proportion of powerful radio galaxies have radio morphologies that are compact on galaxy scales. The two main classes of these objects are Compact Steep-Spectrum (CSS) and Gigahertz Peaked-Spectrum (GPS) sources, both of which typically have double radio structures that suggest a continuity in morphology from the Fanaroff-Riley classes (O'Dea, 1998). They are, however, separated from each other through both their sizes and spectral properties, with CSS sources exhibiting steep radio spectra[6] and structures

---

[6] Radio spectra are most commonly characterised through their spectral indices (α), defined such that $F_\nu \propto \nu^\alpha$, where F_ν is the monochromatic flux density at frequency ν. In this form, the theoretical prediction for a typical synchrotron emitting source, such as the relativistic jets associated with AGN, is $F_\nu \propto \nu^{-0.7}$. This spectrum is expected to rise towards lower frequencies in the few hundred megahertz to few hundred gigahertz region, which makes the gigahertz-peaked spectra of GPS sources particularly unusual; this effect is thought to be caused by free-free or self absorption of the synchrotron radiation by ionised particles in or surrounding the emitting regions (Kellermann & Pauliny-Toth, 1981; O'Dea, 1998; Callingham et al., 2015). With this definition, "steep" spectra are typically characterised by $\alpha \lesssim -0.5$, and "flat" spectra by $\alpha \gtrsim -0.5$. (Note that in some of the literature α is defined by $F_\nu \propto \nu^{-\alpha}$, such that $F_\nu \propto \nu^{-0.7}$ would give $\alpha = 0.7$, but the earlier definition is preferred for this thesis.)

$\lesssim$15 kpc in diameter, and GPS sources exhibiting sub-kpc diameters and convex spectra peaking at gigahertz frequencies (O'Dea, 1998). Both groups are thought to represent young radio sources that will eventually evolve to display extended, Fanaroff-Riley-like structures (O'Dea, 1998; Polatidis & Conway, 2003; Orienti, 2016). For the FRII class in particular, this is supported by the double-lobed "mini-FRII" structures (~0.1–0.3 kpc) shown by all seven CSS/GPS sources in the high-flux-density 2Jy sample in Very Long Baseline Interferometry (VLBI) observations (Tzioumis et al., 2002).

At this point, it is important to note that the advent of highly sensitive radio surveys with large-scale sky coverage has revealed that the radio AGN population is dominated by sources of lower radio power than those outlined above (e.g. Best et al., 2005b; Best & Heckman, 2012), many of which also appear to have compact radio structures (Baldi & Capetti, 2009; Sadler et al., 2014; Whittam et al., 2016; Hardcastle et al., 2019). These have frequently been referred to as "FR0" sources (following Ghisellini, 2011), in order to highlight their lack of extended emission relative to FRI- and FRII-like objects. These sources hold notable importance for one of the projects outlined in this thesis, and, as such, receive more focused attention in a later chapter (Chapter 6).

1.3.3 The unified model

The diversity in the properties of the different classifications of AGN highlights the many ways in which nuclear activity can manifest itself. As outlined in §1.2.3, the commonly accepted paradigm dictates that this activity is fuelled (with the potential exception of LINER sources) by accretion onto the supermassive black holes that are thought to lie at the centre of the vast majority of massive galaxies. In order for this to be the case, an explanation of how the variety of manifestations of the activity could result from the same fuelling source was required. This led to the development of so-called "unified models" of AGN activity.

In the conventional picture (e.g. similar to Rees, 1984; Antonucci, 1993; Urry & Padovani, 1995), the strong gravitational influence of the SMBH allows gas, dust and stars from its near surroundings to settle into a sub-parsec scale disk that orbits around it. The SMBH then grows in mass by accreting material from the inner regions of this disk. Several physical processes within the accretion disk and surrounding regions can then lead to the conversion of a large fraction of the gravitational potential energy in the system to strong electromagnetic radiation over a broad range of wavelengths. Viscous processes in the accretion disk cause it to reach high temperatures and emit intense thermal continuum emission, which often manifests most strongly at ultraviolet wavelengths. A corona of hot electrons above the disk can convert these emitted photons to X-ray energies through inverse Compton scattering. Dense clouds of off-planar gas close to the disk emit broad permitted lines (the broad-line region or BLR), while lower-density clouds of gas (and dust) at larger radial distances emit narrower permitted and forbidden lines (the narrow-line region or NLR), both predominantly at optical, ultraviolet, and infrared wavelengths. A toroidal[7] region of dust surrounding the disk (the torus) absorbs the emission produced in these inner regions and produces thermal radiation at infrared wavelengths. In some cases, powerful relativistic jets launched near the black hole produce synchrotron radio emission at the lowest frequencies and gamma rays at the highest frequencies. These features identify the phenomenon that is referred to as an active galactic nucleus, or AGN.

The ultimate energy source for an AGN is the gravitational potential energy of the material accreted onto the SMBH. For a mass m drawn from a very large distance ($r \to \infty$) to a radius r_{lso} (the last stable orbit) by the gravitational influence of the SMBH, this has the form $V = -GM_{\bullet}m/2r_{lso}$ (in a virialised system, where G is the gravitational constant and $M_{\bullet}$ is the mass of the black hole). Under the assumption that the viscous processes in the accretion disk cause all of this gravitational potential energy to be radiated away, the luminosity provided by mass accreted at rate $\dot{m}$ has the form $L = -GM_{\bullet}\dot{m}/2r_{lso}$. For a non-rotating SMBH, the last stable orbit lies at three Schwarzschild radii ($3r_s$, where $r_s = 2GM_{\bullet}/c^2$; c is the speed of light), placing an upper limit of $L = \frac{1}{12}\dot{m}c^2$ on the resulting luminosity; i.e. a rest-mass energy conversion efficiency of $\epsilon = \frac{1}{12} = 0.08$. For accretion onto a spinning (Kerr) SMBH, the last stable orbit lies at radii below $3r_s$, and full general-relativistic treatments suggest radiative efficiencies of up to $\epsilon \approx 0.40$ (e.g. Bardeen, 1970; Thorne, 1974; Blandford & Znajek, 1977) – this greatly improved efficiency is one of the main reasons that this latter model is favoured for AGN fuelling. Despite these theoretical estimates of the radiative efficiency, values of order $\epsilon = 0.10$ are typically assumed in practice (e.g. Marconi et al., 2004).

The orientation of the active nucleus (more specifically the torus) relative to the line-of-sight of the observer is thought to be the crucial factor in determining whether a Type 1 or Type 2 AGN is seen. Type 2/NLRG nuclei would be viewed along lines of sight for which the emission from the central regions is obscured by the dusty torus, and hence only the narrower forbidden emission lines from the NLR clouds are observed. Type 1/BLRG nuclei are then those that are viewed along unobscured lines of sight towards the central SMBH, and thus emission from the accretion disk and BLR can be

---

[7] Note that in reality, this structure is likely complex, dynamic, and clumpy (e.g. Ramos Almeida & Ricci, 2017).

observed in addition to that from the NLR. A visual representation of the structure of an AGN described by the unified model and the proposed effect of orientation relative to the line-of-sight can be seen in Figure 1.10a ("Radiative-mode AGN").

One major line of evidence in support of these orientation arguments is the fact that the polarised optical spectrum of some Type 2 AGN, which represents the reflected component of light from the inner regions, exhibits the features characteristic of a Type 1 spectrum (e.g. Antonucci & Miller, 1985; Moran et al., 2007; Ramos Almeida et al., 2016). Furthermore, the detections of both Type 1 and Type 2 optical AGN in other wavebands – importantly at hard X-ray ($> 10\,\mathrm{keV}$) and near-infrared wavelengths, where the emission is theoretically much less obscured by the nuclear regions, and mid-infrared wavelengths, where the emission is thought to originate from the torus itself – provide other strong sources of supporting evidence (see Hickox & Alexander, 2018, for an overview).

The different classes of AGN can then be explained in terms of the various different physical properties outlined above, and observations of the expected emission and absorption characteristics of these processes therefore also provide many routes through which AGN can be identified. This then allows AGN to be selected efficiently in large-scale surveys in many different wavebands, a feature that has played an important role in allowing AGN to develop into one of the key components of modern astronomy research.

1.4 The connection between AGN and their host galaxies

As mentioned in §1.2.3, it is now commonly accepted that supermassive black holes (SMBHs) should lie at the centre of the vast majority of massive galaxies ($\mathrm{M}_* \approx 10^{10} - 10^{12}\ \mathrm{M}_\odot$), originally postulated as the "dead remnants" that should exist after phases of nuclear activity (e.g. Lynden-Bell, 1969; Soltan, 1982; Yu & Tremaine, 2002; Ferrarese & Ford, 2005; Ho, 2008). The wide acceptance of the AGN/SMBH model, as well as the growing information available on SMBHs and their host galaxies, has led many studies to suggest that the evolution of SMBHs and their hosts are causally connected. The leading body of evidence in this regard is the fact that the dynamically-inferred masses of these central SMBHs (typically $10^6 - 10^9\ \mathrm{M}_\odot$) are in fact tightly correlated with the stellar velocity dispersions and luminosities of bulge structures in local galaxies (Magorrian et al., 1998; McLure & Dunlop, 2002; Marconi & Hunt, 2003; McConnell & Ma, 2013; Kormendy & Ho, 2013; Läsker et al., 2014; van den Bosch et al., 2015; de Nicola et al.,

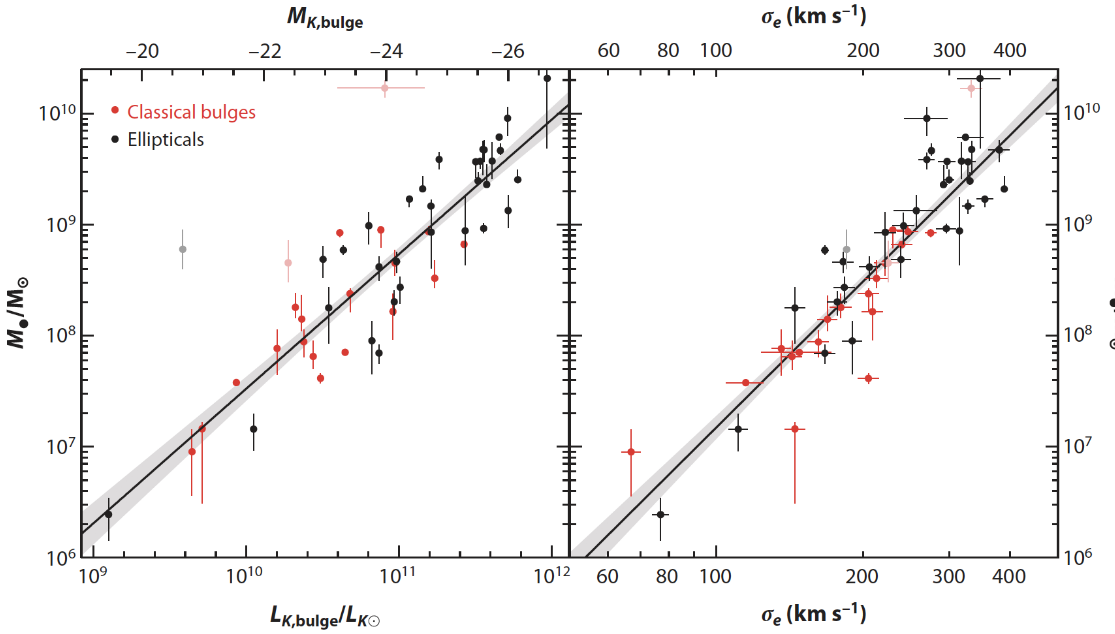

Figure 1.6: The relationship between central supermassive black hole mass and bulge near-infrared (K-band) luminosity or magnitude (left) and stellar velocity dispersion (right) for local galaxies that host classical bulge structures, as originally presented by Kormendy & Ho (2013, Figure 17). The grey, shaded region represents the one-sigma error bound for their least-squares fits.

2019). Examples of these relationships are presented in Figure 1.6.

The radial extent of the gravitational influence of a black hole ($r_\bullet$) can be estimated through the equation

$$r_\bullet = \frac{GM_\bullet}{\sigma^2}, \tag{1.1}$$

where σ is the velocity dispersion of the objects within this region. For the typical masses of SMBHs of the order $10^6 - 10^9$ $\mathrm{M}_\odot$, the gravity of the black hole would only dominate out to a radius of ~1 to 100 pc (Kormendy & Ho, 2013). Since the scale of a galaxy bulge is of a factor of order 10 to 1000 times larger than this (several kpc), this is therefore considered to provide the strongest evidence that SMBHs and their host galaxies must, at some level, co-evolve.

Investigation of how and why the evolution of SMBHs and their host galaxies is linked is an important area of modern astronomy research, and AGN activity is often thought to play a prominent role in mediating the connection (Silk & Rees, 1998; Cattaneo et al., 2009; Fabian, 2012). A major topic in this area is the importance of the AGN "feeding back" a proportion of their large amounts of energy to their host galaxies through powerful outflows of material, driven by their intense radiation fields or the mechanical power of their jets. The energetic potential of AGN can in this sense be easily demonstrated (following Fabian, 2012): if the SMBH radiates 10% of the rest-mass energy of the material it accretes during its lifetime, i.e. $E_{AGN} = 0.1M_{\bullet}c^2$, then the total energy emitted can exceed the binding energy of the galaxy bulge ($E_{gal} = M_{gal}\sigma_{gal}^2$) by a large factor; $E_{AGN}/E_{gal} \gtrsim 50$, if typical values of $M_{\bullet}/M_{gal} \sim 10^{-3}$ (Kormendy & Ho, 2013) and $\sigma_{gal} < 400\mathrm{km\,s^{-1}}$ are assumed. Only a fraction of this energy would hence need to be "fed back" to the surrounding gas in order for it to have a notable effect on the evolution of the host galaxy. In this way, the AGN could then affect the gas supply that fuels star formation (thus influencing the mass and luminosity of the galaxy bulge) and, ultimately, the nuclear activity itself. This popular theory has led to the inclusion of this so-called *AGN feedback* as a crucial component in many models of galaxy evolution (e.g. Di Matteo et al., 2005; Springel et al., 2005; Croton et al., 2006; Ciotti et al., 2010; Croton et al., 2016). A detailed review of AGN feedback is beyond the scope of this introduction, but is addressed in the context of radio AGN in §1.5.1. Feedback associated with these objects is believed to be of particular importance, since it is thought to explain the lack of high mass galaxies in observed galaxy luminosity functions, relative to theoretical predictions (e.g. Bower et al., 2006; Croton et al., 2006).

1.5 Radio AGN: feedback, host galaxy properties, accretion modes, and triggering

Given the key involvement of radio astronomy in launching the field of AGN research (see §1.2.2), investigation of the properties of radio AGN has been a longstanding major topic of study in extragalactic astronomy, in part facilitated by consistent improvements in the capabilities of radio observations. While the physics of their radio jets and their common association with elliptical host galaxies (e.g. Matthews et al., 1964) marks them as interesting objects in their own right, the crucial role of their feedback in modern models of galaxy evolution has highlighted their importance in a broader context, and has resulted in increased interest in their study in the last two decades. This section provides a more focused overview of our current understanding of radio AGN, in terms of their feedback, host galaxy properties, accretion modes, and triggering. The importance of investigating the properties of radio AGN with lower radio powers ($\mathrm{L_{1.4GHz}} \lesssim 10^{25}$ $\mathrm{W\,Hz^{-1}}$) is also covered in this section (§1.5.5), thus introducing the main open research topic that this thesis aims to help address.

1.5.1 Feedback

As mentioned in §1.3.3, many current theoretical models of galaxy evolution include the feedback effects associated with AGN as a vital component. AGN feedback is often divided into two main modes in the literature: "radio mode" (also known as "kinetic mode" or "maintenance mode"), where the AGN jets provide a heating source for the hot gas in the haloes of galaxies and their surrounding environments; and "quasar/QSO mode" (or "radiative mode"), where the AGN drives winds and outflows in the interstellar medium (e.g. Croton et al., 2006; Merloni & Heinz, 2008; Bower et al., 2012; Fabian, 2012). In this picture, the jets of radio AGN are thought to play a particularly important role, as evidence suggests that they are linked with both of these modes of feedback.

X-ray observations of the hot gas surrounding massive galaxies near the centres of clusters and groups show that they often have radiative cooling rates that should cause significant inflows of material. However, the very massive galaxies that should result from the subsequent build up of stellar mass are not observed, which provided a complication for models of galaxy evolution for many years (the *cooling flow problem*; Fabian, 1994). However, high resolution X-ray imaging has revealed "bubbles" and "cavities" in the emission from such environments, which radio observations have shown to in many cases be co-spatial with the powerful, large-scale jets of radio AGN (see reviews of McNamara & Nulsen, 2007 and Fabian, 2012, and references therein); a particularly clear example is shown in Figure 1.7. Estimates of the work done to create these observed structures in the hot gas can be derived from the product of the volume of the structure and the surrounding pressure in the gas (obtained from its temperature and density), and this property is found to correlate well with the energy lost by X-ray emission in the regions of the environments with the highest cooling rates (McNamara & Nulsen, 2007; Rafferty et al., 2008; Fabian, 2012). The co-alignment between the observed X-ray structures and the radio jets, coupled with their measured energetics, mean that these cases are often considered to provide the strongest direct evidence for AGN feedback.

At the time that this observational evidence for feedback was presented, the strong preference for radio AGN to lie in massive galaxies and in dense environments was well known (Best et al., 2005b; Mauch & Sadler, 2007), particularly for the brightest cluster galaxies (BCGs) and extended/diffuse cD galaxies that lie at cluster centres (Burns, 1990; Best et al., 2007). It had also been shown that the heating supplied by the radio jets was sufficient to offset the cooling of the hot gas in the haloes of these galaxies (Best et al.,

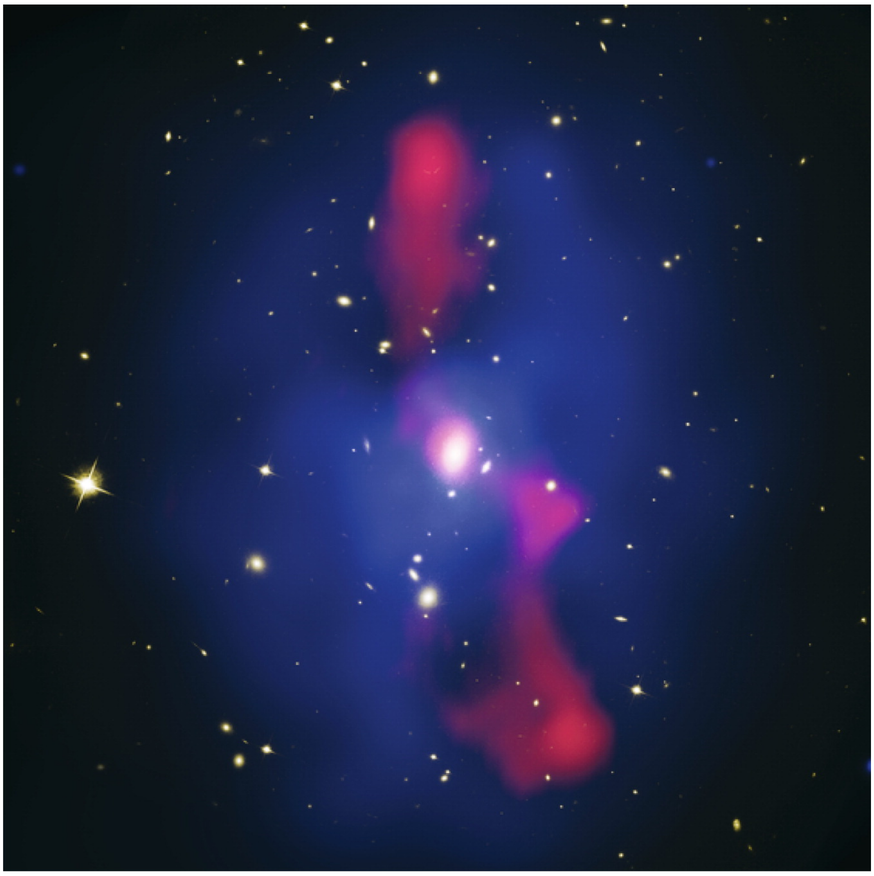

Figure 1.7: A composite image of the optical (Hubble Space Telescope), radio (red; Very Large Array), and X-ray (blue; Chandra) emission associated with the galaxy cluster MS0735.6+7421, which provides particularly strong evidence for the creation of cavities (∼200 kpc in diameter) in the hot, X-ray emitting gas in the intracluster medium by the jets associated with its powerful central radio source. Figure credit: McNamara & Nulsen (2007).

2006). Once these feedback effects were incorporated into cosmological simulations, it was found that they were capable of explaining the discrepancy between the theoretical and observed galaxy luminosity functions at the highest luminosities (Croton et al., 2006; Bower et al., 2006), which demonstrated the importance of including radio AGN feedback in models of galaxy evolution.

In addition to the above feedback processes associated with radio AGN jets on large scales (∼10 kpc – 1 Mpc), there is strong evidence to suggest that they can have a notable effect on the material in the interstellar medium (ISM) within their host galaxies (typically $\lesssim$ 10 kpc). In many active radio galaxies, observational study of the kinematics of the multiphase ISM has provided strong evidence for outflows in warm ionised

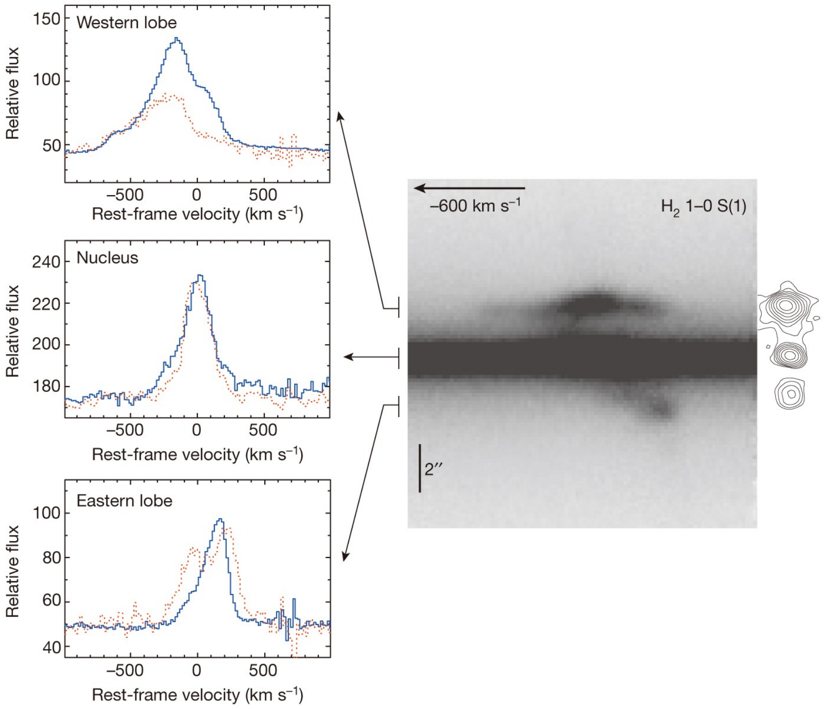

Figure 1.8: An example of the spatial coincidence between the 1.4 GHz radio jet structure (contours) and evidence of kinematic disturbances in the molecular gas emission spectrum (long slit, near infrared) for the active radio galaxy IC 5063. Figure credit: Tadhunter et al. (2014b).

(Tadhunter, 1991; Emonts et al., 2005; Holt et al., 2008), neutral (Morganti et al., 1998, 2005, 2013; Maccagni et al., 2017), and molecular gas (Nesvadba et al., 2010; Alatalo et al., 2011; Dasyra & Combes, 2012; Tadhunter et al., 2014b; Morganti et al., 2015), and the resolved radio structures are often found to be spatially coincident with disturbances in the gas emission (e.g. see Figure 1.8). This is supported by the the strong association found between radio luminosity and broad [OIII]λ5007 emission line profiles in large samples of active galaxies selected from the SDSS (Mullaney et al., 2013; Zakamska & Greene, 2014).

The mechanical power of the radio jets provides an attractive means for driving the outflows in these objects, and simulations of jets propagating through the ISM suggest that even lower power jets can cause significant heating and disruption of the material (Wagner & Bicknell, 2011; Wagner et al., 2012; Mukherjee et al., 2016; Cielo et al., 2018)[8]. An alternative type of molecular gas outflow associated with a more modest level

---

[8] An alternative proposition for luminous AGN such as Type 2 quasars is that the radio emission actually originates from relativistic particles in shocks in winds, which are instead driven by their intense radiation fields (Stocke et al., 1992; Zakamska & Greene, 2014). However, recent study of the high-resolution radio properties of such objects (morphologies, spectra and radio-size-luminosity

of disturbance could also be possible in some cases, where the relatively low observed velocities and the spatial alignment of the disturbances relative to the radio structures imply entrainment or “uplift” of the gas by the jet (e.g. McNamara et al., 2014; Russell et al., 2017, 2019). In either case, however, heating, disruption or displacement of the multiphase ISM by the jets could have a crucial effect on the gas content that is important for forming stars and fuelling the AGN itself – note it has been suggested that this could have a positive (e.g. Gaibler et al., 2012; Fragile et al., 2017) or negative (e.g. Mukherjee et al., 2016; Cielo et al., 2018) effect on star formation, or both (e.g. Tortora et al., 2009; Mukherjee et al., 2018b) .

Due to the strong effect that these two types of feedback could have on the various phases of gas in their host galaxies and surrounding environments (parsec to megaparsec scales), and thus also on subsequent star formation, the jets of AGN are now considered to be crucial components of models of galaxy formation and evolution.

1.5.2 Host galaxy properties

The association between radio AGN and early-type host galaxies has been apparent since the early studies of optical counterparts for extragalactic radio sources (e.g. Matthews et al., 1964). Evidence for the connection has been strengthened by studies of large samples of radio AGN generated by cross-matching radio surveys with those at other wavelengths (e.g. Best et al., 2005b), as well as by more detailed characterisations of the host morphologies in smaller samples (e.g. Dunlop et al., 2003; Ramos Almeida et al., 2011). Aside from this connection with early-type hosts, one of the most striking outcomes of these studies is their demonstration that radio AGN show a strong preference for galaxies with large stellar masses (Dunlop et al., 2003; Best et al., 2005b; Mauch & Sadler, 2007; Tadhunter et al., 2011; Janssen et al., 2012; Sabater et al., 2013, 2019), which also appears to apply to the minority of hosts that show prominent disk components (Tadhunter, 2016). A strong link with high-mass black holes is also often found (Dunlop et al., 2003; Best et al., 2005b; Hickox et al., 2009; Chiaberge & Marconi, 2011; Sabater et al., 2019), which led to suggestions that the black hole mass could be an important driver for the “radio-loudness” of an AGN. This could, however, be a side-effect of the well-known correlation between black hole mass and bulge mass (see §1.4), and recent results suggest that the stellar mass is the main determining factor once this relationship is accounted for (Sabater et al., 2019).

Deriving the levels of star formation in radio galaxies can be complicated by contam-

---

relation) shows that they are typically consistent with those of AGN jets (Jarvis et al., 2019).

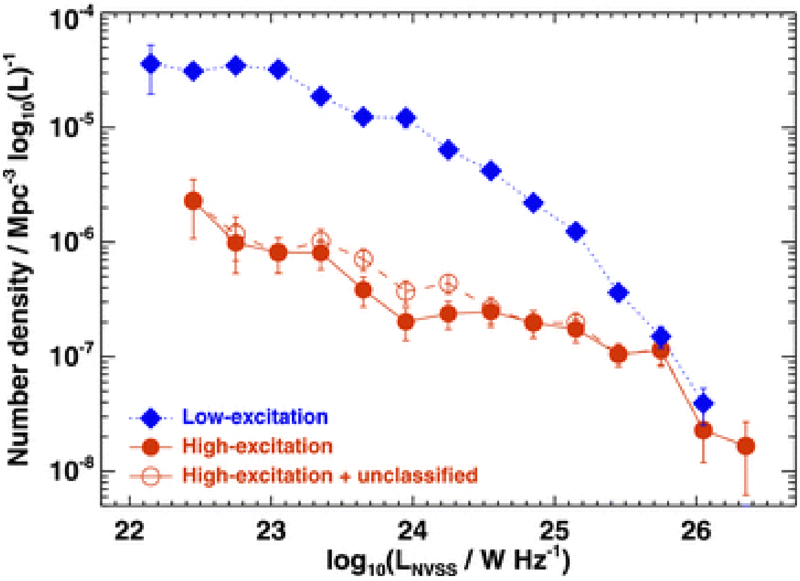

Figure 1.9: The local radio AGN luminosity function at 1.4 GHz, as defined for both HERGs (orange) and LERGs (blue) separately. The orange hollow circles/dashed line show the results if all of the sources that could not be clearly classified as HERG or LERG are included in the HERG population. Figure credit: Best & Heckman (2012).

ination of the relevant ultraviolet, optical, and infrared measurements by AGN-related continuum components (e.g. see summary in Tadhunter, 2016). However, after accounting for these effects, results from a combination of these techniques indicate that while there are some cases of starbursts (Tadhunter et al., 2011), the incidence of clear recent star formation activity in radio galaxies is only ∼ 35% (Dicken et al., 2012). Furthermore, Tadhunter (2016) showed that while some of the powerful 2Jy radio galaxies with measured star formation rates lie on or close to the star-forming "main sequence" (the positive relationship between star formation rate and stellar mass found for local star forming galaxies, e.g. Elbaz et al., 2007; Schreiber et al., 2015), around half are seen to lie below this relation, and so have notably reduced levels of star formation for their stellar masses. Combined with their general association with "red and dead" ellipticals (e.g. Hickox et al., 2009), this suggests that the level of star formation in radio galaxies is generally low; at least at low redshifts, where this has been characterised in detail.

On the other hand, some differences in host properties become apparent when looking beyond the general properties of the population. As introduced in §1.3.1, it is currently widely accepted that active radio galaxies can be divided into two distinct subpopulations, which are often referred to as HERGs (or SLRGs, with strong optical emission line spectra) and LERGs (or WLRGs, with weak optical emission line spectra). The local radio AGN luminosity function at 1.4 GHz reveals that members of both groups are found across the full range of radio luminosities covered by the general population. However, low-excitation sources dominate the population at lower radio luminosities, while high-excitation sources become more dominant at the highest radio luminosities (see Figure 1.9). As well as this difference in their luminosity functions, there is evidence to suggest that HERG and LERG sources have contrasting host properties.

Best & Heckman (2012) found that HERGs typically have both lower stellar masses and lower black hole masses than LERGs, across their full range of radio luminosities. Using samples of HERGs and LERGs matched in stellar mass, redshift, black hole mass and radio power, they also showed that HERGs had significantly bluer $g-r$ colours (see also Janssen et al., 2012), smaller concentrations of emission towards the galaxy centres, and younger stellar populations (based on 4000 Å break measurements), in agreement with hints from the results of previous studies that did not have clean HERG/LERG selections (Kauffmann et al., 2008; Lin et al., 2010). There is also evidence for a stronger association with star formation for SLRGs relative to WLRGs within the 2Jy sample, with many of the SLRGs lying close to the aforementioned "main sequence" and the WLRGs mostly falling well below it (Tadhunter, 2016)[9]. The above results are also supported by the UV/optical (Baldi & Capetti, 2008), mid-infrared (Sadler et al., 2014) and far-infrared (Hardcastle et al., 2013; Gürkan et al., 2015) properties of HERGs and LERGs. The longstanding connection between radio-selected AGN and "red and dead" elliptical galaxies, therefore, appears to be driven by the general dominance of the population by the redder, more massive LERG sources.

1.5.3 Accretion modes

In the context of radio AGN accretion modes and triggering, it is again helpful to look at the properties of SLRGs/HERGs and WLRGs/LERGs as two distinct populations. This is because, in addition to the differences in general galaxy properties outlined above, it is commonly thought that the nuclear activity in these two subpopulations is fuelled by different processes.

The radiative efficiency of the nuclear activity is often expressed in terms of its Eddington ratio, which is the ratio of the bolometric luminosity of the AGN (L_{bol}) to its Eddington luminosity (L_{Edd}), the maximum luminosity the AGN could have before the

---

[9] One caveat in this case is that these star formation rates were calculated using far-infrared luminosities, where a significant contribution to the emission could originate from AGN-heated dust. Given their typically stronger AGN emission, this could affect the SLRGs more than the WLRGs and therefore influence this result – see discussion in Tadhunter (2016).

radiation pressure would overcome the inward gravitational pull on the material fuelling the activity:

$$L_{\mathrm{Edd}} = \frac{4\pi G m_p c}{\sigma_t} M_\bullet = 3.3 \times 10^4 M_\bullet \quad . \tag{1.2}$$

Here, m_p is the mass of a proton and σ_t is the Thomson scattering cross-section; note that the factor of 3.3×10^4 is only valid if L_{Edd} and $M_\bullet$ are expressed in solar units. Since L_{bol} is thought to be directly proportional to the mass accretion rate onto the SMBH ($L_{\mathrm{bol}} = \epsilon \dot{M}_\bullet c^2$, where ϵ is the radiative efficiency; as §1.3.3), the Eddington ratio is also often interpreted as a measure of the rate of accretion.

Building on the conventional unified model outlined in §1.3.3, many studies now argue that AGN with strong and weak optical emission line spectra, regardless of their radio loudness, are fuelled by two inherently different accretion modes (e.g. see reviews of Heckman & Best, 2014; Yuan & Narayan, 2014). In this picture, the traditional AGN classes with strong optical emission line spectra (Seyfert galaxies, quasars, SLRGs, HERGs) are fuelled via a geometrically thin, optically thick accretion disk of cold gas (following Shakura & Sunyaev, 1973), in which viscosity converts the gravitational potential energy to emitted blackbody-like radiation (see Figure 1.10a). The accretion occurs at high rates and the radiation is efficient ($L_{\mathrm{bol}}/L_{\mathrm{Edd}} \approx 1-10\%$; Best & Heckman, 2012). These are the AGN well-described by the unified model outlined in §1.3.3. This type of accretion is often referred to as "radiative-mode" or "quasar-mode", in accordance with the feedback mode of the same name; the two accretion modes outlined here are often implemented into cosmological simulations such that they directly correspond to their associated types of feedback (e.g. Croton et al., 2006, 2016).

The alternative mechanism, which is thought to fuel WLRGs/LERGs, and potentially some stronger LINER sources, is "jet-mode" or "radio-mode" accretion (again named in line with the corresponding feedback mode). In this case, it is thought that an optically thin, geometrically thick, "advection-dominated" or "radiatively-inefficient" accretion flow (ADAF or RIAF) of hotter gas fuels the activity (e.g. Narayan & Yi, 1994, 1995; Narayan, 2005). In this case, a larger proportion of the energy released through viscosity goes towards heating the accreting material, as opposed to being radiated away (Yuan & Narayan, 2014). The accretion here occurs at low rates and is inefficient at producing radiation ($L_{\mathrm{bol}}/L_{\mathrm{Edd}} \lesssim 1\%$; Best & Heckman, 2012; Mingo et al., 2014). In this mode, however, it is thought that relatively more of the gravitational potential

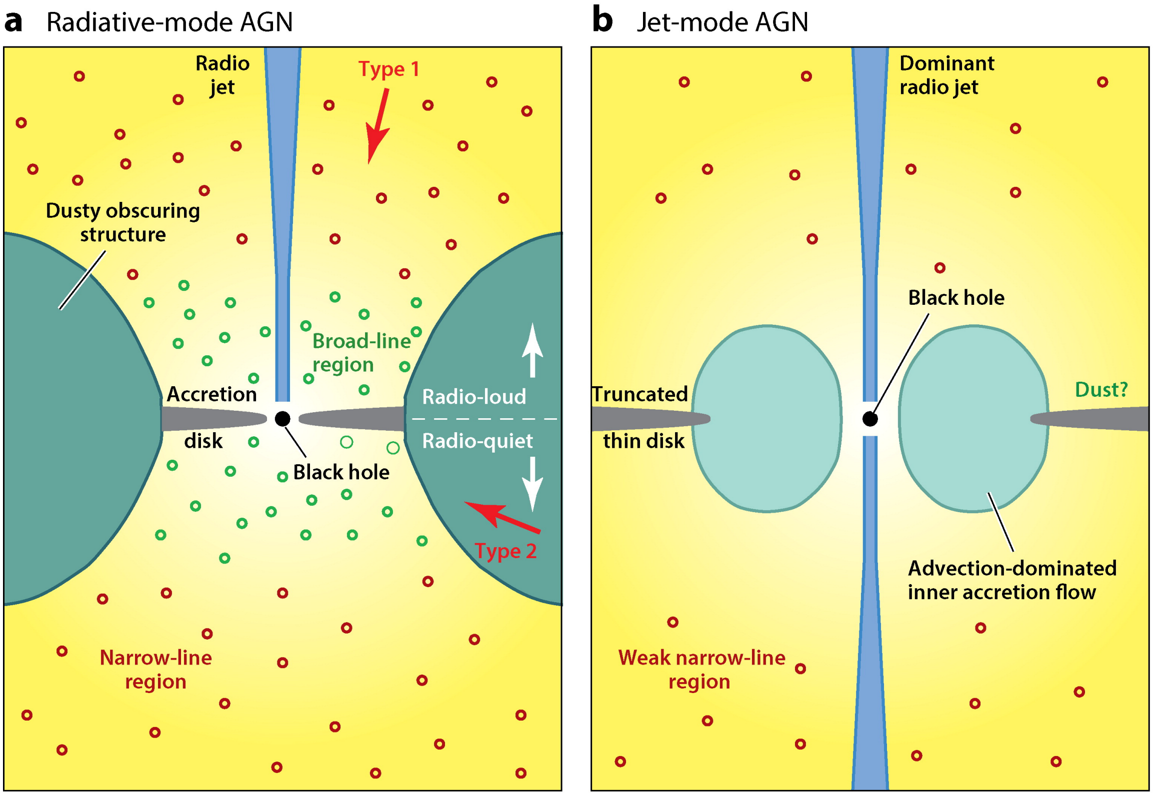

Figure 1.10: Schematic diagrams of the two proposed types of AGN accretion. (a) *Radiative-mode.* A SMBH (BH in the diagram) lies at the centre, which is surrounded by a radiatively-efficient thin accretion disk and dense clouds of gas in the broad-line region, the latter being responsible for the broad permitted emission lines observed for Type 1 Seyfert galaxies, BLRGs, and Type 1 quasars. At larger radial distances, a toroidal dust structure exists, and less dense clouds of gas (the narrow-line region, NLR) emit forbidden lines that have narrower widths than the permitted broad lines. Type 2 Seyferts/quasars, and NLRGs are then AGN that are viewed along lines of sight for which the torus causes obscuration of the emission from the broad-line region and accretion disk. This mode is thought to fuel all AGN with strong optical emission lines (Seyfert galaxies, quasars, and SLRGs/HERGs). (b) *Jet-mode.* A radiatively-inefficient accretion flow of hot gas fuels the nuclear activity. The optical emission lines are weak and narrow, and most of the accreted energy is channelled into powerful radio jets. This mode is thought to fuel AGN with weak optical emission line spectra, such as WLRGs/LERGs, and perhaps some LINER sources. Image credit: Heckman & Best (2014).

energy is channelled into the kinetic power of the relativistic jets[10] (see Figure 1.10b),

---

[10] The exact mechanism responsible for the launching of the jets in both radiative-mode and jet-mode AGN is still the subject of much theoretical research, but it is generally agreed that the interplay between the spin of the SMBH and the magnetic field in its near surroundings provides the main driving force

resulting in the typically weak optical emission spectra observed – note, however, that this does not mean that all low-Eddington-ratio nuclear activity is associated with jets.

There are then two key differences between the two accretion mechanisms :– (i) *Gas phase (close to SMBH)*: radiative-mode accretion is linked with cold gas and jet-mode accretion with hot gas; and (ii) *Radiative efficiency/accretion rate:* their Eddington ratios are significantly different (e.g. Best & Heckman, 2012; Mingo et al., 2014), with radiative-mode AGN being distinctly more efficient in their multiwavelength emission than jet-mode AGN. These factors are often taken into consideration when investigating the galaxy-scale processes that might trigger the nuclear activity, in an attempt to create a coherent overall picture of the fuelling mechanisms for the SLRG/HERG and WLRG/LERG subpopulations.

1.5.4 Triggering

Radio galaxies with strong optical emission spectra have been linked with disturbed/ peculiar optical morphologies since the original optical counterpart identification for Cygnus A by Baade & Minkowski (1954a), who were the first to suggest that the galaxy mergers and interactions could be important for triggering the radio source. Subsequent deep optical imaging studies have provided strong support for this connection, showing that a large fraction of strong-lined radio galaxies display signatures of tidal interactions at high levels of surface brightness, much more frequently than those with weak optical emission lines (e.g. Heckman et al., 1986; Smith & Heckman, 1989b; Ramos Almeida et al., 2011).

This difference is illustrated most clearly by the powerful radio galaxies in the 2Jy sample, for which 94^{+4}_{-7} % of the SLRGs and 27^{+16}_{-9} % of the WLRGs show these features[11] (Ramos Almeida et al., 2011). Comparison with control samples of elliptical galaxies matched in absolute magnitude and imaged at comparable surface brightness depths, also reveals an excess of high-surface-brightness tidal features for the SLRGs relative to the general galaxy population (Ramos Almeida et al., 2012). The 2Jy SLRGs also show a preference for group-like large-scale environments (Ramos Almeida et al., 2013), in which galaxy-galaxy collisions are frequent, but do not have the high relative galaxy velocities found in clusters that might reduce the merger rate (Popesso & Biviano, 2006). Observations of the X-ray emission from the large-scale environments of HERGs also

---

(e.g. following Blandford & Znajek, 1977).

[11] The uncertainties on the proportions presented throughout this thesis are binomial one-sigma confidence intervals, calculated using the method of Cameron (2011).

suggests that they favour lower density groups and clusters, whereas LERGs show a strong preference for very dense clusters (Ineson et al., 2013, 2015). Furthermore, far-IR measurements of the dust content in 2Jy SLRGs indicate that their cool gas masses would be sufficient to fuel their nuclear activity for the duration of their typical lifetimes (Tadhunter et al., 2014a). This is consistent with a picture in which HERGs are fuelled by radiatively-efficient accretion of cold gas, with the tidal forces of galaxy mergers and interactions leading to strong radial gas inflows (e.g. Barnes & Hernquist, 1996) that could fuel the high-Eddington-ratio nuclear activity.

On the other hand, these studies also indicate that galaxy mergers and interactions are not the dominant triggering mechanism for galaxies containing radio AGN with weak optical emission spectra (WLRGs/LERGs). However, their preference for giant early-type host galaxies and very dense cluster environments opens up several other possibilities for their fuelling, connected with the prevalent hot gas content in the galaxy haloes and surrounding intergalactic medium (IGM) in such environments. Allen et al. (2006) and Hardcastle et al. (2007) presented the argument that the direct Bondi accretion of this hot gas would be sufficient to fuel the low-Eddington-ratio activity in LERG sources, inspired by the correlation between the estimated power available from Bondi accretion and the measured jet powers (from cavity properties; see §1.5.1) for several nearby radio galaxies. However, the strength of this relation is uncertain (Russell et al., 2013), and it is hard to explain the most powerful radio sources in this way (e.g. Hardcastle et al., 2007; McNamara et al., 2011; Russell et al., 2013).

More recently, Gaspari et al. (2013, 2015) built upon the simple Bondi argument by accounting for cooling of the hot gas in a turbulent medium prior to accretion (the *Chaotic Cold Accretion* model). In this case, thermal instabilities in the cooling material lead to the formation of clouds and filaments of cold gas. Collisions and tidal interactions between these structures then result in significant loss of angular momentum and rapid accretion of the material, at rates apparently sufficient to fuel even the most powerful radio AGN. It is also possible that cooling flows could supply the gas content necessary to fuel the activity in at least some cases, providing a direct link to the larger-scale IGM (e.g. Tadhunter et al., 1989; Baum et al., 1992; Best et al., 2005b). Ultimately, however, the dominant fuelling mechanism for WLRGs/LERGs is still uncertain, but current evidence suggests that it is typically linked, directly or indirectly, to the hot gas content of the host galaxy haloes and IGM.

1.5.5 The importance of AGN with lower radio powers

In the context of their associated radio emission, AGN have traditionally been separated into two groups: "radio-quiet" and "radio-loud". While this division is mostly arbitrary and can be defined in many ways, quantitative attempts to characterise the separation have been made, and are usually based either on the radio flux density or luminosity of the source (e.g. Peacock et al., 1986), or its radio-to-optical flux density or luminosity ratio (e.g. Schmidt, 1970; Kellermann et al., 1989; Stocke et al., 1992; $\mathcal{R}$, sometimes named the "radio-loudness parameter"). These two definitions originally gained popularity in the context of quasars, following results that appeared to suggest that the distributions of quasar radio flux densities or radio-to-optical flux density ratios were bimodal (e.g. Strittmatter et al., 1980; Kellermann et al., 1989; Stocke et al., 1992). The idea is supported by the fact that the radio luminosity functions for star forming galaxies and nearby Seyfert galaxies, which are typically interpreted as radio-quiet objects, are seen to decline sharply above $\mathrm{L}_{1.4\mathrm{GHz}} \sim 10^{23}$ $\mathrm{W\,Hz^{-1}}$, whereas radio AGN remain relatively common, and so dominate the radio emission above this limit (e.g. Meurs & Wilson, 1984; Sadler et al., 2002). For these reasons, the radio-loud and radio-quiet groupings have often been applied to AGN in general as the field has expanded and developed, and many studies have continued to treat them as two distinct populations as a result.

As mentioned in previous sections of this introduction, however, as the depth and sky coverage of radio surveys have improved, it has become clear that the radio AGN population is in fact dominated by fainter sources than the "radio-loud" objects typically studied as representative of the class, with determinations of the local radio luminosity functions at different frequencies showing large increases in number density towards lower luminosities (Best et al., 2005b; Mauch & Sadler, 2007; Best & Heckman, 2012; Sadler et al., 2014; Sabater et al., 2019). Alongside this, it has been found that these prevalent lower-radio-power AGN predominantly exhibit compact radio structures that are unresolved at the angular resolution limits of typical radio surveys, meaning that compact sources are much more common than extended sources in the general population (e.g. Baldi & Capetti, 2009, 2010; Sadler et al., 2014; Whittam et al., 2016; Hardcastle et al., 2019). Follow-up observations suggest that many of these objects remain compact on small (sub-kiloparsec) physical scales (Baldi et al., 2015, 2019b), contrasting greatly with the large (kiloparsec to megaparsec) FRI/FRII extended radio sources that have received much more focus in the past.

As a consequence of the preferential study of "radio-loud" and/or extended radio sources, as well as the complications introduced by radio emission from star formation at lower radio powers, the majority of the general results for radio AGN described in previous sections were derived based on these rarer high-radio-power objects (e.g. the powerful radio galaxies in the 3CR and 2Jy samples, which typically have $L_{1.4GHz} \gtrsim 10^{25}$ W Hz^{-1}). Meanwhile, comparatively little is known about the more common members of the radio AGN population with lower radio powers and compact radio structures.

The jets of radio AGN with lower radio powers may, in fact, be particularly important in terms of their feedback properties. Firstly, it is seen that the heating of the hot gas haloes in local radio galaxies is dominated by lower-power sources ($L_{1.4GHz} \lesssim 10^{24}$ W Hz^{-1}; Best et al., 2007), meaning that they play a key role in mediating the classic radio mode feedback required to explain the high-luminosity end of the galaxy luminosity function. Furthermore, as mentioned in §1.5.1, simulations suggest that AGN jets can cause significant disturbances even if the intrinsic powers are low, and that they may even affect a larger volume of the ISM in these instances due to longer timescales of interaction (e.g. Mukherjee et al., 2016; Cielo et al., 2018). From an observational perspective, analysis of the ionised gas kinematics of a large sample of optically selected AGN has shown that the broadest [OIII]λ5007 line profiles are linked with AGN with intermediate radio powers ($10^{23} \lesssim L_{1.4GHz} \lesssim 10^{25}$ W Hz^{-1}, peaking at $L_{1.4GHz} = 10^{24}$ W Hz^{-1}; Mullaney et al., 2013). In addition, some of the objects with strong evidence for jet-driven outflows mentioned in §1.5.1 are also found to have intermediate radio powers (e.g. see below).

It is also pertinent to consider that while the intrinsic power of the AGN jets and the observed (synchrotron) radio luminosity are correlated, there is notable scatter around the relation, meaning that the efficiency of the conversion is still uncertain (e.g. Bîrzan et al., 2008; Cavagnolo et al., 2010). This is perhaps unsurprising, given the fact that jets are dynamically-evolving phenomena, for which the observed radio luminosities are additionally thought to depend on source age, environment, and jet particle content (e.g. Kaiser et al., 1997; Hardcastle, 2018, and references therein). This means that low luminosity jets could still be intrinsically powerful (and vice versa), adding further motivation for investigating the properties of radio AGN across a broad range of radio luminosities.

If we are to characterise the true nature of radio AGN and correctly implement them into our models of galaxy evolution, it is therefore crucial to carry out detailed study of the triggering, feedback, and host galaxy properties of those with lower radio powers. HERGs with intermediate radio powers (radio-intermediate HERGs; $10^{22.5} < L_{1.4GHz} < 10^{25}$ W Hz^{-1}) could represent an important sub-population of such radio AGN for several reasons, which are outlined here.

i) **Outflows.** Several objects with well-known, strong, multiphase outflows are radio-intermediate AGN with strong optical emission line (HERG-like) spectra, e.g. IC 5063 (Morganti et al., 1998; Oosterloo et al., 2000; Morganti et al., 2005; Tadhunter et al., 2014b; Morganti et al., 2015), the "Teacup" AGN (Harrison et al., 2015; Ramos Almeida et al., 2017; Lansbury et al., 2018), and the "Beetle" AGN (Villar-Martín et al., 2017). Their association with high levels of disturbance in ionised gas is also seen within large samples of radio AGN extracted from cross-matched surveys (e.g. Mullaney et al., 2013). These objects therefore provide particularly strong evidence for radio AGN feedback.

ii) **Galaxy mergers and interactions.** As mentioned in §1.5.4, HERGs with high radio powers have an association with galaxy mergers and interactions (Heckman et al., 1986; Ramos Almeida et al., 2011, 2012, 2013). Such events could be important for supplying the cold gas necessary for the radiatively-efficient accretion that is thought to fuel their AGN (Croton et al., 2006; Best & Heckman, 2012; Heckman & Best, 2014), and be responsible for their triggering. Study of the triggering mechanisms of lower-radio-power cases is vital for investigating this relationship further.

iii) **Host galaxy types.** An overwhelming majority of powerful radio AGN are hosted by massive elliptical galaxies (e.g. Matthews et al., 1964; Dunlop et al., 2003; Best et al., 2005b), but the few cases selected from local high-flux-density surveys that show evidence for strong disk components – e.g. in the 2Jy (Tadhunter et al., 1993; Dicken et al., 2009) and 3CR samples (Buttiglione et al., 2010) – are typically found to lie towards lower radio powers, and half lie in the radio-intermediate regime (Tadhunter, 2016). Radio-intermediate HERGs are therefore useful for investigating whether or not there is a transition in morphological type towards the predominantly spiral/disk morphologies of Seyfert galaxies (e.g. Adams, 1977), which can be seen as the counterparts of HERGs at the lowest radio powers.

iv) **Radio properties.** High-radio-power SLRGs/HERGs (Tadhunter, 2016) and some low-radio-power Seyfert galaxies (Ulvestad & Wilson, 1984; Morganti et al., 1999; Baldi et al., 2018a) also exhibit double-lobed, FRII-like radio morphologies, which could suggest a link between radiatively-efficient accretion and the jets that produce these types of structures. However, as mentioned above, the majority of the local radio AGN population at lower radio luminosities have compact radio structures that are unresolved at the angular resolution limits of typical radio surveys (e.g. Baldi & Capetti, 2009, 2010; Sadler et al., 2014; Whittam et al., 2016; Hardcastle et al., 2019). These often also remain unresolved in high-resolution observations (mostly LERGs; Baldi et al., 2015, 2019b). Determining whether radio-intermediate HERGs have double-lobed or unresolved radio structures therefore has important implications for AGN accretion and jet production theories.

The main focus of the work described in this thesis is on the latter three of these open topics in AGN research, which have been investigated using targeted observations of radio-intermediate HERGs at optical and radio wavelengths.

1.6 Outstanding questions and this thesis

This chapter has provided a general overview of the key results, terms and definitions from the literature that hold particular relevance for the contents of this thesis. However, this discussion has brought to light some key unanswered questions. These include the following.

- Does the apparent relationship between high-radio-power AGN and galaxy mergers, which is particularly apparent for radiatively-efficient objects, continue for those with intermediate radio powers?
- Are lower-radio-power AGN predominantly associated with elliptical host galaxies, like their high-radio-power counterparts, or late-type (spiral/disk) hosts, as found for Seyfert galaxies?
- How do radio galaxies compare to the general galaxy population in these two aspects?
- How do the radio properties of radio AGN vary towards lower radio powers? Is the apparent connection between double-lobed (FRII-like) radio structures and radiatively-efficient accretion observed for radio-powerful SLRGs/HERGs preserved in the radio-intermediate population?

With the first of these three questions in mind, deep Isaac Newton Telescope/Wide-field Camera (INT/WFC) optical imaging observations of local radio-intermediate HERGs ($z < 0.15$; $10^{22.5} < \mathrm{L}_{1.4\mathrm{GHz}} < 10^{25}$ W Hz^{-1}), high-radio-power 3CR galaxies ($z < 0.3$; typically $\mathrm{L}_{1.4\mathrm{GHz}} \gtrsim 10^{25}$ W Hz^{-1}), and the hosts of local Type 2 quasars ($z < 0.14$,

$L_{[OIII]} \gtrsim 10^{35}$ W) have been acquired, allowing for investigation of the host types and morphological signatures of mergers in these objects. The wide-field nature of these imaging datasets has also allowed similar analysis to be performed for samples of control galaxies within the same image fields, matched to the target samples in terms of stellar mass and redshift. High-resolution, high-sensitivity radio data have also been obtained using the Very Large Array (VLA), in order to investigate the last of the questions listed above. Detailed descriptions of the reduction and analysis of these data sets, along with presentation and discussion of the results, are provided in the remaining chapters of this thesis, which is structured as follows.

- **Chapter 2:** This chapter provides descriptions of the main reduction techniques used to process the optical imaging data, along with details on how the samples were selected for the observations. Some information on the general properties of the galaxies in the various samples is also provided here.

- **Chapter 3:** This chapter concerns the detailed study of the optical morphologies of a sample of 30 local radio-intermediate HERGs ($z < 0.1$, $10^{22.5} < L_{1.4GHz} < 10^{24}$ $\mathrm{W\,Hz^{-1}}$), performed using the deep INT/WFC imaging data. This was done with the view of determining the likely triggering mechanisms for their AGN and the types of host galaxies in which they typically lie. Much of this research has already been published in Pierce et al. (2019).

- **Chapters 4 & 5:** Chapter 4 describes how an online interface was used to classify the morphologies of a large sample of active galaxies (including radio-intermediate HERGs, 3CR sources and Type 2 quasars) that covers a broad range of both radio power and optical emission line luminosity. Classifications for a large number of non-active control galaxies from the general population that lie within the wide fields covered by the INT/WFC images were also obtained using the interface. Details on how these objects were matched to the targets in terms of their stellar masses and redshifts are also provided in this chapter. The analysis of the classifications, which concern the levels of disturbance, types of interaction signature, and overall morphological types (elliptical, spiral/disk, lenticular) associated with the galaxies, is then presented in Chapter 5. This research was performed with the goal of investigating any variations in dominant host types and triggering mechanisms with AGN radio power and or optical emission line luminosity.

- **Chapter 6:** This chapter describes how the high-resolution VLA observations were used to analyse the radio properties of a sample of 16 radio-intermediate HERGs, which constituted a 94% complete subset of the objects studied in Chapter 3 with radio powers in the range $10^{23} < \mathrm{L}_{1.4\mathrm{GHz}} < 10^{24}$ W Hz^{-1}. This was done with the aim of investigating whether or not the apparent connection between radiatively-efficient AGN and double-lobed radio structures is preserved in the intermediate radio power regime. Much of this research has already been published in Pierce et al. (2020).

- **Chapter 7:** A summary and brief discussion of the results outlined in the preceding chapters in the thesis is included here, and the final conclusions of the thesis are presented. Useful future directions for the research in this area are also presented and discussed.

Throughout this thesis, a cosmology described by $H_0 = 73.0$ km s^{-1} Mpc^{-1}, $\Omega_\mathrm{m} = 0.27$ and $\Omega_\Lambda = 0.73$ has been assumed when necessary for calculations.

Chapter 2

Sample selection, optical imaging observations, and data reduction

2.1 Declaration

Some of the observation and data reduction procedures outlined in this chapter have already been described in Pierce et al. (2019). All of this work is my own, except where clearly stated.

2.2 Chapter introduction

Two of the key projects undertaken in order to produce this thesis involved the use of deep optical imaging data for a large number of active galaxies with a broad range of radio powers and optical emission line luminosities (Chapters 3, 4, and 5). This included three samples of radio galaxies and one sample of Type 2 quasars, all at low to intermediate redshifts. The optical imaging data were obtained using targeted observations, and were all taken using the 2.54m Isaac Newton Telescope (INT) at the Observatorio del Roque de los Muchachos in La Palma, Spain[1].

This chapter provides details on the selection and general properties of the samples of radio-intermediate HERGs, powerful 3CR radio galaxies, and Type 2 quasars (§2.3–§2.6), and outlines the methods and techniques involved in the acquisition and reduction of the imaging observations (§2.7 and §2.8). The method used to estimate the limiting surface brightness of the imaging observations is also described (§2.9). The proposals for the observations were prepared by myself or Clive Tadhunter. In all cases, I carried out the reduction of these data myself.

2.3 Radio-intermediate HERGs

One of the main goals of the research presented in this thesis is to use deep, targeted optical imaging data to explore the properties of active radio galaxies with lower radio powers than those that have typically received more attention in previous studies. Its particular focus in this sense is on those with high-excitation optical emission spectra (high-excitation radio galaxies or HERGs) with intermediate radio powers ($22.5 < \log(\mathrm{L}_{1.4\mathrm{GHz}}) < 25.0\ \mathrm{W\,Hz^{-1}}$). With this goal in mind, it was necessary to construct well-defined samples of these sources that were suitable for such observations, given the capabilities of currently available telescopes and observatories. Below, I detail how the

---

[1] This telescope is part of the Isaac Newton Group (ING) of telescopes operated on behalf of the UK Science and Technology Facilities Council (STFC), the Nederlanse Organisatie voor Wetenschappelijk Onderzoek (NWO), and the Instituto de Astrofísica de Canarias (IAC).

samples of these radio-intermediate HERGs were constructed, and provide details on the general properties of the sources that comprise them.

2.3.1 The Best & Heckman parent sample

Each of the radio-intermediate HERG samples was extracted from the catalogue of $18,286$ local radio galaxies produced by Best & Heckman (2012). This sample was constructed by cross-matching radio sources detected in the National Radio Astronomy Observatory (NRAO) Very Large Array (VLA) Sky Survey (NVSS; Condon et al., 1998) and/or Faint Images of the Radio Sky at Twenty centimetres (FIRST) survey (Becker et al., 1995) with galaxies from the seventh data release of the Sloan Digital Sky Survey (SDSS DR7; Abazajian et al., 2009). The optical spectroscopic data considered were taken from the value-added catalogue maintained by the Max Planck Institute for Astrophysics and the Johns Hopkins University (available at: `https://wwwmpa.mpa-garching.mpg.de/SDSS/DR7/`), which provides raw measurements and derived properties (e.g. stellar masses and star-formation rates) based on analysis of the SDSS DR7 spectra – this is referred to as the MPA-JHU value-added catalogue from this point forward.

The high sensitivity of the radio surveys used for the matching meant that intrinsically faint radio sources in the local universe could be included in the sample, with luminosities down to $\mathrm{L}_{1.4\mathrm{GHz}} \approx 10^{23}\,\mathrm{W\,Hz^{-1}}$ being probed at $z \sim 0.1$, and even lower powers being reached at lower redshifts (Best & Heckman, 2012). At these radio powers, processes related to star formation (i.e. mainly synchrotron emission from particles accelerated in supernova-driven shocks) can provide a significant contribution to the emission (e.g. Condon, 1992). With this in mind, Best & Heckman (2012) performed several tests to separate the galaxies with radio emission associated with AGN activity from those where it is linked with strong star formation, considering both the optical and radio properties of the sources. These tests are detailed in §2.3.4. The additional tests performed for sources in the lower-power radio-intermediate HERG sample outlined below (the RI-HERG low sample, §2.3.2), carried out using far-infrared flux measurements, are also described here (as originally presented in Pierce et al., 2019).

Following these tests, the galaxies with radio emission attributed to AGN were then further classified as either high- or low-excitation radio galaxies (HERGs and LERGs; c.f. Chapter 1) through the properties of their optical emission spectra. The approach utilized multiple criteria, which were considered in the order listed below until a successful classification was made.

i) **Excitation index – Buttiglione et al. (2010).** As introduced in Chapter 1, a popular way of separating star-forming, Seyfert, and LINER sources is through their optical emission line ratios, which are often plotted against one another on diagnostic diagrams. When carrying out their analysis of the optical spectral properties of 3CR radio galaxies, Buttiglione et al. (2010) introduced the "excitation index" classification method, which combines several emission line ratios commonly used for diagnostic diagrams into one parameter:

$$\begin{aligned}\mathrm{EI} = \log([\mathrm{OIII}]\lambda5007/\mathrm{H}\beta) - \frac{1}{3}\{&\log([\mathrm{NII}]\lambda6583/\mathrm{H}\alpha) + \\ &\log([\mathrm{SII}]\lambda\lambda6716,6731/\mathrm{H}\alpha) + \log([\mathrm{OI}]\lambda6364/\mathrm{H}\alpha)\}.\end{aligned} \tag{2.1}$$

Using this relation, Buttiglione et al. (2010) found that the distribution of EI was approximately bimodal, with a dividing line at EI ~ 0.95 that they interpreted as separating HERGs (EI $\gtrsim 0.95$) and LERGs (EI $\lesssim 0.95$). This was the classification method employed with the highest priority by Best & Heckman (2012), used for objects where all six of the requisite emission lines were detected and which had an EI at least one standard deviation (1σ) away from 0.95.

ii) **Diagnostic diagrams – Kewley et al. (2006).** If the excitation index method was not usable but four of the emission lines required for one of the typical diagnostic diagrams – [OIII]λ5007/Hβ vs. [NII]λ6583/Hα, [SII]$\lambda\lambda$6716,6731/Hα, or [OI]λ6364/Hα – were detected, then these were used to determine the HERG/LERG classifications. The Seyfert and LINER regions in the diagrams from Kewley et al. (2006) were used to define HERGs and LERGs, respectively, in this case, and the measurements were again required to lie at least 1σ away from the relevant division lines.

iii) **[OIII]λ5007 equivalent width.** If not classified using the previous two methods, Best & Heckman (2012) then identified any source that had an [OIII]λ5007 emission line equivalent width at least 1σ above 5Å as a HERG. Note that this differs from the strong-line/weak-line radio galaxy (SLRG/WLRG) scheme used by Tadhunter et al. (1998), for which a 10Å boundary was chosen to separate the two populations.

iv) **Methods (i)-(iii) with relaxed significance.** If a successful classification was not made by this point, the above classification methods were considered again in the same order, but with the requirement of 1σ significance removed.

v) **[NII]/Hα vs. [OIII]/Hα diagnostic.** The final method utilized the alternative

> [NII]/Hα versus [OIII]/Hα diagnostic diagram from Cid Fernandes et al. (2010), which only requires the [NII]λ6583, Hα, and [OIII]λ5007 emission lines to be detected; for the latter, a detection limit was also used, provided that it was definitive for the classification. This method removed the need to detect the weaker Hβ line used for the other emission line ratio classifications. However, it is less secure, given that the [OIII]/Hα ratio is much more sensitive to reddening than the [OIII]/Hβ ratio. Again, the Seyfert/LINER regions were taken to demarcate the HERG/LERG classifications.

Even after each of these methods had been considered, however, many radio galaxies could still not be classified as HERGs or LERGs. For these remaining cases, the correlation between the [OIII]λ5007 line luminosity and the radio power of the sources was considered, with all the unclassified objects lying below the approximate lower limit of the relationship for HERGs being classified as LERGs (see Section 2.2 and Figure 2 in Best & Heckman, 2012). Following this analysis, Best & Heckman (2012) identified a total of 481 sources in the catalogue as HERGs, providing the parent sample from which both of the radio-intermediate HERG samples studied for this thesis were selected. More details on how these samples were selected for the optical imaging observations are provided in the following subsections.

2.3.2 Sample One – RI-HERG low

Both of the radio-intermediate HERG samples extracted from the Best & Heckman (2012) HERG parent sample were initially selected based on 1.4 GHz radio power. These were originally derived using the NVSS flux densities for the sources, on the basis that its low angular resolution relative to the FIRST survey (∼45” and ∼5”, respectively) would ensure that as much as possible of the radio emission from the source was recovered, given that the sensitivity to diffuse emission decreases with increasing resolution.

For this first sample, the radio power range was limited to $22.5 < \log(\mathrm{L}_{1.4\mathrm{GHz}}) < 24.0$ $\mathrm{W\,Hz^{-1}}$, selected to probe down to much lower radio powers than samples of powerful radio galaxies (typically $\log(\mathrm{L}_{1.4\mathrm{GHz}}) \gtrsim 25.0$ $\mathrm{W\,Hz^{-1}}$) that have received more focused study in the past (e.g. those in the 3CR and 2Jy samples). A cosmological k-correction was applied when calculating these radio powers, by assuming a standard spectral index of $\alpha = -0.7$ (where $F_\nu \propto \nu^\alpha$). The sample was then restricted to objects with low redshifts ($z < 0.1$), to help ensure that the imaging observations of the targets would be sensitive to low-surface-brightness interaction signatures, as was important when determining the likely triggering mechanisms for the nuclear activity (see Chapters 3 and 5). The final constraint was on the right ascension coordinates (α) for the targets, which were restricted to the range 07h 15m $< \alpha <$ 16h 45m to allow a large number of objects to be observed from the La Palma site during the relevant observing window (see Table 2.1 for specific dates). This resulted in the selection of a sample of 32 radio-intermediate HERGs from the Best & Heckman (2012) catalogue that was complete within these constraints.

However, following inspection of the FIRST radio images for these sources, it became apparent that the NVSS flux density measurements for four of the selected objects were contaminated by emission from other radio sources that happened to lie within the NVSS beam centred on the target. For these cases, the FIRST flux density measurements were used to re-calculate the radio powers, and each of these targets consequently had lower radio powers than originally determined. This resulted in two of the sources from the original selection falling below the lower limit of the radio power range used to define the sample. The final first sample therefore comprises 30 radio-intermediate HERGs that meet the selection criteria outlined above, and it is complete within these constraints. Given its lower radio power range relative to the other radio-intermediate HERG sample studied for this thesis (the RI-HERG high sample, §2.3.3), this is referred to as the "RI-HERG low" sample from this point forward.

Some basic properties for these targets are provided in Table 2.1, and the distributions of redshift, stellar mass, 1.4 GHz radio power, and [OIII]λ5007 emission line luminosity are presented in Figure 2.1. The properties for one of the two lower-power sources that did not meet the radio power criterion for the RI-HERG low sample are also included at the bottom of Table 2.1 (J1012+08), due to the fact that it was observed with the VLA as part of the radio interferometry project described in Chapter 6. However, note that this object is not considered as part of the RI-HERG low sample (e.g. when deriving results such as those presented in Figure 2.1), and analysis of its optical morphology is not included in this thesis.

Table 2.1: Basic information for the 30 targets in the RI-HERG low sample and one lower-radio-power target (final row) described in §2.3.2. Column key: (1) full SDSS IDs and in-text abbreviations (in brackets), which are named based on the epoch J2000 right ascension (α) and declination (δ) coordinates for the target – e.g. SDSS J072528.47+434332.4 has α = 07h 25m 28.47s and δ = +43d 43m 32.4s; (2) spectroscopic redshifts, (3) r-band extinction values (from Schlegel et al., 1998) and (4) extinction-corrected r-band magnitudes, obtained through the SDSS DR7 Object Explorer tool (available at: `http://cas.sdss.org/dr7/en/tools/explore/`); (5) 1.4 GHz radio luminosities derived from NVSS flux densities, or FIRST flux densities for J0911+45 and J1358+17 (also J1012+08); (6) [OIII]λ5007 luminosities and (7) stellar masses from the MPA-JHU value-added catalogue for SDSS DR7; (8) starting night date and (9) atmospheric seeing measurements for the target observations.

SDSS ID (Abbr.)	z	A_r (mag)	SDSS r mag (mag)	log(L$_{1.4GHz}$) (W Hz^{-1})	log(L$_{[OIII]}$) (W)	log(M$_*$) (M$_\odot$)	Obs. date	Seeing FWHM (arcsec)
J072528.47+434332.4 (J0725+43)	0.069	0.25	16.37	23.06	33.90	10.9	2017-03-29	1.30
J075756.72+395936.1 (J0757+39)	0.066	0.14	15.36	23.98	34.12	10.8	2017-03-28	1.31
J081040.29+481233.1 (J0810+48)	0.077	0.14	15.87	23.70	33.54	10.9	2017-03-28	1.34
J082717.80+125430.0 (J0827+12)	0.065	0.10	16.00	22.71	33.36	10.7	2017-03-30	1.38
J083637.83+440109.5 (J0836+44)	0.055	0.08	15.25	23.94	33.79	11.1	2017-03-28	1.24
J083856.90+261037.5 (J0838+26)	0.051	0.14	16.41	22.62	33.57	10.3	2017-03-30	1.37
J090239.51+521114.7 (J0902+52)	0.098	0.05	15.50	23.94	33.25	11.4	2017-03-29	1.21
J091107.04+454322.6 (J0911+45)	0.098	0.05	17.33	22.62	33.26	10.7	2017-03-29	1.24
J093141.45+474209.0 (J0931+47)	0.049	0.04	17.07	22.54	33.38	10.0	2017-03-31	1.40
J095058.69+375758.8 (J0950+37)	0.041	0.05	15.29	23.37	33.26	10.8	2017-03-29	1.21
J103655.60+380321.4 (J1036+38)	0.051	0.06	14.45	22.82	33.79	11.2	2017-03-31	1.41
J110009.47+100312.1 (J1100+10)	0.064	0.08	17.24	22.85	32.98	10.2	2017-03-31	1.40
J110852.61+510225.6 (J1108+51)	0.070	0.04	15.89	23.07	33.84	11.0	2017-03-31	1.57

Table 2.1 – continued.

J114740.08+334720.4 (J1147+33)	0.031	0.05	14.29	22.52	33.94	10.7	2017-03-31	1.68
J115020.82+010423.1 (J1150+01)	0.078	0.07	17.70	22.97	33.29	10.7	2017-03-30	1.94
J120611.42+350525.6 (J1206+35)	0.081	0.05	15.71	22.92	33.89	11.1	2017-03-30	1.40
J120640.31+104652.8 (J1206+10)	0.089	0.06	17.62	23.41	33.02	11.0	2017-03-28	1.24
J123641.09+403225.7 (J1236+40)	0.096	0.06	17.82	23.08	33.57	10.5	2017-03-29	1.14
J124322.55+373858.0 (J1243+37)	0.086	0.05	15.69	23.35	33.97	11.2	2017-03-28	1.14
J125739.56+510351.4 (J1257+51)	0.097	0.03	16.34	23.20	33.33	11.1	2017-03-29	1.14
J132450.59+175815.0 (J1324+17)	0.086	0.06	16.67	23.35	33.36	10.7	2017-03-28	1.07
J135152.97+465026.1 (J1351+46)	0.096	0.04	17.04	23.26	33.21	10.6	2017-03-28	1.08
J135817.73+171236.7 (J1358+17)	0.095	0.10	16.87	23.21	33.93	10.9	2017-03-28	1.27
J141217.69+242735.9 (J1412+24)	0.069	0.06	15.42	23.19	33.79	11.1	2017-03-29	1.67
J152948.01+025536.7 (J1529+02)	0.077	0.13	16.56	22.93	33.21	10.8	2017-03-30	1.54
J155511.00+270056.2 (J1555+27)	0.083	0.12	17.36	22.92	33.47	10.4	2017-03-31	2.05
J160110.88+431138.1 (J1601+43)	0.072	0.04	17.09	22.99	34.24	10.4	2017-03-31	1.41
J160953.46+133147.8 (J1609+13)	0.036	0.11	15.06	23.01	32.86	10.8	2017-03-31	1.60
J162237.28+075349.5 (J1622+07)	0.088	0.22	17.10	23.19	33.77	10.6	2017-03-29	1.40
J163045.51+125752.7 (J1630+12)	0.065	0.15	16.93	22.78	33.89	10.1	2017-03-31	2.02
J101207.79+084235.1 (J1012+08)	0.095	0.08	17.34	22.39	33.81	10.5	2017-03-29	1.21

2.3.3 Sample Two – RI-HERG high

The second sample of radio-intermediate HERGs selected from the Best & Heckman (2012) catalogue was chosen to have higher radio powers than the first, constrained to the range $24.0 < \log(\mathrm{L}_{1.4\mathrm{GHz}}) < 25.0\ \mathrm{W\,Hz^{-1}}$; as such, this is referred to as the "RI-HERG high" sample from this point forward. For this sample, inspection of the FIRST images revealed no clear contamination from the emission of other radio sources lying within the scale of the NVSS beam, and so the NVSS flux densities were used to derive the radio powers in all cases. As for the RI-HERG low sample, the targets were restricted to low redshifts to allow for the detection of faint tidal features, but the upper limiting redshift was relaxed to $z < 0.15$ to increase the sample size. Again, the right ascension coordinates were constrained to ensure that the targets were suitable for observations from the La Palma observatory during the relevant observing window, in this case restricted to $07\mathrm{h}\ 45\mathrm{m} < \alpha < 15\mathrm{h}\ 45\mathrm{m}$. These selection criteria resulted in a final sample of 28 radio-intermediate HERGs that is complete within these constraints.

Some basic properties of these 28 targets are provided in Table 2.2, and the distributions of redshift, stellar mass, 1.4 GHz radio power, and [OIII]λ5007 emission line luminosity are presented alongside those of the RI-HERG low sample in Figure 2.1. As seen in the figure, in addition to the higher redshifts and radio powers of the RI-HERG high objects introduced by the new selection criteria, the typical stellar masses and [OIII]λ5007 emission line luminosities are also higher for this latter sample: medians of $\log(\mathrm{M}_*/\mathrm{M}_\odot) = 11.2$ and $\log(\mathrm{L}_{[\mathrm{OIII}]}) = 33.98$ W and $\log(\mathrm{M}_*/\mathrm{M}_\odot) = 10.7$ and $\log(\mathrm{L}_{[\mathrm{OIII}]}) = 33.56$ W for the RI-HERG high and RI-HERG low samples, respectively. The interrelationship between these parameters is important to consider when drawing comparisons between the different samples, and is discussed in later chapters.

Table 2.2: Basic information for the 28 targets in the RI-HERG high sample described in §2.3.3. The columns are identical to those in Table 2.1.

SDSS ID (Abbr.)	z	A_{r} (mag)	SDSS r mag (mag)	log($\mathrm{L_{1.4GHz}}$) ($\mathrm{W\,Hz^{-1}}$)	log($\mathrm{L_{[OIII]}}$) (W)	log($\mathrm{M_*}$) ($\mathrm{M_\odot}$)	Obs. date	Seeing FWHM (arcsec)
J075244.19+455657.4 (J0752+45)	0.052	0.23	14.24	24.52	33.68	11.3	2018-03-11	0.94
J080601.51+190614.7 (J0806+19)	0.098	0.11	15.46	24.55	33.93	11.4	2018-03-11	1.01
J081755.21+312827.4 (J0817+31)	0.124	0.12	16.81	24.39	34.26	11.0	2018-03-11	1.41
J083655.86+053242.0 (J0836+05)	0.099	0.10	15.49	24.09	33.78	11.3	2018-03-13	1.01
J084002.36+294902.6 (J0840+29)	0.065	0.15	14.66	24.73	34.33	11.2	2018-03-11	1.14
J085323.42+092744.2 (J0853+09)	0.116	0.16	16.67	24.58	34.37	10.7	2018-03-12	1.20
J085417.52+420315.4 (J0854+42)	0.142	0.07	17.66	24.18	33.69	10.8	2018-03-13	1.16
J090937.01+343549.3 (J0909+34)	0.137	0.06	17.48	24.40	33.47	10.9	2018-03-13	1.14
J091201.67+532036.6 (J0912+53)	0.102	0.05	15.81	24.57	33.74	11.4	2018-03-12	1.08
J103602.94+525936.1 (J1036+52)	0.142	0.06	17.40	24.16	34.25	10.8	2018-03-13	1.08
J110215.68+290725.2 (J1102+29)	0.106	0.08	15.35	24.57	34.03	11.3	2018-03-12	1.14
J112349.91+201654.4 (J1123+20)	0.130	0.05	16.45	24.61	34.09	11.2	2018-03-12	1.14
J114722.13+350107.5 (J1147+35)	0.063	0.06	14.47	24.74	34.15	11.4	2018-03-11	1.04
J120732.92+335240.1 (J1207+33)	0.079	0.04	15.13	24.83	34.49	11.2	2018-03-11	0.94
J124709.68+324705.0 (J1247+32)	0.135	0.04	16.67	24.36	33.93	11.3	2018-03-13	1.15
J131441.14+284340.7 (J1314+28)	0.140	0.03	16.48	24.22	33.63	11.2	2018-03-13	1.27
J132848.45+275227.8 (J1328+27)	0.091	0.02	16.69	24.59	34.25	10.8	2018-03-11	0.95
J133425.23+381759.4 (J1334+38)	0.063	0.02	16.00	24.25	33.00	10.7	2018-03-11	0.94

Table 2.2 – continued.

J140942.44+360415.9 (J1409+36)	0.149	0.03	17.05	24.88	34.12	11.4	2018-03-13	1.20
J142557.05+392444.9 (J1425+39)	0.143	0.03	16.72	24.12	33.30	11.1	2018-03-13	1.14
J143643.83+080728.3 (J1436+08)	0.051	0.07	14.45	24.01	33.26	11.2	2018-03-11	1.08
J145019.19−010647.4 (J1450−01)	0.119	0.13	16.69	24.52	34.94	11.2	2018-03-12	1.21
J151247.16−014423.3 (J1512−01)	0.146	0.41	17.05	24.79	35.06	10.7	2018-03-13	1.20
J151659.24+051751.5 (J1516+05)	0.051	0.12	15.20	24.45	33.75	10.9	2018-03-12	1.14
J152349.34+321350.2 (J1523+32)	0.110	0.07	16.94	24.68	33.81	10.7	2018-03-12	1.08
J152922.49+362142.2 (J1529+36)	0.099	0.05	15.55	24.06	34.22	11.4	2018-03-12	1.14
J153753.63−005720.6 (J1537−00)	0.137	0.34	17.17	24.67	34.07	10.8	2018-03-13	1.01
J154144.30+472754.8 (J1541+47)	0.110	0.04	16.80	24.56	33.46	11.1	2018-03-12	0.95

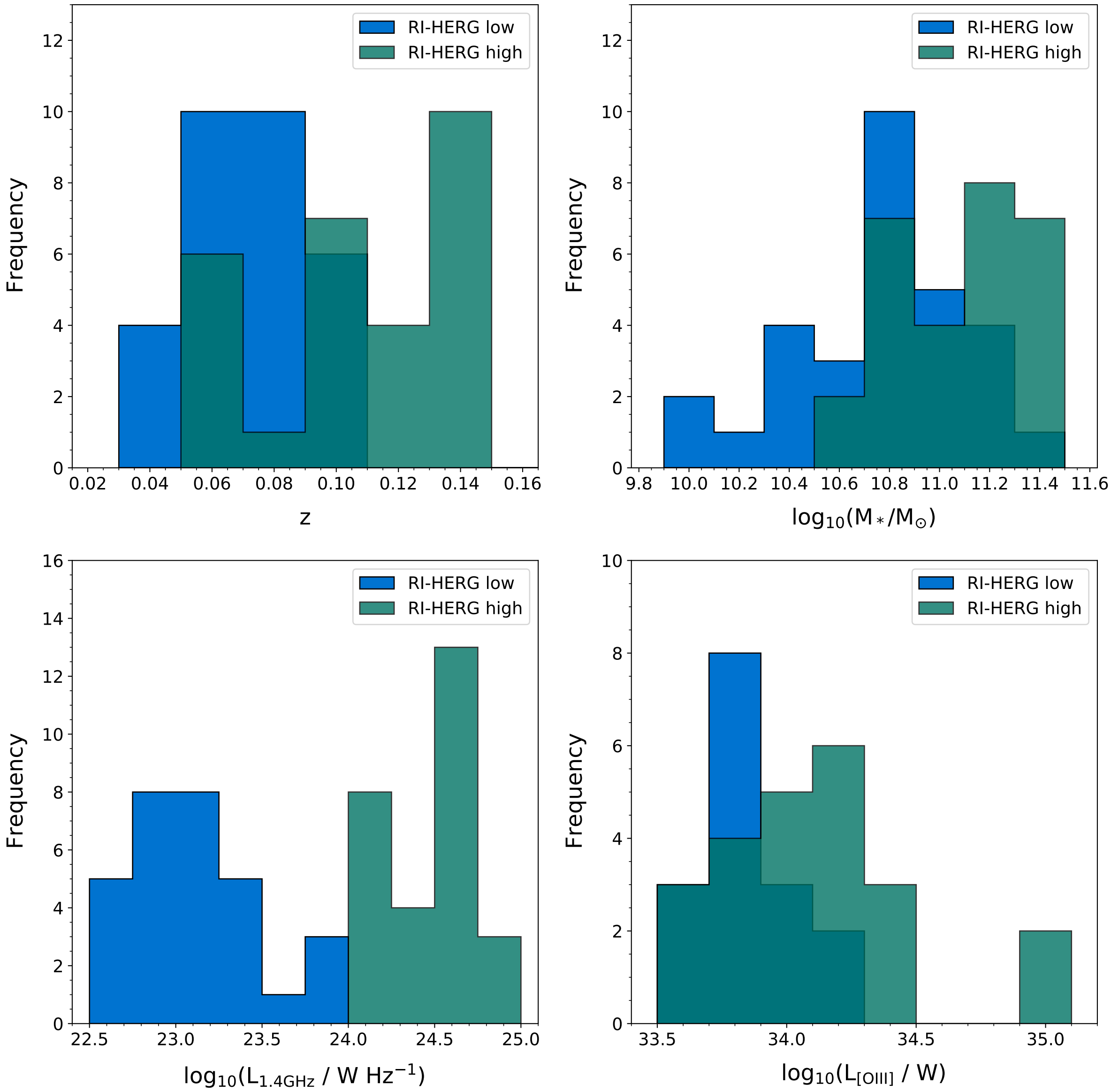

Figure 2.1: Redshift (z), stellar mass (M_*), 1.4 GHz radio power ($L_{1.4GHz}$), and [OIII]λ5007 emission line luminosity ($L_{[OIII]}$) distributions for the sources in the RI-HERG low (blue) and RI-HERG high (teal) samples.

2.3.4 Testing for contamination from star formation

In order to address the possible contamination of the radio AGN sample by radio-quiet AGN in star forming galaxies, Best & Heckman (2012) considered the following three criteria to separate the two populations.

- **D_n(4000) and radio luminosity per unit stellar mass.** In galaxies with older stellar populations, a strong discontinuity arises in the optical spectra at around 4000 Å, the depth of which is typically characterised using the ratio of the average flux densities measured either side of this wavelength – the 4000 Å break strength, $D_n(4000)$ (e.g. Kauffmann et al., 2003). Best et al. (2005a) showed that, when this property is plotted against the ratio of 1.4 GHz radio luminosity to stellar mass, star forming galaxies can be separated cleanly from active radio galaxies, due to the excess radio emission produced by the AGN relative to that expected for a galaxy with a given stellar mass and star formation rate. This was the technique employed by Best & Heckman (2012) to classify the sources as radio AGN in the majority of cases, but this could not be used for the minority that lacked a stellar mass estimate in the MPA-JHU catalogue.

- **Emission-line ratios (the "BPT" method).** As introduced in Chapter 1 (e.g. Figure 1.3), the intensity ratios for common optical emission lines can also be used to separate star forming galaxies from AGN, due to the differences between the physical conditions of the emitting regions in each case. The division suggested by Kauffmann et al. (2003) was used to separate the two populations, with sources classified as AGN using the following emission-line ratio criterion: $\log([\mathrm{OIII}]\lambda5007/\mathrm{H}\beta) > 1.3 + 0.61/(\log([\mathrm{NII}]\lambda6583/\mathrm{H}\alpha) - 0.05)$. This method is not as secure as the first, however, since there is the possibility of contamination of the radio AGN sample by galaxies with optical spectra dominated by radio-quiet AGN, but radio emission dominated by processes related to star formation, given the close association between the AGN and star-forming galaxies (Kauffmann et al., 2003). This technique was also limited by the requirement that all of the relevant emission lines were significantly detected, and was therefore only used for just under 30% of the sources.

- **Hα and radio luminosities.** In addition to radio emission, the Hα emission line luminosity ($L_{\mathrm{H}\alpha}$) provides another indicator of the level of star formation in a galaxy (Kennicutt, 1998), and so it is found to be correlated with radio power in star forming galaxies. In plots of Hα luminosity against 1.4 GHz radio luminosity, galaxies also hosting radio AGN can therefore be separated from star forming galaxies by their excesses in radio emission in this plane (Kauffmann et al., 2008). Best & Heckman (2012) defined a dividing line of $\log(L_{\mathrm{H}\alpha}) = 1.12 \times (\log(L_{1.4\mathrm{GHz}}) - 17.5)$ to classify the sources as radio AGN (where $L_{\mathrm{H}\alpha}$ is in solar units and $L_{1.4\mathrm{GHz}}$ is in $\mathrm{W\,Hz^{-1}}$); note that this division was chosen in order to be conservative, given that the Hα luminosities were not corrected for the effects of extinction.

Three possible results were determined for each test: radio emission from AGN; radio emission from processes linked with star formation; or neither (unclassified). These results were then considered together for each radio source, in order to arrive at a final classification as a radio AGN or star forming galaxy; the explicit details of this process are outlined in Appendix A2 of Best & Heckman (2012). All radio AGN listed in the Best & Heckman (2012) catalog have been classified as such based on these tests, and so all targets in the two radio-intermediate HERG samples (RI-HERG low and RI-HERG high) also meet this criterion.

In addition, alternative tests were performed for Pierce et al. (2019) using the estimated star formation rates (SFRs) calculated for the 6 out of 30 galaxies (20%) in the RI-HERG low sample that are detected in at least one waveband in the Infrared Astronomical Satellite (IRAS) Faint Source Survey (Moshir et al., 1992). The SFRs were calculated using the measured IRAS 60μm and 100μm fluxes, following the method of Calzetti et al. (2010). For the 2 out of these 6 galaxies not detected at 100μm, the average 60μm to 100μm flux ratio for the other four galaxies was used in the calculations when necessary. The estimated radio emission at 1.4 GHz resulting from galaxies with these SFRs was then derived using the prescription of Murphy et al. (2011). From this, it is found that star formation could account for an average of only ∼20% of the 1.4 GHz luminosities obtained from the NVSS flux densities for the six galaxies considered − for 5 out of the 6 galaxies, the contribution is $\lesssim$30%, with the other (J0838+26) having the highest possible contribution, at ∼50%. The results of this process are summarised in Table 2.3.

However, as shown by e.g. Mullaney et al. (2011), the infrared emission in the region of the spectrum covered by IRAS data could be subject to a significant contribution from AGN-heated dust emission, suggesting that the SFRs derived above are not completely reliable and should be treated as upper limits. In addition, it is important to note that 80% of the galaxies in the sample do not have IRAS detections in the Faint Source Survey, and would thus likely have lower relative contributions towards the radio emission from star formation than those reported here. Given the low catalogue detection rate and the likely overestimates of the 1.4 GHz luminosities due to star formation for those that are detected, it appears that radio emission from radio-loud AGN activity provides the dominant contribution in all cases, supporting the results of the tests involving the optical and radio properties of the sources. Thus, it is deemed unlikely that there is significant contamination of the RI-HERG low sample by radio-quiet AGN in star forming galaxies. These tests were not performed for the RI-HERG high sample, since the higher range

Table 2.3: Star formation properties for the six galaxies in the sample with far-infrared detections in the IRAS Faint Source Survey (Moshir et al., 1992). The target IDs and 60μm fluxes are presented, along with estimations of the star formation rates (following Calzetti et al., 2010). The ratio of the expected resultant 1.4 GHz luminosity (following Murphy et al., 2011) to that derived from the NVSS flux densities is displayed in the final column.

Target ID	$F_{60\mu m}$ (Jy)	Star formation rate ($M_\odot$ yr^{-1})	$\frac{L^{SF}_{1.4GHz}}{L^{NVSS}_{1.4GHz}}$
J0810+48	0.685	33.2	0.10
J0838+26	0.628	13.7	0.52
J0950+37	0.410	5.94	0.04
J1108+51	0.487	20.5	0.28
J1243+37	0.449	29.0	0.20
J1609+13	0.856	8.76	0.14

of radio powers covered ($24.0 < \log(L_{1.4GHz}) < 25.0$ W Hz^{-1}) makes the contamination by radio-quiet AGN in star forming galaxies highly unlikely – for example, the number density of star forming galaxies decreases steeply above a radio power of $L_{1.4GHz} = 10^{23}$ W Hz^{-1}, and very few exist at $L_{1.4GHz} \gtrsim 10^{24}$ W Hz^{-1} (e.g. Sadler et al., 2002; Best et al., 2005a; Mauch & Sadler, 2007).

2.4 3CR sources

Some of the first major surveys in the field of radio astronomy were carried out using the Cambridge four-element interferometer (Cambridge, UK), a key outcome of which was the construction of the Third Cambridge Catalogue of radio sources, which contains all objects in the declination range $-22\,\mathrm{d} < \delta < +71\,\mathrm{d}$ with flux densities above 8 Jy at 159 MHz (Edge et al., 1959). Shortly after, further observations at 178 MHz led to a revised version of this catalogue being produced, which included all sources with declination $\delta > -5\,\mathrm{d}$ and flux densities above 9 Jy at 178 MHz (Bennett, 1962). These catalogues, commonly referred to in the literature as the 3C and 3CR catalogues, respectively, provide complete samples of the brightest radio sources in the Northern Hemisphere, and have thus proven to be highly valuable resources for the study of powerful radio galaxies at various redshifts. Although a large amount of complementary multi-wavelength data exists for 3C radio galaxies, the research conducted for this thesis provides the first attempt at characterising the detailed optical morphologies of the sources in the context of AGN triggering, using targeted, deep imaging observations.

Table 2.4: Basic information for the 73 targets in the 3CR sample described in §2.4. Column key: (1) 3CR catalogue name; (2) redshift; (3) epoch J2000 right ascension and (4) declination coordinates, from the references listed in (5) – a. Spinrad et al. (1985), b. Massaro et al. (2010), c. Massaro et al. (2012), d. Donzelli et al. (2007), e. Evans et al. (2010); (6) 1.4 GHz radio power; (7) [OIII]λ5007 luminosity; (8) MPA-JHU equivalent stellar mass (derived from near-infrared luminosities and a conversion factor, as described in Chapter 4); (9) filter, (10) date, and (11) atmospheric seeing measurements for the deep optical imaging observations. The redshifts and 1.4 GHz radio powers were taken from Spinrad et al. (1985), with the latter derived from the 178 MHz flux densities (assuming a spectral index of $\alpha = -0.7$). The [OIII]λ5007 luminosities and upper limits were taken from Buttiglione et al. (2009, 2010, 2011), except for 3C 321 (from Dicken et al., 2010) and 3C 405 (from flux measured by Osterbrock & Miller, 1975; see §2.4). All values have been adjusted in accordance with the cosmology assumed for this thesis, where appropriate.

Name	z	RA	Dec	Ref.	log($L_{1.4\mathrm{GHz}}$) (W Hz^{-1})	log($L_{[\mathrm{OIII}]}$) (W)	log(M_*) ($M_\odot$)	Filter	Obs. Date	Seeing FWHM (arcsec)
3C 20	0.174	00 43 09.18	+52 03 36.1	*b*	26.88	34.52	11.3	*r*	2013-08-06	1.14
3C 28	0.195	00 55 50.65	+26 24 37.3	*a*	26.57	33.94	11.6	*r*	2012-12-13	2.16
3C 33	0.060	01 08 52.86	+13 20 14.2	*e*	25.99	35.16	11.0	*r*	2012-12-13	1.90
3C 33.1	0.181	01 09 44.33	+73 11 57.4	*a*	26.40	35.28	11.6	*r*	2013-08-06	1.17
3C 35	0.067	01 12 01.47	+49 28 35.0	*a*	25.39	32.99	11.0	*r*	2012-12-13	1.49
3C 52	0.285	01 48 28.91	+53 32 28.0	*b*	26.85	$<$ 33.62	11.8	*i*	2016-08-16	1.14
3C 61.1	0.184	02 22 36.07	+86 19 07.8	*a*	26.80	35.45	-	*i*	2016-08-16	1.35
3C 63	0.175	02 20 54.27	−01 56 51.0	*a*	26.53	34.61	11.3	*i*	2016-08-16	1.21
3C 79	0.256	03 10 00.09	+17 05 58.5	*c*	27.10	35.84	11.5	*r*	2013-08-07	1.34
3C 89	0.139	03 34 15.57	−01 10 56.1	*c*	26.33	$<$ 33.49	11.6	*r*	2012-12-13	1.56
3C 93.1	0.243	03 48 46.98	+33 53 14.6	*a*	26.56	35.65	11.5	*r*	2014-09-01	1.36
3C 123	0.218	04 37 04.38	+29 40 13.8	*a*	27.74	34.98	11.4	*r*	2015-02-27	1.42

Table 2.4 – continued.

3C 130	0.109	04 52 52.41	+52 04 53.5	*a*	26.00	$<$ 34.26	12.7	*i*	2016-08-16	1.34
3C 132	0.214	04 56 42.92	+22 49 23.2	*b*	26.58	34.44	11.6	*r*	2015-02-27	1.58
3C 133	0.278	05 02 58.48	+25 16 25.4	*a*	27.04	35.74	11.7	*r*	2013-11-28	1.34
3C 135	0.125	05 14 08.64	+00 56 32.3	*b*	26.19	35.03	10.9	*r*	2012-12-13	1.57
3C 136.1	0.064	05 16 03.11	+24 58 25.0	*a*	25.47	34.42	11.2	*r*	2013-11-28	1.14
3C 153	0.277	06 09 32.55	+48 04 15.6	*a*	26.87	34.61	11.6	*r*	2012-12-13	1.18
3C 165	0.296	06 43 06.70	+23 19 00.3	*a*	26.88	34.65	11.5	*r*	2013-11-28	1.21
3C 166	0.245	06 45 24.10	+21 21 51.2	*c*	26.74	34.64	11.3	*r*	2012-12-13	1.35
3C 171	0.238	06 55 14.72	+54 08 57.5	*b*	26.83	35.87	11.4	*r*	2013-04-09	1.55
3C 173.1	0.292	07 09 18.43	+74 49 31.7	*a*	26.93	33.83	11.8	*r*	2012-12-13	1.20
3C 180	0.220	07 27 04.81	−02 04 31.0	*a*	26.65	35.32	11.4	*r*	2013-04-09	1.42
3C 184.1	0.118	07 43 01.44	+80 26 25.6	*a*	26.00	35.21	11.3	*r*	2013-04-10	1.14
3C 192	0.060	08 05 35.00	+24 09 50.0	*d*	25.58	34.32	10.9	*r*	2013-04-10	1.08
3C 196.1	0.198	08 15 28.10	−03 08 28.0	*c*	26.64	34.50	11.4	*r*	2012-12-13	1.57
3C 197.1	0.130	08 21 33.58	+47 02 37.0	*a*	25.88	33.90	11.1	*r*	2013-04-09	1.35
3C 198	0.082	08 22 31.83	+05 57 07.9	*a*	25.53	33.95	10.5	R	2013-04-08	2.01
3C 213.1	0.194	09 01 05.26	+29 01 47.2	*a*	26.17	34.04	11.1	*r*	2013-04-06	1.36
3C 219	0.174	09 21 08.65	+45 38 58.0	*a*	26.86	34.75	11.6	*r*	2013-04-08	1.59
3C 223	0.137	09 39 52.74	+35 53 58.0	*a*	26.18	35.15	11.0	*r*	2013-04-07	2.17
3C 223.1	0.107	09 41 24.02	+39 44 41.6	*b*	25.57	34.56	11.3	*r*	2012-12-13	1.14
3C 234	0.185	10 01 49.52	+28 47 08.7	*a*	26.80	36.09	11.8	*r*	2013-04-08	1.79

Table 2.4 – continued.

3C 236	0.101	10 06 01.73	+34 54 10.4	*a*	25.87	33.87	11.4	*r*	2012-12-13	1.20
3C 258	0.165	11 24 43.88	+19 19 29.5	*c*	26.18	33.17	-	*r*	2013-04-07	2.20
3C 277.3	0.086	12 54 11.99	+27 37 34.1	*a*	25.54	33.92	11.2	*r*	2013-04-07	2.01
3C 284	0.239	13 11 04.65	+27 28 06.8	*a*	26.60	34.57	11.6	*r*	2013-04-09	1.36
3C 285	0.079	13 21 17.83	+42 35 14.4	*a*	25.57	33.53	11.0	*r*	2013-04-07	1.57
3C 287.1	0.216	13 32 53.25	+02 00 45.8	*a*	26.36	34.71	11.5	*r*	2013-04-08	1.79
3C 288	0.246	13 38 49.99	+38 51 09.5	*a*	26.85	33.63	11.6	*r*	2013-04-06	2.01
3C 300	0.270	14 22 59.86	+19 35 36.7	*b*	26.92	34.99	11.6	*r*	2013-04-06	2.01
3C 303	0.141	14 43 02.74	+52 01 37.5	*a*	26.10	34.72	11.4	*r*	2013-04-08	1.35
3C 303.1	0.267	14 43 14.52	+77 07 27.6	*a*	26.56	35.40	11.2	*r*	2013-04-08	1.18
3C 310	0.054	15 04 57.11	+26 00 58.9	*a*	25.91	33.03	10.6	*r*	2013-04-06	1.79
3C 314.1	0.120	15 10 23.12	+70 45 53.4	*a*	25.92	32.67	10.8	*r*	2013-04-10	1.15
3C 315	0.108	15 13 40.05	+26 07 30.1	*b*	26.05	33.85	10.9	*r*	2013-04-06	1.90
3C 319	0.192	15 24 05.50	+54 28 14.6	*d*	26.52	<33.14	11.1	*r*	2013-04-09	1.21
3C 321	0.096	15 31 43.45	+24 04 18.7	*a*	25.82	35.30	11.4	*r*	2013-04-08	1.57
3C 323.1	0.264	15 47 43.55	+20 52 16.5	*b*	26.63	35.78	12.1	*r*	2013-04-10	1.15
3C 326	0.090	15 52 09.06	+20 05 48.7	*a*	25.92	33.38	11.2	*r*	2013-04-07	2.01
3C 332	0.152	16 17 52.54	+32 22 34.5	*b*	26.10	34.79	11.4	*r*	2013-04-09	1.19
3C 346	0.161	16 43 48.69	+17 15 49.1	*a*	26.21	34.22	11.7	*r*	2013-04-10	1.34
3C 349	0.205	16 59 28.91	+47 02 55.9	*a*	26.53	34.67	11.2	*r*	2013-04-06	1.57
3C 357	0.166	17 28 20.21	+31 46 01.9	*a*	26.19	33.93	11.5	*r*	2013-04-07	2.01

Table 2.4 – continued.

3C 371	0.050	18 06 50.57	+69 49 30.0	*a*	24.67	33.92	11.4	*r*	2013-04-08	1.35
3C 379.1	0.256	18 24 32.98	+74 20 59.0	*c*	26.48	34.84	11.6	*r*	2013-04-09	1.14
3C 381	0.161	18 33 46.21	+47 27 00.7	*a*	26.39	35.35	11.3	*r*	2013-04-07	1.57
3C 382	0.058	18 35 03.38	+32 41 46.9	*a*	25.52	34.76	11.8	*r*	2013-04-10	1.21
3C 388	0.091	18 44 02.37	+45 33 30.0	*a*	26.03	33.68	11.6	*r*	2013-04-09	1.14
3C 390.3	0.056	18 42 08.88	+79 46 17.3	*a*	25.88	35.06	11.2	*r*	2013-04-08	1.21
3C 401	0.201	19 40 25.03	+60 41 36.2	*a*	26.70	34.03	11.5	*r*	2013-04-10	1.18
3C 403.1	0.055	19 52 30.38	−01 17 19.7	*a*	25.32	32.84	10.9	*r*	2013-08-06	1.08
3C 405	0.056	19 59 28.33	+40 44 01.0	*a*	28.15	35.63	11.9	*i*	2016-08-16	1.08
3C 410	0.249	20 20 06.54	+29 42 13.5	*a*	27.12	35.00	12.2	*i*	2016-08-16	1.07
3C 424	0.127	20 48 12.12	+07 01 17.5	*a*	26.12	33.78	10.7	*r*	2013-08-07	1.11
3C 430	0.054	21 18 19.01	+60 48 07.7	*a*	25.70	33.31	11.3	*r*	2013-08-06	1.07
3C 433	0.102	21 23 44.60	+25 04 28.5	*d*	26.49	34.65	11.7	*r*	2013-08-06	1.14
3C 436	0.215	21 44 11.66	+28 10 18.9	*a*	26.69	34.54	11.4	*r*	2013-08-07	1.07
3C 438	0.290	21 55 52.19	+38 00 29.4	*a*	27.39	<34.44	12.0	*r*	2013-11-28	1.14
3C 452	0.081	22 45 48.77	+39 41 16.1	*a*	26.27	34.32	11.2	*r*	2013-08-06	1.14
3C 456	0.233	23 12 28.08	+09 19 26.4	*c*	26.55	35.79	11.4	*r*	2013-08-07	1.14
3C 458	0.289	23 12 52.08	+05 16 49.8	*c*	26.90	35.01	-	*r*	2013-08-07	1.21
3C 460	0.268	23 21 28.47	+23 46 47.5	*a*	26.57	34.76	11.5	*r*	2013-08-07	1.13

The sample of 3CR objects studied for this thesis was extracted from the catalogue of 298 extragalactic 3CR sources with optical observations, as defined by Spinrad et al. (1985). The full sample of objects consists of all 84 3CR galaxies in the catalogue that have redshifts in the range $0.05 < z < 0.3$. The lower redshift limit was imposed to restrict the sample to galaxies with high radio powers ($L_{1.4GHz} \gtrsim 10^{25}$ W Hz^{-1}), while the upper redshift limit chosen to ensure that they were close enough for their optical morphologies to be characterised in detail, and to improve the sensitivity of the imaging observations for faint tidal feature detections.

However, 11 of the selected sources are also included in the 2Jy sample of powerful radio galaxies (e.g. as outlined in Dicken et al., 2009), which has already been studied extensively with deep optical imaging observations in the context of triggering of the nuclear activity (Ramos Almeida et al., 2011, 2012, 2013): 3C 15; 3C 17; 3C 18; 3C 105; 3C 227; 3C 273; 3C 327; 3C 348; 3C 403; 3C 445; and 3C 459. As a result, these sources were excluded from the final sample considered for this research, which therefore contains 73 3CR radio galaxies that meet the redshift constraints. One of these objects, 3C 223, is also a member of the sample of Type 2 quasars outlined below (see §2.5), but is still considered as part of this 3CR sample throughout this thesis. Due to their broad range of sky coordinates, it was necessary for the 3CR objects to be observed during different observing windows across several different years (between 2012 and 2016), as can be seen from the observation dates listed in Table 2.4.

Some basic information on the properties of the sources in the final sample is presented in Table 2.4, mostly extracted from the catalogue of Spinrad et al. (1985). Alternative references were used for the source coordinates in cases where the optical counterpart identifications from Spinrad et al. (1985) were unclear (e.g. galaxy pairs), when possible using the corresponding X-ray source positions (Evans et al., 2010; Massaro et al., 2010, 2012). The 1.4 GHz radio powers were derived from the 178 MHz flux densities, assuming a standard spectral index of $\alpha = -0.7$. The stellar masses were derived from the near-infrared luminosities of the targets, and have been corrected to estimated MPA-JHU equivalent values for direct comparison with SDSS galaxies in the catalogue. This process was important for the control matching procedure involved in later analysis, and is described in detail in Chapter 4.

The spectroscopic properties of the vast majority of the objects in the sample have been determined by Buttiglione et al. (2009, 2010, 2011), who used optical spectra taken with the Telescopio Nazionale Galileo (TNG) on La Palma. The measured [OIII]λ5007 emission line luminosities or upper limits[2] from these studies are listed in Table 2.4, which were only unavailable for three of the sources: the line was not detected in their spectra of 3C 52 and 3C 130, and 3C 405 (Cygnus A) is not included in their samples. For the former two cases, the upper limits provided by these authors for the Hα emission line were used to obtain the estimates listed in Table 2.4, under the assumption that the noise levels in the two regions of the spectrum were equivalent. All emission line measurements presented in the studies were corrected for Galactic reddening.

These authors also used the spectroscopic data to classify the galaxies as HERGs and LERGs, with the excitation index scheme from Buttiglione et al. (2010) being employed in nearly all cases (the first method in §2.3.1). In the following cases, however, not all of the spectral lines required to calculate the excitation index were detected, and so the authors did not provide classifications for these objects: 3C 35; 3C 52; 3C 89; 3C 130; 3C 258; 3C 319; 3C 346; and 3C 438. Due to its requirement of only one emission line detection, the [OIII]λ5007 equivalent width method adopted by Best & Heckman (2012) has instead been used to obtain classifications for these objects in the current analysis (the third method in §2.3.1), with HERGs having $\mathrm{EW}_{\mathrm{[OIII]}} > 5$Å and LERGs having $\mathrm{EW}_{\mathrm{[OIII]}} < 5$Å. The measurements of the continuum level in the region required were estimated from the spectra presented for these objects in Buttiglione et al. (2009) and Buttiglione et al. (2011). For the objects without clear [OIII]λ5007 detections, the measured Hα fluxes or upper limits were employed as upper limits on the [OIII]λ5007 fluxes, for use with the equivalent width criterion (decisive for 3C 52 and 3C 89). When the [OIII]λ5007 or Hα equivalent width values were not decisive for the classification, the spectral region near the expected position of the [OIII]λ5007 line was visually inspected in order to place an upper limit on its line flux (necessary for 3C 130, 3C 319 and 3C 438).

For 3C 405, the [OIII]λ5007 emission line luminosity was calculated from the flux measured by Osterbrock & Miller (1975), which was chosen because of the large circular aperture (9.4 arcsec in diameter) used for the measurements. This was corrected for Galactic reddening by adopting the average $E(B-V)$ value of 0.48 determined by Taylor et al. (2003) from optical spectra of the outer regions of the target galaxy, where the intrinsic reddening is thought to be minimal. Comparison of the measurements of the [OIII]λ5007 emission line flux and nearby continuum level presented in Osterbrock & Miller (1975) identify it as a HERG, by the equivalent width criterion outlined above.

---

[2] These are 3σ upper limits determined from measurements of the noise level in the spectral regions near to the expected positions of the lines, assuming the instrumental resolution as their width (Buttiglione et al., 2009).

The [OIII]λ5007 luminosity provided by Buttiglione et al. (2010) for 3C 321 is greatly inconsistent with other measurements in the literature, and so the value presented in Dicken et al. (2010) was instead used for this object.

It is here noted that Buttiglione et al. (2010, 2011) identified broad permitted lines in the spectra of a minority of the 3CR objects (11 of the 73; 15%), which are indicative of Type 1 AGN: 3C 33.1; 3C 184.1; 3C 197.1; 3C 219; 3C 287.1; 3C 303; 3C 323.1; 3C 332; 3C 382; 3C 390.3; and 3C 410. However, they also showed that the properties of the optical spectra of these broad-line objects (BLOs), including their excitation indices, were otherwise consistent with those of the HERGs that only exhibited narrow forbidden lines. Visual inspection of the optical images suggests that the presence of unobscured nuclei in these objects does not significantly affect the appearance of the host galaxies, and thus this should not have a strong influence on the analysis of their host morphologies (Chapters 4 and 5). As a result, in this thesis, these objects are not distinguished from the narrow-line HERGs, and the 3CR HERG subsample considered in all subsequent analysis is comprised of the members of both groups.

The redshift, stellar mass, 1.4 GHz radio power, and [OIII]λ5007 emission line luminosity distributions for the 3CR sample are presented in Figure 2.2, with the results for HERGs and LERGs displayed separately. The specific HERG and LERG classifications of the objects are presented in Chapter 5, where their optical morphologies are analysed.

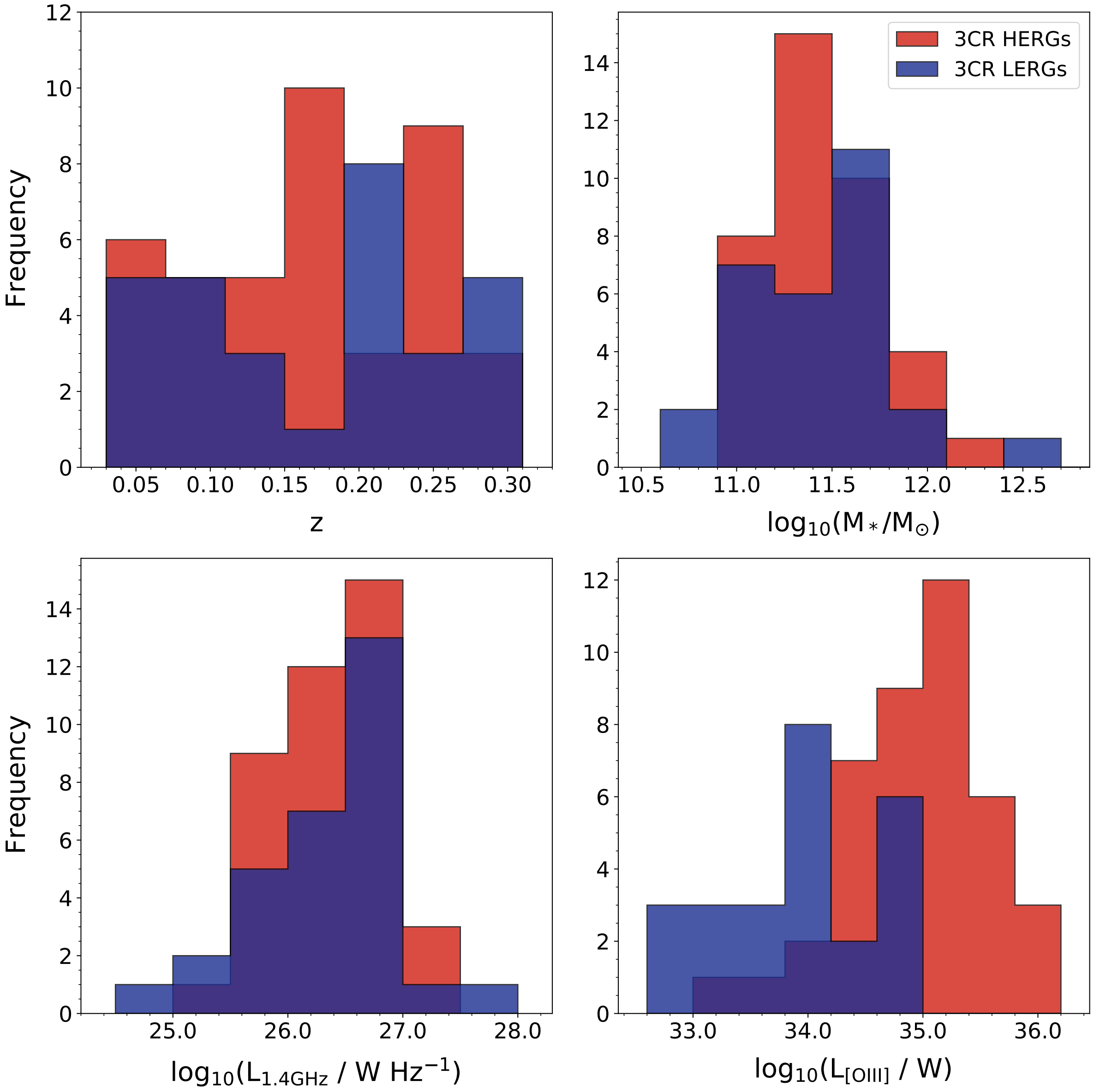

Figure 2.2: Redshift (z), stellar mass (M_*), 1.4 GHz radio power ($L_{1.4GHz}$), and [OIII]λ5007 emission line luminosity ($L_{[OIII]}$) distributions for the HERG (red) and LERG (blue) sources in the 3CR sample. Note that the objects without mass estimates were not considered when plotting the M_* distribution, and the objects with only upper limits on their $L_{[OIII]}$ luminosities were not used for the $L_{[OIII]}$ distribution.

2.5 Type 2 quasars

The last of the samples selected for deep imaging observations consists of Type 2 quasars, which were selected from the large catalogue produced by Reyes et al. (2008) on the basis of [OIII]λ5007 emission line luminosity. This catalogue was generated from the data available in the SDSS spectroscopic database as of July 2006 (round 80% of the Sixth Data Release; Adelman-McCarthy et al., 2008) using several key selection criteria. Firstly, a redshift constraint of $z < 0.83$ was imposed, to ensure that the [OIII]λ5007 emission line would lie in the wavelength range covered by the SDSS spectra. The [OIII]λ5007 line was then required to meet several criteria: i) an equivalent width $>$ 4 Å, to select galaxies with sufficiently strong emission lines; ii) a signal-to-noise ratio of ≥ 7.5; and iii) a luminosity $\geq 10^{8.3}\,\mathrm{L}_{\odot}$. For the objects with redshifts $z < 0.36$, the diagnostic diagrams of Kewley et al. (2001) were employed to classify the ionising source as AGN continuum emission, since all of the required lines were covered by the wavelength range of the spectra. Following this, the Hα and Hβ emission lines were then fitted using Gaussian (Hβ) or non-parametric (Hα) profiles, and visually inspected to exclude sources with broad permitted lines. Alternative methods were used to select Type 2 quasars in the redshift range $0.36 \leq z < 0.83$, but these are not described here since they are not relevant for the sample used for this thesis (see Reyes et al., 2008, for details). The catalogue contains 887 Type 2 quasars selected in this manner.

The sample of Type 2 quasars considered for this thesis includes all of the brightest ($\mathrm{L}_{[\mathrm{OIII}]} \geq 10^{8.4}\,\mathrm{L}_{\odot}$, i.e. $\gtrsim 10^{35}$ W) objects in the Reyes et al. (2008) catalogue at low redshifts $z < 0.14$. Similarly to the other samples described in this chapter, this redshift limit was imposed in order to ensure that the observations would be sufficiently sensitive for the detection of faint interaction signatures. The full sample consists of 48 Type 2 quasars that meet these criteria. Time has been granted to conduct deep imaging observations of all of these targets using the INT, but the sample considered in this thesis only comprises the 25 objects that have been observed up to the current date, which have right ascension coordinates in the range 00h 30m $< \alpha <$ 12h 30m. The remaining 23 targets, with right ascension coordinates in the range 12 30m $< \alpha <$ 22h 00m, will be analysed for a future publication. Once complete, this will constitute the largest set of sensitive, ground-based imaging observations of local Type 2 quasar host galaxies obtained to date.

Some basic information for the sample of 25 Type 2 quasar objects considered here is presented in Table 2.5. As for the radio-intermediate HERG samples, the 1.4 GHz radio powers were derived from their NVSS (Condon et al., 1998) flux densities whenever possible to avoid losses to resolution effects. However, the FIRST flux densities were used for J0858+31 and J1218+08, for which the FIRST images revealed strong contamination from another radio source that would lie within the NVSS beam centred on the target and thus affect its flux density measurement. FIRST flux densities were also used for two other sources, J0818+36 and J1015+00, which were not detected by the NVSS. Two sources in the sample were not detected by either radio survey: J1036+01 and J1223+08. For these objects, upper limits on the 1.4 GHz radio powers were estimated from the 1 mJy limiting flux density of the FIRST catalogue (Becker et al., 1995), the more sensitive of the two surveys.

Despite being selected based on their optical properties, it is seen that the Type 2 quasar sample covers a broad range in radio power, which overlaps significantly with the radio-intermediate regime identified above ($10^{22.5} < \mathrm{L_{1.4GHz}} < 10^{25}$ W Hz^{-1}) and includes two traditionally radio-loud sources ($\mathrm{L_{1.4GHz}} > 10^{25}$ W Hz^{-1}): J1137+61 and 3C 223, the latter also being included in the 3CR sample outlined in §2.4. 3C 223 is considered as part of both samples in all cases, except for when comparisons are being made between the 3CR and Type 2 quasar samples as a whole. Note that the 1.4 GHz radio power and [OIII]λ5007 luminosity from Table 2.4 are also used for this object in Table 2.5, for consistency.

Due to the fact that not all of the targets in the sample were included in the MPA-JHU catalogue, the stellar masses were derived from the near-infrared luminosities of the targets, in the same manner as that performed for the 3CR sources (process described in Chapter 4). Again, these have been corrected to estimated MPA-JHU equivalent values for direct comparison with other SDSS galaxies in the catalogue, as was important for the control matching procedure involved in later analysis. The redshift, stellar mass, 1.4 GHz radio power, and [OIII]λ5007 emission line luminosity distributions for the targets in the sample are presented in Figure 2.3.

Table 2.5: Basic information for the 25 targets in the Type 2 quasar sample described in §2.5. Column key: (1) full SDSS IDs and in-text abbreviations (in brackets), which are named based on the epoch J2000 right ascension (α) and declination (δ) of the target (as in Tables 2.1 and 2.2); (2) spectroscopic redshifts, (3) r-band extinction values (from Schlegel et al., 1998), and (4) extinction-corrected r-band magnitudes, obtained through the SDSS DR16 Object Explorer tool (available at: `http://skyserver.sdss.org/dr16/en/tools/explore/summary.aspx`); (5) 1.4 GHz radio powers or upper limits derived from FIRST or NVSS flux densities (see §2.5); (6) [OIII]λ5007 luminosities from Reyes et al. (2008); (7) MPA-JHU equivalent stellar mass (derived from near-infrared luminosities and a conversion factor, as described in Chapter 4); (8) starting night date and (9) atmospheric seeing measurements for the target observations. *Note that 3C 223 is also a member of this sample, and the 1.4 GHz radio power and [OIII]λ5007 luminosity values from Table 2.4 are instead used here, for consistency.

SDSS ID (Abbr.)	z	A_r (mag)	SDSS r mag (mag)	$\log(L_{1.4\mathrm{GHz}})$ (W Hz^{-1})	$\log(L_{[\mathrm{OIII}]})$ (W)	$\log(M_*)$ ($M_\odot$)	Obs. date	Seeing FWHM (arcsec)
J005230.59−011548.3 (J0052−01)	0.135	0.11	17.64	23.27	35.11	10.8	2020-01-25	1.21
J023224.24−081140.2 (J0232−08)	0.100	0.09	16.65	23.04	35.13	10.8	2020-01-25	1.15
J073142.37+392623.7 (J0731+39)	0.110	0.14	16.94	22.99	35.08	11.0	2020-01-25	1.21
J075940.95+505023.9 (J0759+50)	0.054	0.09	15.68	23.46	35.32	10.6	2020-01-19	1.21
J080224.34+464300.7 (J0802+46)	0.121	0.17	16.94	23.48	35.11	11.1	2020-01-25	1.21
J080252.92+255255.6 (J0802+25)	0.081	0.08	15.15	23.65	35.32	11.3	2020-01-20	1.55
J080523.30+281815.7 (J0805+28)	0.129	0.11	16.71	23.38	35.14	11.4	2020-01-20	1.69
J081842.36+360409.6 (J0818+36)	0.076	0.13	17.06	22.47	35.04	10.6	2020-01-25	1.14
J084135.08+010156.2 (J0841+01)	0.111	0.10	17.13	23.28	35.41	11.1	2020-01-20	1.85
J085810.64+312136.2 (J0858+31)	0.139	0.05	17.63	22.97	35.05	11.1	2020-01-20	1.44
J091544.18+300922.0 (J0915+30)	0.130	0.06	16.39	23.25	35.30	11.2	2020-01-25	1.20
J093952.75+355358.8 (3C 223)	0.137	0.03	16.73	26.18*	35.15*	11.0	2020-01-25	0.95

Table 2.5 – continued.

J094521.33+173753.2 (J0945+17)	0.128	0.06	16.68	24.25	35.48	10.9	2020-01-19	1.57
J101043.36+061201.4 (J1010+06)	0.098	0.06	16.40	24.31	35.19	11.4	2020-01-20	1.57
J101536.21+005459.3 (J1015+00)	0.120	0.08	17.16	22.93	35.23	10.9	2020-01-24	1.57
J101653.82+002857.0 (J1016+00)	0.116	0.08	16.63	23.57	35.14	11.0	2020-01-24	1.57
J103408.58+600152.1 (J1034+60)	0.051	0.02	14.27	23.02	35.36	11.1	2020-01-19	1.34
J103600.37+013653.5 (J1036+01)	0.107	0.09	15.75	<22.42	35.07	11.3	2020-01-25	1.14
J110012.38+084616.3 (J1100+08)	0.101	0.07	15.53	24.14	35.66	11.4	2020-01-25	1.11
J113721.36+612001.1 (J1137+61)	0.111	0.09	16.79	25.53	35.17	10.9	2020-01-20	1.35
J115245.66+101623.8 (J1152+10)	0.070	0.07	15.96	22.63	35.25	10.8	2020-01-25	0.95
J115759.50+370738.2 (J1157+37)	0.128	0.05	16.54	23.34	35.14	11.2	2020-01-20	1.08
J120041.39+314746.2 (J1200+31)	0.116	0.05	16.54	23.42	35.86	11.0	2020-01-20	1.07
J121839.40+470627.6 (J1218+47)	0.094	0.04	16.86	22.67	35.11	10.6	2020-01-25	0.94
J122341.47+080651.3 (J1223+08)	0.139	0.05	17.60	<22.66	35.31	11.0	2020-01-25	0.98

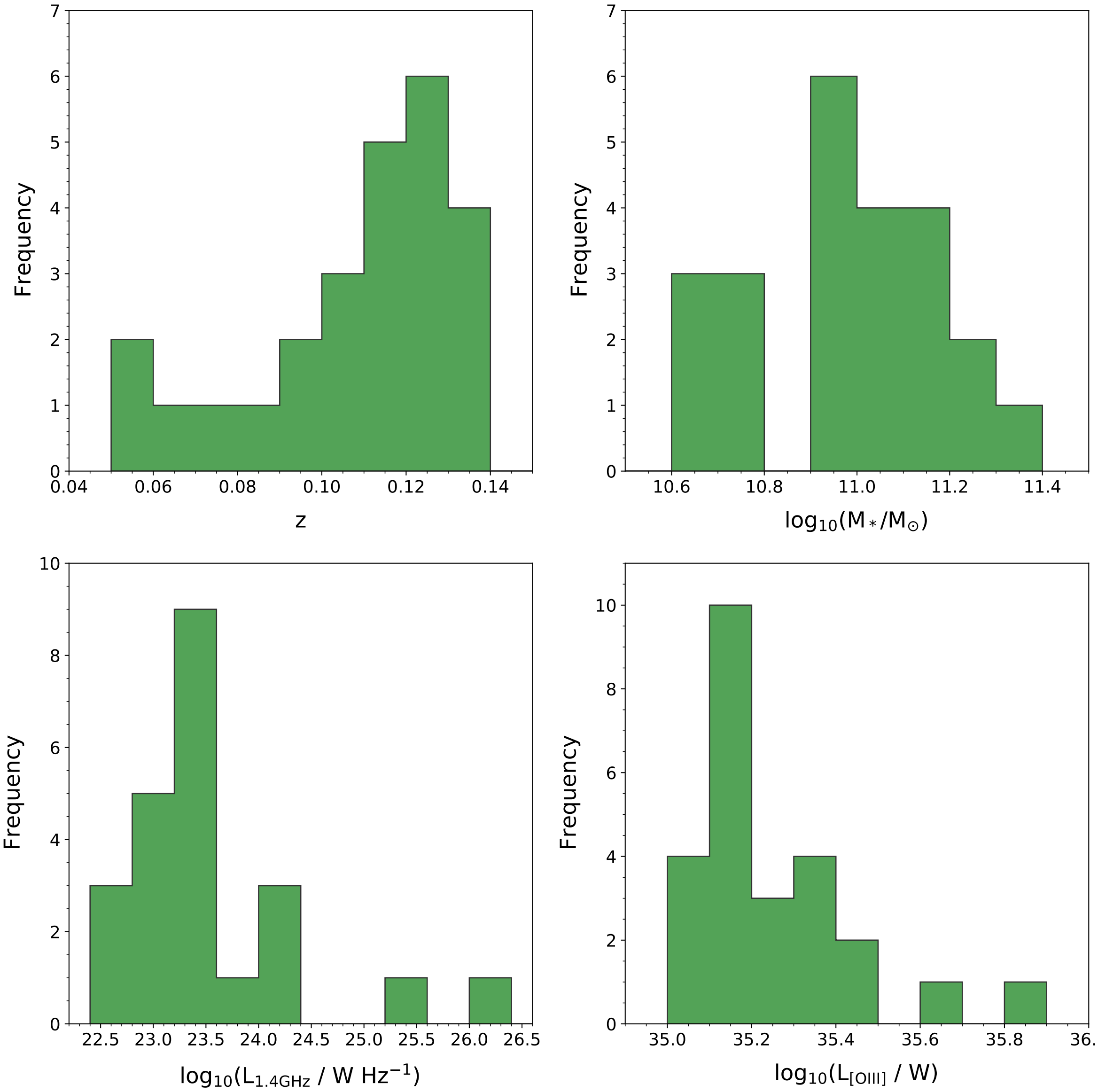

Figure 2.3: Redshift (z), stellar mass (M_*), 1.4 GHz radio power ($L_{1.4GHz}$), and [OIII]λ5007 emission line luminosity ($L_{[OIII]}$) distributions for the galaxies in the Type 2 quasar sample.

2.6 Summary of key sample properties

The radio-intermediate HERG, 3CR, and Type 2 quasar samples described in this chapter include a large number of active galaxies that encompass a broad range of properties. The ranges in redshift, stellar mass, 1.4 GHz radio luminosity, and [OIII]λ5007 emission line luminosity covered by each of the samples are summarised in Table 2.6. The corresponding median values and standard deviations in these properties are also included.

Table 2.6: The ranges, medians, and standard deviations of the redshifts, stellar masses, 1.4 GHz radio powers, and [OIII]λ5007 emission line luminosities of the four samples studied with deep optical imaging observations for this thesis. The total numbers of targets in each sample are included in brackets below the sample names.

		RI-HERG low (30)	RI-HERG high (28)	3CR (73)	Type 2 quasars (25)
z	Range	0.031–0.098	0.051–0.149	0.050–0.296	0.051–0.139
	Med.	0.074	0.110	0.174	0.111
	σ	0.019	0.032	0.077	0.025
$\log(M_*/M_\odot)$	Range	10.0–11.4	10.7–11.4	10.5–12.7	10.6–11.4
	Med.	10.7	11.2	11.4	11.0
	σ	0.3	0.2	0.4	0.2
$\log(L_{1.4GHz})$ ($\mathrm{W\,Hz^{-1}}$)	Range	22.52–23.98	24.01-24.88	24.67–28.15	22.47–26.22
	Med.	23.06	24.54	26.40	23.34
	σ	0.39	0.24	0.58	0.86
$\log(L_{[OIII]})$ (W)	Range	32.86–34.24	33.00-35.06	32.67–36.09	35.04–35.86
	Med.	33.56	33.98	34.64	35.19
	σ	0.35	0.46	0.80	0.19

2.7 Optical imaging observations

All of the deep optical imaging data analysed for this thesis were obtained using the Wide-Field Camera (WFC) attached to the 2.5m Isaac Newton Telescope (INT) at the Observatorio del Roque de los Muchachos, La Palma. The WFC consists of four thinned, anti-reflection-coated 2048 × 4100 pixel CCDs separated by gaps of $660-1098$ μm. With pixel sizes of 0.333 $\mathrm{arcsec\,pixel^{-1}}$, this provides a large total field-of-view of order 34 × 34 $\mathrm{arcmin^2}$. The vast majority of the images were taken through the WFC Sloan r-band filter ($\lambda_{\mathrm{eff}} = 6240\,$Å, $\Delta\lambda = 1347\,$Å), chosen to be consistent with existing SDSS r'-band observations of our targets (see Fukugita et al., 1996, for further details) and the

GMOS-S *r'*-band ($\lambda_{\rm eff}$ = 6300 Å, $\Delta\lambda$ = 1360 Å; for objects with $z < 0.4$) and *i'*-band ($\lambda_{\rm eff}$ = 7800 Å, $\Delta\lambda$ = 1440 Å; for objects with $0.4 < z < 0.7$) observations of radio-loud galaxies in the 2 Jy sample, performed by Ramos Almeida et al. (2011). However, images were taken through the WFC Sloan *i*-band filter ($\lambda_{\rm eff}$ = 7743 Å, $\Delta\lambda$ = 1519 Å) for some of the 3CR sources (3C 52, 3C 61.1, 3C 63, 3C 130, 3C 405, 3C 410), in order to reduce the influence of the bright moonlight that was present in the period in which these observations were performed. 3C 52, 3C 63, and 3C 410 have also been imaged through the *r*-band filter, but the *i*-band observations of these sources were chosen for the analysis due to their higher image quality. 3C 198 was observed through the WFC Harris R-band filter ($\lambda_{\rm eff}$ = 6380 Å, $\Delta\lambda$ = 1520 Å), which has a different response function to the WFC Sloan *r*-band filter, but covers a broadly similar wavelength range.

The observations were conducted in several separate runs between December 2012 and January 2020, on the dates listed in Tables 2.1, 2.2, 2.4, and 2.5. Consequently, the observing conditions varied greatly over the course of the observations. Individual seeing full width at half maximum (FWHM) values for the observations were calculated using the `THELI` package for astronomical image reduction and processing (see Schirmer, 2013, for details), using plots of half-light radius against magnitude for foreground stars in the final coadded images (after the reduction outlined in §2.8). These values are presented in Tables 2.1, 2.2, 2.4, and 2.5, and represent the medians of the measurements from each of the four CCDs. The seeing FWHM measurements range from 0.94 to 2.20 arcsec across the four samples, with a median of 1.21 arcsec. The RI-HERG high and Type 2 quasar samples were observed with the best typical seeing, with medians of 1.14 and 1.20 arcsec and standard deviations of 0.11 and 0.26 arcsec, respectively. The RI-HERG low and 3CR samples were typically observed in poorer seeing conditions, with medians of 1.38 and 1.34 arcsec and standard deviations of 0.26 and 0.32 arcsec, respectively.

The vast majority of the targets were observed using 4 × 700 s exposures, yielding total exposure times of 2800 s per target. Such exposure lengths were necessary for the detection of low-surface-brightness tidal features, but the observations were divided into separate exposures to ensure that the target galaxies were not saturated in individual images. This also allowed dithering of the observations to be performed, which was done in order to overcome the gaps in the images introduced by the spacings between the CCDs; a square dithering pattern was employed for this process, using four pointing offsets of 30 arcsec. Flat-field and image defect corrections were also improved by this dithering.

While this general procedure was applied in almost all cases, some targets were observed in a slightly different manner. 3C 405 and 3C 410 lie in crowded fields that contain a large number of stars, due to their close proximity to the Galactic plane. In these cases, the decision was taken to divide the observations into additional separate exposures that would yield similar total exposure times and reduce the number of stars in the field that were saturated in the individual images: 5 × 500 s for 3C 405 and 7 × 400 s for 3C 410. Only three exposures were obtained for 3C 63 (3 × 700 s) and 3C 458 (3 × 600 s), while five were taken for 3C 236, 3C 326, and J0945+17 (each 5 × 700 s), six for 3C 349 (6 × 700 s) and seven for J1015+00 (7 × 700 s). Four shorter exposures were taken for J1223+08 (4 × 400 s) due to time constraints on the night on which this target was observed.

In addition, there were several cases where some of the individual frames could not be used for the analysis because of issues with the images. One of the observations for each J0836+05, 3C 310, and 3C 236 had to be excluded because of a large number of satellite trails, and so 3 × 700 s, 4 × 700 s, and 3 × 700 s exposures were used for these targets, respectively. One image of 3C 326 was faulty, which left 4 × 700 s usable exposures. Bad striping was visible in one of the CCDs in several observations of the Type 2 quasar objects, which rendered one image for each J0858+31 and J1200+31 unusable and left 3 × 700 s exposures to be used in both cases. The same was true for two of the images for each J0945+17 and J1015+00, which left 3 × 700 s and 5 × 700 s usable exposures for these targets, respectively. Finally, issues with the coordinates for one of the images of J0818+36 meant that only 3 × 700 s exposures could be used for this target. Targets for which only three frames were used were still observed with sufficient dithering, such that the effect of the gaps between the WFC CCDs was minimal.

Despite the differences in individual and total exposure times for some of the targets, similar limiting surface brightnesses are achieved across all observations in each sample (see §2.9). As a result, it is unlikely that these factors have a significant effect on the detection of faint tidal features in the images.

2.8 Optical imaging data reduction

All processing of the target images, from initial reduction to construction of the final mosaic images, was carried out using `THELI` (Schirmer, 2013; latest version available at `https://github.com/schirmermischa/THELI`), an automated astronomical image reduction software package within which the INT/WFC setup is pre-configured. Bias and flat-field corrections for each observation were performed via the subtraction of master bias frames and division of the master flat-field frames, respectively. These master frames were constructed by median-combining individual calibration frames that were taken on the same date as the given target observation. In the minority of cases where these calibration images were not available for the date in question, those taken on the closest date possible were used instead (differences of four nights or less). The individual flat-field images were r-band or i-band dome flats with a median exposure time of 12s. Only the flat-field frames taken with the same filter as those of the relevant target observations were considered in all cases. Removal of the overscan level (noise from the regions of the CCDs not directly exposed to light) was carried out on all calibration and science frames.

At this point, the i-band observations required an additional step in order to remove the notable fringing effects that were visible in the science images, caused by internal reflection within the CCDs. To account for this, a two-pass image background model was created by `THELI`. On the first pass, no detection and masking of the objects in the field was performed, in order to model the brighter background features in the image. The remaining fainter background features were then modelled in the second pass, which was performed after the detection and masking of all objects in the field above a certain threshold; a signal-to-noise per pixel of 1.5 for objects with 5 or more connected pixels was chosen for this processing. This modelling was not necessary for the r-band observations, since this band does not contain the numerous sky emission lines that are present in the i-band that are the major cause of these fringing effects.

An astrometric solution for all calibrated images was calculated in `THELI` through cross-matching object catalogues produced for each image by `SExtractor` (Bertin & Arnouts, 1996) with either the all-sky USNO-B1 catalogue (Monet et al., 2003; for the RI-HERG low sample) or the GAIA DR2 catalogue (Gaia Collaboration et al., 2018; for the other samples) – the imaging data for the RI-HERG low sample were reduced with an earlier version of `THELI` within which the GAIA catalogue was not available. The comparison of these catalogues and the generation of the astrometric solution was performed within `THELI` using the `Scamp` pipeline for astrometry and photometry (see Bertin, 2006). Cross-matching was only carried out for sources with apparent magnitudes ≤ 20 to prevent the astrometry from being overconstrained, while still providing a sufficiently large number of objects to obtain a good solution. Due to the crowded field in the images of 3C 405, the magnitude limit was reduced to ≤ 18 in order to achieve a suitable solution.

To correct for remaining variations in the sky background level across the images, `THELI` was used to produce a sky model and subtract it from the calibrated data. Prior to model creation, objects with a minimum of five connected pixels at a value of $1.5\,\sigma$ above the measured background level were detected and masked using `SExtractor`, as was done for the background modelling outlined above. A sky model convolved with a 60-pixel FWHM Gaussian kernel was found to produce the best results in almost all cases; the exception was J0902+52, for which a FWHM of 200 pixels was required due to a large gradient in the background level near a very bright foreground star. Lastly, coaddition of the four separate calibrated images was performed to produce the final mosaic image for each target, using the positional information from the prior astrometric solutions.

`THELI` was then used to calculate photometric zero points for the coadded images of each of the targets. This was performed through comparison of the derived instrumental magnitudes for stars in the image field with their catalogued magnitudes in the Pan-STARRS1 (Chambers et al., 2016) First Data Release[3]. Only stars with instrumental magnitude errors ≤ 0.05 (as derived by `SExtractor`) and maximum counts $\leq 70\%$ of the saturation level were used for this process. This method has the key advantage of automatically correcting for photometric variability throughout the nights, since the calibration stars are observed at the same time and at the same position on the sky as the galaxy targets. It also removes the reliance on average zero points derived from standard star observations.

2.9 Limiting surface brightness

Determining the limiting surface brightness achieved by deep imaging observations is important, both for assessing the significance of detections of low-surface-brightness structures in the galaxies and for comparing the image sensitivities with those achieved by other studies. However, as outlined by Duc et al. (2015), determinations of surface brightness limits in deep imaging programs often vary, making effective comparisons difficult. Consequently, the technique used to determine the limiting surface brightnesses for the deep optical images is clarified here.

The employed method is based on measurements of the variations in the sky background level in the final coadded images, and closely follows that used by Atkinson et al.

---

[3] Note that for the analysis of the RI-HERG low sample presented in Chapter 3, the catalogued SDSS r-band magnitudes were used to determine the zero points at this stage. However, since not all of the 3CR targets are covered by the SDSS survey footprint, the Pan-STARRS1 magnitudes are used when comparing between the different samples. Both surveys use the AB magnitude system and the difference between the r-band magnitudes is minor, characterised by the following equation: $r_{\mathrm{SDSS}} = r_{\mathrm{P1}} - 0.001 + 0.011(g-r)_{\mathrm{P1}}$ (Tonry et al., 2012).

Table 2.7: The means, medians, and standard deviations of the $\sigma_{\rm sky}$ and $3\sigma_{\rm sky}$ limiting surface brightness measurements (μ_{AB}) for the observations of the four samples studied for this thesis. The values have units of mag arcsec^{-2} and are presented in the Pan-STARRS1 AB magnitude photometric system.

		RI-HERG low	RI-HERG high	Type 2 quasars	3CR (r-band)	3CR (i-band)
$\mu_{AB}^{\sigma_{\rm sky}}$	Mean	28.1	28.3	28.2	28.1	26.9
	Median	28.1	28.3	28.3	28.2	26.9
	Std. dev.	0.3	0.3	0.3	0.4	0.2
$\mu_{AB}^{3\sigma_{\rm sky}}$	Mean	27.0	27.1	27.0	26.9	25.7
	Median	27.0	27.1	27.0	27.0	25.7
	Std. dev.	0.3	0.3	0.3	0.4	0.2

(2013) for their analysis of faint tidal features in wide-field images from the Canada-France-Hawaii Telescope Legacy Survey (CFHTLS). To clarify, these measurements were carried out *after* all reduction had been performed, including the flattening achieved through the subtraction of the sky background model (§2.8). Firstly, the total counts detected within 40 unique circular apertures of one arcsecond in radius were measured, placed in regions of the sky background with minimal or no influence from the haloes of bright objects in the field. For the detailed analysis of the RI-HERG low sample images described in Chapter 3, these were distributed solely in suitable locations across the field of the CCD in which the targets were centred (WFC CCD4). For the analysis described in Chapter 5, the 40 apertures were placed in suitable locations in each of the four WFC CCDs, and were evenly distributed between them (i.e. 10 per CCD). This was due to the fact that the cut-out images of control galaxies (matched to the targets in stellar mass and redshift) required for this latter project were distributed throughout the total field of view covered by the WFC, whereas the analysis outlined in Chapter 3 was restricted to the target CCD only.

The standard deviation in the sky background level within the 40 apertures ($\sigma_{\rm sky}$) was then determined and converted to an apparent magnitude, using the photometric zero points derived as outlined above, to provide final limiting surface brightness measurements. The mean $\sigma_{\rm sky}$ and $3\sigma_{\rm sky}$ limiting surface brightnesses over all r-band observations of the targets are 28.2 mag arcsec^{-2} and 27.0 mag arcsec^{-2}, respectively, and the measured standard deviation for these quantities is 0.3 mag arcsec^{-2}. The values for the i-band observations of the 3CR targets are 26.9 mag arcsec^{-2} ($\sigma_{\rm sky}$) and 25.7 mag arcsec^{-2} ($3\sigma_{\rm sky}$), with a standard deviation of 0.2 mag arcsec^{-2}. $\sigma_{\rm sky}$ and $3\,\sigma_{\rm sky}$ limiting surface brightness magnitudes for all targets in the RI-HERG low sample are presented in Table 3.2 in Chapter 3. Values for the individual target observations are not presented for the RI-HERG high, 3CR, and Type 2 quasar samples. However, a summary of the average values for each sample is presented in Table 2.7.

2.10 Chapter summary

This chapter has detailed how each of the active galaxy samples studied in this thesis were selected, and has described how the deep optical imaging observations and reduction of these data were conducted. These samples of radio-intermediate HERGs, 3CR radio galaxies, and Type 2 quasars encompass a broad range of properties, including their optical emission line luminosities and radio powers, which is important for the goals of the research outlined in Chapter 1. Detailed analysis of the optical morphologies of the objects in the RI-HERG sample is described in Chapter 3. The optical morphologies of all active galaxies in the above samples are then analysed together in Chapter 5, based on classifications obtained using an online interface that is described in Chapter 4. A large number of control galaxies, selected to lie within the wide fields of the INT/WFC images and matched to the targets in terms of stellar mass and redshift (Chapter 4), are also classified in this way.

Chapter 3

Detailed analysis of the optical morphologies of radio-intermediate HERGs

3.1 Declaration

The work described in this chapter was reported in the first of my lead-author publications in Monthly Notices of the Royal Astronomical Society: Pierce et al. (2019), *Do AGN triggering mechanisms vary with radio power? - I. Optical morphologies of radio-intermediate HERGs*. Much of the content of this chapter is presented as it was in the publication, but has been adapted for this thesis where appropriate.

3.2 Chapter introduction

As introduced in Chapter 1, the feedback effects caused by AGN with powerful radio jets have rendered them an important component of current models of galaxy evolution. This feedback is thought to take place both on the scales of individual galaxies, where jets can drive multiphase gas outflows, and in galaxy haloes and the surrounding environments, where the jets inflate bubbles and cavities and prevent the hot gas in these regions from cooling. As outlined at the end of §1.5.5, there is now strong evidence to suggest that the radio jets of HERGs with intermediate radio powers ($22.5 < \log(\mathrm{L}_{1.4\mathrm{GHz}}) < 25.0\ \mathrm{W\,Hz^{-1}}$) could be particularly important for galaxy-scale feedback. These objects are capable of causing kinematic disturbances in the multiphase gas of their host galaxies (e.g. Tadhunter et al., 2014b; Harrison et al., 2015; Ramos Almeida et al., 2017; Villar-Martín et al., 2017), perhaps even more significantly than those with higher radio powers (Mullaney et al., 2013). Adding to this, it is evident from the local radio galaxy luminosity function that radio-intermediate AGN are considerably more common than their counterparts at higher radio powers (e.g. Mauch & Sadler, 2007; Best & Heckman, 2012; Sadler et al., 2014; Sabater et al., 2019). Detailed characterisation of the population of radio-intermediate HERGs is therefore particularly important for investigating the role of radio AGN feedback in galaxy evolution.

In order to correctly implement radio-intermediate HERG feedback into models of galaxy evolution, it is important to know what types of host galaxies they are associated with. At high radio powers, the general population of radio AGN hosts is predominantly composed of elliptical galaxies with high stellar masses (Matthews et al., 1964; Dunlop et al., 2003; Best et al., 2005b; Tadhunter et al., 2011). It is seen, however, that in samples of local radio galaxies selected at high flux densities (e.g. 3CR and 2Jy), the few that show evidence for major disk-like components on cursory inspection of their optical images are typically found towards lower radio powers, and half of these lie in the radio-intermediate regime (Tadhunter, 2016). In addition, it appears that the frequency of late-type hosts could increase at lower radio powers – Sadler et al. (2014) find that 30% of their radio AGN hosts are spiral galaxies at low redshifts (mostly $L_{1.4GHz} \sim 10^{22-23}\,\mathrm{W\,Hz^{-1}}$). Furthermore, Seyfert galaxies, arguably the counterparts of HERGs at the lowest radio powers, are predominantly associated with late-type morphologies (e.g. Adams, 1977). Therefore, the radio-intermediate objects are crucial for investigating the possible transition in host galaxy morphologies along the HERG sequence.

In addition, it is important to determine the likely triggering mechanisms for the nuclear activity. Previous deep optical imaging studies of large samples of powerful radio galaxies demonstrate that those with strong optical emission lines commonly show morphological signatures of galaxy mergers at relatively high surface brightnesses (Heckman et al., 1986; Smith & Heckman, 1989a,b; Ramos Almeida et al., 2011). Most notably, Ramos Almeida et al. (2011, 2012) showed that 94^{+4}_{-7}% of the strong-line radio galaxies (SLRGs)[1] in the 2Jy sample exhibit such tidal features, also showing an excess relative to samples of non-active elliptical galaxies matched in absolute magnitude and image surface brightness depth. The 2Jy SLRGs also show a preference for group-like environments (Ramos Almeida et al., 2013), which are suitable for frequent galaxy-galaxy collisions without the high relative galaxy velocites found in clusters that might reduce the merger rate (Popesso & Biviano, 2006). This, amongst other evidence, has led to suggestions that the cold gas necessary for radiatively efficient accretion in HERGs is supplied by mergers and interactions.

In contrast with the situation for the high radio power HERGs selected in samples such as the 3CR and 2Jy, the lack of systematic study of radio-intermediate HERGs means that the typical host galaxies and fuelling mechanisms have not yet been determined for this population. To this end, this chapter describes how deep optical images of the 30 local HERGs in the RI-HERG low sample (described in Chapter 2) were used to investigate their host morphologies and the likely triggering mechanisms for their nuclear activity. The morphologies were analysed using both visual inspection and light profile modelling, in order to identify any signatures of interactions or mergers in the galaxies and to determine their general morphological types (elliptical, lenticular, or spiral/disk). The sample selection and imaging data reduction was detailed in Chapter 2. The analysis of the reduced images and the subsequent results are outlined in §3.3. The results are then discussed in §3.4, and §3.5 summarises the work and the conclusions drawn.

---

[1] As mentioned in §1.3.1, strong-line radio galaxies are selected based on the equivalent width of the [OIII]λ5007 emission line, but show a strong overlap with the HERG population, which is often selected using emission line ratios (see discussion in Tadhunter, 2016).

3.3 Analysis and results

Following the image reduction processes outlined in Chapter 2, the final coadded images for the RI-HERG low sample were analysed to investigate the detailed optical morphologies of the AGN host galaxies. The first goal was to identify and characterise any tidal features and other interaction signatures associated with the galaxies, in order to provide an indication of the importance of merger-based triggering of the nuclear activity (see §3.3.1). Following this, the morphological classes of the host galaxies were determined via both visual inspection and detailed modelling of their surface brightness profiles, the latter being performed using the two-dimensional fitting algorithm `GALFIT` (Peng et al., 2002, 2010, see §3.3.2). Determining whether the population is primarily composed of early- or late-type galaxies provides an initial impression of how these objects compare to other radio galaxy samples, and is a factor that could be linked to the dominant triggering mechanism for the nuclear activity. The bulge-disk decomposition available from the `GALFIT` models also allows quantitative estimates of the level of disk- or bulge-dominance in the light profiles to be made, assisting with the morphological classifications. The details of this data analysis are presented here.

3.3.1 Tidal features

Classification

Visual inspection of the images was performed by five human classifiers (myself, Clive Tadhunter, Cristina Ramos Almeida, Patricia Bessiere, and Marvin Rose) in order to identify any interaction signatures linked with the AGN host galaxies. To be consistent with the analysis performed on the deep images of the 2Jy radio galaxies (Ramos Almeida et al., 2011, 2012, 2013), the classification scheme of Ramos Almeida et al. (2011) was used for this process. This scheme is adapted from that produced by Heckman et al. (1986) for their study of a selection of powerful radio galaxies, and is based on the morphological disturbances caused by tidal forces in the galaxy merger simulations of Toomre & Toomre (1972) and Quinn (1984). The tidal features and other interaction signature classifications are as follows:

1. **Tail (T)** – a narrow curvilinear feature with roughly radial orientation;
2. **Fan (F)** – a structure similar to a tail, but that is shorter and broader;
3. **Shell (S)** – a curving filamentary structure with a roughly tangential orientation relative to a radial vector from the main body of the galaxy;

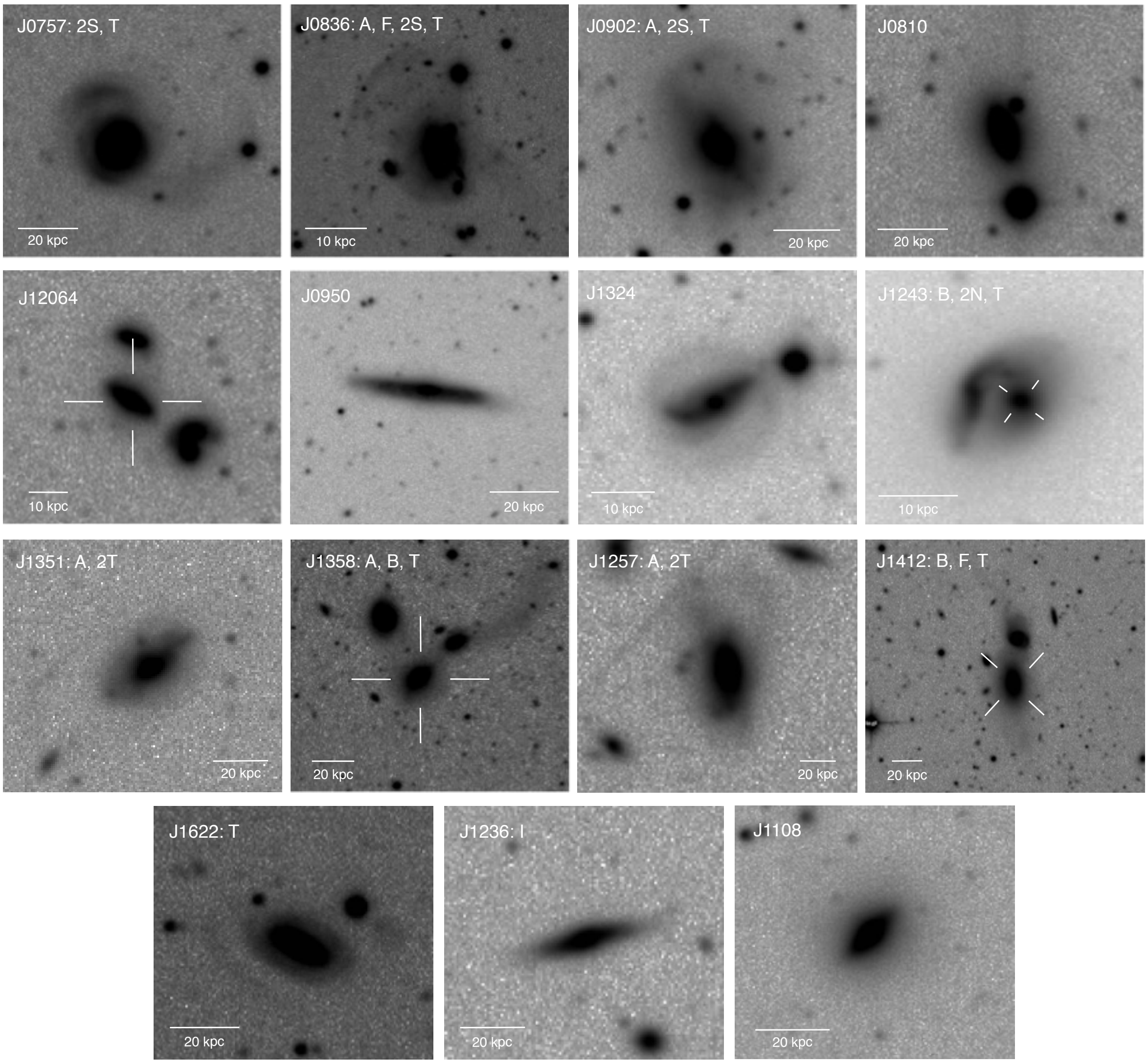

Figure 3.1: Deep r-band images of the half of the RI-HERG low sample with the highest radio powers, lying within the range $23.06 < \log(\mathrm{L}_{1.4\mathrm{GHz}}) < 24.0\ \mathrm{W\,Hz^{-1}}$. The galaxies are also ordered in terms of decreasing radio power from top-left to bottom-right within the figure. The images are centred on the targets and are identified within crosses on the images, where ambiguous. Shortened versions of the abbreviated SDSS IDs are shown for each target, along with any interaction signatures from the classification scheme outlined in §3.3.1 that are associated with the hosts or companions clearly involved in the interactions (bracketed classifications are based on uncertain detections; see text). Note that J1206+10 is here labelled by J12064. Approximate scale bars, equivalent to the indicated projected physical distances in kiloparsecs, are displayed in all cases. The images are oriented such that north is up and east is left.

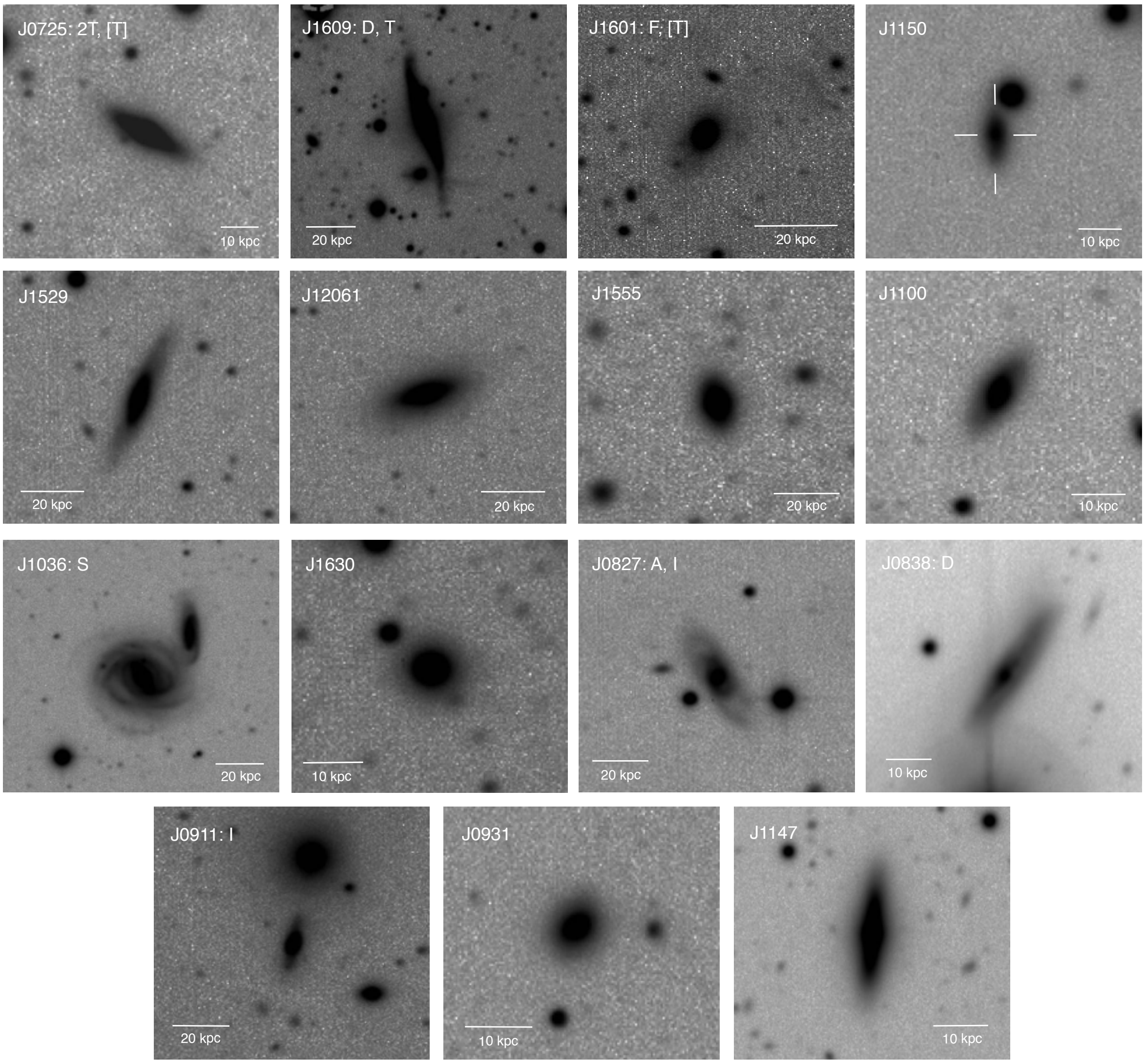

Figure 3.2: As Figure 3.1, but for the half of the RI-HERG low sample with the lowest radio powers, lying within the range $22.5 < \log(L_{1.4\mathrm{GHz}}) < 23.06$ W Hz^{-1}. Note that J1206+35 is here labelled by J12061.

4. **Bridge (B)** – a feature that connects a radio galaxy with a companion;
5. **Amorphous halo (A)** – the galaxy halo is misshapen in an unusual way in the image;
6. **Irregular (I)** – the galaxy is clearly disturbed, but not in a way that fits into any of the previous classification categories;
7. **Multiple nuclei**[2] **(e.g. 2N, 3N)** – two or more brightness peaks within a distance of 9.6 kpc;
8. **Dust lane (D)** – a clear linear dark structure within the galaxy.

A galaxy with a morphology that did not meet any of these criteria, or that only showed evidence of dust lanes (category 8), was classified as undisturbed and hence non-interacting. Examples of each of the different classifications are indicated in Figures 3.1 and 3.2, which display the deep r-band images for the halves of the sample with highest and lowest radio powers, respectively – images within each figure are also ordered by decreasing radio power from top-left to bottom-right.

Each classifier was provided with a FITS image of each of the radio galaxies in the sample and asked to identify and classify any interaction signatures that they believed to be associated with them. The use of these images meant that the image contrast and scale could be manipulated as desired, which was particularly useful for the identification of faint tidal features – note that this differs from the technique used for the second study of the optical morphologies of active galaxies performed for this thesis (Chapters 4 and 5). A brief description of their characteristics (e.g. orientation, extent, faintness) was also required to help avoid confusion when comparing classifications from different individuals. A qualitative estimate of the confidence of the classifications was also recorded by each assessor to aid with the process of combining results to produce final classifications. This method was carried out by each individual independently to avoid any influence from the results of others.

In order to avoid biases introduced by the galaxy properties, most importantly by their radio powers, only the cosmological scale (kpc arcsec^{-1}) for each target was provided to each classifier prior to image inspection – this value was required to identify targets that host multiple nuclei. The independent results were combined by considering each

---

[2] The distance criterion used here is consistent with that used by Smith & Heckman (1989b) and Ramos Almeida et al. (2011), following the theoretical definition of Hoessel (1980) – this radius corresponds to an impact parameter for which members of a typical cluster are expected to experience a close encounter or collision every 10^9 yr, according to Bahcall (1977).

individual classification as a “vote”, such that those voted for by the majority of the classifiers were considered in the final classifications for each target. Failing a favoured result, the noted certainty provided for each individual classification was considered. If no final decision had been made, the classifications were discussed by the assessors to gain an overall consensus. The final classifications for the interaction signatures associated with all galaxies in the sample are presented later, in Table 3.2.

Proportions

Once the classification process had been carried out, the proportions of galaxies in the sample that showed signs of interaction were analysed. In an attempt to reduce ambiguity, the classified galaxies were separated into two categories: (i) “clear interaction signatures”; and (ii) “no clear sign of interaction”. Category (i) only contained galaxies with interaction signatures that the assessors had deemed as certain following the visual classification process. The remaining galaxies, with indefinite or non-visible interaction signatures, were placed in category (ii). Due to the nature of this division, the number of galaxies that are classified as interacting can be considered as a lower limit. Dust lanes (the D classification) were not considered as clear interaction signatures. The proportion of galaxies in the sample that were placed in categories (i) and (ii) are presented in Table 3.1, along with the proportion that showed evidence for each individual type of interaction signature (i.e., T, F, S, B, A, I, 2N, D).

Overall, 53 ± 9 % of the sample showed some signature of a past or ongoing interaction. When the sample is divided into two equally populated bins in radio power, it is found that galaxies in the most radio-powerful half of the sample ($23.06 < \log(\mathrm{L}_{1.4\mathrm{GHz}}) < 24.0$ W Hz^{-1}) show interaction signatures more frequently than those in the least radio-powerful half ($22.5 < \log(\mathrm{L}_{1.4\mathrm{GHz}}) < 23.06$ W Hz^{-1}): 67^{+10}_{-14} % and 40^{+13}_{-11} %, respectively[3] (see Figure 3.6). Conducting a two-proportion Z-test, it is found that the null hypothesis that these two proportions of interacting galaxies are the same can be rejected at a confidence level of 85.7 % ($1.5\,\sigma$). However, given the proportions measured, it is found that a minimum of 63 galaxies would be needed in each half of the sample for the Z-test to reject the null hypothesis at the $3\,\sigma$ level, illustrating the need for more data.

Interestingly, the exact same proportions are found when dividing the sample into two equally populated bins in [OIII]λ5007 luminosity: 67^{+10}_{-14} % for the half with the highest luminosities ($33.56 < \log(\mathrm{L}_{[\mathrm{OIII}]}) < 34.24$ W) and 40^{+13}_{-11} % for the half with the

---

[3] Note that the uncertainties on the proportions have here been updated to binomial one-sigma confidence intervals provided by the method of Cameron (2011), in contrast with those presented in Pierce et al. (2019). This is consistent with the analysis presented in Chapters 5 and 6.

Table 3.1: The number and corresponding proportion of galaxies deemed as having clear interaction signatures and no clear interaction signatures. For those with clear interaction signatures, specific proportions for each of the classifications outlined in §3.3.1 are also presented, in order of decreasing frequency. Only one occurrence of a certain classification of signature is considered for each galaxy, but each different classification is considered individually. The listed uncertainties are standard binomial errors on the proportions.

Classification	Number of galaxies	Proportion of sample
Clear interaction signatures	16	53 ± 9 %
No clear interaction signatures	14	47 ± 9 %
Tidal tail (T)	12	40^{+9}_{-8} %
Amorphous halo (A)	6	20^{+9}_{-5} %
Shell (S)	4	13^{+9}_{-4} %
Irregular (I)	3	10^{+8}_{-3} %
Fan (F)	3	10^{+8}_{-3} %
Bridge (B)	2	7^{+8}_{-2} %
Dust lane (D)	2	7^{+8}_{-2} %
Double nucleus (2N)	1	3^{+7}_{-1} %

lowest luminosities ($32.86 < \log(L_{[OIII]}) < 33.56$ W). Plotting $L_{1.4GHz}$ against $L_{[OIII]}$ for both the morphologically disturbed and undisturbed galaxies in the sample (Figure 3.3) reveals no significant evidence for a correlation between the two parameters, however, as confirmed by a Pearson correlation test ($r = 0.077$, $p = 0.685$). This is in line with what is seen for AGN with intermediate radio powers in other studies (e.g. Best et al., 2005b). As such, $L_{1.4GHz}$ and $L_{[OIII]}$ are independent parameters within the sample, and, in fact, it can be seen in Figure 3.3 that the two sets of proportions are not provided by the same galaxies.

Following cursory visual inspection, however, eight of the galaxies in the sample show clear, highly disturbed morphologies, or are involved in interactions with large-scale tidal tails that are suggestive of major interactions: J0757+39; J0836+44; J0902+52; J1243+37; J1257+51; J1351+46; J1358+17; and J1412+24 (large red stars in Figure 3.3). All of these galaxies lie in the half of the sample with the highest radio powers. Using a two-proportion Z-test, it is found that the null hypothesis that the proportion of highly disturbed galaxies in the two radio-power-divided halves of the sample are the same can be rejected at a confidence level of 99.9 % ($3.3\,\sigma$). Note that given that there were only eight such galaxies in the entire sample, a more significant result could not

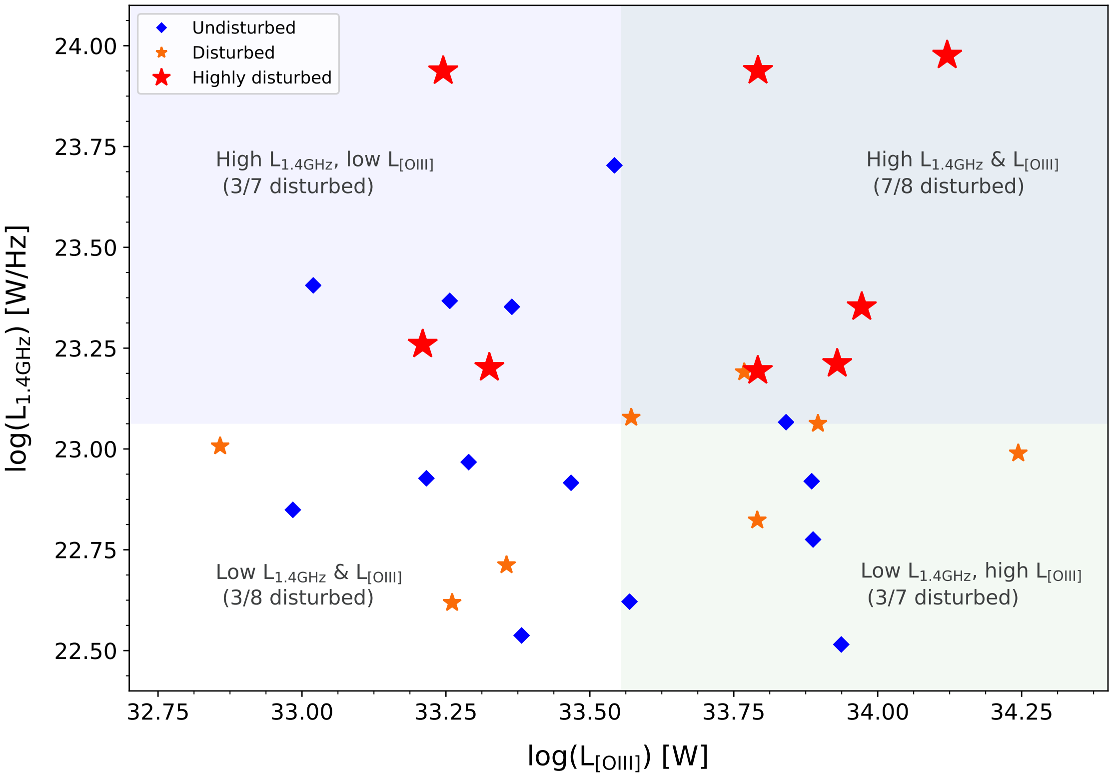

Figure 3.3: A plot of the radio powers at 1.4 GHz against the [OIII]λ5007 luminosities for the galaxies in the current sample. Galaxies with morphological signatures of disturbance are plotted as orange stars, and the larger red stars indicate those with high levels of disturbance. Undisturbed galaxies are plotted as blue diamonds. The blue shaded region indicates the half of the sample with the highest radio powers while the green-grey shaded region denotes the half with the highest [OIII]λ5007 luminosities. The proportion of disturbed galaxies in each quadrant is indicated.

have been observed.

On the other hand, only 5 out of these 8 galaxies lie in the half with the highest [OIII]λ5007 luminosities, with the remaining 3 out of 8 lying in the lower-luminosity half. In this case, a two-proportion Z-test reveals that the null hypothesis that these two proportions are the same can only be rejected at a confidence level of 59.1 % (0.8 σ). These results, therefore, show evidence that the highly disturbed galaxy morphologies are linked with the radio powers of the AGN, but no strong evidence that they are linked with their [OIII]λ5007 luminosities. Further discussion on this matter is reserved for §3.4.1.

Surface brightness

Following their accepted classifications, the surface brightness of each of the detected tidal features was determined. For consistency, these measurements were carried out with a similar method to that used for the limiting surface brightnesses (see Chapter 2), using the average counts measured in apertures of one arcsecond in radius evenly distributed over the full extent of the tidal feature. In this case, however, matching background apertures were also placed in suitable locations surrounding the tidal feature. This allowed the measured count level to be corrected for background contributions arising from either residual sky background or underlying smooth galaxy emission.

The measured surface brightnesses of all visually-confirmed tidal features are listed in Table 3.2, along with their classifications from the scheme outlined above. The measurements were corrected for surface brightness dimming using values provided by the NASA/IPAC Extragalactic Database (NED), and for extragalactic extinction using the r-band extinction values listed in Table 2.1 in Chapter 2. Cosmological k-corrections were also applied following the redshift-colour method of Chilingarian et al. (2010), using the integrated $g-r$ colours calculated from the available SDSS DR7 magnitudes. These corrections were performed to be consistent with those applied by Ramos Almeida et al. (2011) and thus to ensure meaningful comparisons between the measured surface brightness values from the two studies. The values calculated following all corrections are also presented in the table. Surface brightness measurements that are brighter than the σ_{sky} surface brightness limit for the target observation but fainter than the $3\sigma_{\mathrm{sky}}$ limit are considered as uncertain detections, and are included inside square brackets in Table 3.2. The tidal features that were confidently detected ranged in surface brightness from 20.6 mag arcsec^{-2} to 27.0 mag arcsec^{-2}, with a median of 25.4 mag arcsec^{-2}. The standard deviation of these measurements is 1.6 mag arcsec^{-2}.

Table 3.2: Column key: (1) Abbreviated target name; (2) Surface brightness dimming factor (in magnitudes; from NED); (3) Tidal feature classification(s); (4) Measured surface brightness and (5) the value after accounting for dimming, foreground extinction (A_r) and cosmological k-correction; (6) and (7) are the surface brightness limits derived from σ_{sky} and $3\sigma_{\text{sky}}$, respectively.

Target	Dimming	Morphology	μ_{AB} (mag arcsec^{-2})	$\mu_{\text{AB}}^{\text{corr}}$ (mag arcsec^{-2})	$\mu_{\text{AB}}^{\sigma_{\text{sky}}}$ (mag arcsec^{-2})	$\mu_{\text{AB}}^{3\sigma_{\text{sky}}}$ (mag arcsec^{-2})
J0725+43	0.292	2T, [T]	26.10, 26.50, [26.85]	25.49, 25.88, [26.24]	27.83	26.63
J0757+39	0.279	2S, T	23.23, 23.56, 25.41	22.75, 23.08, 24.93	27.99	26.80
J0810+48	0.326	-	-	-	28.39	27.20
J0827+12	0.279	A, I	-	-	27.40	26.21
J0836+44	0.237	A, F, 2S, T	22.64, 25.25, 26.08, 26.36	22.28, 24.89, 25.71, 25.99	28.28	27.09
J0838+26	0.220	D	-	-	27.93	26.74
J0902+52	0.409	A, 2S, T	23.47, 26.38, 23.60	22.92, 25.83, 23.05	28.20	27.00
J0911+45	0.409	I	-	-	27.89	26.70
J0931+47	0.209	-	-	-	28.16	26.97
J0950+37	0.176	-	-	-	28.00	26.81
J1036+38	0.218	S	25.10	24.78	28.23	27.03
J1100+10	0.274	-	-	-	27.97	26.77
J1108+51	0.295	-	-	-	27.99	26.80
J1147+33	0.136	-	-	-	28.27	27.08
J1150+01	0.332	-	-	-	27.41	26.21
J1206+35	0.341	-	-	-	27.20	26.01
J1206+10	0.376	-	-	-	28.18	26.98
J1236+40	0.401	I	-	-	28.09	26.89
J1243+37	0.361	B, 2N, T	20.62, 21.66	20.12, 21.66	27.72	26.53
J1257+51	0.402	A, 2T	24.81, 25.97	24.30, 25.46	27.83	26.64
J1324+17	0.362	-	-	-	27.89	26.69
J1351+46	0.402	A, 2T	23.15, 26.50	22.64, 25.98	28.25	27.06
J1358+17	0.399	A, B, T	25.43, 26.47	24.84, 25.88	28.12	26.92
J1412+24	0.293	B, F, T	24.12, 24.23, 25.63	23.69, 23.80, 25.21	28.07	26.88
J1529+02	0.322	-	-	-	27.78	26.59
J1555+27	0.346	-	-	-	28.12	26.93
J1601+43	0.301	F, [T]	25.08, [26.96]	24.68, [26.56]	28.09	26.90
J1609+13	0.152	D, T	26.17	25.88	27.99	26.80
J1622+07	0.367	T	26.51	25.84	28.05	26.86
J1630+12	0.273	-	-	-	28.14	26.95

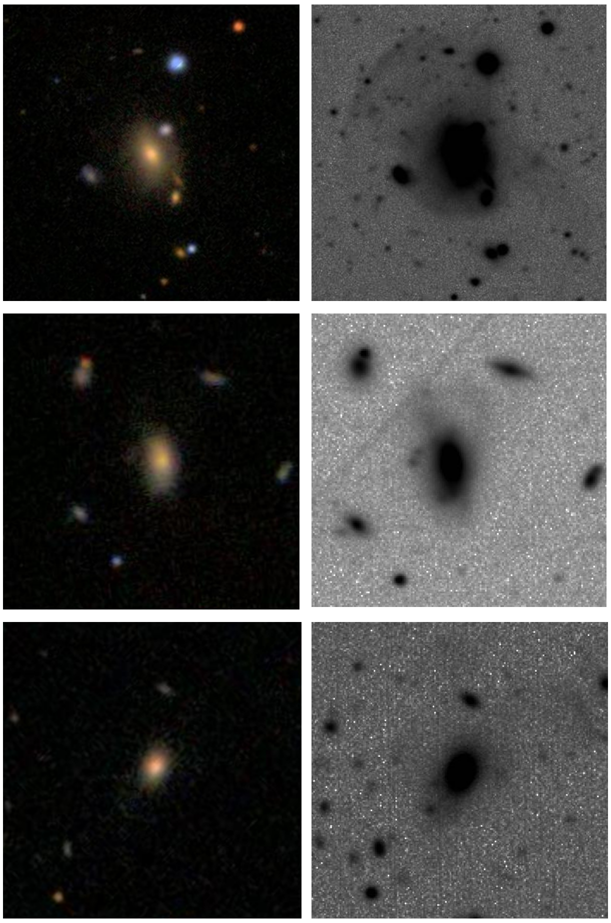

Figure 3.4: Example SDSS (left column; composite g-r-i) and INT/WFC (right column; r-band) images for three galaxies in the sample. The INT/WFC observations reveal interaction signatures that are not visible in the SDSS imaging, highlighting the importance of deep imaging observations for the detection of low-surface-brightness tidal features.

Due mainly to degeneracies in galaxy merger model parameters (e.g. age, mass ratio, impact angle), it is currently difficult to determine physically meaningful properties from the measured surface brightnesses of tidal features. As a result, no detailed conclusions are drawn from the values reported here, although they are useful in a relative sense for comparing between different studies and samples. For instance, here it is useful to note that ~ 40 % of the tidal features that were detected are fainter than the limiting surface brightness of standard depth SDSS images (~ 25 mag arcsec^{-2}; Driver et al., 2016), highlighting the importance of the improved sensitivity provided by the targeted observations. This can be seen clearly for the examples shown in Figure 3.4, where the INT/WFC observations reveal interaction signatures that are not detected in SDSS images.

3.3.2 Host morphologies

Visual inspection

When carrying out the visual inspection process outlined in §3.3.1, the classifiers were also asked to provide comments on the general morphological properties of the host galaxies. This was primarily done to provide an impression of their morphological types. For late-type galaxies, however, assessors also noted the level of disk warping and the rough disk orientation (from edge-on to face-on), which could assist with the interpretation of the interaction signature classifications. Late-type galaxies were those seen to have a significant disk or spiral-like morphology (discarding lenticular galaxies), and were found to be the most popular category within the sample (43^{+9}_{-8}%; 13/30). Early-type galaxies, appearing as elliptical-like or lenticular, were found to comprise 37^{+9}_{-8}% (11/30) of the population, while the remaining 20^{+9}_{-5}% (6/30) were judged to have morphologies too disturbed to classify – the "merger" class. The visual classifications for all the galaxies in the sample are presented in the last column of Table 3.3.

Classifications based on visual inspection are also available for the sample in the public data release for the Galaxy Zoo project (Lintott et al., 2008, 2011). This project required participants to classify galaxies in composite g-, r-, and i-band images from SDSS into one of the following categories: "Elliptical (E)", "ClockWise spirals (CW)", "AntiClockWise spirals (ACW)", "Edge-on spirals (Edge)", "Don't Know (DK)", or "Merger (MG)". The vote fractions provided for the E classification are taken to indicate the likelihood of a galaxy being of early-type, whereas the sum of the vote fractions for the CW, ACW, and Edge classifications ("Combined Spiral", CS) are taken as the likelihood of a galaxy being of late-type.

For the current work, a classification was only accepted if the value of the lower error boundary on the vote fraction for the most popular category was greater than the value of the upper error boundary on the least popular category. In other words, the lower error boundary on the early-type vote fraction was required to be greater than the upper error boundary on the late-type vote fraction for a galaxy to be classed as early-type, and vice versa. The error boundaries considered for the vote fractions were 95% confidence intervals. The vote fraction of the most popular classification was also required to be greater than 0.5 to ensure that the other two categories (DK and MG) were not favoured. Should these conditions not be met, the galaxy morphology was classed as uncertain. From this, it is found that 30^{+9}_{-7}% of the sample (9/30) are classed as early-types, 37^{+9}_{-8}% (11/30) as late-types, and the remaining 33^{+9}_{-7}% (10/30) as uncertain.

As part of the Galaxy Zoo project, an attempt was also made to correct for biases introduced by the magnitude limit of SDSS and varying galaxy appearance with redshift – for details, see Bamford et al. (2009) and Lintott et al. (2011). "Debiased" vote fractions are available for 28 of the galaxies in the sample, and when these results are considered, it is found that $25\,^{+10}_{-6}\,\%$ (7/28) are classed as early-types, $43 \pm 9\,\%$ (12/28) as late-types and the remaining $32\,^{+10}_{-7}\,\%$ (9/28) as uncertain. Since the biases tend to lead to overestimates of the number of early-type galaxies relative to late-types, debiasing of the vote fractions tends to increase the vote fractions for late-type galaxies relative to early-types on the whole, as is reflected here. The visual classification results from both the authors and the Galaxy Zoo project are summarised in Table 3.4 and discussed in §3.4.2.

Light profile modelling

Quantitative characterisation of the light distributions of the host galaxies was performed using the two-dimensional fitting algorithm `GALFIT` (Peng et al., 2002, 2010), which allows for the fitting of multiple structural components to galaxy light profiles. The main motivation for doing this was to better identify the morphological types of the host galaxies (i.e. early-type vs. late-type), and to assess the relative contributions of bulge and disk light. In addition, the residual images generated as part of this process were also useful for clarifying any interaction signatures associated with the host galaxies. A well-defined procedure was followed to improve the consistency of the fitting process, starting with models of minimal complexity and only moving towards more complicated models if completely necessary.

In much of the previous literature, galaxy light distributions have been modelled using Sérsic profiles, and hence this method was adopted during the modelling to allow for direct comparison with past work. In `GALFIT`, the Sérsic profile is described by

$$\Sigma(r) = \Sigma_e \mathrm{exp}\left\{-\kappa\left(\frac{\mathrm{r}}{\mathrm{r_e}}\right)^{\frac{1}{\mathrm{n}}} - 1\right\},$$

where $\Sigma(r)$ is the pixel surface brightness of the galaxy light at radius r, $\Sigma(r_e)$ is the value at r_e, the effective radius of the light profile, n is the Sérsic index, and κ is a constant that is coupled to n (Peng et al., 2002, 2010).

Traditionally, Sérsic profiles with indices around $n = 1$ (exponential) have been found to provide good fits for galaxy disks, and those with $n = 4$ (de Vaucouleurs) for galaxy spheroids (galaxy bulges and elliptical galaxies). Galaxies that appear to show both disk-like and bulge-like components have then been modelled with a combination of these two types of profile in past studies, in an attempt to separate the light profile characteristics for bulge-disk decomposition. Detailed bulge-disk decomposition of very nearby disk galaxies with various Hubble types (from S0 to Sc), however, suggests that classical-bulge-like components can have Sérsic indices as low as $n \sim 1.5$ to 2 at very high resolutions (Gao & Ho, 2017). In an attempt to be as inclusive as possible while still separating disk-like and classical-bulge-like components clearly, the Sérsic indices for disk-like and classical-bulge-like components were constrained to the following ranges: $n = 0.5$ to 1.5 for disk-like (late-type) components; and $n = 2$ to 5 for galaxy spheroid (early-type) components. As well as better distinguishing between disk-like and bulge-like components for determining the overall morphological class of the galaxy, this also had the advantage of minimising the effect of degeneracies in the models.

In addition to the Sérsic profiles, `GALFIT` also requires a representation of the point spread function (PSF) in the form of a FITS image. All modelling profiles are convolved with the PSF to account for the quality of the observational data. In some cases, an individual PSF component was also required in the models to account for strong, unresolved AGN emission at the centre of the galaxies. All PSFs were generated using the average light profile of non-saturated stars in the final coadded images for each of the targets. Two-dimensional surface profile plots of the light from these stars were visually inspected to ensure that they provided an adequate representation of the PSF at good signal-to-noise, considering both the measured seeing of the observations and the characteristic shape of the response from the CCDs. Following this, PSFs could be used in combination with Sérsic profiles for the modelling process.

The procedure used for the fitting involved multiple stages and terminated as soon as a suitable model was obtained. All of the models were produced using at least one Sérsic profile and used up to a maximum of three Sérsic profiles, to avoid unwarranted complexity in the fitting process. Neighbouring stars and galaxies were modelled simultaneously with the targets to minimise their effect on accurate modelling of the host galaxy light profiles. In all cases, pixels above 70% of the saturation level were masked prior to fitting to avoid any issues introduced by the CCD response close to saturation. The process is outlined here:

i) **Single Sérsic profile** – Initially, an attempt was made at fitting a single Sérsic profile, with a Sérsic index constrained to the ranges outlined above for each disk-like and bulge-like profiles. Determining which of the two profiles provided the best fit gave a first impression of the morphological class of the host galaxy (decided based on visual inspection). It was found that this stage alone generated a sufficient model for 4 out of the 30 galaxies (13%), with no additional component required.

ii) **Two Sérsic profiles** – Failing success at stage (i), an attempt was made at fitting a model with two constrained Sérsic components, in the order: 1) one disk-like profile and one bulge-like profile (bulge-disk decomposition); 2) two disk-like or two bulge-like profiles (two-component late-type or early-type). This combination proved sufficient for 14 out of the 30 galaxies (47%), and provided the majority of successful models.

iii) **Two Sérsic profiles + PSF** – For 3 of the 30 galaxies (10%), a PSF component was required in addition to the two Sérsic profiles to model strong, unresolved AGN emission. The PSF components were only accepted after the presence of strong emission lines had been confirmed from inspection of the SDSS spectra.

iv) **Three Sérsic profiles** – The most complex cases required a model with three constrained Sérsic components to produce a suitable fit. These were all decomposed into disk-like and bulge-like components, either as two disk-like profiles and one bulge-like profile, or two bulge-like profiles and one disk-like profile. This was necessary for 2 of the 30 galaxies (7%). If a good fit was still not obtainable at this point, the fitting process was terminated to avoid unwarranted complexity in the models.

In total, the overall light profiles of 23 (77%) of the host galaxies were deemed to be recovered with reasonable accuracy using this process. The majority of models for the remaining seven objects failed due to issues related to the highly disturbed nature of the galaxy morphologies, due to mergers (J0757+39, J1243+37, J1257+51, J1351+46). The unusual morphology of J1324+17 meant that a suitable fit could not be obtained before the models became too complex – it is possible that this target has also been disturbed by an interaction, although the classifiers did not deem this clear enough for the galaxy to be classified as such. In the case of J0810+48, the presence of a nearby bright star caused any modelling attempts to produce an inaccurate representation of the galaxy light profile. Finally, a large proportion of the inner regions of the galaxy J1147+33 was saturated in the exposures, so any model fitting to this galaxy was deemed unreliable.

Table 3.3: The results from detailed modelling of the host galaxy light profiles using `GALFIT`. The abbreviated target names are shown in Column 1, as listed in Table 3.2. For each model component, Columns 2-6 provide: (2) the component type (i.e. Sérsic or PSF) and its classification as bulge-like (B), disk-like (D), or intermediate (I) for multi-component fits; (3) the Sérsic index; (4) the effective radius in kpc; (5) the axis ratio; (6) the derived apparent magnitude. Columns 7-10 then present information derived from the overall models (combination of all components): (7) total apparent magnitude; (8) ratio of bulge-to-disk light (where relevant); (9) ratio of bulge-to-total light; (10) ratio of disk-to-total light. The morphological types from the visual inspection performed by the authors are also presented in Column 11, with their classifications as either mergers or early- (E) or late-type (L) galaxies indicated in brackets.

Target (1)	Comp. Type (2)	n (3)	R_e (kpc) (4)	b/a (5)	m_c (6)	m_t (7)	B/D (8)	B/T (9)	D/T (10)	Visual class. (11)
J0725+43	Sérsic (B)	2.00	0.78	0.67	17.94	16.75	0.50	0.33	0.67	Lenticular (E)
	Sérsic (D)	0.92	5.06	0.22	17.19					
J0757+39	-	-	-	-	-	-	-	-	-	Merger
J0810+48	-	-	-	-	-	-	-	-	-	Lenticular (E)
J0827+12	Sérsic (B)	2.00	1.42	0.58	17.73	16.35	0.39	0.28	0.72	Spiral (L)
	Sérsic (D)	0.75	6.16	0.46	16.70					
J0836+44	Sérsic	5.00	6.70	0.64	15.08	15.08	-	-	-	Merger
J0838+26	Sérsic (B)	3.29	4.02	0.35	16.08	15.20	0.79	0.44	0.56	Edge-on disk (L)
	Sérsic (D)	0.50	9.67	0.22	15.83					
J0902+52	Sérsic	5.00	14.42	0.70	15.23	15.23	-	-	-	Merger
J0911+45	Sérsic (I)	2.00	1.74	0.46	18.38	17.52	-	-	-	Spiral (L)
	Sérsic (I)	1.50	6.79	0.25	18.21					
	PSF	-	-	-	21.91					
J0931+47	Sérsic	3.13	0.55	0.36	17.82	17.02	-	-	-	Elliptical (E)

Table 3.3 – continued.

	Sérsic	2.00	2.55	0.89	17.72					
J0950+37	Sérsic (B)	2.54	6.74	0.23	15.78	15.12	1.21	0.55	0.45	Edge-on disk (L)
	Sérsic (D)	0.50	14.06	0.11	15.99					
J1036+38	Sérsic (B)	5.00	6.22	0.54	14.94	14.36	1.41	0.59	0.41	Spiral (L)
	Sérsic (D)	0.50	12.63	0.76	15.31					
J1100+10	Sérsic (B)	2.00	1.38	0.34	17.89	17.41	1.80	0.64	0.36	Spiral (L)
	Sérsic (D)	0.52	4.49	0.39	18.53					
J1108+51	Sérsic (B)	2.00	1.50	0.74	16.65	15.87	1.48	0.60	0.40	Lenticular (E)
	Sérsic (D)	1.36	4.86	0.20	16.86					
	PSF (B)	-	-	-	18.28					
J1147+33	-	-	-	-	-	-	-	-	-	Lenticular (E)
J1150+01	Sérsic (B)	2.11	2.64	0.52	18.51	17.69	0.89	0.47	0.53	Spiral (L)
	Sérsic (D)	0.50	4.08	0.20	18.38					
J1206+35	Sérsic (B)	5.00	10.00	0.40	15.77	15.62	6.78	0.87	0.13	Lenticular (E)
	Sérsic (D)	0.96	5.75	0.20	17.85					
J1206+10	Sérsic (B)	5.00	5.82	0.62	17.78	17.35	2.04	0.67	0.33	Spiral (L)
	Sérsic (D)	0.50	4.49	0.18	18.55					
J1236+40	Sérsic (B)	2.00	1.33	0.62	19.74	17.88	0.22	0.18	0.82	Edge-on disk (L)
	Sérsic (D)	0.61	6.29	0.16	18.09					
J1243+37	-	-	-	-	-	-	-	-	-	Merger
J1257+51	-	-	-	-	-	-	-	-	-	Merger

Table 3.3 – continued.

J1324+17	-	-	-	-	-	-	-	-	-	Spiral (L)
J1351+46	-	-	-	-	-	-	-	-	-	Merger
J1358+17	Sérsic	3.79	1.63	0.27	18.71	16.96	-	-	-	Elliptical (E)
	Sérsic	2.91	5.11	0.61	17.20					
J1412+24	Sérsic	4.79	2.56	0.56	16.18	15.38	-	-	-	Elliptical (E)
	Sérsic	2.00	9.66	0.62	16.08					
J1529+02	Sérsic (B)	5.00	2.78	0.70	18.05	16.56	0.34	0.25	0.75	Edge-on disk (L)
	Sérsic (D)	0.50	5.63	0.19	17.84					
	Sérsic (D)	0.82	10.78	0.18	17.46					
J1555+27	Sérsic (B)	4.16	1.39	0.51	17.99	17.51	1.79	0.64	0.36	Lenticular (E)
	Sérsic (D)	0.50	4.49	0.39	18.62					
J1601+43	Sérsic	4.44	1.59	0.62	17.07	17.07	-	-	-	Elliptical (E)
J1609+13	Sérsic (B)	2.00	4.00	0.77	16.37	15.09	0.59	0.31	0.69	Edge-on disk (L)
	Sérsic (D)	1.50	3.97	0.04	17.00					
	Sérsic (D)	0.50	9.87	0.13	15.79					
J1622+07	Sérsic (D)	0.50	4.64	0.30	17.81	17.23	0.09	0.09	0.91	Spiral (L)
	Sérsic (D)	0.50	9.33	0.54	18.42					
	PSF (B)	-	-	-	19.90					
J1630+12	Sérsic	4.10	1.63	0.88	16.93	16.93	-	-	-	Elliptical (E)

In cases that required at least two Sérsic profiles for accurate modelling, the morphology and model parameters for the subcomponents were inspected to search for distinct bulge-like and disk-like components. For J0911+45, the model components cannot be separated in this way. In this case, both components have Sérsic indices that lie in the range $n = 1 - 2$, and their two-dimensional morphologies are intermediate between those of bulges and disks. Similar cases have been identified in previous studies (Floyd et al., 2004; Inskip et al., 2010; Falomo et al., 2014; Urbano-Mayorgas et al., 2019), and these are here referred as "intermediate" (I) components. It is also noted that J1036+38 shows a highly detailed spiral arm, bulge, and bar structure, along with signatures of past or ongoing interactions. Detailed fitting of these structures was not performed, and, as such, the accuracy of the model for this galaxy is reduced in comparison with the others.

The key parameters for each of the individual components of the GALFIT models are presented in Table 3.3. Where appropriate, the derived bulge-to-disk light ratios (B/D) and their respective contributions to the total light profile (B/T and D/T) are reported. These ratios were not calculated for models that produced good fits to the overall light profile but did not separate into bulge-like and disk-like components. It is found that the majority of galaxies for which both bulge and disk components were required were disk-dominated (8 out of 15), having a median bulge-to-disk ratio of B/D ~ 0.8. All four single-Sérsic models and three two-Sérsic models (one also with a PSF component) required only early-type profiles. When added to the bulge-dominated galaxies, it is hence found that 14 out of the 23 galaxies that could be modelled ($61\,^{+9}_{-11}\,\%$) have early-type profiles, with 8 out of 23 ($35\,^{+11}_{-8}\,\%$) having late-type profiles (disk-dominated) and one of the 23 ($4\,^{+9}_{-1}\,\%$) having an intermediate profile.

Given that there is a mixture of morphological types found within the sample, it is also interesting to determine whether there is any relationship between the level of bulge-dominance in the galaxy light profiles and the AGN radio power or optical luminosity. Figure 3.5 shows the fraction of light contributed by the bulge-like components of the GALFIT models to the total, against both $\mathrm{L_{1.4GHz}}$ and $\mathrm{L_{[OIII]}}$ for all galaxies that were modelled successfully – this excludes J0911+45, which has only intermediate components. Here, galaxies with only early-type components in their models are considered as having all of their light contributed by a bulge component. From this, it is clear that there is no significant trend in the bulge-dominance of the galaxy light with either $\mathrm{L_{1.4GHz}}$ or $\mathrm{L_{[OIII]}}$, as confirmed by Pearson correlation tests ($r = 0.301$, $p = 0.173$ and $r = 0.338$, $p = 0.124$, respectively). This suggests that although the radio-intermediate HERGs represent a greatly changed population of morphological types relative to their predom-

Table 3.4: The number and corresponding proportion of galaxies in the sample with the indicated morphological classfications. The results from visual inspection, both in this work and from the Galaxy Zoo project (Lintott et al., 2008, 2011), and detailed light profile modelling using `GALFIT` (Peng et al., 2002, 2010) are presented. Note that debiased Galaxy Zoo results were only available for 28 of the galaxies, as indicated.

Visual inspection	Number	Prop.
Late-type (Spiral/disk)	13	43^{+9}_{-8} %
Early-type (Elliptical/Lenticular)	11	37^{+9}_{-8} %
Mergers	6	20^{+9}_{-5} %

Galaxy Zoo	Number	Prop.
Late-type (Spirals)	11	37^{+9}_{-8} %
Early-type (Ellipticals)	9	30^{+9}_{-7} %
Uncertain (Merger/“Don’t Know”)	10	33^{+9}_{-8} %

Galaxy Zoo – *debiased (28 only)*	Number	Prop.
Late-type (Spirals)	12	43 ± 9 %
Early-type (Ellipticals)	7	25^{+10}_{-6} %
Uncertain (Merger/“Don’t Know”)	9	32^{+10}_{-7} %

Light profile modelling	Number	Prop.
Late-type	8	27^{+9}_{-6} %
– *one component*	*0*	–
– *disk-dominated*	*8*	–
Early-type	14	47 ± 9 %
– *one component*	*7*	–
– *bulge-dominated*	*7*	–
Intermediate	1	3^{+7}_{-1} %
Undetermined	7	23^{+9}_{-6} %
– *mergers (major disturbance)*	*5*	–
– *fitting issues*	*2*	–

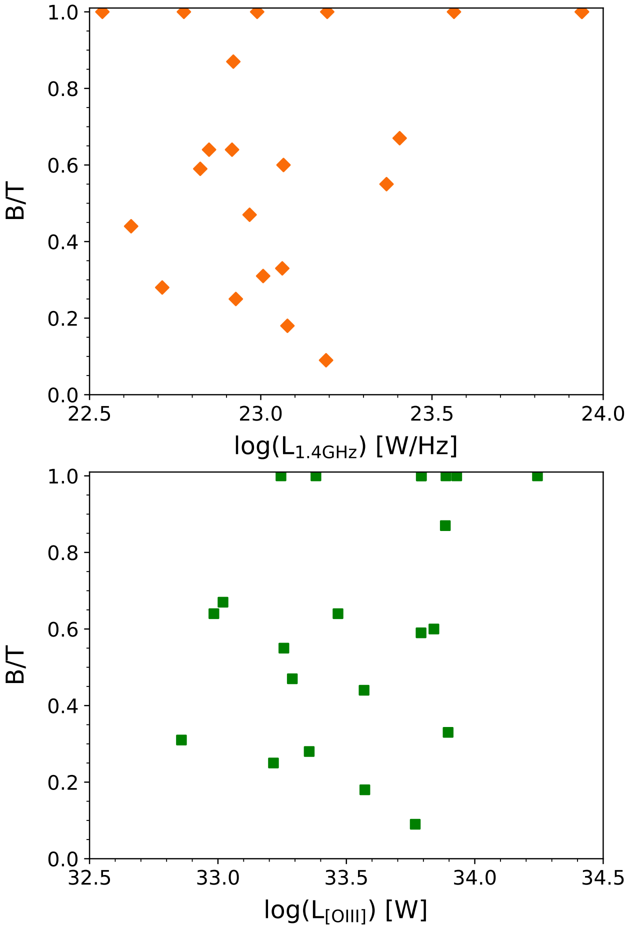

Figure 3.5: The fraction of the total light represented by the bulge-like components in the GALFIT models (B/T) against the radio powers (upper panel) and [OIII]λ5007 luminosites (lower panel) of the sources. All galaxies with successful models are included, excluding the galaxy that has only intermediate components (J0911+45). Galaxies with light profiles represented by only early-type components are considered to have B/T = 1.

inantly giant elliptical counterparts at high radio powers, the galaxy morphologies do not change gradually with the radio or optical luminosity of the AGN. Rather, there is a mixture of morphological types at all optical/radio luminosities in the radio-intermediate range. However, the dependence of the rates of different morphological types on radio power is investigated in more detail in Chapter 5, where the morphologies across the much broader range of radio power covered by all active galaxies studied in this thesis are considered.

3.4 Discussion

The analysis of deep r-band images of 30 local radio-intermediate HERGs has allowed for the detailed characterisation their optical morphologies, including both signatures of past or ongoing interactions and their overall morphological types. In §3.3.1, it was shown that 53 ± 9 % of the sample show interaction signatures, with the proportions within the most radio-powerful and least radio-powerful halves of the sample being 67^{+10}_{-14}% and 40^{+13}_{-11}%, respectively. These exact same proportions are found for the respective halves of the sample with the highest and lowest [OIII]λ5007 luminosities. It is found, however, that all eight of the galaxies that show the highest levels of disturbance lie in the most radio-powerful half of the sample. This is not seen when the sample is divided in two by [OIII]λ5007 luminosity, where 5 out of 8 of these galaxies lie in the half of the sample with the highest luminosities and 3 out of 8 in the half with the lowest luminosities (see Figure 3.3).

Both visual inspection and in-depth modelling of the host galaxy light distributions revealed a mixture of morphological types within the sample (§3.3.2), with half showing evidence of a significant disk-like contribution to the galaxy light profile: 8 are classified as late-type based on `GALFIT` models (disk-dominated) and 14 as early-type (bulge-dominated or elliptical). The remainder proved unsuitable for accurate bulge-disk decomposition, four because of very highly disturbed morphologies resulting from mergers or interactions. Through comparison with previous work on radio AGN triggering and host morphologies, the implications of these results are discussed in this section.

3.4.1 Triggering of the nuclear activity

Importance of galaxy mergers and interactions

The focus of previous studies of radio AGN triggering has primarily been the most radio-powerful AGN (e.g. those in the 3CR and 2Jy samples), most probably because these were the easiest objects to study when the field began to develop (see Chapter 1). As discussed in §3.2, radio AGN with high-excitation optical emission spectra (HERGs or SLRGs), such as those considered here, are often linked with an accretion mode in which cold gas fuels the black hole through a geometrically thin, optically thick accretion disk (e.g. see Heckman & Best, 2014). Study of exactly what would cause the radial inflow of gas towards the innermost regions to trigger the nuclear activity has produced mixed results, with possible mechanisms including the tidal torques introduced by galaxy mergers and interactions or the action of non-axisymmetric features in galaxy disks, such as bars, oval distortions, and spiral arms (e.g. Hopkins & Quataert, 2010; Heckman & Best, 2014).

To date, the most extensive deep imaging study for radio-powerful AGN with high-excitation optical emission has been carried out by Ramos Almeida et al. (2011, 2012, 2013) for SLRGs in the 2Jy sample ($0.05 < z < 0.7$), which provides strong evidence to suggest that major galaxy interactions could trigger the nuclear activity. Ramos Almeida et al. (2011) find that $94^{+4}_{-7}\,\%$ of the SLRGs in their sample show high-surface brightness signatures of past or ongoing interactions, corroborating prior suggestions that radio galaxies with strong optical emission have highly disturbed optical morphologies (Heckman et al., 1986; Smith & Heckman, 1989a,b). They also found that the rate of merger signatures was significantly higher than those found for control samples of elliptical galaxies in both the OBEY survey (Tal et al., 2009) and the Extended Groth Strip (EGS; Zhao et al., 2009) matched in galaxy luminosity and redshift, when the same surface brightness limits are considered (Ramos Almeida et al., 2012). In addition, Ramos Almeida et al. (2013) find the 2Jy SLRGs to preferentially reside in group-like environments that are denser than those of the EGS control galaxies but less dense than the cluster-like environments of the WLRGs in the sample. Group-like environments are well-suited to galaxy mergers, having a relatively high galaxy density that results in frequent mergers and interactions, but without the high velocity dispersions of clusters that can suppress the galaxy merger rate (Popesso & Biviano, 2006).

In the upper panel of Figure 3.6, the proportion of radio AGN that show tidal features and other interaction signatures is plotted against the radio power at 1.4 GHz ($L_{1.4\mathrm{GHz}}$) for both the radio-intermediate HERGs and the SLRGs in the 2Jy sample. Comparing the two samples in their entirety[4], the proportion of interacting galaxies in the radio-intermediate sample is found to be 53 ± 9 % (16/30), a difference at the $3.8\,\sigma$ level from that found for the SLRGs in the 2Jy sample ($94^{+4}_{-7}\,\%$; Ramos Almeida et al., 2011). Dividing the RI-HERG low sample by radio power, it is also seen that disturbed galaxies are found more frequently in the most radio-powerful half ($67^{+10}_{-14}\,\%$) of the sample than in the least radio-powerful half ($40^{+13}_{-11}\,\%$) – a difference at the $1.5\,\sigma$ level. These results therefore appear to be consistent with a reduction in the proportion of radio AGN with high-excitation optical emission lines that are triggered by galaxy interactions with decreasing radio power.

---

[4] Note that the results for HERGs and SLRGs are here compared directly, despite the differences in their classification criteria. However, following the [OIII]λ5007 equivalent width criterion used by Best & Heckman (2012), for which radio AGN with $\mathrm{EW}_{[\mathrm{OIII}]} > 10$ Åwould be classified as HERGs, all objects classified as SLRGs would also be classified as HERGs (see Chapter 2, §2.3).

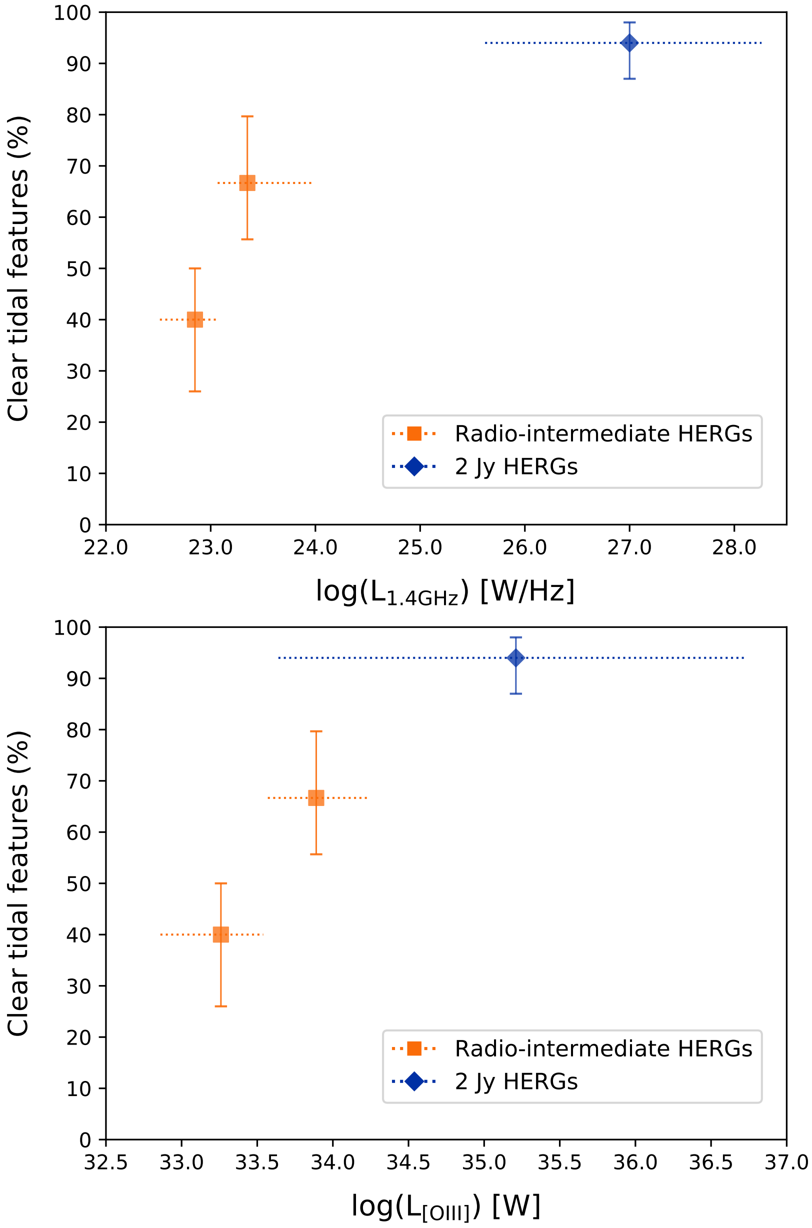

Figure 3.6: The percentage of HERGs in the RI-HERG low sample (orange squares) and SLRGs in the 2Jy sample (blue diamonds; Ramos Almeida et al., 2011) that show clear tidal features, plotted against their 1.4 GHz radio powers (top panel) and their [OIII]λ5007 luminosities (bottom panel). The results for each half of the radio-intermediate sample when divided by their $L_{1.4GHz}$ or $L_{[OIII]}$ values are shown separately. The horizontal lines indicate the relevant $L_{1.4GHz}$ or $L_{[OIII]}$ ranges in each case, and the points represent their median values. Note that although the HERG and SLRG classification schemes are different, they are in broad agreement with one another.

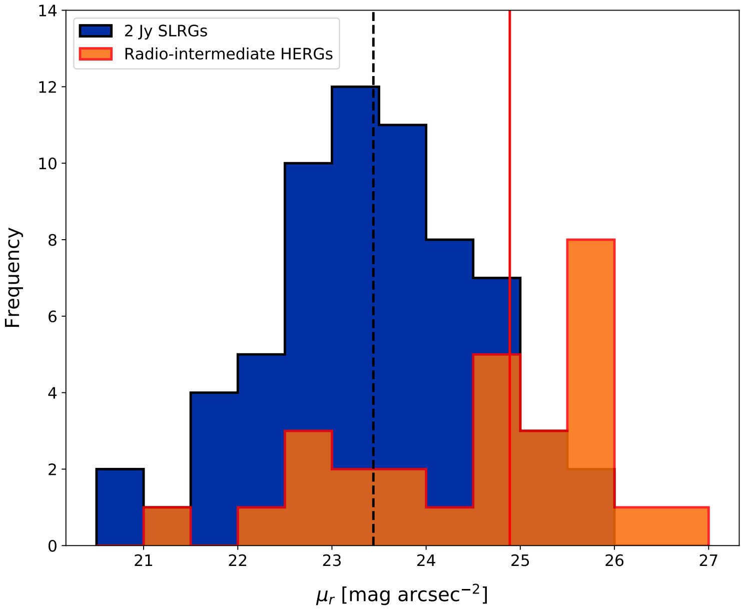

Figure 3.7: The distributions of tidal feature surface brightness measurements for the radio-intermediate HERGs (orange) and 2Jy SLRGs (blue; Ramos Almeida et al., 2011). All values are in the AB system, and are corrected for surface brightness dimming, foreground galactic extinction and cosmological k-correction. The median values are indicated by the solid red line for the radio-intermediate HERGs and the dashed black line for the 2Jy SLRGs.

As shown in §3.3.1, however, the same proportions are found when the sample is divided into two equally populated bins in [OIII] λ5007 luminosity ($L_{[OIII]}$): 67^{+10}_{-14} % for the higher $L_{[OIII]}$ half and 40^{+13}_{-11} % for the lower $L_{[OIII]}$ half. The lack of correlation between $L_{1.4GHz}$ and $L_{[OIII]}$ for the galaxies in the sample also means that the galaxies responsible for the measured proportions in each case are, in fact, different (see Figure 3.3). In the lower panel of Figure 3.6, these proportions are again compared to those found for the 2Jy SLRGs, but this time plotted against $L_{[OIII]}$. From this, it is seen that the results are also consistent with a reduction in the level of merger-based triggering with decreasing optical ($L_{[OIII]}$) power, often also considered to be a proxy for the bolometric luminosity of the AGN (e.g. Heckman et al., 2004).

A further point of interest comes from comparing the measured surface brightnesses for the interaction signatures in the two studies. Figure 3.7 shows the distribution of surface brightness measurements for the tidal features both from this work and Ramos Almeida et al. (2011), after accounting for surface brightness dimming, foreground galactic extinction and cosmological k-correction. Although both studies have comparable image depths, it is seen that the 2Jy SLRGs typically show interaction signatures of higher surface brightness – the faintest securely detected features have (corrected) surface brightnesses of $\mu_r^{\rm corr} = 25.88\,{\rm mag\,arcsec^{-2}}$ (Ramos Almeida et al., 2011) and $\mu_r^{\rm corr} = 25.99\,{\rm mag\,arcsec^{-2}}$ (this work), but the median values are $\mu_r^{\rm corr} = 23.44\,{\rm mag\,arcsec^{-2}}$ and $\mu_r^{\rm corr} = 24.84\,{\rm mag\,arcsec^{-2}}$, respectively. This suggests that the 2Jy SLRGs are likely to be triggered by more highly disruptive mergers and interactions than those that may trigger the radio-intermediate HERGs.

However, there are some caveats to consider when comparing the results from this current work with those from the 2Jy studies. Firstly, it is seen that all the SLRGs in the 2Jy sample for which stellar masses have been measured have values $\sim 10^{11}$ $M_\odot$ and above (Tadhunter, 2016). This is above the median value for the radio-intermediate HERGs in the current sample ($10^{10.8}$ $M_\odot$), which can have stellar masses that are down to an order a magnitude lower ($\sim 10^{10}$ $M_\odot$). In addition, a mixture of early-type and late-type galaxies are seen in the RI-HERG low sample, whereas the vast majority of 2Jy radio galaxies are associated with early-type morphologies. Finally, although there is a high degree of overlap between the HERG and SLRG classifications, the schemes are not entirely equivalent (see Tadhunter, 2016).

Highly disturbed galaxies

The discussion in the previous section was based on the detection of *any* sign of morphological disturbance, regardless of its level. This includes objects for which the low-surface-brightness features are only visible after careful manipulation of the image contrast levels. However, for a subset of eight objects, the signs of galaxy interactions are obvious even on cursory inspection of the images. This subset of highly disturbed systems includes all six of the galaxies that the authors deemed too disturbed to classify accurately by visual inspection (J0757+39, J0836+44, J0902+52, J1243+37, J1257+51, J1351+46; the "merger" class), four of which could also not be modelled with `GALFIT` on this basis (J0757+39, J1243+37, J1257+51, J1351+46). A further two galaxies are included based on the fact that they are strongly interacting with companion galaxies (J1358+17, J1412+24), as demonstrated by the presence of large-scale tidal features that provide an alternative indication of ongoing major mergers (e.g. see Duc et al., 2015). In addition, it is seen that 6 out of 8 of these galaxies have at least one tidal feature at relatively high surface brightness ($\leq 24\,{\rm mag\,arcsec^{-2}}$), including all five galaxies with surface brightnesses greater than the median measured for the 2Jy SLRGs, which show frequent signs of high levels of morphological disturbance.

When the sample is divided in two by radio power, *all* of these eight highly disturbed systems are found to lie in the half of the sample with the highest radio powers. In contrast, they lie in both halves of the sample when divided by their [OIII]λ5007 luminosities. Comparing the proportions found in each of the two halves in both cases, a $3.3\,\sigma$ difference in proportions is found when dividing the sample by radio power, but only a $0.8\,\sigma$ difference when dividing by [OIII]λ5007 luminosity. It is important to note that there are only eight of these highly disturbed galaxies in the entire sample, and so a more significant result could not have been observed when the division by radio power is made. Therefore, these resuts suggest that triggering through major galaxy interactions is linked with the radio powers of the HERGs, but not so strongly linked with their [OIII]λ5007 luminosities.

In combination with the results discussed in §3.4.1, this is therefore consistent with a picture in which the relative importance of mergers and interactions for triggering radio AGN with HERG spectra is related to their radio powers. In line with the results of Ramos Almeida et al. (2011, 2012, 2013), mergers appear to be important for triggering those with higher radio powers, with all of the most highly disturbed galaxies in the radio-intermediate sample lying in the half with the highest radio powers, notably including the three most-radio powerful sources. This is aligned with a reduction in the proportion of radio-intermediate HERGs that show any sign of disturbance from the most radio-powerful half to the least-radio powerful half of the sample, suggesting that other triggering mechanisms must be important when moving towards lower radio powers.

3.4.2 Host morphologies

As mentioned in §3.2, powerful radio galaxies (typically $L_{1.4\mathrm{GHz}} > 10^{25}$ W Hz^{-1}) have long been associated with giant elliptical hosts (e.g. Matthews et al., 1964; Dunlop et al., 2003; Best et al., 2005b). There are, however, some suggestions that late-type hosts could be more common towards lower radio powers (Sadler et al., 2014; Tadhunter, 2016). This could be particularly apparent for HERGs, if Seyfert galaxies are indeed considered to be their low-radio-power equivalents. Crudely, one might therefore expect that radio-intermediate HERGs would manifest as a mixed population of galaxy morphologies, representing the transition from early-type galaxies at higher radio powers to late-type galaxies at lower radio powers.

Table 3.4 compares the morphological classifications of the galaxies in the sample obtained from visual inspection, both from this work and the Galaxy Zoo project, and from the detailed light profile modelling performed using `GALFIT` – the methods are both described in §3.3.2. Regardless of the technique, it is immediately clear that there is no dominant class of host galaxy morphology, and that radio-intermediate HERGs do in fact represent a mixture of late-type and early-type morphologies. As discussed in §3.3.2, however, there is evidence to suggest that the idea that the host morphology – as quantified using the B/T ratio – changes gradually with radio or optical AGN luminosity along the HERG sequence can also be ruled out.

Considering the results of the visual inspection, it is seen that the proportion of galaxies classified as late-type and early-type are consistent between this work and the Galaxy Zoo project, with a slight preference for late-types relative to early-types. The main difference between the two lies in the higher proportion of hosts categorised as "Merger" or "Don't Know" in the Galaxy Zoo results compared to those classified to be merging by the authors. This is perhaps unsurprising, given the relative inexperience of the participants in the project and the common occurrence of lenticular galaxies, which are hard to categorise in the Galaxy Zoo classification scheme.

It is important to note, however, that visual classifications of morphological types are always subject to biases (e.g. see Cabrera-Vives et al., 2018), which, despite attempts (e.g. Bamford et al., 2009; Willett et al., 2013), are difficult to correct for, especially when considering small sample sizes. This provided strong motivation for performing detailed modelling of the galaxy light profiles, with the goal of providing a more quantitative basis for the galaxy classifications. Interestingly, the proportion of early-type hosts relative to late-types is seen to be higher in this case, in contrast with the results of the visual inspections. It is worth noting, on the other hand, that a total of 15 out of the 30 galaxies in the sample required both bulge-like and disk-like components to fit their light profiles, a proportion comparable to the number classified as late-types from the visual classifications. In addition, the majority of multicomponent models were disk-dominated, as is evidenced by the median bulge-to-disk ratio of B/D $\sim$ 0.8.

One further point of interest is that the presence of major disk components in the galaxy light profiles opens up the possibility of AGN triggering via secular mechanisms related to galaxy disks, as mentioned in §3.4.1. Disk instabilities have been suggested as an important alternative triggering mechanism for AGN below quasar luminosities (e.g. Menci et al., 2014), although it is uncertain that this would be important outside of the violent conditions expected in clumpy disk galaxies at higher redshifts (Bournaud et al., 2012). However, it is thought that the weaker and flatter bulges sometimes seen in late-type galaxies could be built up by instabilities in the disks (Kormendy & Kennicutt, 2004), which could simultaneously trigger the nuclear activity. In addition, bar-driven fuelling could contribute in at least some cases (e.g. Galloway et al., 2015). Given the reduced proportion of interacting galaxies and the increased proportion of late-type hosts that are found in the RI-HERG low sample relative to radio-powerful AGN, this suggests that such processes could collectively provide a viable alternative triggering mechanism to mergers for radio-intermediate HERGs.

3.5 Chapter summary and conclusions

Much previous work concerning radio AGN has focused on those with the highest radio luminosities, due in most part to their ease of detection in the first flux-density-limited radio surveys. However, deeper surveys have revealed that radio-powerful examples are rare cases in the general population of local radio AGN, and it has been shown that HERGs with intermediate radio powers can significantly disturb the warm and cool ISM phases in their hosts through jet-driven outflows. Therefore, the jets associated with radio-intermediate HERGs can potentially have a significant effect on the evolution of their host galaxies, and more detailed study is required to establish the properties of the population.

This deep optical imaging study of a sample of 30 local radio-intermediate HERGs has allowed for the detailed characterisation of the optical morphologies of their host galaxies for the first time. The main results are as follows:

- 53 ± 9 % (16/30) of the galaxies in the sample show morphological signatures of a past or ongoing merger event based on visual inspection by several independent classifiers, a significantly lower proportion ($3.8\,\sigma$) than that found for the SLRGs in the 2Jy sample (94^{+4}_{-7} %).

- In terms of proportions, the most radio-powerful half of the sample has a $1.5\,\sigma$ higher level of morphological disturbance than the least radio-powerful half – 67^{+10}_{-14} % (10/15) and 40^{+13}_{-11} % (6/15), respectively. The exact same proportions are measured when dividing the sample by [OIII]λ5007 luminosity, however, despite no evidence for a correlation between $L_{1.4\mathrm{GHz}}$ and $L_{[\mathrm{OIII}]}$ being found.

- Eight galaxies in the sample have highly disturbed morphologies or large-scale tidal tails, suggestive of major galaxy interactions. It is found that all of these galaxies lie in the most radio-powerful half of the sample (a $3.3\,\sigma$ result), including the three galaxies with the highest radio powers. In contrast, 5 out of 8 of these galaxies lie in the half of the sample with the highest [OIII]λ5007 luminosities and 3 out of 8 in the lower half, a difference of only $0.8\,\sigma$.

- Results from detailed light profile modelling and visual classification indicate that the host galaxies of radiatively-efficient AGN with intermediate radio powers have mixed morphological types. Many show signs of strong disk components (50 ± 9 %; 15/30) in the models, and the majority of multi-component fits are disk-dominated ($53\,^{+12}_{-13}$ %; 8/15) with a median B/D ~ 0.8. This contrasts with the predominantly early-type host galaxies of traditionally radio-powerful AGN.

Taken together, these results suggest that the relative importance of triggering HERG activity through galaxy mergers and interactions reduces with radio power. However, mergers appear to remain important for triggering HERGs with higher radio powers, even within the radio-intermediate population. Moving to lower radio powers, the lower proportion of interaction signatures suggests a reduced importance for merger-based triggering. Given the higher proportion of late-type galaxy morphologies in the RI-HERG low sample, this could be associated with an increased importance for secular triggering mechanisms related to processes in galaxy disks (e.g. disk instabilities, the action of bars).

The research described in Chapters 4 and 5 expands the study of the optical morphologies of active galaxies to a much broader range of radio powers and [OIII]λ5007 luminosities. This allows for further investigation of the potential radio power and/or optical luminosity dependence of the AGN triggering mechanism implied by these first results, using a much larger total sample size. A large number of non-active control galaxies from the general population, matched to the targets in terms of both stellar mass and redshift, were also classified alongside these active galaxies, in order to account for underlying trends in these properties that may influence the results obtained.

Chapter 4

The dependence of AGN host morphology on optical and radio luminosity – I. Methodology and control matching

4.1 Declaration

The work described in this chapter is my own, except where explicitly stated. All analysis was performed by myself.

4.2 Chapter introduction

As presented in Chapter 3, detailed analysis of the optical morphologies of galaxies in the RI-HERG low sample revealed a much lower proportion of galaxy mergers and interactions than that found for radio-powerful SLRGs in the 2Jy sample (Ramos Almeida et al., 2011). Combined with the fact that a significantly larger fraction of galaxies in the more radio-powerful half of the sample showed interaction signatures than of those in the lower-radio-power half, this suggested a possible radio-power-dependence for triggering of the AGN by these events. However, the possibility of a dependence on optical or bolometric luminosity could not be ruled out, given that similar, albeit weaker, trends were also seen with [OIII]λ5007 luminosity.

In addition, the sources in the RI-HERG low sample were found to show a mixture of morphological types, a large fraction of which had clear spiral or disk structures. This contrasts greatly with the predominantly elliptical hosts associated with radio-powerful AGN, and suggests a possible transition along the HERG sequence (with decreasing radio power) towards the typical spiral- or disk-like morphologies of radio-quiet Seyfert galaxies. In this case, however, there was no evidence for a gradual trend with radio power or [OIII]λ5007 luminosity within the sample.

To provide a more definitive test of the picture suggested by these results, the optical morphological analysis was expanded to consider a much larger sample of active galaxies that encompassed a broad range of both radio power and [OIII]λ5007 luminosity. The deep optical INT/WFC imaging observations of the galaxies in the RI-HERG high, 3CR and Type 2 quasar samples outlined in Chapter 2 were taken for this purpose, increasing the total sample size from 30 to 156 active galaxies with radio powers in the range $22.47 \leq \log(\mathrm{L}_{1.4\mathrm{GHz}}) \leq 28.15$ W Hz^{-1} and optical luminosities in the range $32.67 \leq \log(\mathrm{L}_{[\mathrm{OIII}]}) \leq 36.09$ W (see Chapter 2 for more specific details on each sample).

While these samples are largely composed of AGN that are thought to be accreting in a radiatively-efficient manner (i.e. HERGs or quasars), the high-radio-power 3CR sample ($24.67 \leq \log(\mathrm{L}_{1.4\mathrm{GHz}}) \leq 28.15$) also contains 30 radiatively-inefficient LERGs. These were included so that the 3CR results could be directly compared with those obtained for the 2Jy sample, which also covers high radio powers ($25.62 \leq \log(\mathrm{L}_{1.4\mathrm{GHz}}) \leq 28.26$) and a mixture of radiatively-efficient and radiatively-inefficient AGN (SLRGs and WLRGs, in this case; Ramos Almeida et al., 2011, 2012, 2013).

One of the main outcomes of the 2Jy studies was that different results were found for the SLRGs and WLRGs in the sample: i) a much lower fraction of the WLRGs showed signatures of mergers and interactions than the SLRGs (27^{+16}_{-9}% and 94^{+4}_{-7}%, respectively), both of which differed from quiescent elliptical galaxies matched in stellar mass and redshift (∼50%; Ramos Almeida et al., 2011, 2012); ii) the WLRGs prefer moderately dense cluster environments in which high relative galaxy velocities could reduce the merger rate (Popesso & Biviano, 2006), while the SLRGs prefer group environments, where frequent interactions with lower relative galaxy velocities can occur (Ramos Almeida et al., 2013). These results are consistent with the idea that galaxy mergers and interactions are important for triggering radiatively-efficient AGN, but not radiatively-inefficient AGN, at high radio powers. Characterising the optical morphologies of the galaxies in the 3CR sample therefore also provides the opportunity to test this picture in more detail, using a large sample of powerful radio galaxies not yet studied in this manner (73, compared to the 46 2Jy objects). The much larger number of radiatively-inefficient AGN in the 3CR sample – 30 LERGs, compared with the 11 WLRGs in the 2Jy sample – is particularly important in this sense.

Due to the much larger sample size studied for this aspect of the optical imaging research, it was not possible to carry out the morphological analysis with the detailed approach used for the galaxies in the RI-HERG low sample (described in Chapter 3). For this second project, an online interface similar to that used for the Galaxy Zoo studies (Lintott et al., 2008, 2011) was utilised to obtain key morphological classifications from several different researchers in a more time efficient manner. The improved efficiency afforded by this interface also meant that a large number of control galaxies could be classified alongside the active galaxies, which were matched to the targets in both stellar mass and redshift. These controls were non-active SDSS galaxies from the MPA-JHU catalogue that happened to lie within the regions of sky covered by the INT/WFC images of the active galaxies, and thus were also matched to the targets in terms of image depth and quality.

The interface classification method outlined in this chapter offers several key improvements over previous detailed studies of the optical morphologies of radio galaxies and the hosts of Type 2 quasars (e.g. Ramos Almeida et al., 2011, 2012; Bessiere et al., 2012), including the analysis presented in Chapter 3. The self-consistency of the imaging observations of the active galaxies and control galaxies offers a major improvement over the comparisons between the active galaxies and matched elliptical galaxies performed by Ramos Almeida et al. (2012) and Bessiere et al. (2012), since the observing setups, observing conditions and achieved image sensitivities were different for the active and non-active galaxies in these cases. In addition, classifications of a much larger number of control galaxies could be obtained using the current method when compared to these previous studies – a total of 378 (see §4.4), over twice the number considered by Ramos Almeida et al. (2012) – due to the efficiency of the interface classification process. Moreover, the active galaxy and control galaxy images were presented randomly to the classifiers and no information on the nature of the galaxy in question was provided, with the only clue about their properties being the standardised physical scales of the images. This meant that the classifications obtained were largely blind, and so were less prone to the effects of conscious and subconscious biases that may have affected the previous classification analyses. Finally, the use of images with fixed contrast levels and sizes (set by their projected physical scales) reduced the levels of individual classifier bias involved in the classification process.

This chapter outlines the interface classification approach that was adopted for this research, and describes in detail the procedure used to match the active galaxies to the control galaxies. It is structured as follows. Details on the new approach for the morphological classifications and the set up of the online interface used to obtain them are presented in §4.3. Information on the method used to select the matched control galaxies is provided in §4.4. The "postage stamp" images of the active galaxies used in the online classification interface are then presented in §4.5. The chapter is summarised in §4.6. Descriptions of the analysis of the classifications, along with presentation and discussion of the results of the project, are reserved for Chapter 5.

4.3 The new classification approach and online interface

One of the main difficulties faced by past imaging studies of galaxy morphologies has been the need for compromise between the level of detail of the analysis and the size of the sample studied. Detailed characterisation of the morphologies of individual galaxies, such as that performed for both the 2Jy sample (Ramos Almeida et al., 2011, 2012) and the RI-HERG low sample (Chapter 3), has the advantage of optimising the amount of information that is extracted from the available data. As described in Chapter 3, this includes the ability to identify faint interaction signatures after careful manipulation of the image contrast levels, to measure the surface brightness of these tidal features and to perform detailed modelling of the galaxy light profiles.

While this approach works well for studies of small to moderately sized samples, however, it becomes inefficient when working with larger sample sizes. One technique that can be employed in such cases is the method made popular by the Galaxy Zoo project (Lintott et al., 2008, 2011), where brief visual inspection and classification of "postage stamp" images of the target galaxies is performed. The main advantage of this approach is the ability to quickly accumulate classifications for large numbers of galaxies[1], which, although at the cost of reduced detail, greatly improves both the time efficiency and the statistics of the analysis. In addition, both the image appearance and the possible classification categories can be standardised, which reduces the effect of biases introduced by individual participant behaviour during the classification process.

From the study of the RI-HERG low sources, it is also interesting to note that the key result that all of the most highly disturbed galaxies lie in the most radio-powerful half of the sample was based solely upon cursory visual inspection of the images. Furthermore, while the `GALFIT` modelling allowed for bulge-disk decomposition of the light profiles, the proportion of galaxies in the sample that were found to have significant disk components using this method (50 ± 9 %) was consistent with the fraction of late-type galaxies identified through visual inspection both by the researchers (43^{+9}_{-8} %) and by Galaxy Zoo project participants (37^{+9}_{-8} %, and 43 ± 9 % when debiased). These results suggested that reasonable identifications of host types and disturbed morphologies could be obtained from more basic visual inspection of the galaxy images.

Because of the much larger sample of active galaxies involved in this second project, it was therefore decided that a method closely following the Galaxy Zoo approach would be used for the morphological analysis. The greatly improved time efficiency offered also opened up the possibility of classifying many non-active control galaxies alongside the targets, which provided a significant advantage over the analysis performed for the RI-HERG low sample in particular. This approach has also been used successfully by Gordon et al. (2019) to classify the optical morphologies of a very large sample of LERGs and matched control galaxies (a project for which I was one of the classifiers). The results from this study could therefore be compared directly with those from this new research. Details on the online interface and the classification method used for the current project are provided in the following subsections.

---

[1] As an extreme example, in the initial half a year of the Galaxy Zoo project, over 40 million total classifications had been carried out by citizen science volunteers for the almost 900,000 SDSS galaxies included (Lintott et al., 2008).

4.3.1 Online interface

The online interface used for this project was made with the Zooniverse Project Builder platform at Zooniverse.org[2], a citizen science web portal that stemmed from the initial Galaxy Zoo project by Lintott et al. (2008, 2011). Through this constructed interface, eight researchers (myself, Clive Tadhunter, Yjan Gordon, Sara Ellison, Cristina Ramos Almeida, Chris O'Dea, Liam Grimmett, and Lydia Makrygianni) were shown images of active galaxies and control galaxies in a randomised manner, such that they did not know which they were classifying, and were asked to answer multiple choice questions concerning their optical morphologies. No additional information on the nature of the galaxy to be classified was provided, in order to avoid introducing any biases related to the individual galaxy properties (e.g. target name, stellar mass, redshift, radio power, optical luminosity). However, two scale bars of 10 kpc in size were included on each image to assist with determination of multiple nuclei classifications (see §4.3.2). The images were centred on the targets and fixed to be of 200 kpc × 200 kpc in size at the redshift of the galaxy in question, in all cases (as in Gordon et al., 2019).

One disadvantage of carrying out the classifications in this way is that the ability to fully manipulate the image contrast levels for identifying morphological structures with a range of different surface brightnesses is lost. However, the interface was set up with several features that partially accounted for this issue, offering an improvement on similar past studies in this sense. Firstly, two stamp images with different contrast levels were displayed alongside each other for each galaxy: one of high contrast, for clearer identification of high-surface-brightness tidal features and the overall morphological types (spiral/disk, elliptical, etc.); and one of low contrast, for clearer identification of faint morphological structures. The contrast levels for these two images were chosen manually on a case-by-case basis, with consideration given to the appearance of both the target galaxy structures and the objects and/or image defects within the 200 kpc square surrounding region. In addition, the interface was set up such that the participants could zoom in or out and pan around the image to look at specific regions in more detail. The image could also be rotated or inverted if desired. All of these features are displayed in Figure 4.1, in which the appearance of the interface is presented.

To provide the participants with further assistance when carrying out the classifications, a tutorial was available to be viewed at all stages of the classification process, accessed by clicking the tab visible in Figure 4.1. This provided a brief introduction to

---

[2] Available at: `https://www.zooniverse.org/lab`. Maintained by the Citizen Science Alliance collaboration (`https://www.citizensciencealliance.org/index.html`).

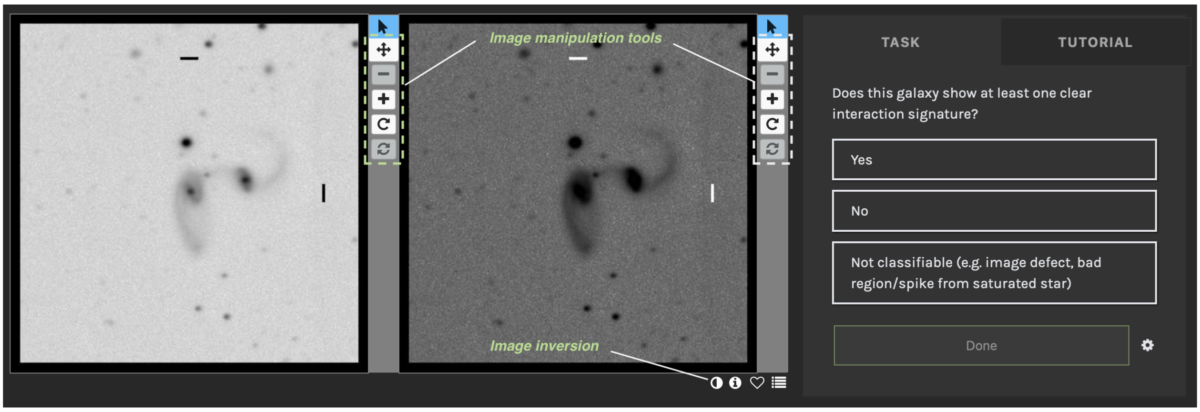

Does this galaxy show at least one clear interaction signature?

Figure 4.1: An image of the online interface used for the optical morphological classifications, showing the high-contrast (left) and low-contrast (right) images of the subject galaxy and the first multiple choice question. From top to bottom, the tools within the dashed boxes could be used to pan, zoom out, zoom in, rotate, and reset the images of the galaxy at each of the two contrast levels independently. The indicated button in the bottom right of the images could also be used to invert the image colours.

the project and the interface, but also gave more specific guidance for answering each of the multiple choice questions, including example images for each of the interaction signature and host type classification categories. The questions and possible answers are outlined in the next subsection.

4.3.2 Classification questions

Using the interface, participants were required to answer up to three multiple choice questions related to the morphological appearance of the subject galaxies. The first of these is displayed in Figure 4.1, where the participants were required to answer the question “**Does this galaxy show at least one clear interaction signature?**” using one of the following options:

i) **Yes**;

ii) **No**;

iii) **Not classifiable (e.g. image defect, bad region/spike from saturated star)**.

The lattermost option was included for cases in which it was not possible to determine whether or not the galaxy was disturbed due to issues with the displayed image, for instance because of image defects. As for the previous study of the RI-HERG low sample, dust lanes were included as one of the interaction signature classifications at this stage, and so participants were required to select "Yes" for this question even when a dust lane was the only feature they deemed clearly visible.

Should the participant have answered "Yes" to this first question, they were then asked to identify the type(s) of interaction signature that they had seen. To do this, they had to answer the question "**What types of interaction signature are visible?**" using the following options:

i) **Tail (T)**;
ii) **Fan (F)**;
iii) **Shell (S)**;
iv) **Bridge (B)**;
v) **Amorphous halo (A)**;
vi) **Irregular (I)**;
vii) **Multiple nuclei (2N, 3N...)**;
viii) **Dust lane (D)**;
ix) **Tidally interacting companion (TIC)**.

In this case, the participants were allowed to select as many of the possible options as necessary, to ensure that multiple interaction signatures could be identified for each galaxy when present. The categories were chosen to closely match those from the interaction signature classification scheme detailed in Chapter 3 (also consistent with Ramos Almeida et al., 2011, 2012; Bessiere et al., 2012), with definitions that were mostly identical to those outlined before (in §3.3.1). The exception was the "Multiple Nuclei (2N, 3N...)" category, for which the nuclei were here only required to be within approximately 10 kpc of each other (previously 9.6 kpc; see Chapter 3). This was due to the reduced accuracy with which projected distances could be estimated using this new approach, with the participants being mainly reliant on the 10 kpc scale bars provided on the images (see §4.3.1).

As shown above, a new category was also added to the scheme presented in Chapter 3 for the current analysis: "Tidally interacting companion (TIC)". This was added to account for cases in which a close companion shows evidence for a tidal interaction with the main target, whether or not the target itself shows clear interaction signatures – this includes cases where the distance limit criterion for the "Multiple Nuclei (2N, 3N...)" class was not met. In line with the other category descriptions in Chapter 3, this can be defined as signifying cases where "a companion galaxy shows clear morphological disturbance that is suggestive of a tidal interaction with the main target (e.g. with direction aligned towards/away from the central target)".

Finally, the classifiers were required to answer the question "**On first impression, what is the morphological type of the galaxy?**" using one of the following responses:

i) **Spiral/disk**;

ii) **Elliptical**;

iii) **Lenticular**;

iv) **Merger (too disturbed to classify)**;

v) **Unclassifiable (due to image defects, *not* merger)**.

Again, these options were chosen to be consistent with the host type classifications obtained from visual inspection of the RI-HERG low sources in Chapter 3. As for the first question, the last option was included for cases where the participant thought that issues with the image quality meant that they could not provide an accurate classification.

Once a participant had provided answers to the two or three relevant questions outlined above, the results were recorded by the web portal system and the galaxy in question was not shown to them again. This meant that repeat classifications of the subjects were avoided, and that the efficiency of the classification process was improved.

4.4 Control galaxy selection

Use of the online interface meant that morphological classifications could be obtained more quickly than when using the method outlined in Chapter 3. The use of standardised images and classification categories, along with the randomised presentation of the subject images, also greatly reduced the level of bias involved in the classification process. One of the major advantages of these features was that it opened up the possibility of classifying a large number of "control" galaxies from the general (non-active) population alongside the active galaxies, in a relatively unbiased manner. In this way, it would then be possible to test whether any trends found were specific to the properties of the active galaxies selected, or whether they were a by-product of an underlying feature of the general galaxy population that had not been considered.

In order to ensure an appropriate comparison between the active galaxies and the general galaxy population, it was necessary to select non-active control galaxies that were matched to the targets in terms of stellar mass and redshift. Given that the majority of active galaxies in the samples studied were selected from SDSS-based catalogues, and that a proportion of the 3CR objects also lie within the SDSS footprint, a large number of SDSS galaxies were found to lie within the fields covered by the target images. Because of the large crossover with the regions of sky observed for SDSS DR7 in particular, many of these sources were also included in the MPA-JHU value added catalogue. This meant that a large amount of supplementary information was available for these galaxies, including spectroscopic redshifts and, in the vast majority of cases, estimates of their stellar masses, as required. The MPA-JHU catalogue therefore provided a suitable pool of galaxies from which to select the matched controls.

This section describes how the large sample of control galaxies used for this project was selected from the MPA-JHU catalogue, through consideration of their required stellar masses, redshifts, and sky coordinates. While the catalogue also contained stellar mass estimates for all of the galaxies in the RI-HERG low and RI-HERG high samples, it did not include estimates for a large proportion of the 3CR sources (largely due to their sky coordinates). This was also true for many of the objects in the Type 2 quasar sample. Suitable estimates of the stellar masses of these galaxies therefore had to be obtained in a different manner, prior to carrying out the control matching. The method used to calculate stellar mass estimates for the galaxies in these samples, based on their near-infrared luminosities, is detailed in §4.4.1. More specific details on the control matching procedure are then provided in §4.4.2. This includes the matching performed for the objects in the Type 2 quasar sample, which was carried out *after* the morphological classifications were obtained using the online interface due to their late inclusion in the project.

4.4.1 Stellar mass calculations

Prior to identifying suitable matched control galaxies, it was first necessary to ensure that estimates of the stellar masses were available for all of the targets to be matched. All objects in the RI-HERG low and RI-HERG high samples had existing stellar mass estimates in the MPA-JHU value added catalogue from which the control galaxies were also extracted, and so no additional calculations were required for these sources. However, 63 of the galaxies in the 3CR sample (86%) and 12 of the galaxies in the Type 2 quasar sample (48%) did not have these values available. As a result, estimates of the stellar masses for these objects had to be obtained in a different manner.

Initial stellar mass estimates for all galaxies in the 3CR and Type 2 quasar samples were derived from their Two Micron All Sky Survey (2MASS; Skrutskie et al., 2006) K_s-band luminosities, using the colour-dependent mass-to-light ratio prescription of Bell et al. (2003) for this waveband. This was chosen primarily because the low mass stars that are expected to comprise the majority of the stellar mass in typical galaxies radiate strongly at these wavelengths (Chabrier, 2003). In addition, relative to the optical band, it is much less sensitive to foreground dust extinction, and it shows reduced variation in mass-to-light ratio between galaxies with broadly different star formation histories (e.g. Bell & de Jong, 2001; Bell et al., 2003). This method was used to derive stellar mass estimates for *all* of the objects in both the 3CR and Type 2 quasar samples (i.e. the MPA-JHU values were not used for any of these galaxies), for consistency both within and between the two samples.

The Bell et al. (2003) mass-to-light ratio prescription for the 2MASS K_s-band has the following form (in solar units):

$$\log(M/L)_{K_s} = -0.206 + 0.135 \times (B - V)\,. \tag{4.1}$$

A $B - V$ colour of 0.95 was used, in line with the expected value for a typical elliptical galaxy at zero redshift (e.g. Smith & Heckman, 1989b). An additional factor of 0.15 dex was subtracted in order to convert to a Kroupa initial mass function (IMF) for the stellar population (Kroupa, 2001), in accordance with the IMF assumed for the MPA-JHU stellar mass estimates. A final value of $\log(M/L)_{K_s} = -0.228$ was thus used for the calculations.

Where possible, the "total" K_s-band magnitudes[3] listed in the 2MASS Extended Source Catalogue (Jarrett et al., 2000) were used to derive the luminosities for the calculations, in order to ensure that as much as possible of the galaxy flux was encapsulated (XSC magnitudes, hereafter). These values were available for 44 of the 73 3CR sources (60%) and 19 of the 25 Type 2 quasars (76%). Failing this, the magnitudes listed in the 2MASS Point Source Catalogue (Skrutskie et al., 2006), derived from PSF profile fitting, were considered (hereafter PSC magnitudes). These were available for all 6 of the

---

[3] Derived by extrapolating the radial surface brightness profile measured within a 20 mag arcsec^{-2} elliptical isophote to a radius of around four scale lengths (from Sérsic-like exponential fitting), in an attempt to account for the flux lost below the background noise.

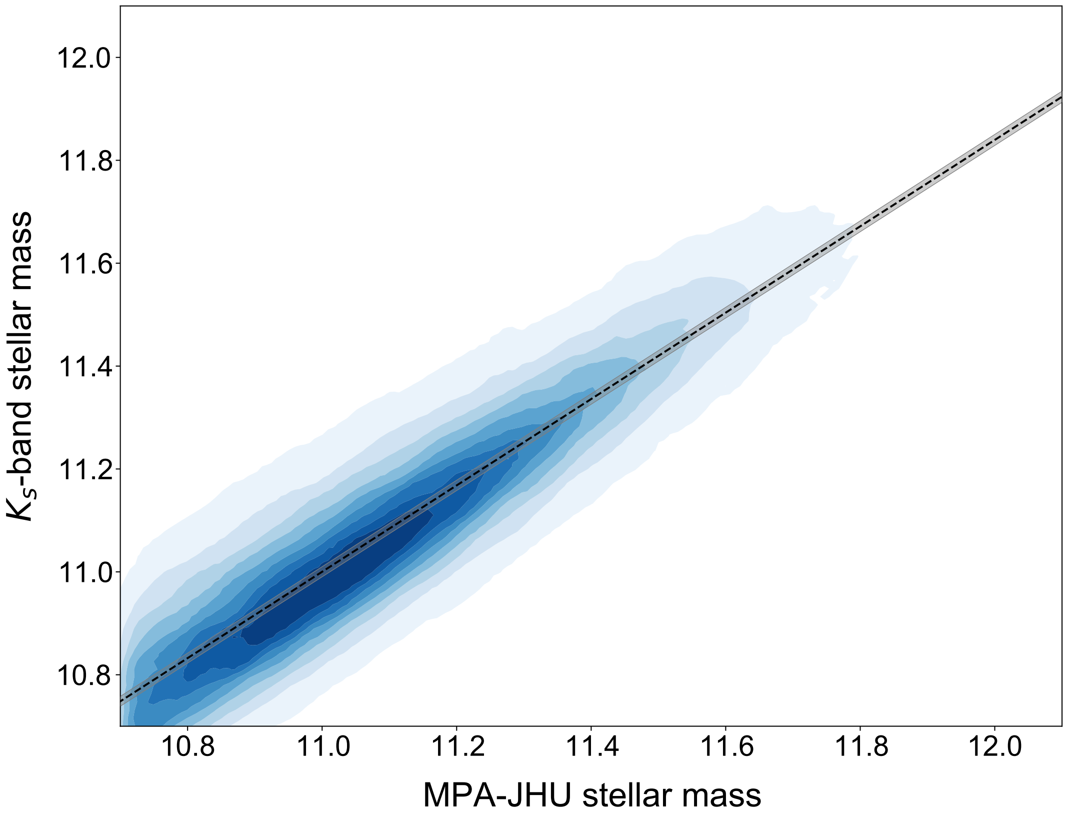

Figure 4.2: A contour plot of the K_s-band and MPA-JHU stellar mass estimates for the 238,418 galaxies in the MPA-JHU catalogue with 2MASS XSC magnitudes. The line of best fit derived from linear regression is plotted (black), with the grey shaded region representing the one-σ error bounds for the fit.

remaining Type 2 quasars and 26 out of the 29 remaining 3CR galaxies (90%). Three of the 3CR sources – 3C 61.1, 3C 258, and 3C 458 – therefore did not have either 2MASS XSC or PSC magnitudes available. Stellar mass estimates were not calculated in these cases, and, consequently, the control matching was not performed for these sources. However, these objects were still considered for the morphological classifications and are included in comparisons of the results obtained for the 3CR sample and their matched controls (Chapter 5). This was done under the assumption that the stellar masses for these sources, which represent a small minority of the full 3CR sample (4%), are likely to be similar to those of the other 3CR objects.

The main disadvantage of using the PSC measurements was the loss of sensitivity to emission from the extended regions of the target galaxies. In an attempt to account for this effect, a correction was derived from the difference between the XSC and PSC magnitudes for the large number of galaxies in the MPA-JHU catalogue that had both measurements available. Considering all MPA-JHU galaxies with redshifts in the range covered by both the 3CR and Type 2 quasar samples ($0.05 < z < 0.3$), a median magnitude difference of $K_s^{\rm PSC} - K_s^{\rm XSC} = 0.811$ was determined, with a standard deviation of 0.311. No significant evidence for a relationship between these differences and the measured PSC magnitude or redshift was found, as confirmed by Pearson correlation tests ($r = -0.121$ and $r = 0.100$, respectively, with negligible p-values). As a result, a fixed value of 0.811 was subtracted from the PSC magnitudes to convert them to estimated XSC magnitudes in all cases, with the latter then being used in the subsequent calculations.

Following this, an extragalactic extinction correction was subtracted from the XSC or corrected PSC magnitudes, using the K-band values of Schlafly & Finkbeiner (2011)[4]. A cosmological k-correction was also applied, using the $k(z) \approx (2.1 \pm 0.3)z$ formulation given in Bell et al. (2003), which is independent of galaxy spectral type. The corrected magnitudes were then converted to solar luminosities by assuming a solar 2MASS K_s-band absolute magnitude of 3.27 (Willmer, 2018), after which Equation 4.1 was applied to obtain the stellar mass estimates.

As a final step, the same technique was used to determine K_s-band stellar mass estimates for galaxies in the MPA-JHU catalogue with 2MASS XSC magnitudes available. This was done with the goal of obtaining a correction to align the K_s-band stellar mass estimates with the MPA-JHU values. Since individual SDSS $g - i$ colours were available for the MPA-JHU galaxies, a second prescription from Bell et al. (2003) that utilized these measurements was employed in this case: $\log(M/L)_{K_s} = -0.211 + 0.137 \times (g - i)$. The procedure was otherwise identical to that described above; this again included the subtraction of an additional 0.15 dex to convert to a Kroupa IMF. All XSC-matched galaxies with MPA-JHU stellar mass estimates in the range $10.7 \leq \log(\mathrm{M}_*/\mathrm{M}_\odot) \leq 12.0$ were considered for the comparison, in approximate agreement with the range of K_s-band stellar mass estimates derived for the 3CR and Type 2 quasar samples – while some of the 3CR sources had K_s-band estimates larger than $\log(\mathrm{M}_*/\mathrm{M}_\odot) = 12.0$, this upper limit was chosen because of the large uncertainties determined for the MPA-JHU estimates above this value.

The K_s-band and MPA-JHU stellar mass estimates for the ~240,000 galaxies considered for the comparison are plotted against each other in Figure 4.2. The line of best fit displayed in the figure has the form $\log(\mathrm{M}_*/\mathrm{M}_\odot)_{\mathrm{K_s}} = 0.84 \log(\mathrm{M}_*/\mathrm{M}_\odot)_{\mathrm{MPA-JHU}} + 1.77$, as derived from linear regression. The typical scatter around the relation is 0.01. No

---

[4] Downloaded from the IRSA Galactic Dust Reddening and Extinction online service, available at: `https://irsa.ipac.caltech.edu/applications/DUST/`.

significant evidence that the difference between the stellar mass estimates varies with $g - i$ colour, redshift, 2MASS XSC K_s-band magnitude, or the values of either of the stellar mass estimates was found, based on Pearson correlation tests. Consequently, this relation was employed to convert K_s-band stellar mass estimates to corresponding MPA-JHU stellar mass estimates in all cases. The final MPA-JHU-equivalent stellar mass estimates for the 3CR and Type 2 quasars are presented in Chapter 2 in Tables 2.4 and 2.5, respectively.

4.4.2 Matching procedure

The MPA-JHU value-added catalogue contains a large amount of raw and derived data for 927,552 galaxy spectra from SDSS DR7, including the spectroscopic redshifts and stellar mass estimates[5] that were crucial for the control matching. Given the significant crossover between the fields covered by the INT/WFC images and the SDSS DR7 survey footprint, the catalogue therefore provided a suitable "pool" from which to select matched control galaxies for the active galaxies. Prior to performing the control matching, however, the following steps were taken to limit the control pool to galaxies with more suitable properties.

i) **Coordinate restriction.** The first constraint on the number of galaxies that could be used for the matching was the requirement that they should lie within the regions of sky covered by the INT/WFC images of the active galaxies. This was by far the most restrictive requirement, with only 2,744 of the objects listed in the catalogue meeting this criterion (0.3%).

ii) **Removal of likely AGN.** The MPA-JHU catalogue was constructed solely of objects that had been spectroscopically classified as galaxies in SDSS DR7, with the exception being some objects that had originally been targeted as galaxies but were later classified as quasars. However, the spectral types of both galaxies and quasars were also sub-classified based on the properties of their [OIII]λ5007, Hα, Hβ, and [NII]λ6583 emission lines (if strongly detected), as follows:

   - **AGN** – Flux ratios meeting the criterion $\log([\mathrm{OIII}]/\mathrm{H}\beta) > 0.7 - 1.2\,\{\log([\mathrm{NII}]/\mathrm{H}\alpha) - 0.4\}$;

---

[5] These were obtained from fitting of the stellar population synthesis models of Bruzual & Charlot (2003) to the SDSS broadband *ugriz* photometry for the galaxies. The method is similar to that described by Kauffmann et al. (2003), who instead used spectroscopic features to characterise the fits. A comparative discussion of these methods is available at: `https://wwwmpa.mpa-garching.mpg.de/SDSS/DR7/mass_comp.html`.

- **Star-forming galaxy** – Flux ratios meeting the criterion $\log([\mathrm{OIII}]/\mathrm{H}\beta) < 0.7 - 1.2\,\{\log([\mathrm{NII}]/\mathrm{H}\alpha) - 0.4\}$;
- **Starburst galaxy** – Meeting the criterion for a star-forming galaxy but has Hα equivalent width > 500 Å;
- **Broad-line object** – Lines detected at the $10\,\sigma$ level with velocity dispersion $> 200\ \mathrm{km\,s^{-1}}$ at the $5\,\sigma$ level (can be in conjunction with any other sub-classification).

All sources that had been sub-classified as either AGN or non-star-forming broad-line objects were removed from consideration. Star-forming or starburst galaxies were not removed. This left 2,615 galaxies in the control pool.

iii) **Removal of remaining targets.** The three galaxies from our target samples that remained in the control pool at this point were removed, leaving 2,612 objects.

iv) **Removal of duplicate objects.** The MPA-JHU catalogue contains duplicate identifications for a large number of galaxies, based on them having more than one SDSS spectral observation. Any remaining duplicates were taken out of the control pool at this point, which left 2,413 sources available for the matching.

All of the matched controls used for the analysis were selected from this final restricted pool of 2,413 galaxies, following matching in terms of the galaxy stellar mass estimates and redshifts. As mentioned, this matching was not performed for the three galaxies in the 3CR sample for which stellar mass estimates could not be obtained from 2MASS magnitudes (§4.4.1): 3C 61.1; 3C 258; and 3C 458. In addition, while producing the high- and low-contrast versions of the target images, it was found that the image for 3C 452 could not be used for the classification analysis – a saturated bright star ruined the image appearance at its location. The Type 2 quasars were also not considered at this stage, although matching was performed for these objects after the classifications had been obtained (see below). A total of 127 active galaxies (58 radio-intermediate HERGs and 69 3CR sources) were therefore considered for control matching. Repeat selections of controls that matched multiple active galaxies were permitted throughout the matching process, in order to maximise the number of possible matches available for each target.

Redshift matches were determined using separate criteria for the radio-intermediate HERG and 3CR samples:

1. $z_{\rm target} - 0.01 < z_{\rm control} < z_{\rm target} + 0.01$, for matching to the RI-HERG low and RI-HERG high samples;
2. $z_{\rm target} - 0.02 < z_{\rm control} < z_{\rm target} + 0.02$, for matching to the 3CR sample.

Here, an increased tolerance was allowed for the 3CR matching due to the fact that their typically high stellar masses (median $\log(\mathrm{M}_*/\mathrm{M}_\odot) = 11.4$) made the selection of matched controls more difficult (see below). All control galaxies with suitable redshifts then needed to meet both of the following two stellar mass criteria:

1. $(\log(\mathrm{M}_*/\mathrm{M}_\odot) + \sigma)_{\rm control} > (\log(\mathrm{M}_*/\mathrm{M}_\odot) - \sigma)_{\rm target}$;
2. $(\log(\mathrm{M}_*/\mathrm{M}_\odot) - \sigma)_{\rm control} < (\log(\mathrm{M}_*/\mathrm{M}_\odot) + \sigma)_{\rm target}$;

i.e. the one-σ uncertainties on the stellar mass estimates for the target and the control were required to overlap (as in Gordon et al., 2019). A total of 1,581 unique control galaxies were found to meet these selection criteria, an average of ∼12 per active galaxy considered. However, since repeat selections of controls were permitted, the true number of matches was in fact much larger than this (8,700).

On the other hand, in addition to the four 3CR sources not considered for the matching (listed above), no matches were found for a further 10 of the 3CR sources using these criteria: 3C 130; 3C 234; 3C 323.1; 3C 346; 3C 371; 3C 382; 3C 405; 3C 410; 3C 430; and 3C 433. These sources had stellar mass estimates in the range $11.3 \leq \log(\mathrm{M}_*/\mathrm{M}_\odot) \leq 12.7$, with a median of 11.8, and redshifts in the range $0.05 \leq z \leq 0.26$, with a median of 0.11. A large fraction of the galaxies in the control pool had redshifts in the range covered by these 3CR sources (73%), and had a similar median value, at 0.10. However, only 10% had stellar mass estimates in the required range, with only 0.2% being at or above the median value of 11.8. The lack of success in the matching was therefore likely driven by the large stellar masses of these 3CR sources. Overall, the procedure was thus successful in finding matches for 117 out of the 127 targets considered for the matching (92%).

In order to reduce the total number of galaxies that the project participants would need to classify, only the 5 controls with the smallest differences between the target and control stellar mass estimates were considered for each active galaxy. This requirement had the additional advantage of counteracting the potential selection of controls with large uncertainties, which was a weakness of the stellar mass matching criteria used. In cases where the target had fewer than 5 matches, all of the available controls were considered. These objects were: J1036+38 (RI-HERG low), with 4 matches; 3C 52, with

3 matches; 3C 236, with 2 matches; and 3C 132, 3C 388, 3C 438, J1630+12 (RI-HERG low), J0752+45, J1147+35, and J1436+05 (RI-HERG high), with only one match each. A total of 551 control selections (388 unique galaxies, 163 repeats) were made for the 118 matched targets remaining at this point, an average of 4.7 per galaxy.

Once the up to 5 nearest matches had been selected for each matched active galaxy, preliminary stamp images for the controls were produced for use with the classification interface. These had the standardised size of 200 kpc × 200 kpc, in line with those created for the targets. The images were then briefly inspected in order to check for any issues that could affect the classifications, such as bad image regions, defects or crowding/source confusion. In some cases, the control galaxy structures were also found to extend beyond the edge of the INT/WFC images. From this inspection, it was found that 19 control galaxy images were not suitable for the classifications due to the aforementioned issues. In these cases, replacement controls were obtained by producing images of the next closest matches in stellar mass until a control with a suitable image was found. In this way, all controls were successfully replaced, but with 10 additional repeat selections (551 total selections with 173 repeats). This left a final sample of 378 unique control galaxies with images to be used for the classification analysis.

Due to their late inclusion in the project, control matching for the Type 2 quasar sample was only performed after the interface classifications had been obtained. The controls for these targets were hence selected from the 378 control galaxies selected as matches to objects in the other active galaxy samples. The criteria used for the matching were identical to those used for the RI-HERG low and RI-HERG high samples: (i) $z_{\rm target} - 0.01 < z_{\rm control} < z_{\rm target} + 0.01$, for the redshift matching; (ii) $(\log(\rm M_*/M_\odot) + \sigma)_{\rm control} > (\log(\rm M_*/M_\odot) - \sigma)_{\rm target}$ and $(\log(\rm M_*/M_\odot) - \sigma)_{\rm control} < (\log(\rm M_*/M_\odot) + \sigma)_{\rm target}$, for the stellar mass matching. Using these criteria, it was found that 202 of the 378 galaxies were also matches to at least one of the galaxies in the Type 2 quasar sample. This included matches for each of the Type 2 quasar objects – 582 matches in total, when multiple matches for each control galaxy were considered – with the number of matches for each individual target ranging from 4 to 47. As before, the 5 controls with the smallest differences between active galaxy and control galaxy stellar mass were selected for the control sample, and repeat selections were allowed. Only four matched controls were available for J1100+08, which were hence all included in the sample. A total of 124 control selections were therefore made for the 25 Type 2 quasar objects (91 unique control galaxies, 33 repeats).

Figure 4.3 shows the stellar mass and redshift distributions for each of the active

Table 4.1: The results of two-sample Kolmogorov-Smirnoff (KS) tests performed for the redshift and stellar mass distributions of the active galaxy samples and their respective matched control samples. Both the test statistic (D) and the p-value are presented in each case. Note that the values listed for the 3CR sample were derived considering only the 59 objects for which control matches were successfully found.

	RI-HERG low	RI-HERG high	3CR (matched)	Type 2 quasars
z	$D = 0.084$	$D = 0.119$	$D = 0.075$	$D = 0.099$
	$p = 0.988$	$p = 0.857$	$p = 0.922$	$p = 0.971$
$\log(M_*/M_\odot)$	$D = 0.076$	$D = 0.163$	$D = 0.095$	$D = 0.115$
	$p = 0.996$	$p = 0.519$	$p = 0.726$	$p = 0.913$

galaxy samples and their respective matched control galaxy samples, which demonstrate the success of the matching – note that only the 59 3CR sources with matched controls were considered for these plots. Two-sample Kolmogorov-Smirnov tests performed on these distributions provided no significant evidence for rejecting the null hypothesis that the targets and their matched controls are drawn from the same underlying distribution, in all cases. The results of these tests are presented in Table 4.1.

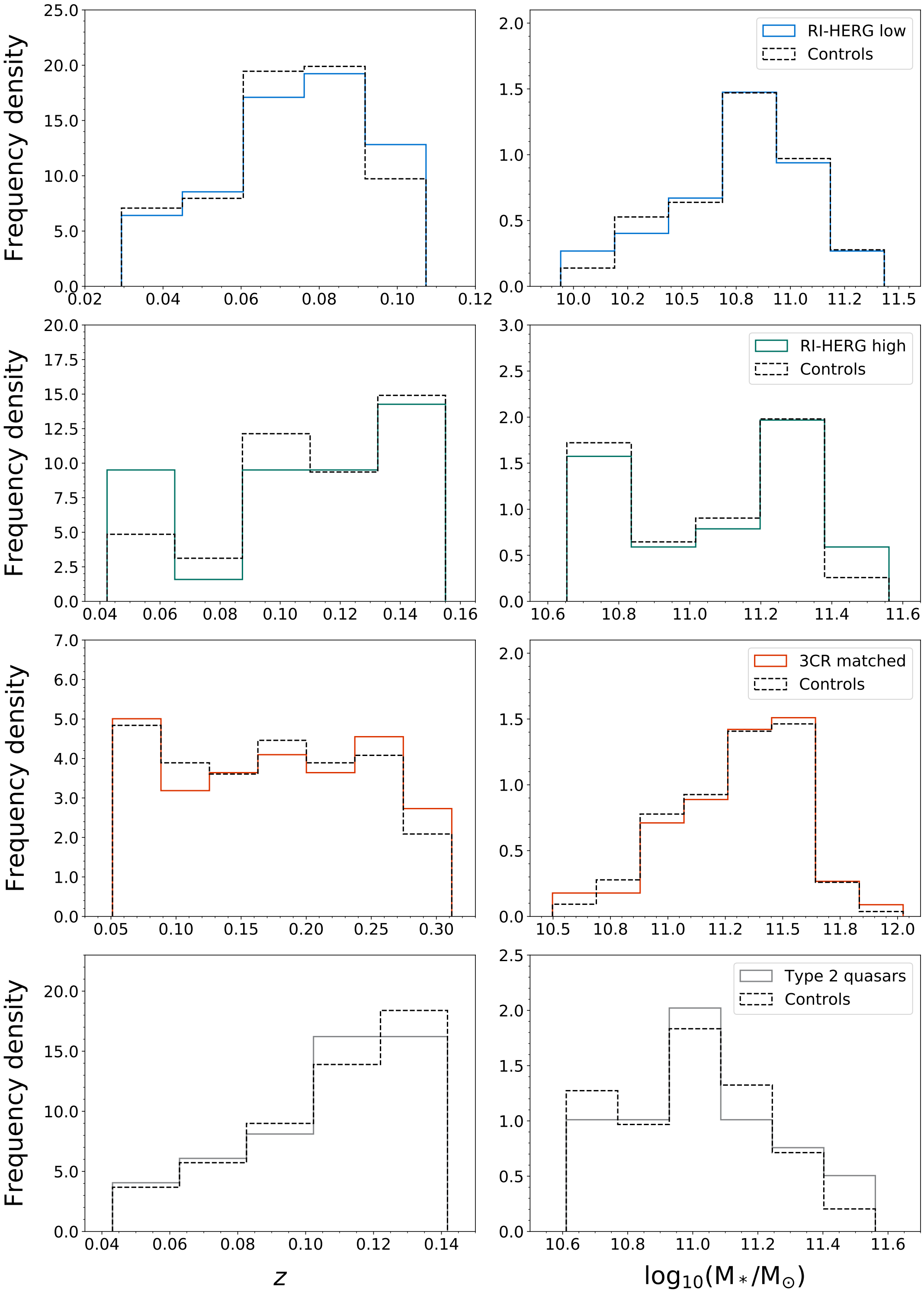

Figure 4.3: The redshift (left column) and stellar mass (right column) distributions for the galaxies in each of the four active galaxy samples, alongside the corresponding distributions for their matched controls.

4.5 Target images

With the 58 radio-intermediate HERGs (30 RI-HERG low, 28 RI-HERG high), 25 Type 2 quasars, 72 3CR sources (3C 452 was not included due to its image issues), and 378 matched control galaxies, images for a total of 533 galaxies were considered for the morphological classification analysis. As a final step before the collection of the classifications through the online interface, two postage stamp images with the properties described in §4.3.1 were produced for each of these galaxies: one with high contrast (better for high-surface-brightness interaction signatures and morphological types) and one with low contrast (for low-surface-brightness interaction signatures), both of 200 kpc × 200 kpc in size at the redshift of the galaxy in question. Two scale bars of 10 kpc in length were also added to each image to assist classifiers with the identification of the "Multiple nuclei (2N, 3N...)" class of interaction signature, when required.

All of the images used in the interface for the galaxies in the Type 2 quasar (Figures 4.4, 4.5, and 4.6), RI-HERG high (Figures 4.7, 4.8, and 4.9), and 3CR (Figures 4.10, 4.11, 4.12, 4.13, 4.14, 4.15, 4.16, and 4.17) samples are presented here, ordered by target name within each sample. These images are not included for the RI-HERG low sources for the sake of brevity, due to the fact that images for these targets have already been presented in Chapter 3 (Figures 3.1 and 3.2). Note that stamp images extracted from both observations of 3C 223 were uploaded to the interface for classification – this object is a member of both the 3CR and Type 2 quasar samples and was imaged as part of both sets of observations, as a result (see Chapter 2). The two sets of results obtained for this object were useful for investigating the effect of observing conditions and image quality on the classifications (Chapter 5, §5.4.1).

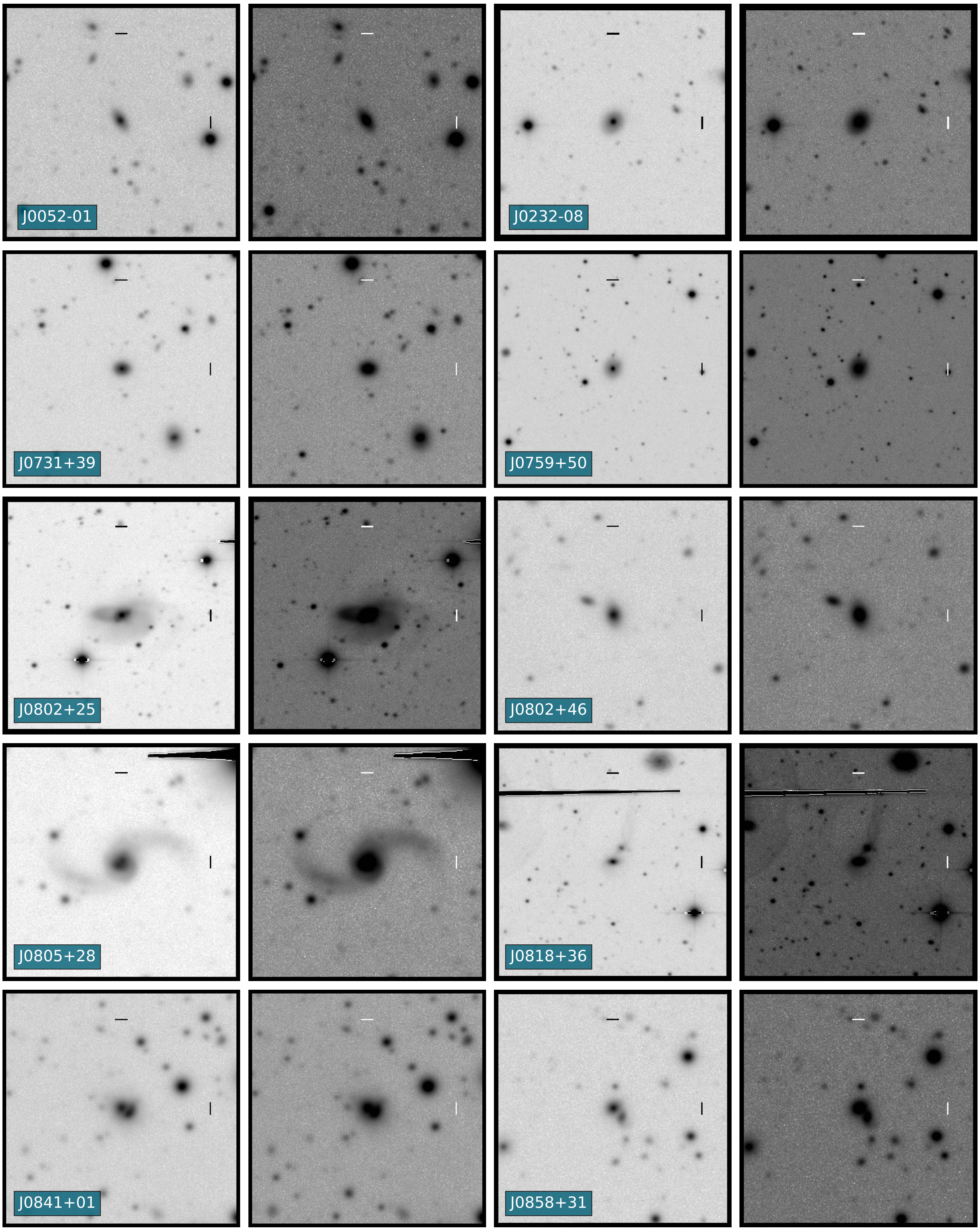

Figure 4.4: The high and low contrast images (left- and right-hand images for each target, respectively) used in the online classification interface for the first ten galaxies in the Type 2 quasar sample. All images were scaled to be of 200 kpc × 200 kpc at the redshift of the target, and 10 kpc scale bars were included at the top and right hand sides to assist with the classification process. The target names are included in the bottom-left of the high contrast images.

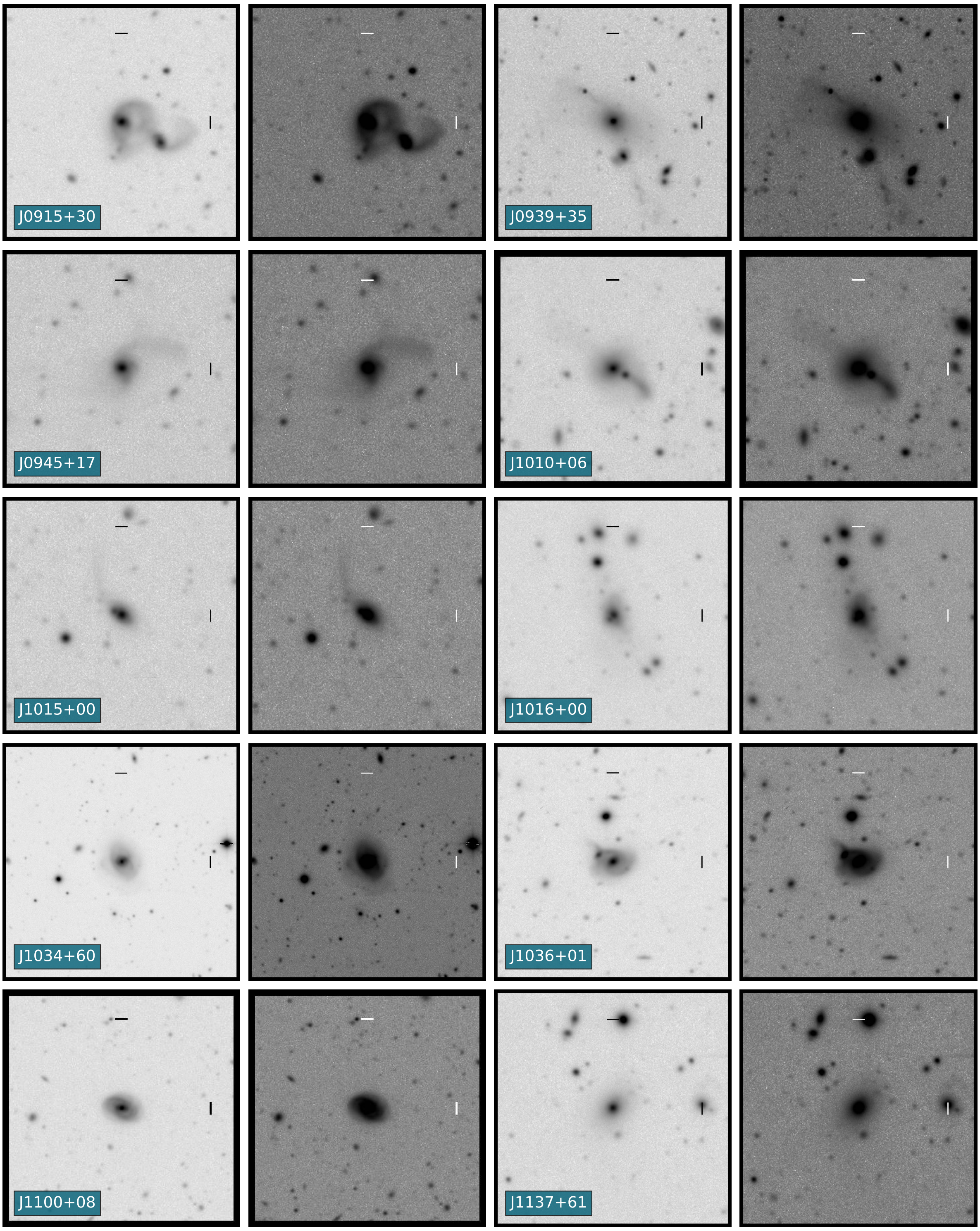

Figure 4.5: As Figure 4.4, but for the next ten galaxies in the Type 2 quasar sample.

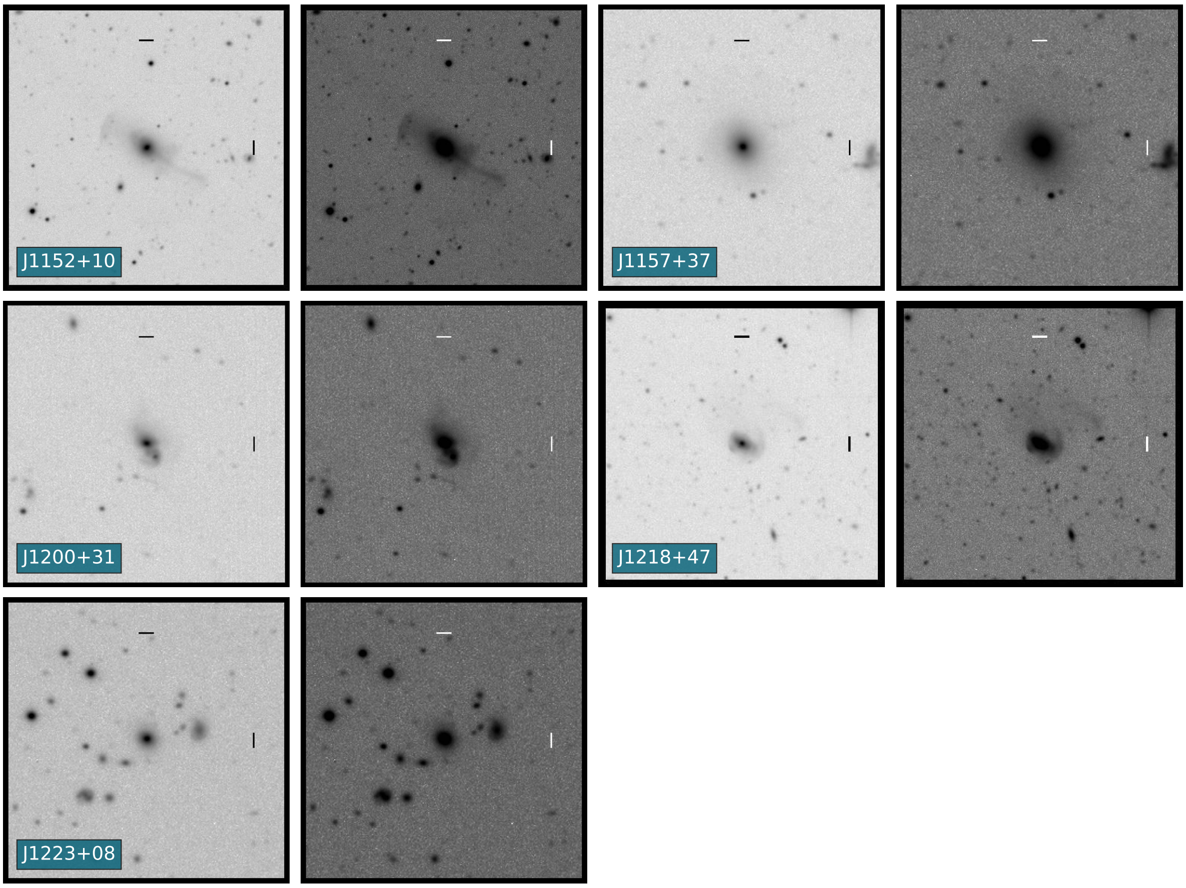

Figure 4.6: As Figure 4.4, but for the final five galaxies in the Type 2 quasar sample.

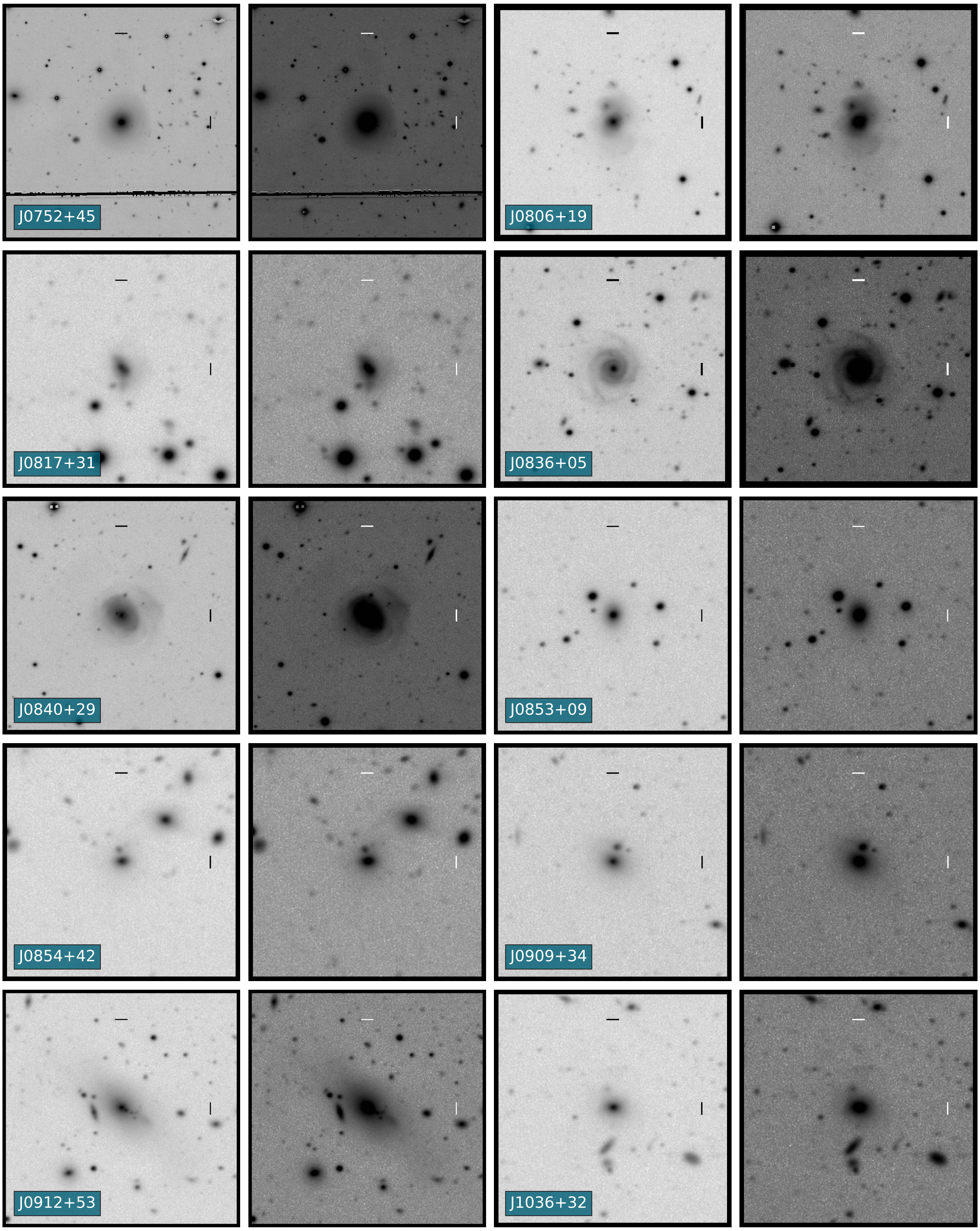

Figure 4.7: The high and low contrast images (left- and right-hand images for each target, respectively) used in the online classification interface for the first ten galaxies in the RI-HERG high sample. All images were scaled to be of 200 kpc × 200 kpc at the redshift of the target, and 10 kpc scale bars were included at the top and right hand sides to assist with the classification process. The target names are included in the bottom-left of the high contrast images.

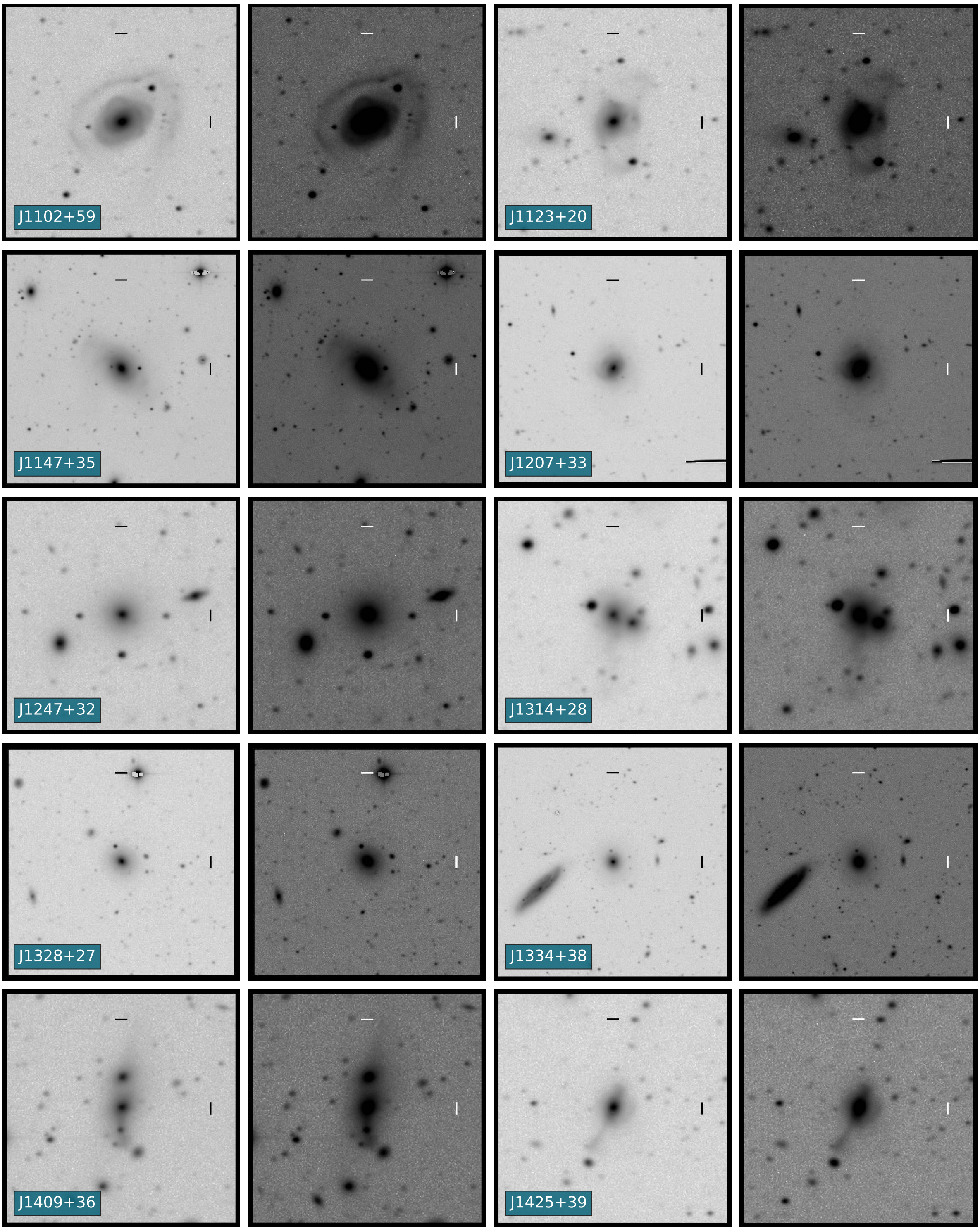

Figure 4.8: As Figure 4.7, but for the next ten galaxies in the RI-HERG high sample.

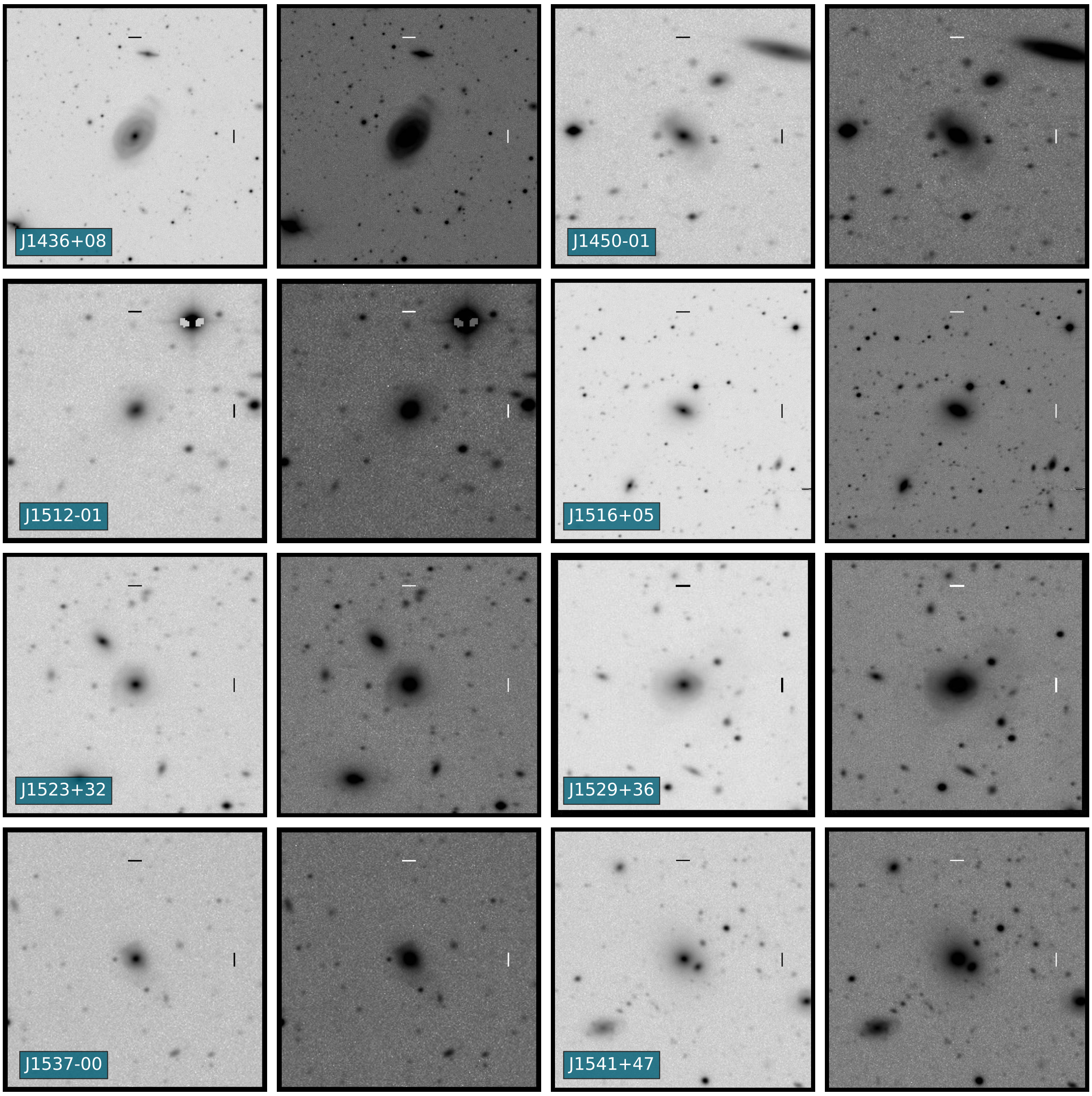

Figure 4.9: As Figure 4.7, but for the final eight galaxies in the RI-HERG high sample.

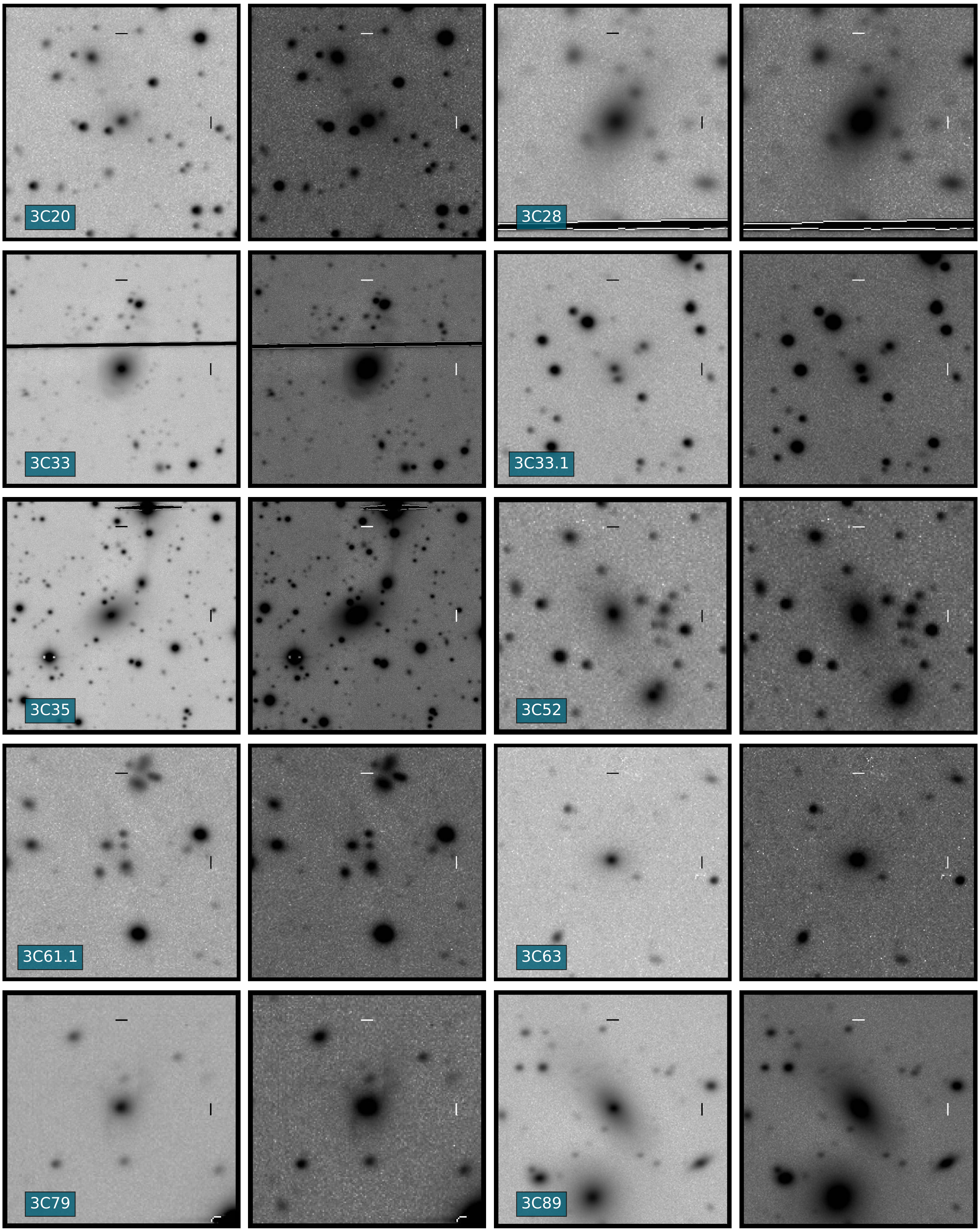

Figure 4.10: The high and low contrast images (left- and right-hand images for each target, respectively) used in the online classification interface for the first ten galaxies in the 3CR sample. All images were scaled to be of 200 kpc × 200 kpc at the redshift of the target, and 10 kpc scale bars were included at the top and right hand sides to assist with the classification process. The target names are included in the bottom-left of the high contrast images.

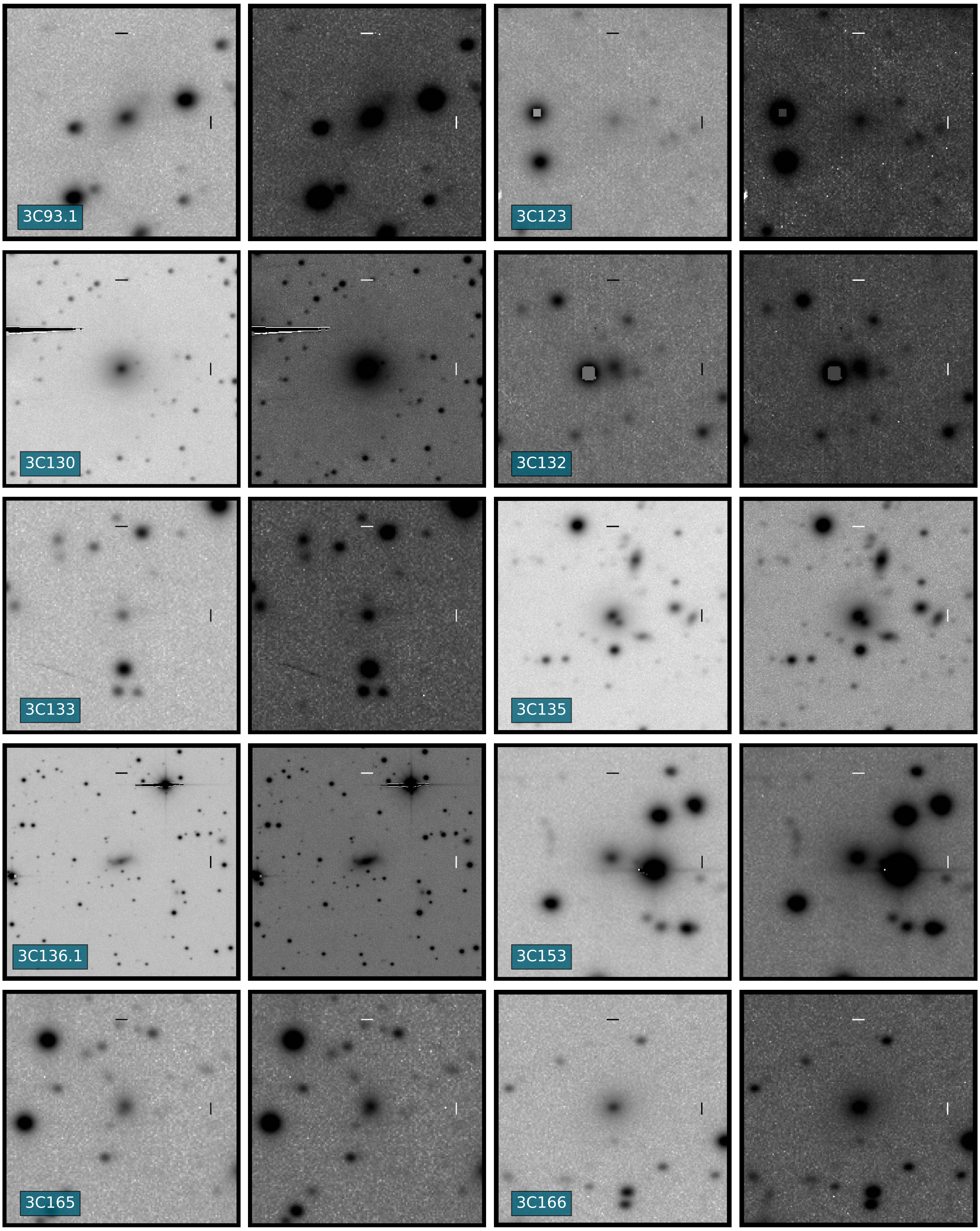

Figure 4.11: As Figure 4.10, but for the next ten galaxies in the 3CR sample.

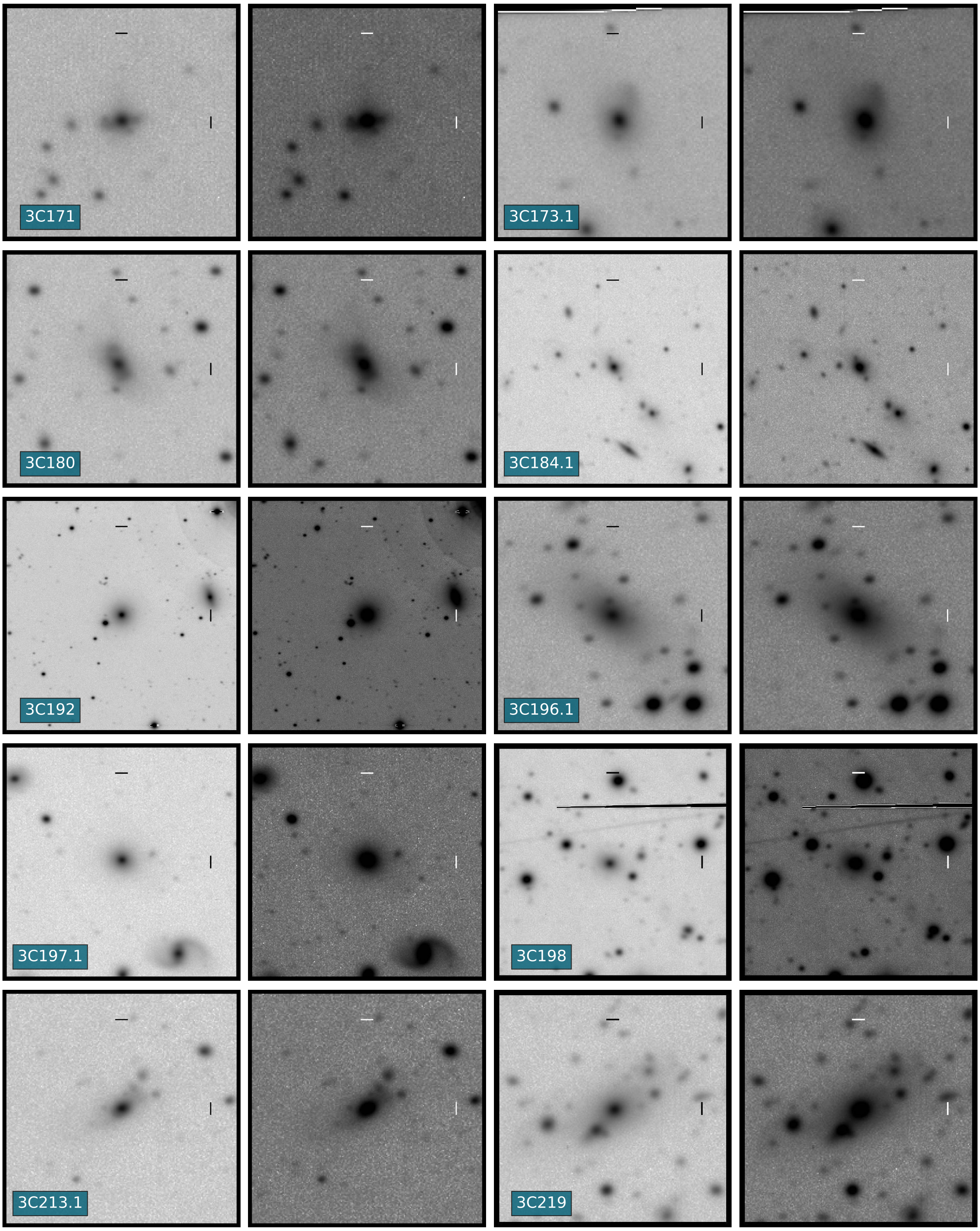

Figure 4.12: As Figure 4.10, but for the next ten galaxies in the 3CR sample.

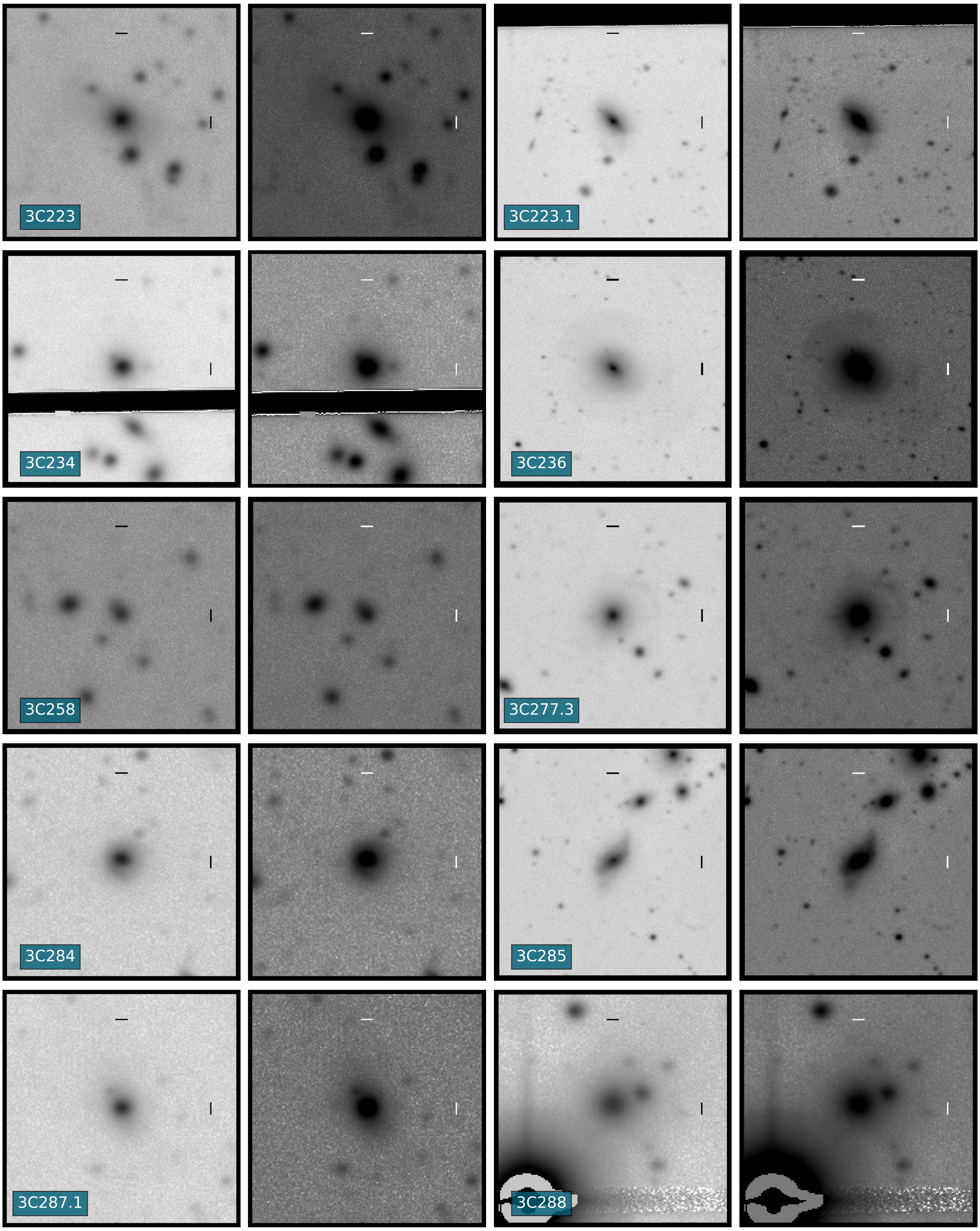

Figure 4.13: As Figure 4.10, but for the next ten galaxies in the 3CR sample.

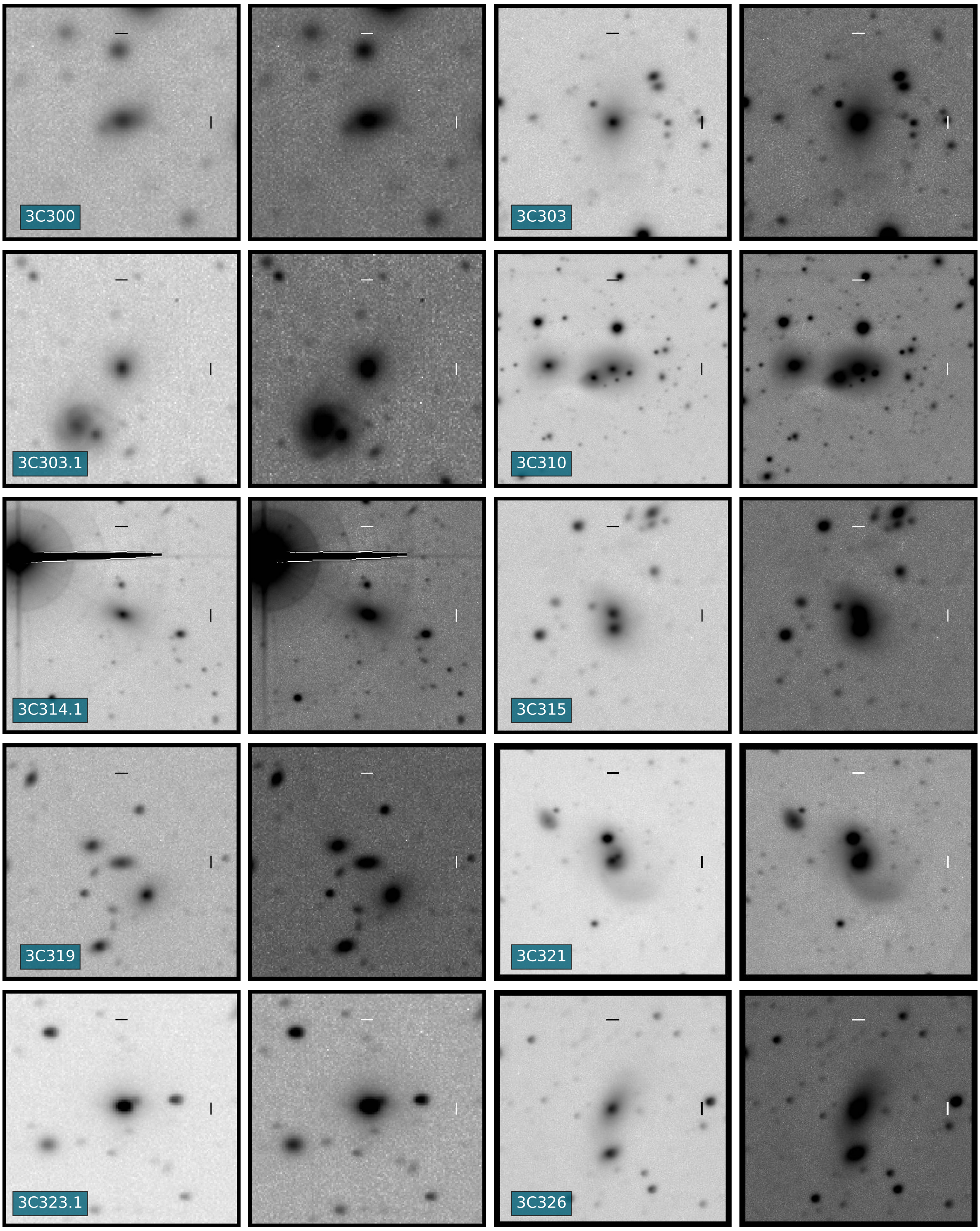

Figure 4.14: As Figure 4.10, but for the next ten galaxies in the 3CR sample.

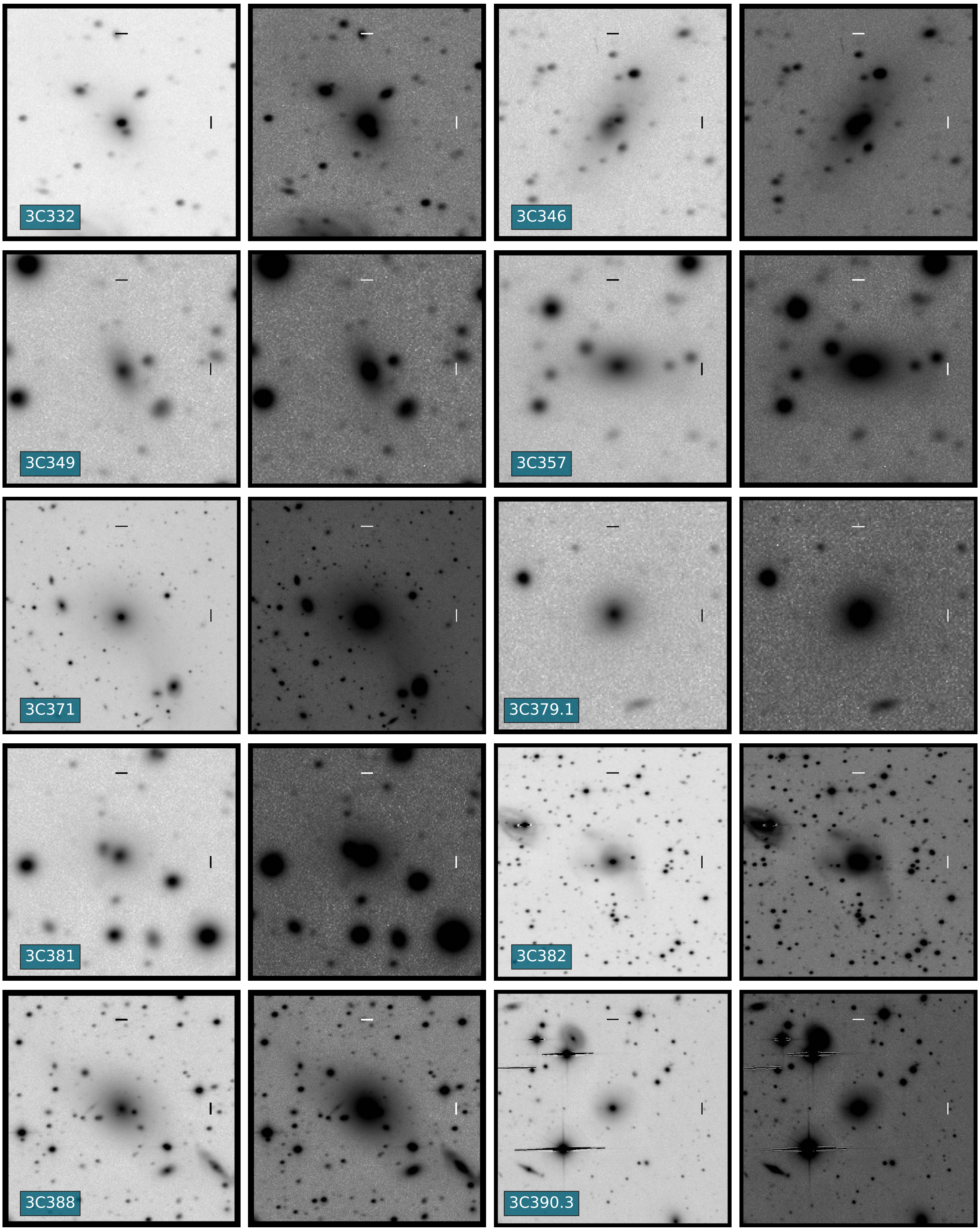

Figure 4.15: As Figure 4.10, but for the next ten galaxies in the 3CR sample.

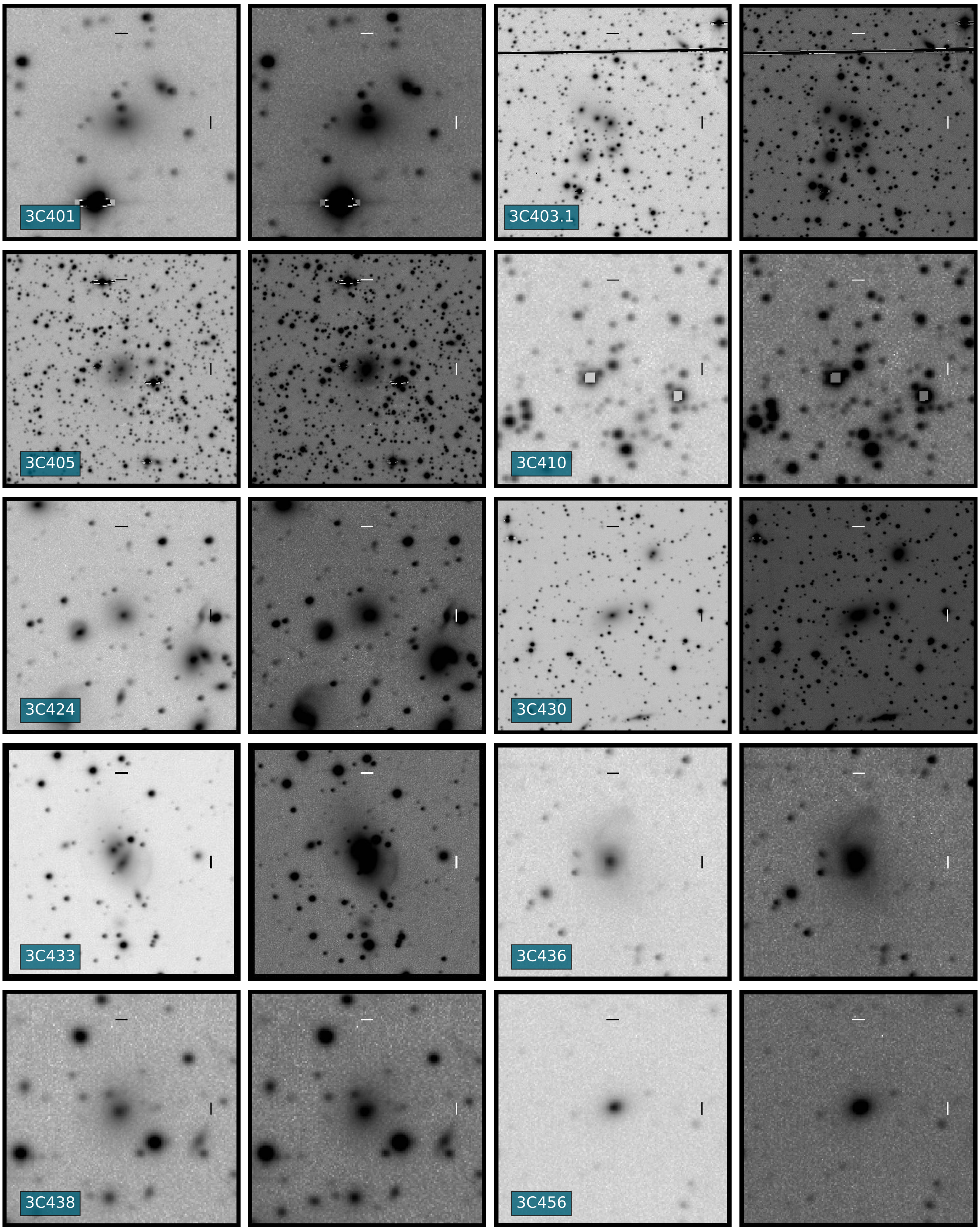

Figure 4.16: As Figure 4.10, but for the next ten galaxies in the 3CR sample.

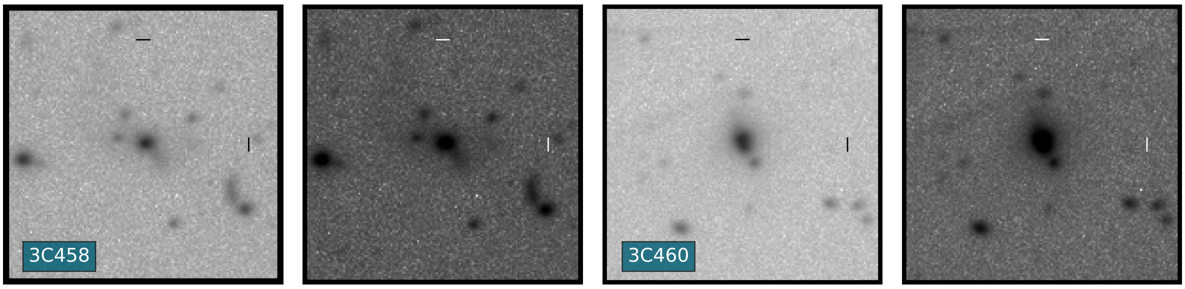

Figure 4.17: As Figure 4.10, but for the final two galaxies in the 3CR sample.

4.6 Chapter summary

The results of the detailed morphological analysis carried out for the galaxies in the RI-HERG low sample (Chapter 3) implied that the importance of merger-based triggering of their AGN may depend on its radio power and/or optical luminosity. The fraction of late-type hosts was also found to be much higher in this population, indicating a possible transition from the predominantly elliptical morphologies of powerful radio galaxies to the spiral- or disk-like morphologies often associated with low-radio-power Seyferts. In order to test these ideas in more detail, it was therefore necessary to expand this morphological analysis to a much larger sample of active galaxies encompassing a broad range of both radio power and optical emission line luminosity.

This chapter has described how, in this case, an online interface was instead used to obtain key morphological classifications of these active galaxies in a standardised and more time efficient manner. Through this interface, a very large sample of non-active control galaxies, matched to the targets in terms of both stellar mass and redshift, were also classified randomly alongside the active galaxies. Details on how this control galaxy sample was extracted from the MPA-JHU catalogue have also been provided. This included a description of the near-infrared mass-to-light ratio method used to derive stellar mass estimates for the active galaxies that did not have MPA-JHU values available.

Following the control matching and the collection of the morphological classifications through the online interface, the results for both the active galaxies and matched control galaxies were then analysed to investigate the relationships outlined above. The details of this analysis are presented in Chapter 5.

Chapter 5

The dependence of AGN host morphology on optical and radio luminosity – II. Rates of disturbance and host types

5.1 Declaration

The work described in this chapter is my own, except where explicitly stated. All analysis was performed by myself.

5.2 Chapter introduction

Use of the online interface described in Chapter 4 facilitated the fast collection of morphological classifications for the large number of active galaxies in the RI-HERG low, RI-HERG high, 3CR, and Type 2 quasar samples outlined in Chapter 2, which cover a broad range in both 1.4 GHz radio power and [OIII]λ5007 luminosity. This allows a test of the idea that both the typical host galaxy types and the importance of merger-based triggering of radiatively-efficient AGN may depend on radio power or optical emission line luminosity, as suggested by the results of the detailed morphological analysis of the galaxies in the RI-HERG low sample (Chapter 3). The inclusion of the 30 LERGs in the 3CR sample also means that the rate of mergers can be investigated for active galaxies with radiatively-inefficient AGN, and directly compared with the results for radiatively-efficient HERGs and Type 2 quasar hosts. The picture suggested by the radio-powerful 2Jy galaxies, in which mergers are much less important for the triggering of radiatively-inefficient AGN than radiatively-efficient AGN at high radio powers (Ramos Almeida et al., 2011, 2012, 2013), can therefore also be tested with these objects.

A large sample of non-active control galaxies from the MPA-JHU catalogue that lay within the fields of the INT/WFC images of the targets was also selected for classification using the interface, matched to the targets in terms of both stellar mass and redshift (as described in §4.4.2). Randomised and blind classification of these objects alongside the targets served the purpose of both reducing biases in the classifications and allowing for direct comparison between the active galaxies and matched non-active galaxies from the general population. The results for the active galaxies can then also be expressed relative to those obtained for the control galaxies, in order to reduce the influence of underlying galaxy properties on the measurements. This is important when comparing the classifications obtained for the different samples and when discussing them in the context of those found in the literature.

The interface method offered a significant improvement over the control comparisons performed for the previous more detailed studies of the morphologies of radio galaxies and the hosts of Type 2 quasars, for which a much smaller number of controls with images from different sets of observations were considered (Ramos Almeida et al., 2012; Bessiere et al., 2012). In the latter case, the galaxies were also classified with prior knowledge of the nature of the galaxy in question (i.e. whether it was an active or non-active control galaxy), potentially leading to biases in the results. Furthermore, the standardisation of the appearances and sizes of the interface images meant that the levels of individual classifier bias were also reduced relative to previous more detailed analysis, such as that performed for the RI-HERG low sample in Chapter 3.

In this chapter, the analysis of the classification results for the active galaxies and matched controls obtained through the online interface is presented, and discussed in the context outlined above. The chapter is structured as follows. The results relating to each of the morphological classification questions asked to classifiers in the interface are discussed in turn in §5.3, considering those obtained for both the active galaxies and their matched controls: rates of disturbance – §5.3.1; merger stage for disturbed galaxies – §5.3.2; the host galaxy types – §5.3.3. The complete results are then compared with those obtained from similar studies in the literature in §5.4, and discussed in the context of the triggering mechanisms (§5.4.2) and host galaxies (§5.4.3) for the various types of AGN considered. Prior to this discussion, the interpretation of the interface classifications is considered, through comparison with classifications obtained from more detailed analysis of the 3CR and RI-HERG low samples (§5.4.1). The results and conclusions of the study are then summarised in §5.5.

5.3 Analysis and results

Through the online interface, eight researchers provided morphological classifications for each of the 533 galaxies involved in the project: myself; Clive Tadhunter; Yjan Gordon; Sara Ellison; Cristina Ramos Almeida; Chris O'Dea; Liam Grimmett; and Lydia Makrygianni. These were obtained by collecting the researchers' responses to the three questions introduced in §4.3.2, which addressed the presence or absence of morphological disturbance, the specific types of interaction signatures visible (for disturbed galaxies), and the general morphological types of the galaxies, respectively. In the same manner as the morphological classification analysis performed for the RI-HERG low sample (described in Chapter 3, §3.3.1), each response selected by the classifiers was considered as a "vote" for that particular classification category. A classification was then only accepted when the number of votes it received exceeded a certain threshold, the value of which was dependent on the question considered.

In this section, the results related to each of the three classification questions are addressed in turn: the rates of general morphological disturbance found for each of the active galaxy and matched control samples are presented in §5.3.1; the results found for the specific interaction signature categories associated with disturbed galaxies are discussed in §5.3.2; and the morphological types are then addressed in §5.3.3. The classifications obtained for the individual active galaxies are presented and summarised in §5.3.4, although they are not discussed in detail in this thesis. The raw classification voting data for the active galaxies are presented in Appendix A.

Note that the results presented in this chapter were derived with the inclusion of the 3CR objects that do not currently have matched controls. These sources comprise a minority of the objects in the 3CR sample (13 out of 72; 18%) and a small minority of those in the full active galaxy sample (8%), and it is found that their inclusion does not have a significant effect on the results obtained and the conclusions drawn from them. However, while their properties are generally consistent with the other 3CR sources, their stellar masses are high, as noted in Chapter 4: in the range $11.3 \leq \log(\mathrm{M}_*/\mathrm{M}_\odot) \leq 12.7$, with a median of 11.8. The influence that this may have on the results is considered in §5.3.1 and §5.3.3.

5.3.1 The rates of morphological disturbance

The main goal of this second optical imaging project was to determine how the importance of galaxy mergers and interactions for triggering AGN varies with their radio powers and/or optical emission line luminosities. This topic was addressed by the first question asked to the classifiers in the online interface:

1) Does this galaxy show at least one clear interaction signature?

- Yes;
- No;
- Not classifiable (e.g. image defect, bad region/spike from saturated star).

This question was answered by all eight classifiers for every galaxy in the sample and only one of the listed responses could be selected when answering it. A threshold of 5 out of 8 votes was chosen as the lower limit for accepting a certain classification in all cases (i.e. a simple majority). In this instance, the goal was simply to test whether or not the classifier believed that the galaxy had been disturbed by a merger or interaction. Here, cases where 5 or more votes were recorded for “Yes” were taken to confirm that the galaxy was disturbed, and those where 5 or more votes were recorded for “No” were

Table 5.1: The proportions of galaxies classed as disturbed, not disturbed, and uncertain for all of the active galaxy and matched control samples classified using the online interface, as presented in Figure 5.1. The results for the 3CR HERG and LERG subsamples are included in separate columns, alongside those found for the full 3CR sample. Proportion uncertainties were estimated following the method of Cameron (2011).

		RI-HERG low	RI-HERG high	3CR (full)	3CR HERGs	3CR LERGs	Type 2 quasars
Disturbed	AGN	$37^{+9}_{-8}\,\%$	$57^{+9}_{-10}\,\%$	$53 \pm 6\,\%$	$66^{+7}_{-8}\,\%$	$37^{+9}_{-8}\,\%$	$64^{+8}_{-10}\,\%$
	Cont.	$24^{+4}_{-3}\,\%$	$35^{+5}_{-4}\,\%$	$27^{+3}_{-2}\,\%$	$27^{+4}_{-3}\,\%$	$26^{+4}_{-3}\,\%$	$26 \pm 4\,\%$
Not disturbed	AGN	$53 \pm 9\,\%$	$39^{+10}_{-8}\,\%$	$39^{+6}_{-5}\,\%$	$24^{+8}_{-5}\,\%$	$57^{+8}_{-9}\,\%$	$36^{+10}_{-8}\,\%$
	Cont.	$69^{+3}_{-4}\,\%$	$60^{+4}_{-5}\,\%$	$67 \pm 3\,\%$	$66^{+3}_{-4}\,\%$	$68 \pm 4\,\%$	$69 \pm 4\,\%$
Uncertain	AGN	$10^{+8}_{-3}\,\%$	$4^{+7}_{-1}\,\%$	$8^{+4}_{-2}\,\%$	$10^{+7}_{-3}\,\%$	$7^{+8}_{-2}\,\%$	$0^{+7}\,\%$
	Cont.	$7^{+3}_{-2}\,\%$	$6^{+3}_{-1}\,\%$	$7^{+2}_{-1}\,1\%$	$7^{+2}_{-1}\,\%$	$6^{+3}_{-1}\,\%$	$6^{+3}_{-1}\,\%$

taken to indicate that the galaxy was not disturbed. Any other distribution of votes (including any number for "Not classifiable") was considered as an uncertain case.

Initial proportions

Figure 5.1 shows the proportions of galaxies classed as disturbed, not disturbed, and uncertain for all samples classified using the online interface. The results for the active galaxy samples are presented alongside those for their corresponding matched control samples in all cases. The significance of the differences between the active galaxy samples and matched control samples is shown in each case, as estimated using the two-proportion Z-test. The proportions measured for each of the active galaxy and matched control samples are presented in Table 5.1.

From these results, it is seen that the AGN show a preference for disturbed galaxies relative to their matched controls in all cases, supported by the measured proportions for both the disturbed and not disturbed categories. Across the radio AGN samples, the degree of significance for these differences appears to decrease with radio power. The Type 2 quasars, however, also show a significant preference for disturbed morphologies relative to their matched controls ($3.7\,\sigma$), suggesting that the optical emission line luminosity could also be important in this context. In-depth analysis of the relationships with radio power and optical emission line luminosity is included in the following subsection.

Previous study of the powerful radio galaxies in the 2Jy sample suggests that the hosts of radiatively-efficient radio AGN (SLRGs) are typically more likely to be merging/interacting than those of radiatively-inefficient radio AGN (WLRGs; Ramos Almeida

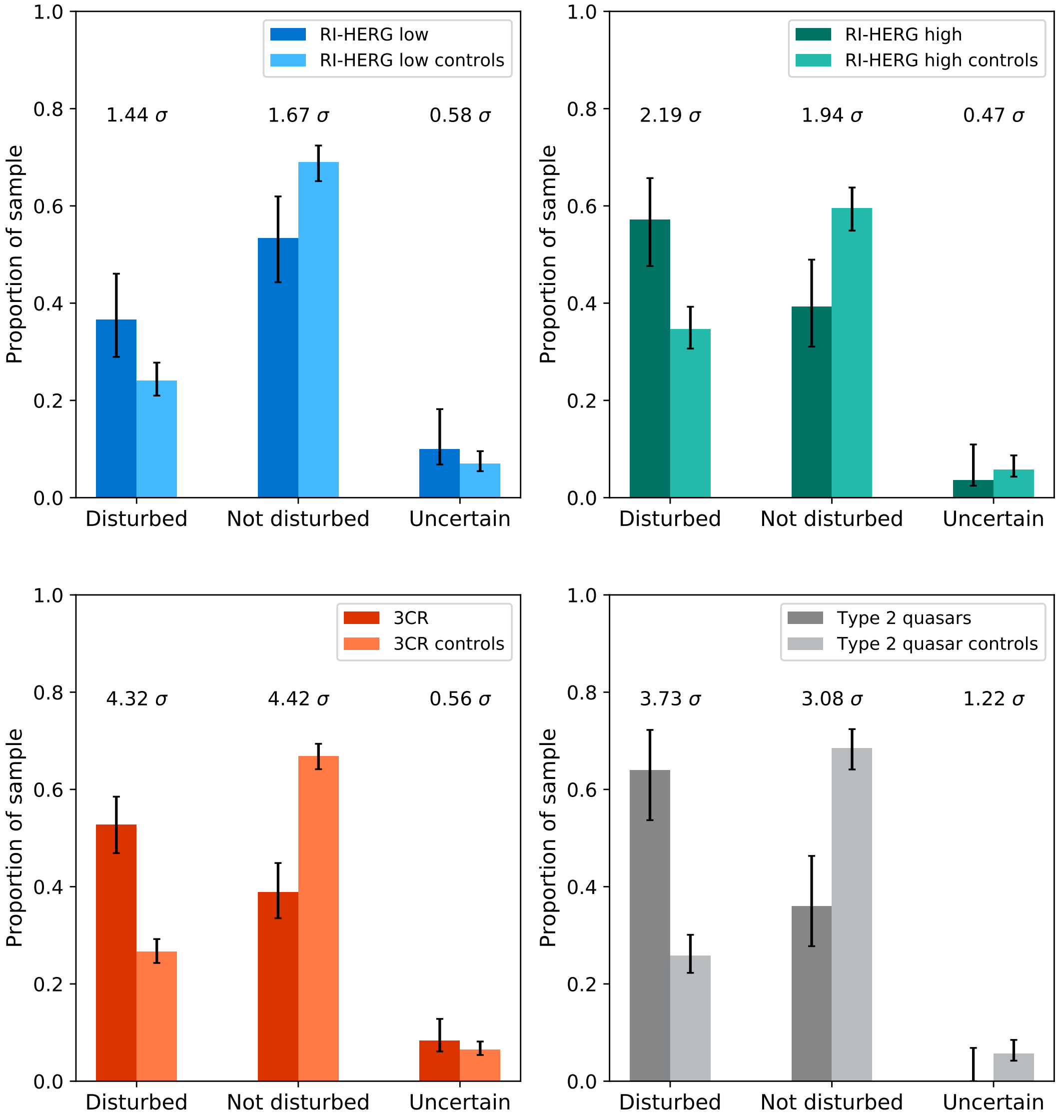

Figure 5.1: The proportions of galaxies classed as disturbed, not disturbed, or uncertain for each of the samples classified using the online interface. The results for the active galaxy samples are presented alongside those for their respective matched control samples, with the significance of the difference between the measured proportions for each category indicated in all cases (from two-proportion Z-tests). The exact proportions are presented in Table 5.1.

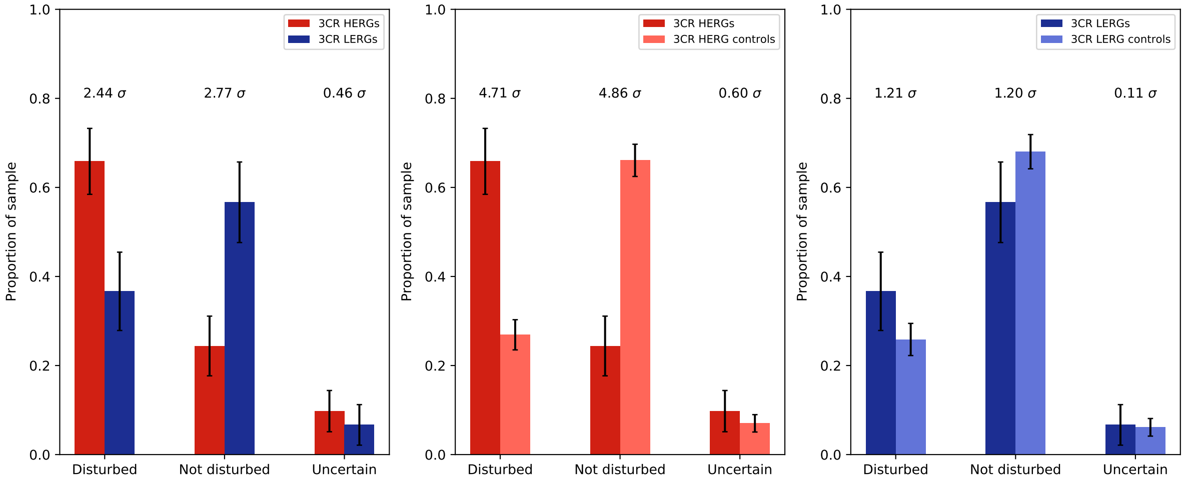

Figure 5.2: As Figure 5.1, but for the HERGs and LERGs in the 3CR sample. In this case, the results for the two samples are presented both alongside each other (first panel) and with those for their respective matched control samples (second and third panels).

et al., 2011, 2012, 2013). In terms of their rates of disturbance, Ramos Almeida et al. (2011) found that 94^{+4}_{-7} % of the SLRGs and 27^{+16}_{-9} % of the WLRGs in the sample showed clear signatures of mergers and interactions, which differ at the 4.7 σ level according to a two-proportion Z-test. The inclusion of both HERGs and LERGs in the 3CR sample allows this picture to be tested with a larger sample.

Figure 5.2 again shows the measured proportions for the disturbed, not disturbed, and uncertain categories outlined above, but in this case comparing the results for the 3CR HERG and LERG subsamples and their respective matched control samples (the proportions measured for these samples are also listed in Table 5.1). These measurements appear to support the picture suggested by the 2Jy results, with HERGs showing an increased preference for disturbed morphologies both relative to their matched controls and to the LERGs. There is also evidence to suggest that the large difference between the disturbance rates for the 3CR sources and their matched control samples (seen in Figure 5.1) is predominantly driven by the HERGs, with the HERG proportions showing $\sim$5 σ differences with respect to those of their matched controls and the LERG proportions only exhibiting $\sim$1 σ differences. However, the significance of the difference between the HERG and LERG proportions is much lower than that found between the 2Jy SLRGs and WLRGs, with a two-proportion Z-test suggesting that the null hypothesis of them being the same can only be rejected at the 2.4 σ level. One caveat with this comparison is that, as mentioned in previous chapters, the SLRG/WLRG and HERG/LERG classification schemes are not equivalent. The 2Jy classifications were also obtained through more detailed morphological analysis based on higher quality imaging observations. The effects of these factors on this comparison are discussed in more detail in §5.4.2.

Given that the proportions of galaxies in each sample that were classified as uncertain were small, the trends in the results found for the disturbed galaxies are largely consistent with the opposite trends found for those classified as not disturbed, as can be seen in Figures 5.1 and 5.2. Therefore, only the galaxies securely classified as disturbed (i.e. above the 5-vote threshold) are considered for the remainder of the analysis in this subsection.

Relationship with radio power and optical emission line luminosity

The detailed morphological analysis of the galaxies in the RI-HERG sample presented in Chapter 3 suggested that the association between AGN and merging galaxies could be strongly dependent on radio power and more weakly dependent on optical emission line luminosity. The significant excesses in the proportions of disturbed galaxies in the 3CR and Type 2 quasar samples, both relative to their respective matched control samples and to the RI-HERG samples, suggest that both properties could be important, but do not provide clear evidence as to which is the main driver of the trend. Further analysis is therefore necessary to investigate these relationships in more detail.

The 1.4 GHz radio powers and [OIII]λ5007 emission line luminosities for all of the active galaxies studied for the project are plotted in Figure 5.3, which also shows whether the participants classified their morphologies as disturbed, not disturbed or uncertain using the online interface. Upper limits are shown for the objects that did not have 1.4 GHz or [OIII]λ5007 detections (points with arrows). The marker sizes for galaxies classed as disturbed or not disturbed are scaled to represent the number of votes that were recorded for the category, ranging from the 5-vote acceptance threshold (smallest) to the maximum of 8 votes (largest), and therefore provide an indication of the certainty of the classifications in each case. Demarcations between the radio-loud, radio-intermediate, and radio-quiet regimes, as well as between quasar-like and optically-fainter AGN, are also included. The individual samples are not indicated, but almost exactly correspond to the following: 3CR = radio-loud AGN/radio-loud Type 2 quasars; RI-HERG high and low = radio-intermediate AGN (separation at $L_{1.4\mathrm{GHz}} = 10^{24}$ W Hz^{-1}); Type 2 quasar = radio-intermediate/radio-quiet Type 2 quasars. Note that the classification based on the higher-quality image of 3C 223 from the Type 2 quasar observations was used for

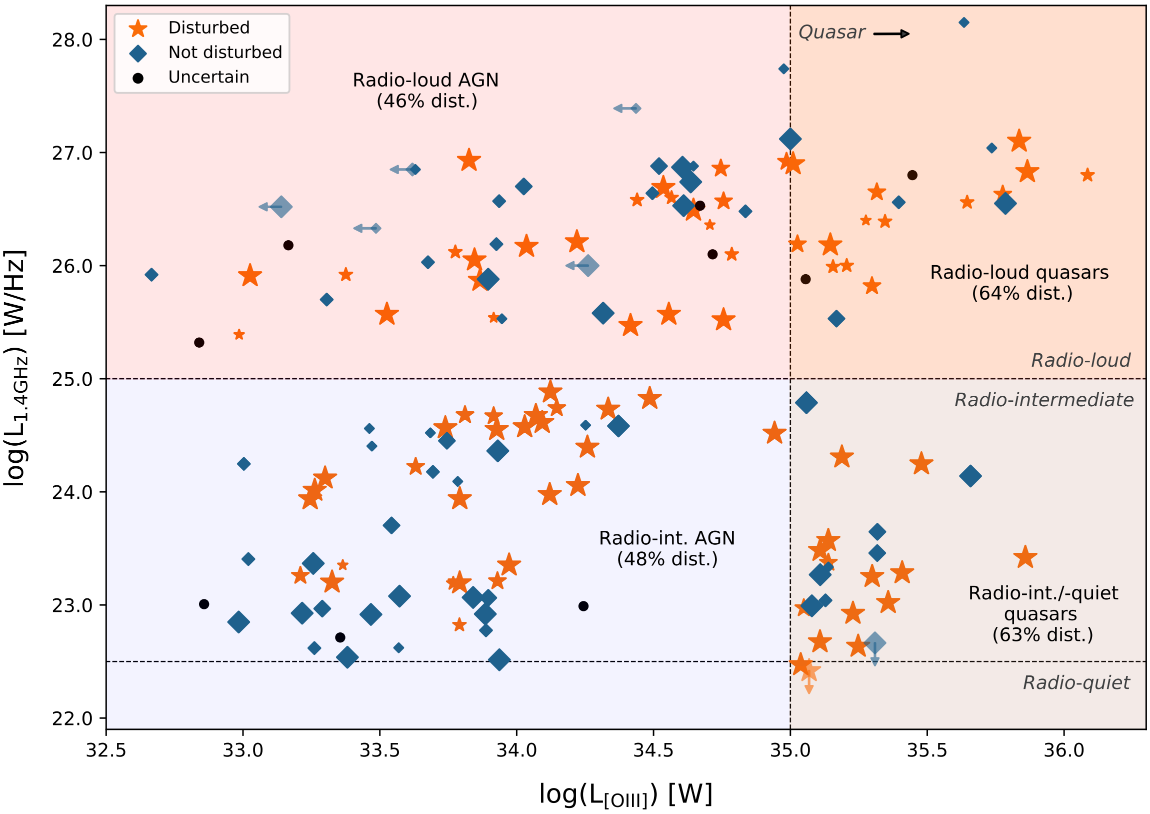

Figure 5.3: The 1.4 GHz radio powers and [OIII]λ5007 emission line luminosities for all active galaxies classified using the online interface, plotted with markers that indicate whether they were classed as disturbed (orange stars), not disturbed (blue diamonds), or uncertain (black dots). The marker sizes for the disturbed and not disturbed objects are scaled to indicate the number of votes the categories received, increasing in size from 5 votes (smallest; the threshold for acceptance) to 8 votes (largest; the maximum possible number). Galaxies classified as uncertain did not meet the 5-vote threshold for either of these two classifications, and have uniformly sized markers. Fainter points with arrows attached represent upper limits on the radio powers (vertical) and [OIII]λ5007 luminosities (horizontal). The dividing lines between radio-loud ($L_{1.4GHz} \geq 10^{25}$ W Hz^{-1}), radio-intermediate ($10^{22.5} < L_{1.4GHz} < 10^{25}$ W Hz^{-1}), and radio-quiet ($L_{1.4GHz} \leq 10^{22.5}$ W Hz^{-1}) regimes, and between quasar-like ($L_{[OIII]} \geq 10^{35}$ W) and optically-fainter AGN, are also indicated. The percentages of disturbed galaxies in the four key regions of the plot are presented (including objects with upper limits).

this figure, since the result was more decisive[1].

As shown in the figure, the proportions of disturbed galaxies in the four key regions of the plot are as follows: 46 ± 7 % of the radio-loud AGN; $64\,^{+9}_{-11}$ % of the radio-loud quasar-like AGN; $48\,^{+7}_{-6}$ % of the radio-intermediate AGN; and $63\,^{+9}_{-11}$ % of the radio-intermediate/radio-quiet Type 2 quasars. From these values, it is seen that the disturbance rates for both the radio-loud and radio-intermediate/radio-quiet Type 2 quasar regions are higher than those found for the corresponding optically-fainter regions in both radio power regimes, which provides an initial suggestion that AGN with quasar-like [OIII]λ5007 luminosities could be more strongly linked with disturbed host galaxies. The difference is not significant, however, with two-proportion Z-tests indicating that the null hypothesis that the proportions in the Type 2 quasar and corresponding optically-fainter regions are the same can only be rejected at confidence levels of 83.2 % ($1.4\,\sigma$) and 75.9 % ($1.2\,\sigma$) for the radio-loud and radio-intermediate regimes, respectively. Combining the results for Type 2 quasars and optically-fainter AGN at all radio powers suggests a slightly more significant difference, with the Z-test indicating that the null hypothesis that the proportions for the two classes are the same can be rejected at the 92.8 % confidence level ($1.8\,\sigma$). In contrast, performing the same tests for radio-loud and radio-intermediate AGN across all optical emission line luminosities suggests that the proportions for the two classes differ at a confidence level of 10.4 % ($0.13\,\sigma$). These results therefore provide some evidence that mergers and interactions are more important for triggering AGN with quasar-like optical emission line luminosities than those with weaker emission lines, across all radio powers.

The picture suggested by these results is, however, complicated by the fact that there could be some underlying co-dependence between the AGN 1.4 GHz radio powers and [OIII]λ5007 luminosities. Pearson correlation tests[2] suggest that there is a moderate but significant positive correlation between the two parameters in the RI-HERG high and 3CR samples ($r = 0.517$, $p = 0.005$ and $r = 0.533$, $p < 10^{-5}$, respectively) but that they are not significantly correlated in the RI-HERG low and Type 2 quasar samples ($r = 0.077$, $p = 0.648$ and $r = 0.118$, $p = 0.591$, respectively). This is consistent with the findings of previous studies, where it is seen that the optical emission line luminosity and radio power are strongly correlated for powerful radio AGN but more weakly for those with lower radio powers (e.g. Rawlings & Saunders, 1991; Zirbel & Baum, 1995;

---

[1] This object is part of both the 3CR and Type 2 quasar samples and was observed twice (see Chapter 2), although in very different seeing conditions: seeing FWHM values of 2.23 arcsec and 0.95 arcsec, respectively. Stamp images from both observations were uploaded for classification (Chapter 4).

[2] Note that active galaxies with upper limits on either their 1.4 GHz radio powers or [OIII]λ5007 luminosities were not considered for the correlation tests.

Best et al., 2005b). A significant but weaker positive correlation is also found when considering all of the active galaxy samples combined ($r = 0.315$, $p < 10^{-4}$), although this is driven by the stronger correlations seen for the RI-HERG high and 3CR sources, which represent the majority of the total objects (100 out of 155).

Another caveat of the above proportion comparisons is that they include the radiatively-inefficient LERGs in the 3CR sample, for which triggering of the nuclear activity by mergers and interactions is thought to be less important (as mentioned in §5.3.1). In order to investigate the relationship between disturbed galaxies and radio power or optical emission line luminosity in more detail, both with and without the inclusion of the LERGs, the proportions of disturbed active galaxies across the full ranges of 1.4 GHz radio power and [OIII]λ5007 luminosity covered by the samples were analysed. Figure 5.4 shows the proportions of galaxies classified as disturbed in bins of 1.4 GHz radio power and [OIII]λ5007 luminosity for all of the active galaxies considered for the project. These proportions are also expressed as "enhancements" relative to those measured for their matched controls, i.e. the ratios of the fractions of disturbed active galaxies in each bin to those found for the corresponding matched control galaxies ($f_{\mathrm{AGN}}/f_{\mathrm{cont}}$). The distributions for all active galaxies (including LERGs) and for all HERGs and Type 2 quasars are presented separately.

The distributions with 1.4 GHz radio power for both the disturbed proportions and their enhancements relative to the matched controls are not significantly different for the full active galaxy sample and for the HERGs and Type 2 quasar objects across the full range of radio powers covered. Both are consistent with a general increase in the rates of disturbance in the two lower-radio-power bins – note that the proportions are actually identical for the two samples in these regions, since only HERGs and Type 2 quasar objects are found at these radio powers – but the differences between the proportions in the two bins are not highly significant (at the $1.5\,\sigma$ level), and this trend is not seen when the enhancement ratios are considered. There are suggestions that the disturbance rate for the HERG/Type 2 quasar subsample is higher than that of the full active galaxy sample in the two higher-radio-power bins, but these are again not significant when considering either the disturbed proportions or the enhancements. However, in the third radio power bin ($25.31 \leq \log(\mathrm{L}_{1.4\mathrm{GHz}}) \leq 26.73\ \mathrm{W\,Hz^{-1}}$), the enhancement ratios for both the full active galaxy sample and the HERG/Type 2 quasar subset show $\sim 3\,\sigma$ excesses above equality between the active galaxy and control galaxy disturbance rates.

As found for the distributions with radio power, the disturbed proportions for the full active galaxy sample and the HERGs/Type 2 quasars are consistent over the full

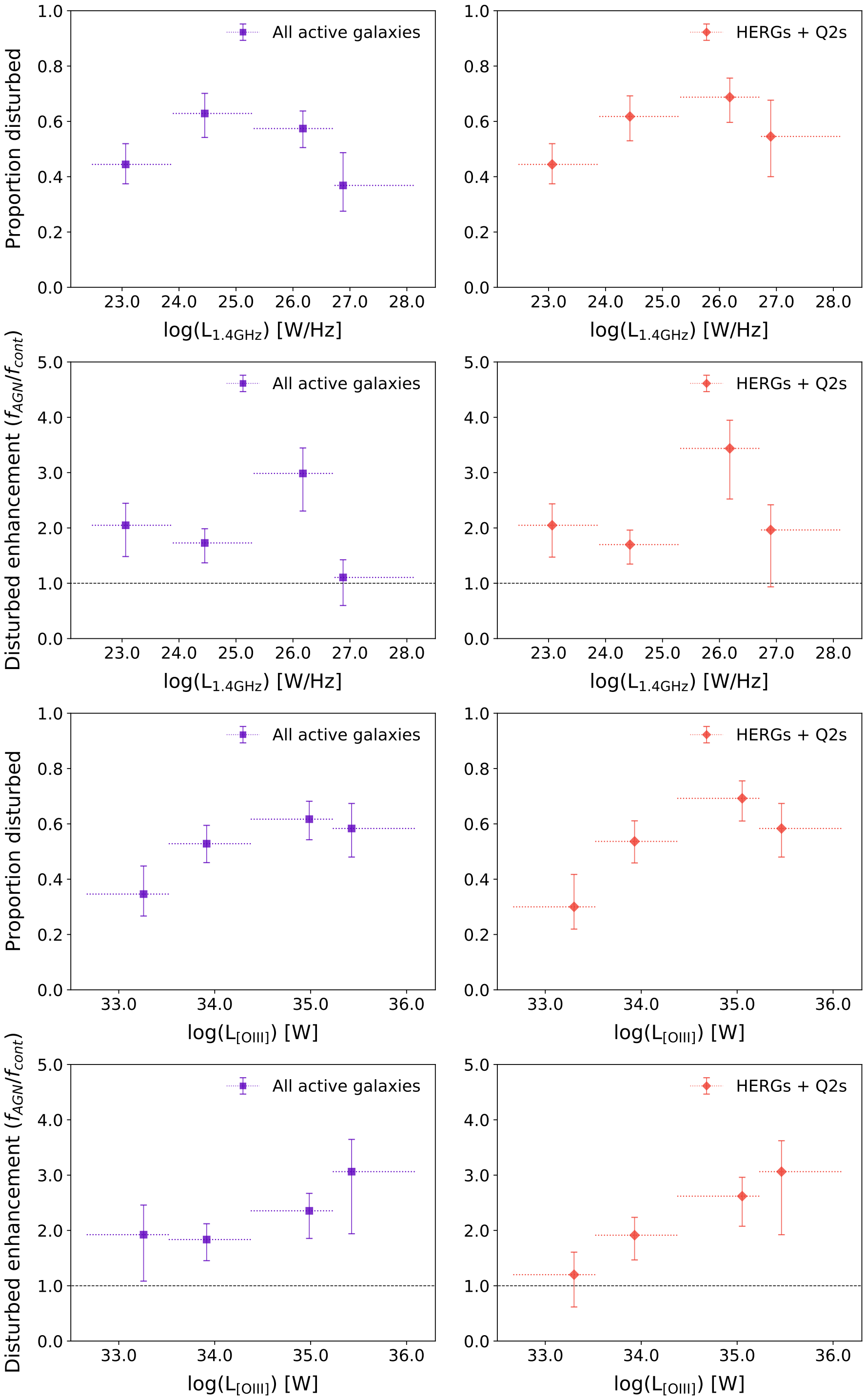

Figure 5.4: The disturbed proportions and enhancement ratios ($f_{\rm AGN}/f_{\rm cont}$) in bins of logarithmic 1.4 GHz radio power and [OIII]λ5007 emission line luminosity for all active galaxies (left column) and for all HERGs and Type 2 quasars (right column) classified using the online interface. In all cases, the markers represent the median values for the active galaxies in each bin, the ranges of which are indicated by the dotted lines. A line representing equality between the proportions measured for active galaxies and their matched control galaxies is shown on the enhancement plots.

range of [OIII]λ5007 luminosity covered. Suggestions of a general increase towards higher luminosities is seen, but again is of low significance. In this case, however, a positive, seemingly linear trend is observed in the disturbed enhancement ratio distribution for the HERGs/Type 2 quasar objects with [OIII]λ5007 luminosity. A Pearson correlation test provides evidence for a strong positive correlation between the disturbed enhancement ratios and the median [OIII]λ5007 luminosities for the binned HERG/Type 2 quasar data, significant at the 97.2% level: $r_{\rm HERG} = 0.972$, $p_{\rm HERG} = 0.028$. Bootstrapping analysis shows that the strength of this correlation, as characterised by the Pearson r-statistic, is not sensitive to the uncertainties in the measured enhancements, with the derived r values showing little spread around those determined from the initial test: $r_{\rm HERG} = 0.972^{+0.012}_{-0.053}$ (one-σ confidence interval). The same trend is not seen clearly in the corresponding plot for the full active galaxy sample, and a Pearson correlation test in this case indicates that there is not a significant correlation: $r_{\rm full} = 0.772$, $p_{\rm full} = 0.228$. The correlation is therefore much stronger when the LERGs are excluded, and only the HERGs and Type 2 quasar hosts are considered. This suggests that mergers and interactions become increasingly important for triggering radiatively-efficient AGN towards higher optical emission line luminosities, but that this relationship is not likely to apply to radiatively-inefficient AGN.

Overall, these results provide evidence that the importance of galaxy mergers and interactions for triggering radiatively-efficient AGN is strongly dependent on [OIII]λ5007 emission line luminosity, but not strongly dependent on 1.4 GHz radio power, in contrast with the results from the more detailed analysis of the RI-HERG low sample (Chapter 3). The observed difference between the distributions of the proportions of disturbed active galaxies and their enhancement ratios also serves to highlight the importance of the control matching process. Further discussion on these matters is reserved for §5.4.

Relationship with stellar mass and redshift

In addition to the relationship with the radio powers and optical emission line luminosities of the active galaxies, it is interesting to determine how the rates of disturbance relate to the galaxy stellar masses and redshifts. Investigation of the relationship with stellar mass was also important for ensuring that the particularly large stellar masses of the unmatched objects in the 3CR sample did not strongly affect the results outlined in the previous subsections. Figure 5.5 shows the distributions in disturbed proportions for the active galaxies and matched control galaxies with both stellar mass and redshift – note that 3C 130 was not considered for the former plot due to its abnormally large stellar mass relative to those for all other galaxies in the project ($\log(M_*/M_\odot) = 12.7$). The distributions with stellar mass for the matched active galaxies and the full active galaxy sample are shown separately, to illustrate the effect of including the unmatched 3CR objects. The distributions with redshift for these two samples are very similar, and so only the results for the full active galaxy sample are shown, for clarity.

From the figure, it is seen that the active galaxies were consistently classified as disturbed more frequently than the matched controls across the full range of stellar mass and redshift. The exceptions to this rule are the lowest bin in stellar mass, for both the full active galaxy sample and its matched subset, and the highest stellar mass bin, for the matched active galaxy distribution only. This confirms the result that the active galaxies are in general more frequently disturbed, as originally indicated by the proportions presented in Table 5.1 and Figure 5.1. No clear trend is visible with redshift for either the active galaxies or matched controls, although there is a highly significant excess in the disturbed fraction for the active galaxies with $0.08 \lesssim z \lesssim 0.14$ ($4.6\,\sigma$). This is most likely caused by the high rates of disturbance found for the RI-HERG high and Type 2 quasar samples, the median redshifts of which both lie within this bin ($z = 0.110$ and $z = 0.111$, respectively). On the other hand, a positive trend with stellar mass is seen for both the active galaxies and the matched control galaxies. This is steeper for the active galaxies, and therefore the significance of the excess in the disturbed proportions relative to the matched controls is seen to increase with stellar mass in this range – $5.0\,\sigma$ and $4.3\,\sigma$ in the third and fourth bins, respectively, when considering the full active galaxy sample.

Overall, there is little or no difference between the disturbed proportion distributions with stellar mass for the full active galaxy sample and for the subset with matched controls, with the exception of the highest mass bin ($11.78 < \log(M_*/M_\odot) < 12.25$). In this range, there are only two matched active galaxies (3C 52 and 3C 438) and two controls, all four of which were classified as not disturbed. The number of active galaxies in the mass bin increases to 7 when the unmatched sources are included, 3 of which were classified as disturbed ($43\,^{+18}_{-15}\,\%$). This proportion reduces to $38\,^{+18}_{-13}\,\%$ if 3C 130 ($\log(M_*/M_\odot) = 12.7$) is also considered (not shown on the plot due to its unusually large stellar mass). However, it is found that the unmatched objects do not have typically larger stellar masses than the two matched active galaxies in this stellar mass range, with the values for these latter two objects lying either side of the median value for the unmatched objects. Although the galaxy numbers are small, this is consistent with the idea that the apparent discrepancy in the proportions is not caused by a relationship

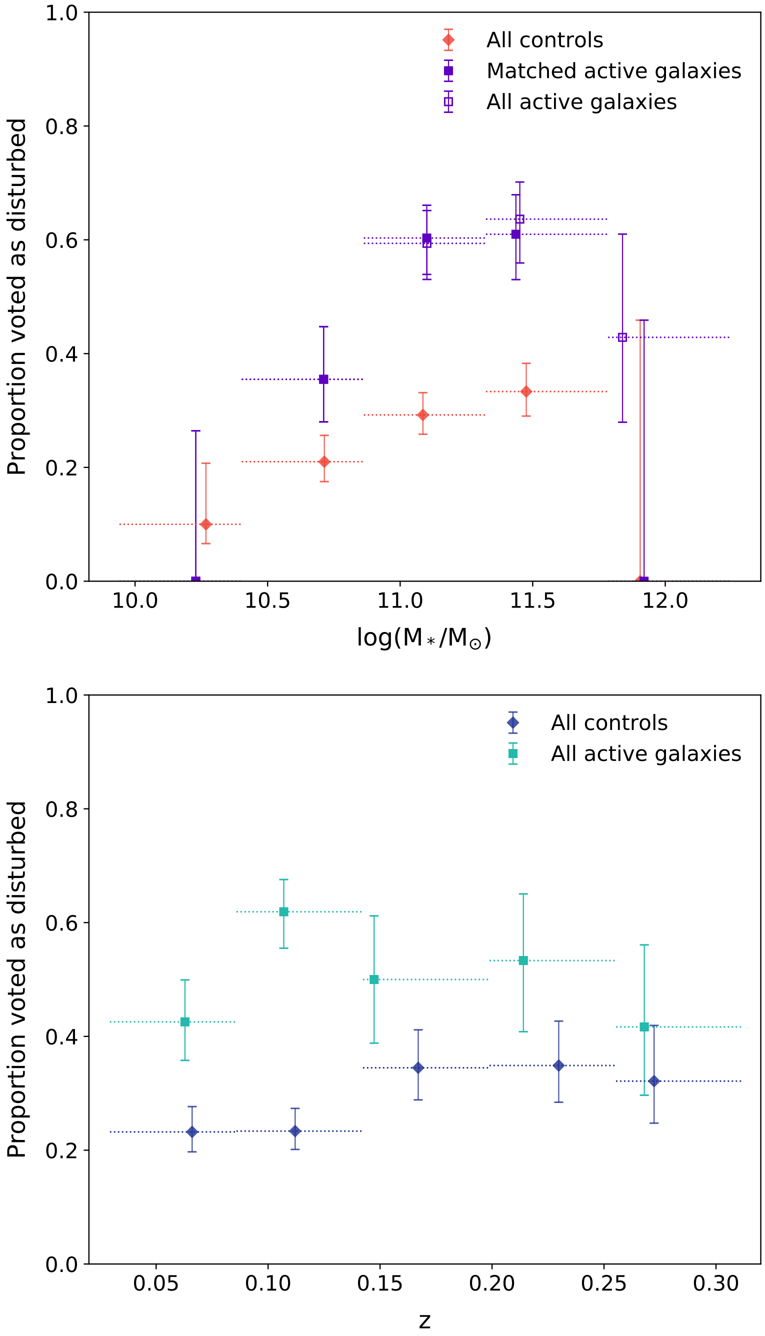

Figure 5.5: The proportions of active galaxies and matched control galaxies classified as disturbed in bins of stellar mass and redshift. The proportions are plotted at the median stellar masses and redshifts of the active galaxies and control galaxies in each bin. For the plot against stellar mass, the results for the full active galaxy sample (unfilled points, including the unmatched 3CR sources) and for the active galaxies with control matches (filled points) are shown separately. The distributions with redshift for the full active galaxy sample and matched subset are consistent, and so only the results for the full active galaxy sample are shown for this plot, for clarity.

with stellar mass.

On the other hand, it is found that all 3 of the disturbed active galaxies with stellar masses above $\log(\mathrm{M}_*/\mathrm{M}_\odot) > 11.8$ are HERGs (3 out of 5; $60^{+16}_{-22}\,\%$), while all 3 of the LERGs with stellar masses above this value were classed as not disturbed. This is consistent with the significantly higher rates of disturbance found for the HERGs in the full 3CR sample relative to their matched controls and to the 3CR LERGs (§5.3.1), and indicates that this relationship is preserved at the highest stellar masses. In combination, these factors therefore suggest that the apparent discrepancy between the proportions for the full active galaxy sample and its matched subset is more likely caused by the higher proportion of LERGs in the highest mass bin, and not by the stellar mass of the host galaxy. This suggests that the inclusion of the higher stellar mass objects without matched controls should not have a significant influence on the derived rates of disturbance, although further classifications of suitable matched control galaxies are needed to put this on a firmer footing.

5.3.2 Interaction signatures and merger stage

The second question in the online interface asked the researchers to identify the specific types of interaction signature that they had seen in the galaxy images, with the goal of better characterising the types and stages of the mergers and interactions identified:

2) What types of interaction signature are visible?

- Tail (T);
- Fan (F);
- Shell (S);
- Bridge (B);
- Amorphous halo (A);
- Irregular (I);
- Multiple nuclei (2N, 3N...);
- Dust lane (D);
- Tidally interacting companion (TIC).

This question was only answered in cases where classifiers had already indicated that clear interaction signatures were visible in the galaxy images by responding “Yes” to the

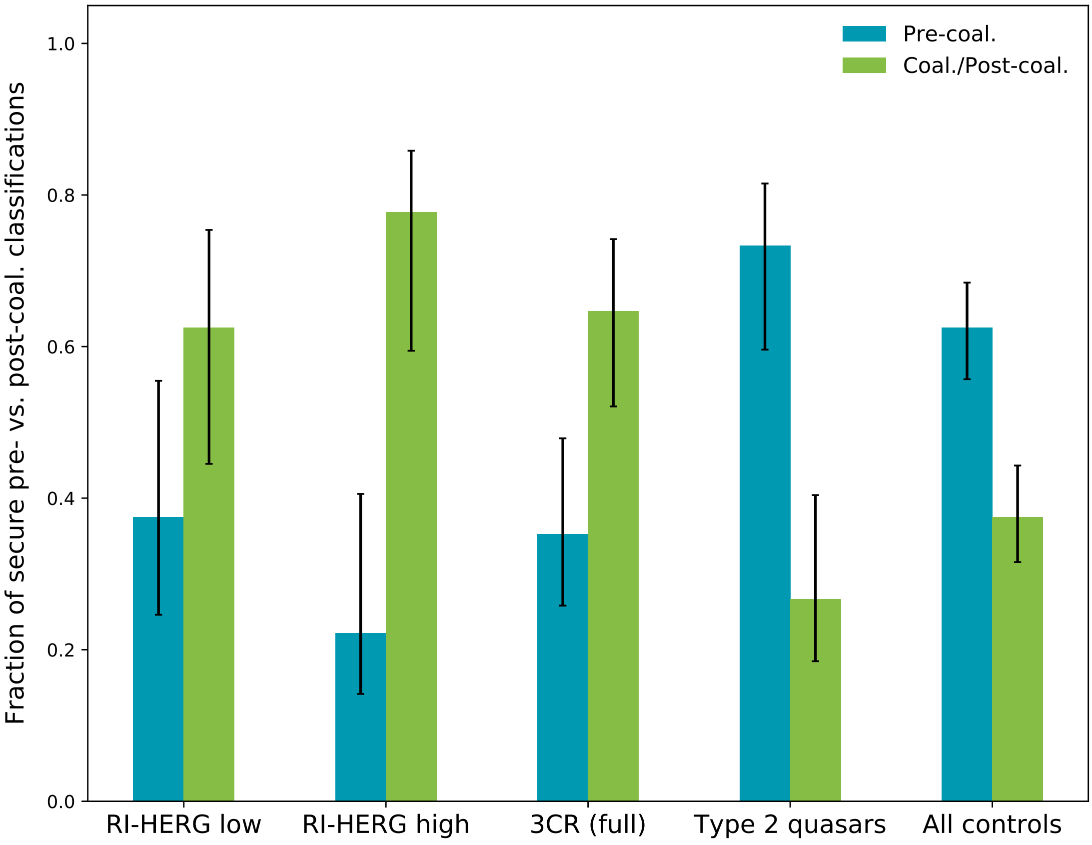

Figure 5.6: The proportions of disturbed galaxies in each of the active galaxy samples that show evidence for pre-coalescence or post-coalescence interactions. The values for the disturbed galaxies in the full control sample are also presented. Only galaxies with secure classifications of pre- or post-coalescence interaction signatures were considered for the analysis (see text), and the proportions shown were derived relative to the combined total number of these classifications for each sample. The exact measured proportions are listed in Table 5.2.

first question. Given that several different types of interaction signature could be present at the same time, multiple responses could be selected when answering this question. As a result of these two factors, the total number of votes recorded for each galaxy across the different interaction signature categories varied constantly. An interaction signature classification was therefore required to meet two criteria in order to be accepted. Firstly, the threshold of 5 out of 8 votes must have been met for the first question, ensuring that only the galaxies accepted as being disturbed were included in the analysis. Secondly, the majority of the classifiers that had answered “Yes” to the first question must have voted for that particular interaction signature category, i.e. 3 out of 5, 4 out of 6, 4 out of 7, or 5 out of 8.

The main aim of this question was to determine whether or not the galaxy appeared

Table 5.2: The proportions of galaxies with interaction signatures that are indicative of pre-coalescence or post-coalescence mergers and interactions, as presented in Figure 5.6. All proportions are expressed relative to the combined total number of secure pre- and post-coalescence classifications within each sample. Proportion uncertainties were estimated following the method of Cameron (2011).

	RI-HERG low	RI-HERG high	3CR (full)	Type 2 quasars	All controls
Pre-coalescence	$37.5^{+18}_{-13}\,\%$	$22^{+18}_{-8}\,\%$	$35^{+13}_{-9}\,\%$	$73^{+8}_{-13}\,\%$	$62.5^{+6}_{-7}\,\%$
Post-coalescence	$62.5^{+13}_{-18}\,\%$	$78^{+8}_{-18}\,\%$	$65^{+9}_{-13}\,\%$	$27^{+13}_{-8}\,\%$	$37.5^{+7}_{-6}\,\%$

to be in the early stages or late stages of a merger or interaction, i.e. prior to the coalescence of the nuclei ("pre-coalescence") or after their coalescence ("coalescence/post-coalescence"), based on the types of interaction signatures it was associated with. For this purpose, the "Bridge (B)", "Tidally interacting companion (TIC)", and "Multiple nuclei (MN)" classifications were considered to indicate early-stage or pre-coalescence interactions, while the remainder were classified as late-stage or coalescence/post-coalescence interactions – the latter are hereafter referred to as late-stage or post-coalescence, for brevity. This approach is mostly consistent with that of Ramos Almeida et al. (2011, 2012) and Bessiere et al. (2012), with the exception of the new "Tidally interacting companion (TIC)" category that was added for this project. On the occasions when both early-stage and late-stage interaction signature classifications were accepted, the interaction was considered to be of early-stage/pre-coalescence, for consistency with these previous studies.

Figure 5.6 shows the proportions of disturbed radio galaxies, Type 2 quasar objects, and control galaxies with secure interaction signature classifications that are suggestive of early-stage/pre-coalescence or late-stage/post-coalescence events, based on the categorisation outlined above. The measured proportions for each sample are provided in Table 5.2. Late-stage interactions appear to be favoured for the disturbed galaxies in each radio galaxy sample, with the largest difference between the late-stage and early-stage proportions being found for the RI-HERG high sample. A large difference is also found when considering the measured proportions for all radio galaxies combined: $32^{+9}_{-7}\,\%$ and $68^{+7}_{-9}\,\%$ for early- and late-stage interaction signatures, respectively. These results agree well with the those found for the powerful radio galaxies in the 2Jy sample, for which $35^{+12}_{-9}\,\%$ and $65^{+9}_{-12}\,\%$ of the disturbed objects with $z < 0.3$ show a preference for pre- and post-coalescence interactions, respectively (Ramos Almeida et al., 2011).

In contrast with the radio galaxy samples, the Type 2 quasars show a strong preference for early-stage (73^{+8}_{-13} %) relative to late-stage (27^{+13}_{-8} %) interactions. This does not agree with the results found for the hosts of Type 2 quasars with moderate redshifts ($0.3 < z < 0.41$) studied by Bessiere et al. (2012), for which similar fractions of pre-coalescence and post-coalescence interactions are found in the disturbed galaxies: 47^{+13}_{-12} % and 53^{+12}_{-13} %, respectively. The results for the Type 2 quasar objects in the current project are more consistent with those found for the disturbed galaxies in the control sample, for which proportions of 62.5^{+6}_{-7} % and 37.5^{+7}_{-6} % were measured for the early-stage and late-stage interaction signatures, respectively. Two-proportion Z-tests suggest that the null hypothesis that the proportions of early-stage and late-stage interactions in the control sample and Type 2 quasar sample are the same can only be rejected at a confidence level of $0.8\,\sigma$. On the other hand, the measurements for the control sample contrast significantly with those found for the radio galaxies, with the same tests indicating that the proportions of early-stage and late-stage interactions in the control sample and combined radio galaxy sample differ at a confidence level of $2.8\,\sigma$. Note that all of the above results are preserved if the radio galaxies with [OIII]λ5007 luminosities above the Type 2 quasar threshold ($L_{[OIII]} > 10^{35}$ W) are not considered for the analysis – the early-stage and late-stage proportions remain the same, but have slightly larger uncertainties (32^{+10}_{-7} % and 68^{+7}_{-10} %).

Overall, the interaction signature classifications from the interface therefore suggest that radio AGN are preferentially triggered in the late stages of galaxy mergers and interactions, while Type 2 quasars are preferentially triggered in their early stages. Since the latter preference is not significantly different from that found for the control galaxies, the results are also consistent with the idea that the merger stage is not important for the triggering of Type 2 quasars. Regardless of this, AGN host galaxies with both pre- and post-coalescence interaction signatures are found in each of the active galaxy samples. Therefore, if the galaxy mergers and interactions are responsible for triggering each of the types of AGN considered, this can occur at several different phases during these events.

5.3.3 Host galaxy types

The final question in the online interface asked the classifiers to indicate the overall morphological type of the galaxy in the image:

3) On first impression, what is the morphological type of the galaxy?

- Spiral/disk;

Table 5.3: The proportions of galaxies with host types classed as elliptical, spiral/disk, lenticular, merger, or uncertain for all of the active galaxy and matched control samples classified using the online interface, as presented in Figure 5.7. The results for the 3CR HERG and LERG subsamples are included in separate columns, alongside those found for the full 3CR sample. Proportion uncertainties were estimated following the method of Cameron (2011).

		RI-HERG low	RI-HERG high	3CR (full)	3CR HERGs	3CR LERGs	Type 2 quasars
Elliptical	AGN	$17^{+9}_{-5}\,\%$	$60^{+8}_{-9}\,\%$	$86^{+3}_{-5}\,\%$	$78^{+5}_{-8}\,\%$	$97^{+1}_{-7}\,\%$	$52^{+9}_{-10}\,\%$
	Cont.	$49 \pm 4\,\%$	$56^{+4}_{-5}\,\%$	$73^{+2}_{-3}\,\%$	$78 \pm 3\,\%$	$71^{+3}_{-4}\,\%$	$47^{+5}_{-4}\,\%$
Spiral/disk	AGN	$47 \pm 9\,\%$	$14^{+9}_{-4}\,\%$	$1^{+3}\,\%$	$2^{+5}_{-1}\,\%$	$0^{+6}\,\%$	$8^{+9}_{-3}\,\%$
	Cont.	$34 \pm 4\,\%$	$25^{+4}_{-3}\,\%$	$16 \pm 2\,\%$	$14^{+3}_{-2}\,\%$	$16^{+4}_{-3}\,\%$	$37^{+5}_{-4}\,\%$
Lenticular	AGN	$10^{+8}_{-3}\,\%$	$0^{+6}\,\%$	$0^{+2}\,\%$	$0^{+4}\,\%$	$0^{+6}\,\%$	$4^{+8}_{-1}\,\%$
	Cont.	$4^{+2}_{-1}\,\%$	$3^{+2}_{-1}\,\%$	$1^{+1}\,\%$	$2^{+2}_{-1}\,\%$	$1^{+2}\,\%$	$5^{+3}_{-1}\,\%$
Merger	AGN	$0^{+6}\,\%$	$4^{+7}_{-1}\,\%$	$3^{+3}_{-1}\,\%$	$5^{+6}_{-2}\,\%$	$0^{+6}\,\%$	$12^{+10}_{-4}\,\%$
	Cont.	$1^{+2}\,\%$	$2^{+2}_{-1}\,\%$	$1^{+1}\,\%$	$1^{+1}\,\%$	$1^{+2}\,\%$	$1^{+2}\,\%$
Uncertain	AGN	$27^{+9}_{-6}\,\%$	$21^{+10}_{-6}\,\%$	$10^{+5}_{-2}\,\%$	$15^{+7}_{-4}\,\%$	$3^{+7}_{-1}\,\%$	$24^{+10}_{-6}\,\%$
	Cont.	$11^{+3}_{-2}\,\%$	$14^{+4}_{-3}\,\%$	$9 \pm 2\,\%$	$6^{+2}_{-1}\,\%$	$11^{+3}_{-2}\,\%$	$9^{+3}_{-2}\,\%$

- Elliptical;
- Lenticular;
- Merger (too disturbed to classify);
- Unclassifiable (due to image defects, *not* merger).

This was mainly done with the aim of investigating whether or not there was any variation the longstanding relationship between radio AGN and early-type host galaxies with radio power, as suggested by the mixed population of late- and early-type galaxies found for the RI-HERG low sample in Chapter 3. As with the first, this question was compulsory, and only one of the available responses could be selected for each galaxy. As a result, a threshold of 5 out of 8 votes was again used for accepting a classification. If this was not met for any of the options (excluding the "Unclassifiable (due to image defects, *not* merger)" category), the galaxy was classed as having an uncertain host type.

Figure 5.7 shows the proportions of the active galaxy samples that were classified into the morphological type categories listed above, alongside the corresponding results for their matched control samples. The results for the 3CR HERG and LERG subsamples are also presented in the final two panels. The measured morphological type proportions for all samples are provided in Table 5.3. With the exception of the RI-HERG low sample,

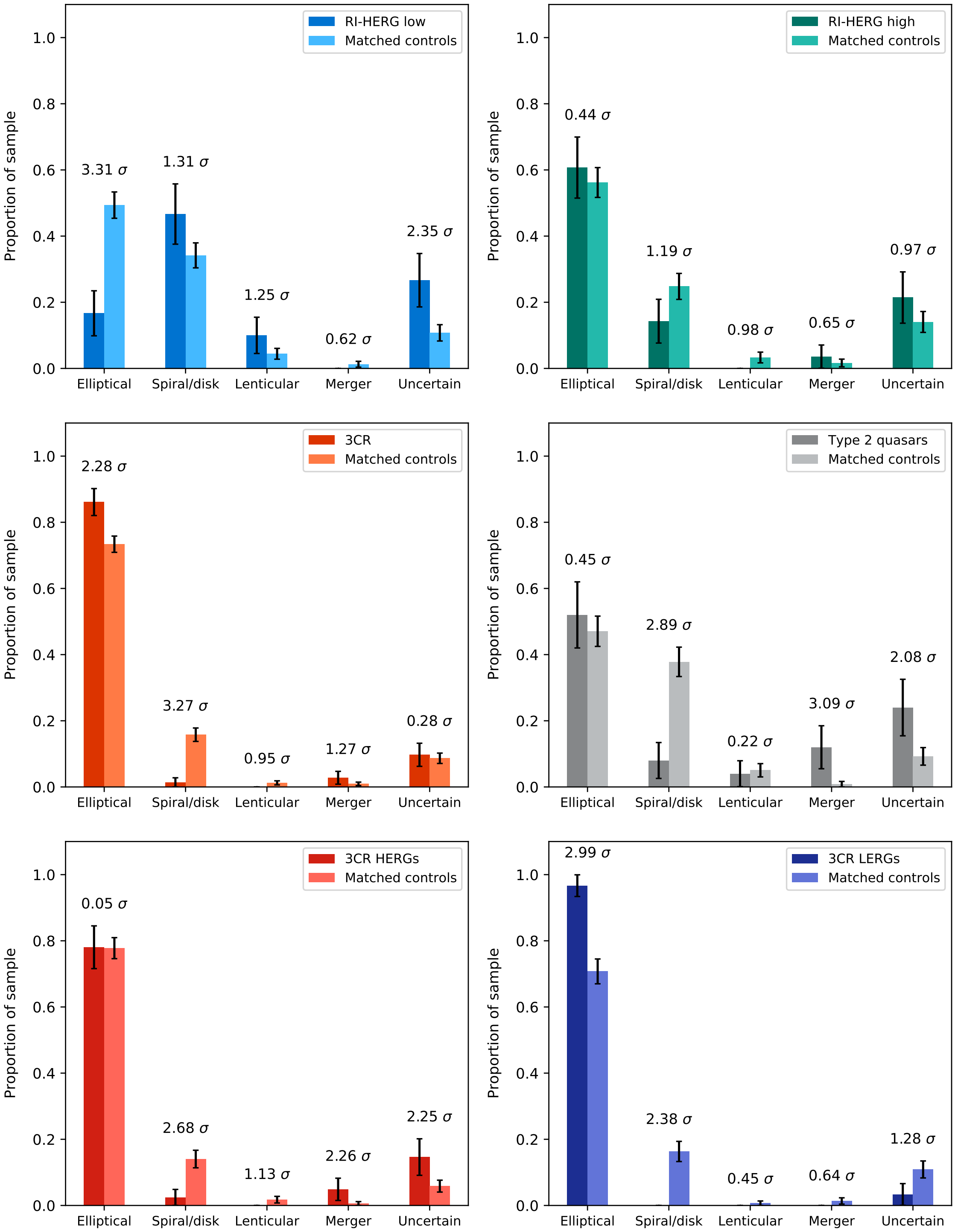

Figure 5.7: The proportions of galaxies with morphological types classed as elliptical, spiral/disk, lenticular, merger, or uncertain for each of the samples classified using the online interface (exact proportions in Table 5.3). The results for the active galaxy samples are presented alongside those for their respective matched control samples, with the significance of the difference between the measured proportions for each category indicated in all cases (from two-proportion Z-tests). The final two plots show the results for the 3CR sample when separated into its HERG and LERG subsamples.

it is found that the majority of the galaxies in each radio galaxy sample were classified as having elliptical morphologies, and small proportions were deemed to have spiral or disk-like morphologies. Their respective matched controls show relative excesses in the latter in all cases, with the same exception. However, the significance of the excess of ellipticals relative to the matched control proportions is only greater than $1\,\sigma$ in the 3CR sample ($2.3\,\sigma$) and its LERG subsample ($3.0\,\sigma$). Given that the proportions measured for the 3CR HERGs and their matched controls are consistent (a $0.05\,\sigma$ difference), it is therefore likely that the 3CR LERGs drive the observed difference seen for the full 3CR sample. The majority of the Type 2 quasar hosts are also classed as ellipticals, and a significant deficit in the proportion of spiral or disk morphologies is found relative to their matched controls (at the $2.9\,\sigma$ level). In this case, however, a significant excess in the merger category is also found ($3.1\,\sigma$), consistent with the high rate of disturbance determined for the sample ($64^{+8}_{-10}\,\%$; §5.3.1).

In order to investigate the relationship between AGN host type and radio power in more detail, the proportions of active galaxies with morphologies classified as early-type and late-type were compared across the full range of radio powers covered. Here, all galaxies classified as either elliptical or lenticular were considered to be of early-type, and those classed as spirals or disks were considered to be of late-type, consistent with the analysis presented in Chapter 3.

Figure 5.8 shows the proportions of early-type and late-type galaxies in bins of 1.4 GHz radio power and [OIII]λ5007 emission-line luminosity for the full active galaxy sample and, separately, for only the HERGs and Type 2 quasars. A strong positive correlation is observed between the early-type proportions and medians of the 1.4 GHz radio power bins for both the full active galaxy sample ($r_{\rm full} = 0.994$, $p_{\rm full} = 0.006$) and the HERG and Type 2 quasar subset ($r_{\rm HERG} = 0.998$, $p_{\rm HERG} = 0.002$), according to Pearson correlation tests. This is coupled with a strong negative correlation for the proportion of late-type galaxies in both cases ($r_{\rm full} = -0.993$, $p_{\rm full} = 0.007$ and $r_{\rm HERG} = -0.997$, $p_{\rm HERG} = 0.003$). Pearson correlation tests also suggest strong correlations with [OIII]λ5007 luminosity, although these are found to be of lower significance than the relationships with 1.4 GHz radio power: $r_{\rm full} = 0.868$, $p_{\rm full} = 0.132$ and $r_{\rm HERG} = 0.972$, $p_{\rm HERG} = 0.028$, and $r_{\rm full} = -0.978$, $p_{\rm full} = 0.022$ and $r_{\rm HERG} = -0.985$, $p_{\rm HERG} = 0.003$ for the early- and late-type proportions, respectively. In contrast with the rates of disturbance, this suggests that the host types are more strongly linked with the radio power of the AGN than the optical emission-line luminosity.

As mentioned in §5.3.1, it is interesting to investigate the underlying trends in the

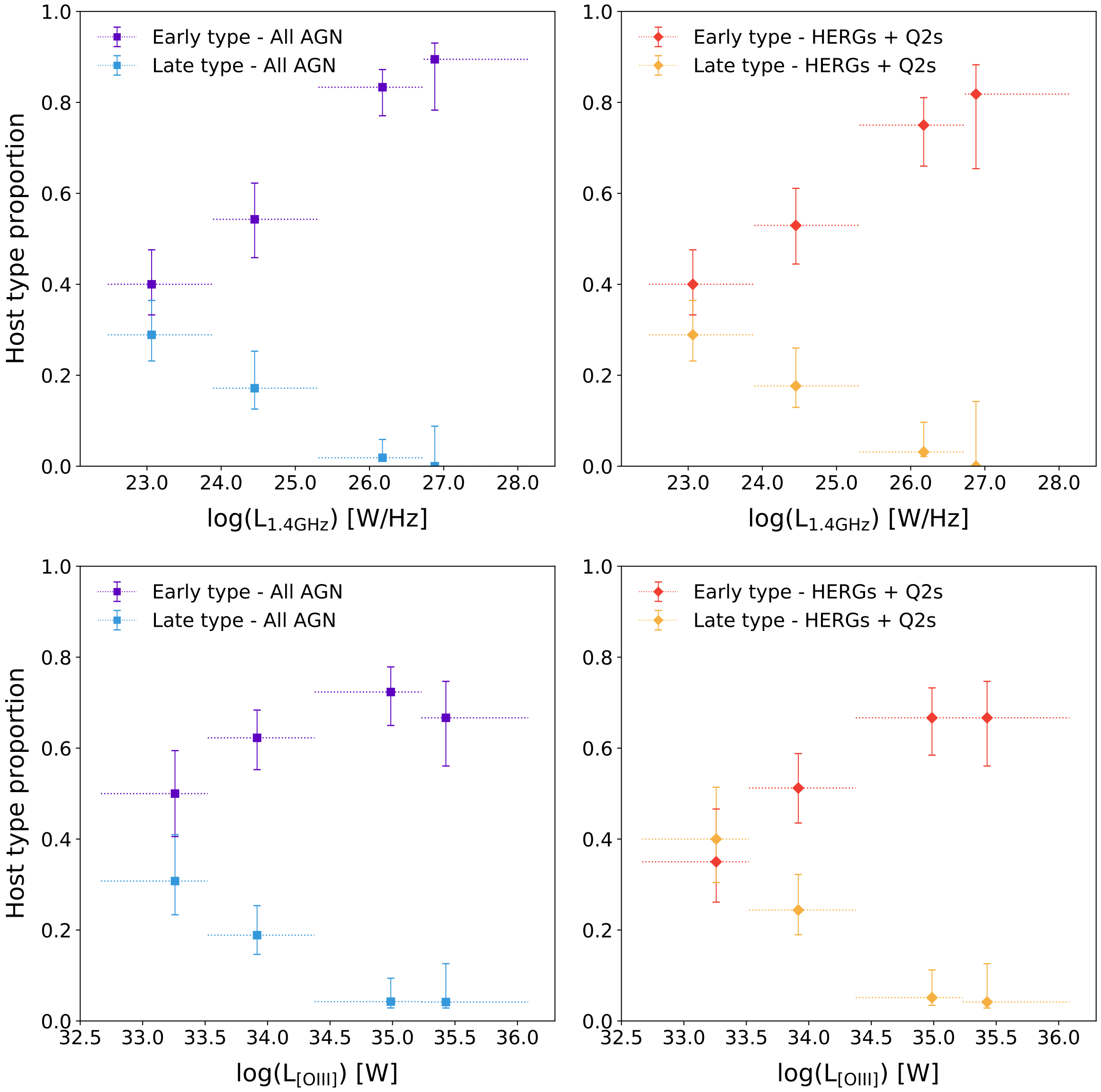

Figure 5.8: The proportions of active galaxies classed as having early-type (elliptical or lenticular) and late-type (spiral or disk) morphologies against their 1.4 GHz radio powers (top panels) and [OIII]λ5007 emission-line luminosities (bottom panels).

measured proportions with stellar mass and redshift. Figure 5.9 shows the proportions of early-type and late-type galaxies as a function of their stellar mass estimates and redshifts for all of the active galaxies and control galaxies included in the project (note that 3C 130 was again not considered for the former plot due to its very large stellar mass). From this, it is found that both the active galaxies and controls show similar general trends in their host type proportions with both stellar mass and redshift in all cases. The fractions of active galaxies with early-type morphologies are seen to be mostly consistent with the early-type control galaxies across the full range of stellar masses observed, with the largest difference being the excess of early-type controls in the fourth mass bin ($11.3 \lesssim \log(\mathrm{M}_*/\mathrm{M}_\odot) \lesssim 11.8$; a difference at the $1.9\,\sigma$ level). On the other hand, the proportions of late-type control galaxies are higher than those measured for the active galaxies in all cases, with the most significant difference being found in the third bin ($10.8 \lesssim \log(\mathrm{M}_*/\mathrm{M}_\odot) \lesssim 11.3$; at the $3.0\,\sigma$ level). It is found that all active galaxies and control galaxies above a stellar mass of $\log(\mathrm{M}_*/\mathrm{M}_\odot) > 11.8$ are classed as early types. The majority of the unmatched 3CR objects have stellar masses above this limit, and so the inclusion of these objects is not expected to have a significant influence on the morphological type results.

A strong positive correlation between the proportion of early-type morphologies and redshift is found for both the full active and control galaxy samples, as confirmed by Pearson correlation tests: $r_{\mathrm{AGN}} = 0.945$, $p_{\mathrm{AGN}} = 0.012$ and $r_{\mathrm{cont}} = 0.984$, $p_{\mathrm{cont}} = 0.002$, respectively. This is coupled with strong negative correlations in the proportions of late-type galaxies with increasing redshift, in both cases: $r_{\mathrm{AGN}} = -0.907$, $p_{\mathrm{AGN}} = 0.033$ and $r_{\mathrm{cont}} = -0.974$, $p_{\mathrm{cont}} = 0.005$. These trends therefore follow those found for the variations in morphological type proportions with radio power seen for the active galaxies (Figure 5.8), suggesting an underlying relationship between radio power and redshift. This is likely to at least partly be a consequence of the use of radio galaxy samples selected from flux-density-limited surveys, given that objects must have increasingly high radio powers with increasing redshift in order to be selected. A Pearson correlation test reveals evidence for a moderate but highly significant correlation between radio power and redshift within the active galaxy samples, which supports this idea: $r_{\mathrm{AGN}} = 0.682$, $p_{\mathrm{AGN}} < 10^{-22}$.

On the other hand, the fact that the proportions of early-type and late-type control galaxies also show similar trends with redshift indicates that another underlying effect is also apparent. One possible explanation is that high-radio-power active galaxies would more often require control matches with both high redshifts and high stellar masses, as

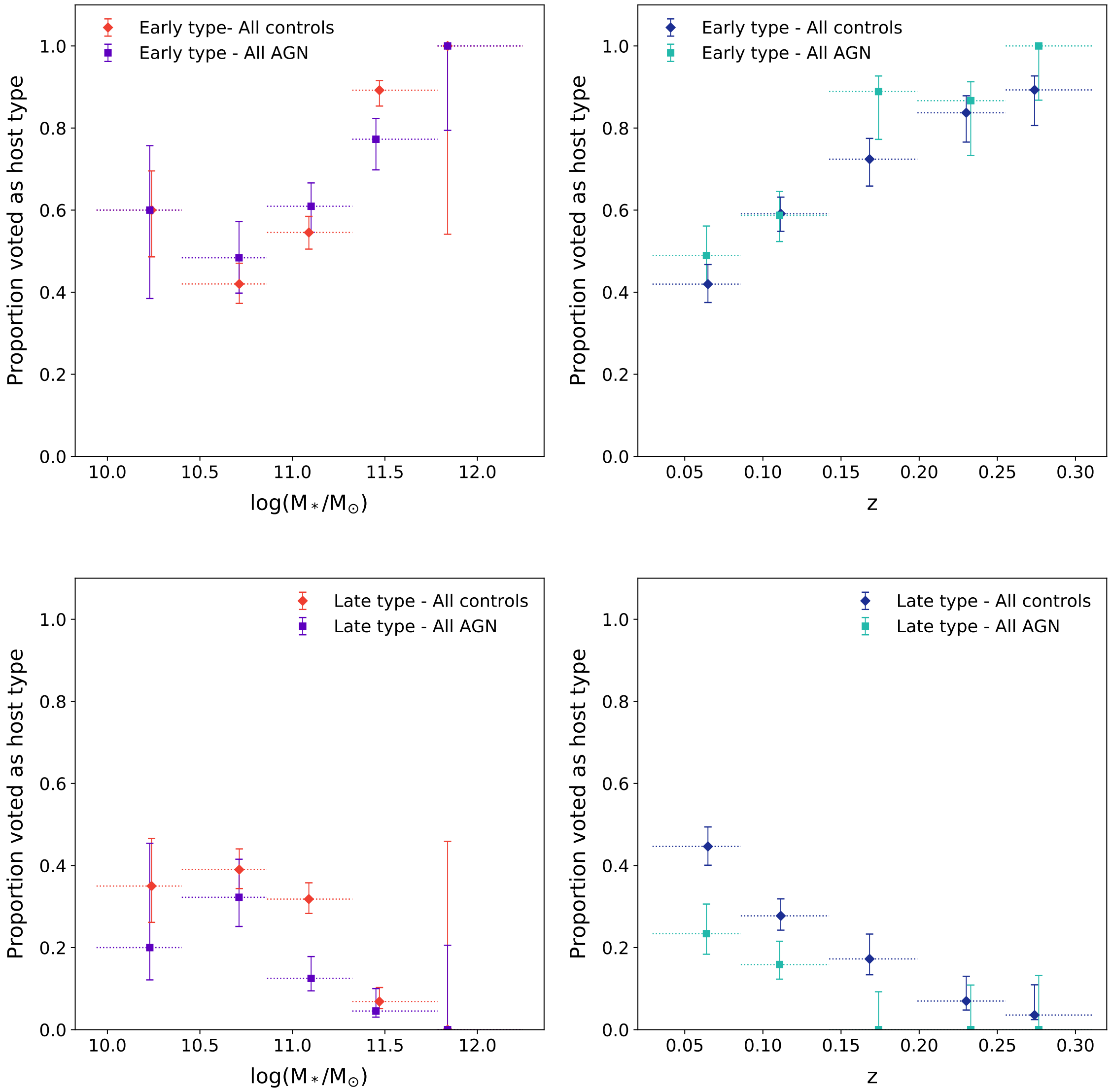

Figure 5.9: The proportions of active galaxies and control galaxies classed as having early-type (elliptical or lenticular) and late-type (spiral or disk) morphologies against their stellar mass estimates and redshifts.

a consequence of their typically high stellar masses and their relationship with redshift due to the flux density selection effect. Given the strong association between early-type galaxies and high stellar masses seen in the control sample (top left panel of Figure 5.9), the latter requirement would then cause the preferred selection of early-type relative to late-type galaxies at higher redshifts – note that this must be a natural effect, since no morphological matching was performed during the control selection.

Another contributing factor could be the increased difficulty of identifying more detailed morphological structures at higher redshifts, which could result in the increased selection of the elliptical or lenticular classifications relative to the spiral/disk category for more distant objects. This would simultaneously explain the redshift trends seen for the early-type and late-type proportions in both the active galaxies and matched control galaxies. This effect has also been observed for the host type classifications obtained from the very large samples of SDSS galaxies studies for the Galaxy Zoo projects; there termed "classification bias" (Bamford et al., 2009; Willett et al., 2013). These two explanations are difficult to disentangle, and it is likely that both factors would contribute to the observed redshift trends. However, since they would affect both the active galaxies and their matched controls equally, the conclusions drawn from relative comparisons (i.e. the enhancement ratios) should remain unaffected.

One final thing to note is that while the control galaxies were matched to the targets in terms of their stellar masses and redshifts, matching of their morphological types was not performed. It is therefore important to check that the difference between the rates of disturbance for the active galaxies and control galaxies were not caused by the general preference for late-type morphologies exhibited by the latter objects (Figure 5.7). Across the full sample of galaxies studied in the project, i.e. including all active galaxies and control galaxies, it is found that $30\,^{+3}_{-2}\,\%$ of the early types and $26 \pm 4\,\%$ of the late types were classified as disturbed. A two-proportion Z-test indicates that the null hypothesis that these two proportions are the same can be rejected at the $0.9\,\sigma$ level. There is thus little evidence for a significant difference between the disturbance rates of the early-type and late-type galaxies studied, and the general excess of late-type galaxies in the control samples relative to the active galaxy samples should therefore not affect the comparison of their disturbance fractions. This shows that matching of the morphological types would have had little effect on the results presented in §5.3.1.

Taken together, the results described in this section are consistent with the longstanding idea that powerful radio AGN are hosted by massive early-type galaxies. However, only the radio-powerful LERGs in the 3CR sample show a significant preference for early-type morphologies relative to galaxies from the general population with matching stellar masses and redshifts. In addition, the results also suggest that the fraction of early-type hosts decreases strongly with decreasing radio power, while the proportion of late-type hosts shows the opposite trend. Since the sample is dominated by HERGs and Type 2 quasar objects, this supports the picture of a transition in the dominant host types for radiatively-efficient AGN from massive early-type galaxies at high radio powers to late-type hosts at low radio powers (i.e. like Seyfert galaxies), as suggested in Chapter 3.

5.3.4 Full classification results

While the morphologies of the individual active galaxies are not discussed in detail in this thesis, the results for all active galaxies classified using the online interface are presented here, for reference. Table 5.4 provides a summary of the classifications for each of the active galaxies in the 3CR, RI-HERG high, and Type 2 quasar samples, respectively, as obtained through the online interface. The results for the RI-HERG low sample are then shown in Table 5.5, alongside those obtained from the more detailed analysis presented in Chapter 3. Some basic information for the targets is also presented in each table, including an indication of the radio power regime in which they belong, defined using the following ranges: (i) $\mathrm{L_{1.4GHz}} \geq 10^{25}$ $\mathrm{W\,Hz^{-1}}$ – radio-loud (RL); (ii) $10^{22.5} < \mathrm{L_{1.4GHz}} < 10^{25}$ $\mathrm{W\,Hz^{-1}}$ – radio-intermediate (RI); (iii) $\mathrm{L_{1.4GHz}} \leq 10^{22.5}$ $\mathrm{W\,Hz^{-1}}$ – radio-quiet (RQ). The optical classifications are also included, where HERGs and LERGs are defined as outlined in Chapter 2 and Type 2 quasars (Q2 in the final column) meet the criterion: $\mathrm{L_{[OIII]}} \geq 10^{35}$ W. It is found that 5 of the 3CR objects with [OIII]λ5007 luminosities that meet this latter criterion were identified as broad-line objects by Buttiglione et al. (2010, 2011) – 3C 33.1, 3C 184.1, 3C 323.1, 3C 390.3, and 3C 410 (see Chapter 2, §2.4) – and these are hence denoted as Type 1 quasars (Q1) in the optical classification column. Note that 3C 198 was classified as a star-forming galaxy (SF) by Buttiglione et al. (2010) based on its optical emission line flux ratios, and is the only object of its kind in the project (Chapter 2).

Table 5.4: A summary of the classification results for the active galaxies in the 3CR, RI-HERG high, and Type 2 quasar samples, as obtained using the online interface. Columns 1 to 4 provide the target names, the samples in which they are included, the redshifts, and the stellar mass estimates, respectively, as presented in Chapter 2. Columns 5 to 7 show the final classifications obtained from each of the three questions asked in the online interface (outlined in detail in §4.3.2). Non-bracketed interaction signatures in Column 6 indicate classifications that received a majority vote share, while those inside brackets did not meet this vote threshold. Column 8 provides the radio power regime (RL = radio-loud, RI = radio-intermediate, RQ = radio-quiet) and optical class for the targets, where Q1 indicates a Type 1 quasar and Q2 indicates a Type 2 quasar (both with $L_{[OIII]} \geq 10^{35}$ W). 3C 198 is the only object classified as a star-forming galaxy (SF) based on its optical emission line flux ratios (Chapter 2).

Target	Sample	z	$\log(M_*)$ ($M_\odot$)	Q1 - Disturbance	Q2 - Interaction signatures	Q3 - Host type	Radio/Optical class
3C 20	3CR	0.174	11.3	Not dist.	–	Elliptical	RL-HERG
3C 28	3CR	0.195	11.6	Not dist.	–	Elliptical	RL-LERG
3C 33	3CR	0.059	11.0	Disturbed	F, S, (A), (D), (T), (TIC)	Elliptical	RL-HERG/Q2
3C 33.1	3CR	0.181	11.6	Disturbed	MN, (B), (TIC)	Elliptical	RL-HERG/Q1
3C 35	3CR	0.067	11.0	Disturbed	TIC, (F), (S), (T)	Elliptical	RL-LERG
3C 52	3CR	0.285	11.8	Not dist.	–	Elliptical	RL-LERG
3C 61.1	3CR	0.186	–	Uncertain	–	Elliptical	RL-HERG/Q2
3C 63	3CR	0.175	11.3	Not dist.	–	Elliptical	RL-HERG
3C 79	3CR	0.255	11.5	Disturbed	T, (A)	Elliptical	RL-HERG/Q2
3C 89	3CR	0.138	11.6	Not dist.	–	Elliptical	RL-LERG
3C 93.1	3CR	0.244	11.5	Disturbed	(A), (B), (F), (T)	Elliptical	RL-HERG/Q2
3C 123	3CR	0.218	11.4	Not dist.	–	Elliptical	RL-LERG
3C 130	3CR	0.109	12.7	Not dist.	–	Elliptical	RL-LERG

Table 5.4 – continued.

3C 132	3CR	0.214	11.6	Disturbed	(A), (B), (F), (MN), (T), (TIC)	Elliptical	RL-LERG
3C 133	3CR	0.277	11.7	Not dist.	–	Elliptical	RL-HERG/Q2
3C 135	3CR	0.127	10.9	Disturbed	MN, (TIC)	Elliptical	RL-HERG/Q2
3C 136.1	3CR	0.064	11.2	Disturbed	(A), (F), (I), (T)	Uncertain	RL-HERG
3C 153	3CR	0.276	11.6	Not dist.	–	Elliptical	RL-LERG
3C 165	3CR	0.295	11.5	Not dist.	–	Elliptical	RL-LERG
3C 166	3CR	0.245	11.3	Not dist.	–	Elliptical	RL-LERG
3C 171	3CR	0.238	11.4	Disturbed	F, (A), (I), (T), (TIC)	Uncertain	RL-HERG/Q2
3C 173.1	3CR	0.292	11.8	Disturbed	(A), (B), (F), (MN), (S), (T)	Elliptical	RL-LERG
3C 180	3CR	0.220	11.4	Disturbed	A, (D), (F), (T)	Elliptical	RL-HERG/Q2
3C 184.1	3CR	0.118	11.3	Disturbed	T, (A), (B), (F), (MN), (TIC)	Elliptical	RL-HERG/Q1
3C 192	3CR	0.059	10.9	Not dist.	–	Elliptical	RL-HERG
3C 196.1	3CR	0.198	11.4	Not dist.	–	Elliptical	RL-LERG
3C 197.1	3CR	0.130	11.1	Not dist.	–	Elliptical	RL-HERG
3C 198	3CR	0.081	10.5	Not dist.	–	Elliptical	RL-SF
3C 213.1	3CR	0.194	11.1	Disturbed	A, (B), (F), (S), (T)	Elliptical	RL-LERG
3C 219	3CR	0.174	11.6	Disturbed	TIC, (A), (B)	Elliptical	RL-HERG
3C 223[3]	3CR	0.136	11.0	Disturbed	(A), (B), (F), (T), (TIC)	Elliptical	RL-HERG/Q2
3C 223.1	3CR	0.107	11.3	Disturbed	T, (A), (F)	Spiral/disk	RL-HERG
3C 234	3CR	0.184	11.8	Disturbed	(A), (B), (F), (MN), (TIC)	Elliptical	RL-HERG/Q2
3C 236	3CR	0.098	11.4	Disturbed	S, (A), (D), (F)	Elliptical	RL-LERG

Table 5.4 – continued.

3C 258	3CR	0.165	–	Uncertain	–	Elliptical	RL-HERG
3C 277.3	3CR	0.085	11.2	Disturbed	S, (A), (F), (MN), (T)	Elliptical	RL-HERG
3C 284	3CR	0.239	11.6	Disturbed	(A), (B), (F), (S), (T)	Elliptical	RL-HERG
3C 285	3CR	0.079	11.0	Disturbed	(A), (D), (F), (I), (T), (TIC)	Uncertain	RL-HERG
3C 287.1	3CR	0.215	11.5	Disturbed	(A), (B), (F), (TIC)	Elliptical	RL-HERG
3C 288	3CR	0.246	11.6	Not dist.	–	Elliptical	RL-LERG
3C 300	3CR	0.270	11.6	Disturbed	A, (F), (I), (T)	Elliptical	RL-HERG
3C 303	3CR	0.141	11.4	Uncertain	–	Elliptical	RL-HERG
3C 303.1	3CR	0.267	11.2	Not dist.	–	Elliptical	RL-HERG/Q2
3C 310	3CR	0.054	10.6	Disturbed	TIC, (A), (B)	Elliptical	RL-LERG
3C 314.1	3CR	0.119	10.8	Not dist.	–	Elliptical	RL-LERG
3C 315	3CR	0.108	10.9	Disturbed	(A), (B), (MN), (S), (T), (TIC)	Elliptical	RL-LERG
3C 319	3CR	0.192	11.1	Not dist.	–	Uncertain	RL-LERG
3C 321	3CR	0.096	11.4	Disturbed	MN, T, (A), (B), (F), (TIC)	Merger	RL-HERG/Q2
3C 323.1	3CR	0.264	12.1	Disturbed	(A), (F), (MN), (T), (TIC)	Elliptical	RL-HERG/Q1
3C 326	3CR	0.088	11.2	Disturbed	(A), (B), (F), (S)	Elliptical	RL-LERG
3C 332	3CR	0.151	11.4	Disturbed	MN, (A), (B), (TIC)	Elliptical	RL-HERG
3C 346	3CR	0.161	11.7	Disturbed	MN, (A), (B), (F), (T), (TIC)	Uncertain	RL-HERG
3C 349	3CR	0.205	11.2	Uncertain	–	Elliptical	RL-LERG
3C 357	3CR	0.166	11.5	Not dist.	–	Elliptical	RL-LERG
3C 371	3CR	0.050	11.4	Disturbed	(A), (B), (S), (T), (TIC)	Elliptical	RI-LERG

Table 5.4 – continued.

3C 379.1	3CR	0.256	11.6	Not dist.	–	Elliptical	RL-HERG
3C 381	3CR	0.160	11.3	Disturbed	(A), (B), (F), (MN), (S), (T), (TIC)	Elliptical	RL-HERG/Q2
3C 382	3CR	0.057	11.8	Disturbed	A, T, (F), (I), (S)	Uncertain	RL-HERG
3C 388	3CR	0.090	11.6	Not dist.	–	Elliptical	RL-LERG
3C 390.3	3CR	0.056	11.2	Uncertain	–	Elliptical	RL-HERG/Q1
3C 401	3CR	0.201	11.5	Not dist.	–	Elliptical	RL-LERG
3C 403.1	3CR	0.055	10.9	Uncertain	–	Elliptical	RL-LERG
3C 405	3CR	0.056	11.9	Not dist.	–	Elliptical	RL-HERG/Q2
3C 410	3CR	0.248	12.2	Not dist.	–	Elliptical	RL-HERG/Q1
3C 424	3CR	0.127	10.7	Disturbed	A, (F), (S), (TIC)	Elliptical	RL-LERG
3C 430	3CR	0.054	11.3	Not dist.	–	Elliptical	RL-LERG
3C 433	3CR	0.101	11.7	Disturbed	S, (A), (B), (I), (MN), (T), (TIC)	Merger	RL-HERG
3C 436	3CR	0.214	11.4	Disturbed	A, T, (D), (F), (S)	Uncertain	RL-HERG
3C 438	3CR	0.290	12.0	Not dist.	–	Elliptical	RL-LERG
3C 456	3CR	0.233	11.4	Not dist.	–	Elliptical	RL-HERG/Q2
3C 458	3CR	0.290	–	Disturbed	T, (A), (B), (F), (TIC)	Elliptical	RL-HERG/Q2
3C 460	3CR	0.268	11.5	Disturbed	(A), (B), (D), (I), (MN), (S), (T), (TIC)	Elliptical	RL-LERG
J0752+45	RI-HERG high	0.052	11.3	Not dist.	–	Elliptical	RI-HERG
J0806+19	RI-HERG high	0.098	11.4	Disturbed	A, TIC, (B), (F), (I), (S), (T)	Uncertain	RI-HERG
J0817+31	RI-HERG high	0.124	11.0	Disturbed	F, (A), (I), (MN), (T), (TIC)	Merger	RI-HERG

Table 5.4 – continued.

J0836+05	RI-HERG high	0.099	11.3	Not dist.	–	Spiral/disk	RI-HERG
J0840+29	RI-HERG high	0.065	11.2	Disturbed	S, (A), (I), (MN), (T)	Spiral/disk	RI-HERG
J0853+09	RI-HERG high	0.116	10.7	Not dist.	–	Elliptical	RI-HERG
J0854+42	RI-HERG high	0.142	10.8	Not dist.	–	Elliptical	RI-HERG
J0909+34	RI-HERG high	0.137	10.9	Not dist.	–	Elliptical	RI-HERG
J0912+53	RI-HERG high	0.102	11.4	Disturbed	MN, (A), (F), (T), (TIC)	Elliptical	RI-HERG
J1036+32	RI-HERG high	0.142	10.8	Uncertain	–	Elliptical	RI-HERG
J1102+59	RI-HERG high	0.106	11.3	Disturbed	S, (A), (I), (T)	Spiral/disk	RI-HERG
J1123+20	RI-HERG high	0.130	11.2	Disturbed	T, (A), (B), (F), (S), (TIC)	Uncertain	RI-HERG
J1147+35	RI-HERG high	0.063	11.4	Disturbed	A, T, (F), (MN), (S)	Elliptical	RI-HERG
J1207+33	RI-HERG high	0.079	11.2	Disturbed	A, (F), (I), (S), (T)	Uncertain	RI-HERG
J1247+32	RI-HERG high	0.135	11.3	Not dist.	–	Elliptical	RI-HERG
J1314+28	RI-HERG high	0.140	11.2	Disturbed	A, T, (F), (MN), (S), (TIC)	Elliptical	RI-HERG
J1328+27	RI-HERG high	0.091	10.8	Not dist.	–	Elliptical	RI-HERG
J1334+38	RI-HERG high	0.063	10.7	Not dist.	–	Elliptical	RI-HERG
J1409+36	RI-HERG high	0.149	11.4	Disturbed	B, T, TIC, (A), (F)	Elliptical	RI-HERG
J1425+39	RI-HERG high	0.143	11.1	Disturbed	F, T, (A), (S)	Elliptical	RI-HERG
J1436+08	RI-HERG high	0.051	11.2	Disturbed	S, (A), (F), (T)	Spiral/disk	RI-HERG
J1450-01	RI-HERG high	0.119	11.2	Disturbed	F, (A), (S), (T), (TIC)	Uncertain	RI-HERG
J1512-01	RI-HERG high	0.146	10.7	Not dist.	–	Elliptical	RI-HERG/Q2
J1516+05	RI-HERG high	0.051	10.9	Not dist.	–	Uncertain	RI-HERG

Table 5.4 – continued.

J1523+32	RI-HERG high	0.110	10.7	Disturbed	A, (I), (S), (T)	Uncertain	RI-HERG
J1529+36	RI-HERG high	0.099	11.4	Disturbed	A, (F), (I), (S)	Elliptical	RI-HERG
J1537-00	RI-HERG high	0.137	10.8	Disturbed	A, F, (S)	Elliptical	RI-HERG
J1541+47	RI-HERG high	0.110	11.1	Not dist.	–	Elliptical	RI-HERG
J0052-01	Type 2 quasar	0.135	10.8	Not dist.	–	Lenticular	RI-Q2
J0232-08	Type 2 quasar	0.100	10.8	Not dist.	–	Elliptical	RI-Q2
J0731+39	Type 2 quasar	0.110	11.0	Not dist.	–	Elliptical	RI-Q2
J0759+50	Type 2 quasar	0.054	10.6	Not dist.	–	Elliptical	RI-Q2
J0802+25	Type 2 quasar	0.121	11.1	Disturbed	A, T, (F), (I), (MN), (S)	Merger	RI-Q2
J0802+46	Type 2 quasar	0.081	11.3	Not dist.	–	Elliptical	RI-Q2
J0805+28	Type 2 quasar	0.129	11.4	Disturbed	MN, T, (A), (S), (TIC)	Uncertain	RI-Q2
J0818+36	Type 2 quasar	0.076	10.6	Disturbed	B, T, TIC, (F), (S)	Uncertain	RQ-Q2
J0841+01	Type 2 quasar	0.111	11.1	Disturbed	MN, TIC, (A), (B), (D), (T)	Elliptical	RI-Q2
J0858+31	Type 2 quasar	0.139	11.1	Disturbed	TIC, (B), (MN), (T)	Elliptical	RI-Q2
J0915+30	Type 2 quasar	0.130	11.2	Disturbed	B, T, TIC, (F), (I)	Merger	RI-Q2
3C223[2]	Type 2 quasar	0.137	11.0	Disturbed	T, TIC, (A), (B), (D), (F)	Elliptical	RL-Q2
J0945+17	Type 2 quasar	0.128	10.9	Disturbed	T, (A), (F), (MN), (S)	Uncertain	RI-Q2
J1010+06	Type 2 quasar	0.098	11.4	Disturbed	T, TIC, (A), (B), (MN), (S)	Elliptical	RI-Q2
J1015+00	Type 2 quasar	0.120	10.9	Disturbed	MN, T, (A), (B), (TIC)	Uncertain	RI-Q2
J1016+00	Type 2 quasar	0.116	11.0	Disturbed	MN, T, (A), (F), (I), (TIC)	Elliptical	RI-Q2

Table 5.4 – continued.

J1034+60	Type 2 quasar	0.051	11.1	Disturbed	A, (F), (I), (S), (T), (TIC)	Uncertain	RI-Q2
J1036+01	Type 2 quasar	0.107	11.3	Disturbed	TIC, (A), (B), (F), (MN), (T)	Spiral/disk	RQ-Q2
J1100+08	Type 2 quasar	0.101	11.4	Not dist.	–	Spiral/disk	RI-Q2
J1137+61	Type 2 quasar	0.111	10.9	Not dist.	–	Elliptical	RL-Q2
J1152+10	Type 2 quasar	0.070	10.8	Disturbed	F, S, T, (A), (I)	Uncertain	RI-Q2
J1157+37	Type 2 quasar	0.128	11.2	Not dist.	–	Elliptical	RI-Q2
J1200+31	Type 2 quasar	0.116	11.0	Disturbed	TIC, (A), (B), (F), (MN), (S), (T)	Elliptical	RI-Q2
J1218+47	Type 2 quasar	0.094	10.6	Disturbed	A, S, (I), (MN), (T), (TIC)	Merger	RI-Q2
J1223+08	Type 2 quasar	0.139	11.0	Not dist.	–	Elliptical	RQ-Q2

---

[3] 3C 223 is a member of both the 3CR and Type 2 quasar samples and was classified twice, using stamp images extracted from both of its two available sets of observations. This was useful for determining the effect of observing conditions and image quality on the classifications (see §5.4).

Table 5.5: A summary of the classification results for the RI-HERG low sample as obtained from the online interface, presented alongside those from the detailed analysis described in Chapter 3. The columns are largely similar to those in Table 5.4, with the exception of the second column, which here indicates the method used to obtain the classifications. Since this sample is entirely composed of radio-intermediate HERGs, none of which meet the Type 2 quasar luminosity criterion, the columns detailing radio and optical classes are now excluded. The distinction between "highly disturbed" (obvious from cursory inspection) and "disturbed" (seen after manipulation of the image appearance) galaxies is included for the results from Chapter 3. Bracketed interaction signature classifications again indicate those that did not meet receive a majority vote share in the online interface method (as in Table 5.4). However, those in square brackets represent classifications of visually identified signatures from the detailed analysis with surface brightnesses fainter than the 3 $\sigma_{\rm sky}$ surface brightness limit but brighter than the 1 $\sigma_{\rm sky}$ value (see Chapter 3, §3.3.1). The host type classifications listed for the detailed analysis method are those obtained from visual classification (§3.3.2).

Target	Method	z	log(M_*) ($M_\odot$)	Disturbance	Interaction signatures	Host type
J0725+43	Interface	0.069	10.9	Not disturbed	–	Spiral/disk
	Detailed analysis			Disturbed	2T, [T]	Lenticular
J0757+39	Interface	0.066	10.8	Disturbed	S, T, (A), (I)	Spiral/disk
	Detailed analysis			Highly disturbed	2S, T	Merger
J0810+48	Interface	0.077	10.9	Not disturbed	–	Lenticular
	Detailed analysis			Not disturbed	–	Lenticular
J0827+12	Interface	0.065	10.7	Uncertain	–	Spiral/disk
	Detailed analysis			Disturbed	A, I	Spiral
J0836+44	Interface	0.055	11.1	Disturbed	S, (A), (F), (MN), (T), (TIC)	Uncertain
	Detailed analysis			Highly disturbed	A, F, 2S, T	Merger
J0838+26	Interface	0.051	10.3	Not disturbed	–	Spiral/disk
	Detailed analysis			Not disturbed	D	Edge-on disk

Table 5.5 – continued.

J0902+52	Interface	0.098	11.4	Disturbed	A, T, (F), (I), (S)	Uncertain
	Detailed analysis			Highly disturbed	A, 2S, T	Merger
J0911+45	Interface	0.098	10.7	Not disturbed	–	Spiral/disk
	Detailed analysis			Disturbed	I	Spiral
J0931+47	Interface	0.049	10.0	Not disturbed	–	Elliptical
	Detailed analysis			Not disturbed	–	Elliptical
J0950+37	Interface	0.041	10.8	Not disturbed	–	Spiral/disk
	Detailed analysis			Not disturbed	–	Edge-on disk
J1036+38	Interface	0.051	11.2	Disturbed	TIC, (A), (B), (S), (T)	Spiral/disk
	Detailed analysis			Disturbed	S	Spiral
J1100+10	Interface	0.064	10.2	Not disturbed	–	Uncertain
	Detailed analysis			Not disturbed	–	Spiral
J1108+51	Interface	0.070	11.0	Not disturbed	–	Lenticular
	Detailed analysis			Not disturbed	–	Lenticular
J1147+33	Interface	0.031	10.7	Not disturbed	–	Spiral/disk
	Detailed analysis			Not disturbed	–	Lenticular
J1150+01	Interface	0.078	10.7	Not disturbed	–	Lenticular
	Detailed analysis			Not disturbed	–	Spiral
J1206+35	Interface	0.081	11.1	Not disturbed	–	Uncertain
	Detailed analysis			Not disturbed	–	Lenticular

Table 5.5 – continued.

J1206+10	Interface	0.089	11.0	Not disturbed	–	Spiral/disk
	Detailed analysis			Not disturbed	–	Spiral
J1236+40	Interface	0.096	10.5	Not disturbed	–	Spiral/disk
	Detailed analysis			Disturbed	I	Edge-on disk
J1243+37	Interface	0.086	11.2	Disturbed	MN, TIC, (A), (B), (D), (I), (S), (T)	Uncertain
	Detailed analysis			Highly disturbed	B, 2N, T	Merger
J1257+51	Interface	0.097	11.1	Disturbed	T, (A), (F), (I)	Uncertain
	Detailed analysis			Highly disturbed	A, 2T	Merger
J1324+17	Interface	0.086	10.7	Disturbed	I, (S), (T)	Spiral/disk
	Detailed analysis			Not disturbed	–	Spiral
J1351+46	Interface	0.096	10.6	Disturbed	(A), (D), (F), (I), (MN), (S), (T)	Uncertain
	Detailed analysis			Highly disturbed	A, 2T	Merger
J1358+17	Interface	0.095	10.9	Disturbed	B, TIC, (A), (F), (T)	Elliptical
	Detailed analysis			Highly disturbed	A, B, T	Elliptical
J1412+24	Interface	0.069	11.1	Disturbed	B, TIC, (A), (T)	Elliptical
	Detailed analysis			Highly disturbed	B, F, T	Elliptical
J1529+02	Interface	0.077	10.8	Not disturbed	–	Spiral/disk
	Detailed analysis			Not disturbed	–	Edge-on disk
J1555+27	Interface	0.083	10.4	Not disturbed	–	Uncertain
	Detailed analysis			Not disturbed	–	Lenticular

Table 5.5 – continued.

J1601+43	Interface	0.072	10.4	Uncertain	–	Elliptical
	Detailed analysis			Disturbed	F, [T]	Elliptical
J1609+13	Interface	0.036	10.8	Uncertain	–	Spiral/disk
	Detailed analysis			Disturbed	D, T	Edge-on disk
J1622+35	Interface	0.088	10.6	Disturbed	S, (A), (T)	Spiral/disk
	Detailed analysis			Disturbed	T	Spiral
J1630+12	Interface	0.065	10.1	Not disturbed	–	Elliptical
	Detailed analysis			Not disturbed	–	Elliptical

5.4 Discussion

The analysis of the morphological classifications obtained through the online interface has revealed excesses in the rates of disturbance for each of the active galaxy samples relative to their matched control samples. These excesses are found to be strongly correlated with the [OIII]λ5007 emission line luminosities of the AGN, but not strongly correlated with their 1.4 GHz radio powers. The secure interaction signature classifications (i.e. those that received a majority vote share) suggest that the disturbed galaxies in the radio-selected samples (RI-HERG low, RI-HERG high, 3CR) were more commonly associated with post-coalescence/late-stage interactions, while the Type 2 quasars showed a preference for pre-coalescence/early-stage interactions. It was also found that while the majority of AGN have early-type hosts, this fraction appears to decrease with decreasing radio power. The proportion of late-type hosts shows the opposite trend.

In this section, these results are discussed in detail and compared with those found in the literature, in relation to both the importance of merger-based triggering of the nuclear activity (§5.4.2) and the link with host galaxy morphology (§5.4.3). Firstly, however, the results of the interface classifications are compared with those obtained from more detailed analysis performed for the RI-HERG low sample (Chapter 3) and the 3CR sample, and general considerations for interpretation of the interface classification results are discussed (§5.4.1).

5.4.1 Interpretation of the online interface classifications

The online interface provided a means for obtaining morphological classifications of a large sample of active galaxies and matched control galaxies in a time-efficient manner. The use of a standardised image format and set classification questions/categories, as well as the randomisation of the galaxy images presented, also allowed the levels of individual classifier bias to be greatly reduced. The fact that the classifiers did not know whether they were classifying an active galaxy or control galaxy also offered a major advantage over many previous studies in this regard. Despite these advantages, it is important to consider how this choice of method may have influenced the results before comparing them with those in the literature. Here, the classifications of the objects obtained using the online interface are compared with previous classifications determined from more detailed visual inspection (i.e. with the ability to manipulate the image contrast and scale as required), as performed for both the RI-HERG low (Chapter 3) and 3CR samples. The dependence of the results on the choice of voting threshold is also considered, along with the effect of the variations in observing conditions across the different sets of observations.

Comparison with detailed inspection – The RI-HERG low sample

Table 5.5 compares the classification results obtained through the online interface and through the detailed analysis presented in Chapter 3, for all of the galaxies in the RI-HERG low sample. In terms of the levels of disturbance, the results agree well between the two methods, with the same classifications (either both disturbed or both not disturbed) being determined for 23 out of the 30 objects (77%) from both. Most importantly, this includes the eight galaxies that in Chapter 3 were identified as "highly disturbed" based on cursory visual inspection, all of which were classified as disturbed by either 7 (J1351+46, J1358+17) or all 8 (J0757+39, J0836+44, J0902+52, J1243+37, J1257+51, J1412+24) of the researchers in the online interface.

Of the remainder, 3 galaxies (10% of the sample) were classified as having an uncertain level of disturbance (4 votes disturbed, 4 votes not disturbed) through the online interface but as disturbed in the more detailed analysis (J0827+12, J1601+43, J1609+13). A further 3 galaxies (10%) had secure classifications as not disturbed from the interface (i.e. meeting the 5-vote threshold) that disagreed with the disturbed classifications from the more detailed analysis (J0725+43, J0911+45, J1236+40). As can be seen from the images presented in Figures 3.1 and 3.2 in Chapter 3, all of these galaxies exhibit subtle morphological signatures of disturbance, and, because of the limited image manipulation afforded by the interface method, the lack of agreement between the two methods is therefore unsurprising. The final galaxy, J1324+27, was the only object classified as disturbed when using the online interface but as not disturbed in the detailed analysis. This galaxy was a borderline case, however, with 5 votes recorded for disturbed and 3 for not disturbed, and it is seen to exhibit an unusual spiral structure that could be interpreted either as a sign of disturbance or as that of an undisturbed late-type galaxy.

When considering the online interface classifications, it is found that only 11 out of 30 (37^{-8}_{+9} %) of the galaxies in the RI-HERG low sample are classed as disturbed, compared with the 16 out of 30 (53 ± 9 %) found from the more detailed analysis – a difference at the $1.3\,\sigma$ level. When dividing the sample into two halves by radio power, however, the two methods give the same proportion of disturbed galaxies for the half with the highest radio powers (10 out of 15; 67^{-14}_{+10} %), but a much reduced proportion is found for the lower-radio-power half from the interface classifications (1 out of 15; 7^{-2}_{+13} %) – note, however, that the latter contains the three uncertain cases.

This suggests that the galaxies in the higher-radio-power half of the sample exhibit more major levels of disturbance than those in lower-radio-power half, supporting the conclusions drawn based on the "highly disturbed" galaxies in the sample in Chapter 3 (§3.4.1). From the interface classifications, the two-proportion Z-test now indicates that the null hypothesis that the two proportions are equal can be rejected at a confidence level of $3.4\,\sigma$, compared to the value of $1.5\,\sigma$ obtained previously. Repeating this analysis in terms of [OIII]λ5007 luminosity, proportions of 7 out of 15 ($47\,^{-12}_{+13}\,\%$) and 4 out of 15 ($27\,^{-8}_{+14}\,\%$) are measured for the high-luminosity and low-luminosity halves of the sample, respectively, a difference of only $1.1\,\sigma$.

These results therefore initially appear to support the idea that the importance of radio AGN triggering is strongly dependent on radio power but more weakly dependent on optical emission line luminosity, as suggested in Chapter 3, which conflicts with the conclusions drawn from the interface classifications for the full active galaxy sample. However, these results consider only the measured proportions of disturbed galaxies, which, as shown in §5.3.1, depend strongly on stellar mass for both active and non-active galaxies. Within the RI-HERG low sample, Pearson correlation tests suggest that there is a moderate but significant correlation between stellar mass and 1.4 GHz radio power ($r = 0.569$, $p = 0.001$), but no significant correlation between stellar mass and [OIII]λ5007 luminosity ($r = 0.095$, $p = 0.617$), which could thus influence the results observed. In support of this, while the disturbed proportions for radio-intermediate active galaxies are also positively correlated with radio power in the current project, this is not observed when the matched control galaxy proportions are taken into consideration (i.e. the enhancement ratios in Figure 5.4). These factors therefore provide evidence that the relationship with radio power seen in Chapter 3 is in fact a consequence of an underlying trend with stellar mass in the general galaxy population, again highlighting the importance of performing the control matching.

Considering the results for the host types, it is found that the classifications from the two methods agree for 18 of the 30 galaxies in the sample (60%). However, 8 of the remainder were classed as uncertain (27%), and so secure classifications (with $\geq$5 votes) from the interface only disagreed for 4 of the galaxies (13%). Of this latter group, 3 out of 4 galaxies were classed as lenticular by one of the two methods and as late-type (spirals/disks) by the other, two categories that are difficult to distinguish between when using the interface method due to the reduced ability to identify finer structures. Interestingly, in the more detailed analysis, the host types for 5 out of the 8 uncertain cases from the interface classifications were deemed too disturbed to classify (the “Merger” host type class). This would have caused difficulty when classifying these objects using the interface, and could explain their classification as uncertain cases. Therefore, although the rate of complete consistency is lower than for the classifications of morphological disturbance, there still appears to be good general agreement between the two methods, given these factors.

Comparison with detailed inspection – The 3CR sample

In addition to the previous classifications performed for the RI-HERG low sample, five researchers (Clive Tadhunter, Cristina Ramos Almeida, Pablo Doña Girón, Patricia Bessiere, and myself) have previously carried out detailed morphological classifications of 68 of the 72 3CR objects classified using the online interface – 3C 61.1, 3C 123, 3C 130, and 3C 132 did not have suitable images available at the time these classifications were made. As with the RI-HERG low sample, these were based on visual inspection of the full INT/WFC FITS images of the targets, which allowed the classifiers to manipulate the image contrast and scale as required. The full results are not presented here, but are used to provide an independent measure of the level of disturbance in the galaxies for comparison with the results obtained from the online interface. The classifications were again determined from majority voting, in order to be consistent with the other analyses. Therefore, a galaxy was only classified as disturbed if at least 3 out of the 5 classifiers had reported clear signs of disturbance.

From these more in-depth classifications, it is found that 49 out of the 68 objects (72^{-6}_{+5} %) are classed as disturbed. Only 37 of these 68 galaxies (54 ± 6 %) were classified as disturbed using the online interface, a difference at the $2.1\,\sigma$ level. The methods are found to agree on disturbed or not disturbed classifications in 49 of the 68 cases (72%), thus exhibiting a slightly lower rate of agreement than the RI-HERG low sample (77%). As found for the latter sample, the vast majority of the disagreements concerned objects for which the signs of disturbance were subtle, and these are thus understandable given the limitations of the interface technique. Furthermore, the 3CR sample also includes many objects with higher redshifts than the other active galaxy samples, for which the morphological appearance is more sensitive to the image quality. This is particularly important given the relatively poor seeing measured for many of the 3CR observations (see Table 2.4 in Chapter 2).

There were, however, two cases of galaxies that had significant levels of disturbance visible in their FITS images, but which were not classed as disturbed based on the interface classifications: 3C 303 and 3C 405 (Cygnus A). As shown in Figure 5.10, 3C 303

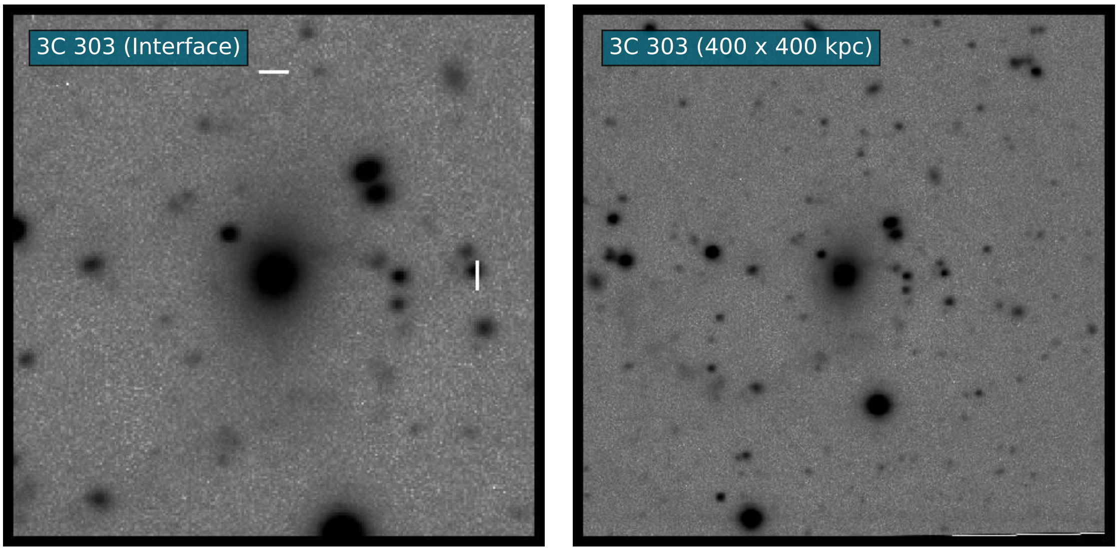

Figure 5.10: A demonstration of the limitations of the standardised image sizes used in the interface, which were scaled to be of 200 × 200 kpc in projected distance at the redshift of the target galaxy. 3C 303 exhibits a large-scale tail-like feature to the South-East (bottom left of image) that is observed on projected distances of up to ∼160 kpc. This is outside the range covered by the image used for the interface classifications, but can be seen in stamp images of the target with larger projected scales (e.g. as in the 400 × 400 kpc image shown).

exhibits a large-scale tail-like tidal feature that can be seen out to a projected distance of ∼160 kpc from the galaxy centre, which extends beyond the range covered by the 200 × 200 kpc stamp image used for the interface classifications. 3C 405 has a clear, small-scale double-nucleus structure in its centre that can be identified in its FITS image, but this is not clear in the interface images because of their poorer appearance when zoomed in – note that Baade & Minkowski (1954a) suggested that this latter radio source was associated with a galaxy merger from the first photographic plate observations of the source (as mentioned in Chapter 1). Since both of these galaxies are clearly disturbed upon inspection of their FITS images, this highlights one of the limitations of using images with standardised sizes in the online interface to obtain the classifications when compared to more detailed visual inspection.

Finally, as observed in the interface results, the HERGs (32 out of 40; $80\,^{-7}_{+5}\,\%$) are found to be more frequently disturbed than the LERGs (17 out of 27; $63\,^{+8}_{-10}\,\%$) in the more detailed analysis. This difference is, however, less significant than that determined from the interface classifications: $1.5\,\sigma$ and $2.4\,\sigma$, respectively. Given the improved ability to detect more subtle, low surface brightness features with the detailed inspection, this suggests that the HERGs are more highly disturbed than the LERGs, and are hence more likely to be triggered during more major merger events.

Dependence on voting threshold

Throughout the analysis, a particular classification was only accepted if it had received a majority vote share from the classifiers. For the classifications obtained from the compulsory first and third questions asked to researchers in the interface, this translated to a threshold of 5 out of 8 votes. For the second question, which was only seen if a classifier had indicated that they thought the galaxy was disturbed, an interaction signature classification was only accepted if: (i) the galaxy had been classified as disturbed, based on the 5-vote threshold; (ii) the majority of the classifiers that answered the second question had selected the given category (either 3 out of 5, 4 out of 6, 4 out of 7, or 5 out of 8). These thresholds were selected in order to use as much of the data as possible, but while still taking into account the level of certainty recorded for a given classification. Analysis performed considering higher vote thresholds would make the classifications more secure, but would result in fewer confirmed classifications and more uncertain cases. Lower vote thresholds would result in conflicting classifications.

Regardless of this, it is useful to ensure that varying the acceptance thresholds would not have a dramatic effect on the results of the analysis and the conclusions drawn, most importantly in terms of the rates of disturbance found. Figure 5.11 shows the proportions of disturbed galaxies in each of the active galaxy samples and matched control samples that would be measured if different vote thresholds had been used. While the results obtained for thresholds of 4 votes and below do not represent majority vote shares, these are included on the plots since they could still suggest that minor levels of disturbance are present.

In the figure, it is seen that the differences between the proportions measured for the active galaxies and matched controls are mostly consistent for the RI-HERG low, RI-HERG high, and 3CR LERG samples across the full range of thresholds. The difference between the disturbed proportions for the RI-HERG high sample and its matched control sample in fact increases as higher vote thresholds are considered. This is also exhibited, more prominently, by the Type 2 quasar objects and their matched controls. This shows that more certain classifications are more prevalent for the active galaxies in these two samples than for their matched controls, which could in turn suggest relatively higher levels of major disturbance. This shows that the conclusions drawn from the 5-vote threshold results would be unaffected if a higher value was chosen, and in fact would be strengthened for the RI-HERG high and Type 2 quasar samples if higher vote thresholds

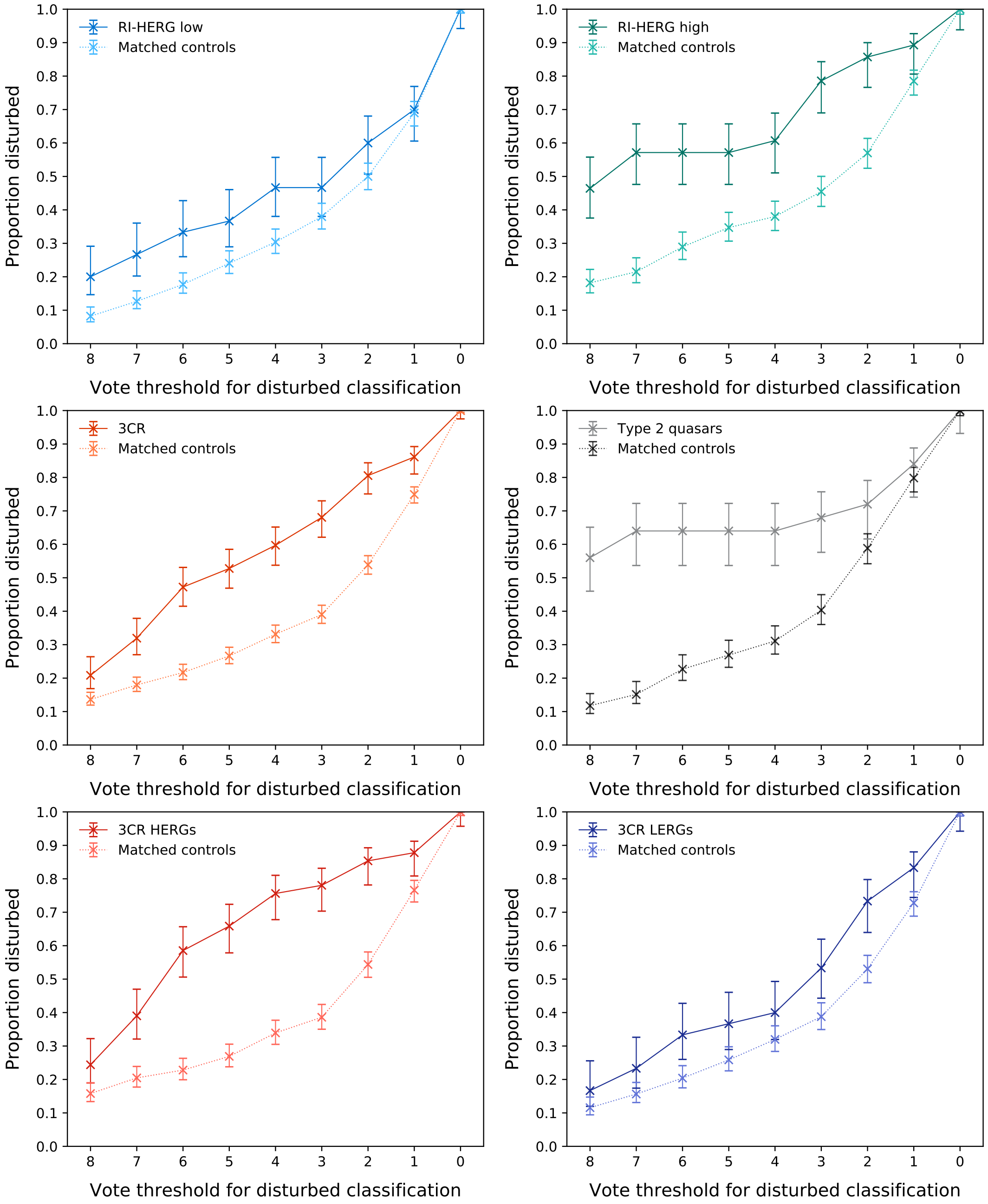

Figure 5.11: The proportions of galaxies classed as disturbed for each of the active galaxy samples and matched control samples classified using the online interface against the threshold number of votes used for the acceptance of a disturbed classification. Proportion uncertainties were estimated following the method of Cameron (2011).

were considered.

On the other hand, the differences between the proportions of disturbed galaxies in the 3CR sample and its matched control sample are found to vary noticeably over the full range of vote thresholds. This effect is amplified for the HERGs in the sample but is not seen for the LERGs, suggesting that the former subgroup is responsible for the divergence observed in the full 3CR sample. While the differences are little affected when a 6-vote threshold is considered, the disturbed proportions in the 3CR and 3CR HERG samples become more consistent with those measured for the controls at thresholds of 7 and 8 votes, indicating that certain signs of disturbance are relatively rare for these objects.

Although not presented here, similar analysis for the morphological type classifications reveals that the differences between the measured proportions for the active galaxies and the control galaxies would also remain consistent. Overall, it therefore seems that even though the exact values of the proportions would change if a different vote threshold was chosen, this would affect the different galaxy samples in a largely self-consistent manner. While changes in the proportions would affect the comparisons of these values with those found in the literature, this means that the conclusions drawn based on relative comparisons between the samples classified using the interface would not be significantly affected. Importantly, this includes all results that consider the ratios of the proportions measured for the active galaxies and their matched control galaxies (the enhancement ratios).

The effect of observing conditions

One final point of consideration is the effect that the variation in observing conditions could have on classifications of the different active galaxy samples. This was particularly important to consider, given that this could preferentially affect the active galaxies rather than the control galaxies – the randomised selection of the control galaxies meant that they were well distributed across the different sets of target galaxy observations, whereas the observing conditions were of fairly consistent quality over the course of each individual observing run (i.e. for the observations of each of the active galaxy samples). As seen from the measurements of the limiting surface brightness outlined in Chapter 2, §2.9, the average depth achieved by the r-band observations is consistent across the different samples, at $\sim$27 $\mathrm{mag\,arcsec^{-2}}$ for detections at $3\,\sigma$ above the sky background variations. The atmospheric seeing conditions did, however, vary considerably between the different samples, with the RI-HERG high and Type 2 quasar images exhibiting typically lower seeing FWHM values (medians of 1.14 arcsec and 1.20 arcsec, respectively) than the RI-HERG low and 3CR observations (medians of 1.38 arcsec and 1.34 arcsec, respectively).

The effect of different seeing conditions on the image quality can be seen from the two images of 3C 223 taken for the 3CR (Figure 4.13) and Type 2 quasar observations (Figure 4.5; presented in Chapter 4). These were taken with the same INT/WFC setup, but have greatly different seeing FWHM values that lie towards the two extremes of the range of values measured for the target observations: 2.17 arcsec and 0.95 arcsec, respectively. Both of these images were uploaded to the interface, and the galaxy was securely classified as disturbed in both cases. However, the number of votes recorded for a disturbed classification (6 for the 3CR image and 8 for the Type 2 quasar image) and for the various interaction signature categories (5 with 3 votes for the 3CR image and 4 with $\geq$4 votes for the Type 2 quasar image) indicated less certainty in the classifications when the 3CR image was considered. As with the other limitations, it appears that major levels of disturbance should still have been identifiable in the interface for the observations taken in poorest seeing, but minor details may have been harder to determine. The observing conditions are therefore not expected to have an additional consequence on the classifications.

Final comments

This subsection has shown that the morphological classifications obtained from more detailed analysis tend to lead to higher overall rates of disturbance than those obtained through the online interface, which is typically caused by the reduced sensitivity of the latter method to more subtle morphological features. While similar loss of detail could be caused by variations in the seeing conditions across the different observations, the classifications obtained from the two different observations of 3C 223 suggest that this would not have a strong effect on the identification of major morphological disturbances. Crucially, all of the galaxies in the RI-HERG low sample that were identified as "highly disturbed" from the more detailed analysis in Chapter 3 were also classified as disturbed through the interface, with high levels of certainty. The conclusions drawn from the analysis of the interface classifications were also shown to be little affected by the vote threshold used for their acceptance.

Overall, this suggests that the interface classifications provide a good representation of major levels of disturbance but not of minor levels, and the derived rates of disturbance should therefore be treated as lower limits. Furthermore, the lower sensitivity to more subtle morphological details could lead to the preferential classification of early-type hosts relative to late-types. However, it appears that any limitations introduced by the interface method should affect the active galaxies and their matched control samples equally, and so any conclusions based on relative comparisons between the two should be secure in all cases. This again highlights the importance of the control matching process.

5.4.2 The rates of disturbance and AGN triggering

The importance of galaxy mergers and interactions for triggering AGN has been the subject of much debate, although the most popular picture is that radiatively-efficient AGN (e.g. HERGs/SLRGs/quasars) and radiatively-inefficient AGN (e.g. LERGs/WLRGs) are triggered and fuelled in different ways (e.g. Heckman & Best, 2014; Yuan & Narayan, 2014). In this picture, radiatively-efficient AGN are fuelled by a cold gas flow from a standard accretion disk (c.f. Shakura & Sunyaev, 1973), and hence a sufficient supply of such gas must be available to the central SMBH in order to initiate and sustain this type of nuclear activity. The strong inflows of gas caused by the tidal forces associated with galaxy mergers and interactions (e.g. Barnes & Hernquist, 1996) therefore provide an attractive mechanism for triggering and fuelling the AGN in these objects. Radiatively-inefficient AGN are then thought to be fuelled by an optically thin, geometrically thick accretion flow of hotter gas (c.f. Narayan & Yi, 1994, 1995; Narayan, 2005). At high radio powers, the favoured fuelling mechanisms in this case are often linked with the prevalent hot gas supply in the galaxy haloes and the dense larger-scale environments in which these active galaxies are typically found to lie, with mergers and interactions thus being relatively less important. The results obtained from the analysis of the interface classifications are now discussed in this context.

Powerful radio galaxies – Comparison with the 2Jy sample

Previous deep, ground-based optical observations of powerful radio galaxies have revealed frequent morphological signatures of galaxy mergers and interactions, which, in keeping with the picture outlined above, are found to be more prevalent in those also exhibiting strong optical emission lines (Heckman et al., 1986; Smith & Heckman, 1989a,b; Ramos Almeida et al., 2011). In particular, Ramos Almeida et al. (2011) found that 94^{-7}_{+4}% of the SLRGs in the 2Jy sample display these signatures, which were also found to preferentially lie in the moderate-density group environments that favour the frequent occurrence of these events (Ramos Almeida et al., 2013). In contrast, evidence for morphological disturbance was found in only 27^{-9}_{+16} % of the 2Jy WLRGs (Ramos Almeida et al., 2011), which were also found to be predominantly associated with denser cluster environments (Ramos Almeida et al., 2013), where the high relative galaxy velocities can have a negative effect on the merger rate (Popesso & Biviano, 2006).

Ramos Almeida et al. (2012) also showed that the rates of disturbance are considerably lower for non-active early-type galaxies with comparable luminosities, redshifts, and image depths than for the 2Jy SLRGs, showing disturbance fractions of 53% ($z < 0.2$, from the OBEY survey; Tal et al., 2009) and 48% ($0.2 \leq z < 0.7$, from the Extended Groth Strip; Zhao et al., 2009) when interaction signatures with the same surface brightness limits are considered. However, both of these proportions are notably higher than the value measured for the 2Jy WLRGs (27^{-9}_{+16} %). The Extended Groth Strip galaxies also exhibit a significant preference (at the $3\,\sigma$ level) for less dense environments than the 2Jy radio galaxies with redshifts $0.2 \leq z < 0.7$ (21 SLRGs, one WLRG), suggesting that group or moderate density cluster environments play an important role in the triggering and fuelling of powerful radio AGN (Ramos Almeida et al., 2013).

Considering the results obtained for the 3CR HERGs alone, it is seen that 66^{-8}_{+7} % of the objects are classed as disturbed based on the interface classifications, which is lower than the fraction determined for the 2Jy SLRGs from Ramos Almeida et al. (2011) when the same redshift limits are considered: 95^{-10}_{+2} % (18 out of 19 objects at $z < 0.3$), for the latter. A two-proportion Z-test indicates that the null hypothesis that these proportions are the same can be rejected at a confidence level of $2.4\,\sigma$. Although part of this discrepancy can be attributed to the limitations of the interface classification method (§5.4.1), there is still a slight difference (at the $1.5\,\sigma$ level) when the proportion from more detailed inspection of the 3CR HERGs is considered (80^{-7}_{+5} %; see §5.4.1).

A two-sample Kolmogorov-Smirnov (KS) test provides no strong evidence for rejecting the null hypothesis that the 1.4 GHz radio power distributions for the 3CR HERGs and 2Jy SLRGs at equivalent redshifts ($z < 0.3$) are drawn from the same parent distribution ($D = 0.146$, $p = 0.892$), and so it is unlikely that the discrepancy is linked with the radio powers of the objects. The same conclusion is also drawn from a KS test performed for the distributions in [OIII]λ5007 luminosity ($D = 0.281$, $p = 0.208$). Stellar masses estimated from the K-band magnitudes of 30 objects in the 2Jy sample suggest that the 2Jy objects have values $\sim 10^{11} - 10^{12}$ M$_\odot$ (Tadhunter, 2016), which is similar to the range covered by the 3CR sources ($10^{10.8} - 10^{12.7}$ M$_\odot$). Furthermore, while the SLRG and HERG classification schemes differ, it is found that all except one of the 3CR HERGs would also be classified as SLRGs based on the [OIII]λ5007 equivalent

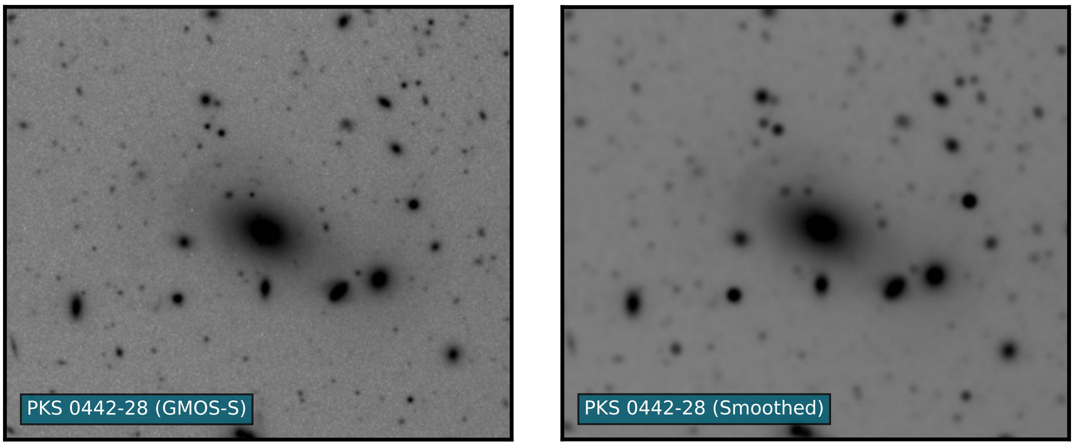

Figure 5.12: An example of the effects of seeing on the identification of faint interaction signatures, showing the GMOS-S image of PKS 0442-28 before (seeing FWHM = 0.55 arcsec) and after its smoothing to the median seeing FWHM of the 3CR INT/WFC observations (1.34 arcsec). PKS 0442-28 is an intermediate redshift SLRG ($z = 0.147$) from the 2Jy sample that exhibits a faint and sharp shell structure to the North-East (image oriented North up, East left). The feature has a measured surface brightness (corrected for foreground extinction, k-correction and dimming) of $\mu_{\rm AB}^{\rm corr} = 25.37$ mag arcsec^{-2} in the GMOS-S r'-band, and is one of the faintest interaction signatures identified for the 2Jy objects. The contrast levels of the two images are identical.

width >10 Å criterion used for the 2Jy sample. One factor that could contribute towards the difference is the fact that the classifications of the 2Jy objects were performed with prior knowledge that the sources were active galaxies, although this was also the case for the classifications obtained from more detailed inspection of the 3CR sources. The observed difference in the rates of disturbance is therefore surprising, given the apparent similarities between the properties of the two samples.

One possible explanation for the disagreement is the difference between the observing setups and conditions for the two different sets of observations. The 2Jy r'-band observations were taken using the *Gemini* Multi-Object Spectrograph South (GMOS-S) detector attached to the 8.1m *Gemini* South telescope, in good seeing conditions: full-width at half maximum (FWHM) values from 0.4 to 1.15 arcsec, with a median of 0.8 arcsec (Ramos Almeida et al., 2011). In contrast, the 3CR INT/WFC observations had much higher seeing FWHM values: in the range 1.07 to 2.20 arcsec, with a median of 1.34 arcsec. Although limiting surface brightness values for the 2Jy observations were not estimated, the faintest securely detected interaction signature had a measured surface brightness of $\mu_{\rm AB} = 27.27$ mag arcsec^{-2} (before corrections), suggesting a similar sensitivity to the 3CR r-band images (median $\mu_{AB}^{3\sigma_{\rm sky}} = 27.0$ mag arcsec^{-2}). Hence, while the achieved depths appear to be comparable, the 3CR images were all taken in poorer seeing conditions than those typical of the 2 Jy observations, which has the potential to affect the identification of faint interaction signatures with detailed structures. The larger number of pixels in the target galaxy regions also means that the 2Jy images have better sampling than the INT/WFC observations.

To examine the effects of seeing, Figure 5.12 presents the GMOS-S image for an example of a 2Jy SLRG that exhibits a faint and sharp shell structure (PKS 0442-28), alongside a version that has been smoothed (using a Gaussian kernel) to the median seeing FWHM of the 3CR observations (1.34 arcsec). From this, it can be seen that although some detail is lost in the smoothed image, the shell structure (to the North-East) remains clearly visible. Since this target was imaged in very good seeing conditions (0.55 arcsec), and the feature is one of the faintest interaction signatures identified for the 2Jy objects ($\mu_{\rm AB}^{\rm corr} = 25.37$ mag arcsec^{-2}), it appears that the difference in seeing would not have a strong effect on the identification of faint tidal features – this is consistent with what was found from the earlier comparison of the two observations of 3C 223 that were taken in greatly different seeing conditions (§5.4.1). It is therefore unlikely that this effect can account for the discrepancy between the 3CR HERG and 2Jy SLRG proportions, and the origin of the difference remains uncertain.

Turning to the 3CR LERGs, it is found that only $37\,^{-8}_{+9}\,\%$ are classed as disturbed based on the interface classifications, while a proportion of $63\,^{+8}_{-10}\,\%$ is measured based on more detailed inspection of the 3CR images: a difference at the $2.0\,\sigma$ level, based on a two-proportion Z-test. As mentioned in the previous subsection, this suggests that the levels of minor relative to major disturbances are much higher in these objects, given the reduced sensitivity afforded by the interface method to more subtle morphological features (§5.4.1). Regardless, both of these figures are larger than the value of $20\,^{+17}_{-7}\,\%$ determined for the 2Jy WLRGs at the same redshifts (2 out of 10 objects at $z < 0.3$), with the Z-test indicating that this latter proportion differs from the two 3CR LERG measurements at the $1.0\,\sigma$ and $2.3\,\sigma$ levels, respectively.

Again, a two-sample KS test indicates no strong evidence for rejecting the null hypothesis that the 3CR LERG and 2Jy WLRG 1.4 GHz radio power distributions are drawn from the same underlying distribution ($D = 0.400$, $p = 0.160$). In this case, however, a KS test performed for the [OIII]λ5007 luminosity distributions suggests that the null hypothesis of them being drawn from the same parent distribution can be rejected with ∼99.9% confidence ($D = 0.680$, $p = 0.001$), with the 3CR LERGs showing a preference for higher values relative to the 2Jy WLRGs: $32.67 \leq \log(\mathrm{L}_{[\mathrm{OIII}]})_{\mathrm{3CR}} \leq 34.98$

W Hz^{-1}, with median $\log(\mathrm{L}_{[\mathrm{OIII}]})_{3\mathrm{CR}} = 33.92$ W Hz^{-1}, and $32.01 \leq \log(\mathrm{L}_{[\mathrm{OIII}]})_{2\mathrm{Jy}} \leq 33.71$ W Hz^{-1}, median $\log(\mathrm{L}_{[\mathrm{OIII}]})_{2\mathrm{Jy}} = 33.43$ W Hz^{-1}, respectively. Given the strong correlation between [OIII]λ5007 luminosity and the enhancement of disturbed active galaxies relative to their matched controls even within the full active galaxy sample (§5.3.1, Figure 5.4), this could explain the increased proportion of disturbed galaxies in the 3CR LERG sample relative to that measured for the 2Jy WLRGs.

Interestingly, the rate of disturbance determined for the 3CR LERGs from the more detailed inspection (63^{+8}_{-10} %) is comparable with that determined by Ramos Almeida et al. (2012) for the non-active early-type galaxies in the general population at $z < 0.2$ (53%, from the OBEY survey). This suggests that a large contribution towards the seemingly high rate of disturbance observed for the 3CR LERGs could be caused by their underlying association with massive early-type galaxies, which have significant rates of disturbance at low to intermediate redshifts. This is supported by the fact that the disturbed proportions derived from the current interface classification analysis for the 3CR HERGs show a much more significant excess relative to their matched controls than the 3CR LERGs: $4.7\,\sigma$ and $1.2\,\sigma$, respectively. The results are therefore consistent with the idea that galaxy mergers and interactions are highly important for triggering the most powerful radio galaxies with radiatively-efficient AGN, but have relatively lower importance for triggering those with radiatively-inefficient AGN.

Comparison with radio-intermediate LERGs

Recently, study of the optical morphologies of a large sample of low redshift ($z < 0.07$) LERGs with mostly intermediate radio powers ($10^{21.7} < \log(\mathrm{L}_{1.4\mathrm{GHz}}) < 10^{25.8}$ W Hz^{-1}, median 10^{23} W Hz^{-1}) was undertaken by Gordon et al. (2019). The 282 LERGs were classified alongside 1622 control galaxies matched in stellar mass, redshift and large-scale environment, using a similar online interface technique to that used for the current analysis. While the Dark Energy Camera Legacy Survey (DECaLS; Dey et al., 2019) images used by Gordon et al. (2019) reach a greater surface brightness depth ($\mu_r \sim 28$ mag arcsec^{-2}; Hood et al., 2018) than the INT/WFC images ($\mu_r \sim 27$ mag arcsec^{-2}), this is expected to have little effect on the classifications, given the reduced sensitivity to low-surface-brightness features when using the interface method (see §5.4.1). There is also little difference between the median seeing FWHM values between the two sets of images: 1.18 arcsec (median across all DECaLS r-band observations; Dey et al., 2019) and 1.21 arcsec (across all of the current INT/WFC observations). These results are hence directly comparable with those obtained from the online interface classifications of the current sample. The main caveat to note is that the classifiers were able to indicate whether the level of disturbance was “major” or “minor” when classifying the objects as disturbed, whereas the disturbed classifications in the current work encompass both.

Overall, Gordon et al. (2019) found that the rates of disturbance for the LERGs (both minor and major) and their matched controls are largely consistent. In comparison, while the higher-radio-power LERGs in the 3CR sample show an excess in their disturbance fraction relative to their matched controls, its significance is low ($1.2\,\sigma$). Furthermore, the 1.4 GHz radio power and [OIII]λ5007 emission line luminosity are found to be strongly correlated for the 3CR objects – a Pearson correlation test gives $r = 0.679$ and $p < 10^{-3}$ for the 3CR LERGs with available [OIII]λ5007 measurements in particular – which suggests that the 3CR LERGs ($10^{24.67} < \log(\mathrm{L_{1.4GHz}}) < 10^{27.74}$ $\mathrm{W\,Hz^{-1}}$, median $10^{26.42}$ $\mathrm{W\,Hz^{-1}}$) would typically have higher optical emission line luminosities than the Gordon et al. LERGs. This could therefore explain the slight excess relative to the matched controls found for the 3CR LERGs but not for the radio-intermediate LERGs, given that the rate of disturbance in the current active galaxy sample was found to be positively correlated with [OIII]λ5007 emission line luminosity across the full range of values covered.

Gordon et al. (2019) do, however, find a highly significant excess ($>4\,\sigma$) in the fraction of LERGs that exhibit major disturbances relative to their matched controls for the lower stellar mass objects in their sample ($\log(\mathrm{M_*/M_\odot}) < 10.97$), which is preserved when their subset of controls with matched morphological types is considered ($>2.5\,\sigma$). They also find a significant deficit ($>2.5\,\sigma$) in the proportion of LERGs that were found to have minor disturbances compared to the matched controls at the high-mass end of the sample ($\log(\mathrm{M_*/M_\odot}) > 11.3$). For the same ranges in stellar mass for the 3CR LERGs, it is found that $60\,^{-22}_{+16}\,\%$ (3 out of 5) of the low-mass objects and $26\,^{-8}_{+12}\,\%$ of the high-mass objects (5 out of 19) were classified as disturbed, which constitute a $2.2\,\sigma$ excess and $0.3\,\sigma$ deficit relative to the matched controls, respectively. Assuming that the two studies are equally sensitive to both major and minor levels of disturbance, there is therefore some evidence to support the low-mass merger excess found by Gordon et al. (2019). However, there is no significant evidence in support of a low-mass deficit. It is interesting to note that for the 3CR LERGs, this goes against the general trend of an increasing proportion of disturbance with increasing stellar mass, which was observed for both the full active galaxy sample and the full control galaxy sample in the current work (Figure 5.5).

The overall rates of disturbance determined for the radio-intermediate LERGs and their matched controls, considering classifications of both minor and major disturbances, are 28.7 ± 1.1 % and 27.3 ± 0.5 %, respectively, a difference at a confidence level of $< 0.5\,\sigma$ (Gordon et al., 2019). Considering the combined interface classification results for the RI-HERG low and RI-HERG high samples from the current analysis ($10^{22.5} < \log(L_{1.4\mathrm{GHz}}) < 10^{25}$ W Hz^{-1}; $z < 0.15$), disturbance rates of 47^{-6}_{+7} % and 29 ± 3 % are found for the radio-intermediate HERGs and their matched controls, a difference at the $2.7\,\sigma$ level. Since the proportions measured for the control samples from both analyses are consistent (a $< 0.5\,\sigma$ difference), this suggests that the merger rates for radio-intermediate HERGs are significantly higher than for radio-intermediate LERGs – a two-proportion Z-test indicates that the null hypothesis that the disturbance proportions are equal can be rejected at a confidence level of $2.7\,\sigma$. Overall, both sets of results are therefore consistent with the idea that galaxy mergers and interactions are generally less important for triggering the nuclear activity in LERGs than in HERGs, but suggest that they may be more important for triggering LERGs with higher radio powers and/or optical emission line luminosities.

Comparison with other Type 2 quasar samples

Previous models of galaxy mergers and interactions suggest that they offer an effective means for triggering and fuelling quasar activity (e.g. Sanders et al., 1988; Di Matteo et al., 2005; Hopkins et al., 2008). However, at low to intermediate redshifts, previous searches for morphological signatures of these events in the host galaxies of the brightest AGN have yielded mixed results, with studies suggesting both high and low rates of disturbance for objects selected via their strong nuclear emission in optical, infrared, and X-ray wavebands (e.g. Dunlop et al., 2003; Floyd et al., 2004; Bennert et al., 2008; Veilleux et al., 2009; Cisternas et al., 2011; Treister et al., 2012; Villforth et al., 2014; Hong et al., 2015; Villforth et al., 2017). At redshifts of $1 \lesssim z \lesssim 3$, the epoch in cosmic time when AGN activity is thought to have peaked (e.g. Aird et al., 2015), observational studies tend to find no significant evidence for enhanced rates of disturbance in the hosts of bright AGN relative to matched control samples of non-active galaxies (e.g. Kocevski et al., 2012; Mechtley et al., 2016; Marian et al., 2019; Shah et al., 2020). However, there is some evidence that those with moderate or bright radio emission ($\log(L_{1.4\mathrm{GHz}}) \gtrsim 10^{23}$ W Hz^{-1}; Chiaberge et al., 2015) or luminous, heavily obscured AGN (identified at infrared wavelengths; Donley et al., 2018) have significantly higher merger rates than matched non-active galaxies at these higher redshifts. As a result, this has called into question the conventional picture of quasar-like activity being triggered in galaxy mergers and interactions.

A large number of these studies have, however, been based on relatively shallow-depth Hubble Space Telescope (HST) imaging observations (typically one orbit per galaxy or less) of the hosts of unobscured (Type 1) quasars. While the HST offers a greatly improved image resolution compared to typical ground-based observations, its collecting area is relatively small compared to large ground-based telescopes. Furthermore, the small pixel scales of its detectors mean that diffuse galaxy structures are spread over a large number of pixels. Given the readout noise of the CCD, this results in a lower signal-to-noise in each pixel, despite the lower sky background contribution for space-based observations. The importance of deeper imaging with the HST for the detection of low surface brightness features is clearly demonstrated by Bennert et al. (2008), who found that 4 out of 5 of the quasar host galaxies classed as undisturbed in the study of Dunlop et al. (2003) exhibited significant tidal features in their deeper (five orbit) HST imaging observations with the more sensitive Advanced Camera for Surveys (ACS) detector.

In addition to these factors, the bright light from the Type 1 nucleus can have a strong effect on the appearance of the galaxy, which introduces difficulties related to the accurate subtraction of a point-spread function (PSF) profile. This also causes complications when attempting to compare the quasar host morphologies with those of matched control galaxies, with some studies opting to insert an artificial central point source into the latter in order to address this issue (Villforth et al., 2014, 2017). For obscured Type 2 quasars, selected based on their extreme [OIII]λ5007 emission line luminosities (e.g. Zakamska et al., 2003; Reyes et al., 2008), the direct light from the AGN is diminished by obscuring material along the line of sight to the nucleus, and so the complications related to the bright central point source are avoided. In the unification scheme outlined in Chapter 1, the central engines in Type 1 and Type 2 objects are otherwise the same, and so study of their host galaxies offers an attractive alternative means for investigating the triggering of quasar activity in galaxy mergers.

Despite this advantage, relatively little focused research on the detailed host morphologies of Type 2 quasars has been undertaken. The few previous studies of such objects, which have typically focused on intermediate redshift samples[4] ($0.1 \lesssim z \lesssim 0.6$), have yielded mixed results for the rates of disturbance (summarised in Table 5.6), in agreement with the findings of other studies of highly luminous AGN. As shown in the

---

[4] All of these samples were extracted from the catalogues of Zakamska et al. (2003) or Reyes et al. (2008), with the current Type 2 quasar sample being selected from the latter (Chapter 2, §2.5). The objects were typically selected to have $\log(L_{[OIII]}/L_{\odot}) > 8.3$ or 8.4 ($L_{[OIII]} \gtrsim 10^{35}$ W). The exception is the more luminous objects in Wylezalek et al. (2016), which have $\log(L_{[OIII]}/L_{\odot}) > 9.0$ ($L_{[OIII]} \gtrsim 10^{35.5}$ W).

table, it is found that the studies based on relatively shallow-depth HST observations (again at most one orbit per object) typically find lower disturbance rates than those based on deep, ground-based imaging. However, it is interesting to note that the highest rate of disturbance determined from HST observations is found in the study considering images with the longest exposures (2000–2500 s; Wylezalek et al., 2016), from which a limiting surface brightness of 25 to 26 mag arcsec^{-2} is achieved (rest-frame "yellow" band, between V and R; Zakamska et al., 2006). The other HST studies, which find lower rates of disturbance, are based on much shorter exposures (<1000 s; Urbano-Mayorgas et al., 2019; Zhao et al., 2019). This indicates that while the HST is not optimised for the detection of low-surface-brightness interaction signatures, the depth achieved by the observations used is a particularly important factor, thus supporting the findings of Bennert et al. (2008; see above). This effect is also seen in the ground-based imaging studies, with the lowest rate of disturbance found being derived from images with short exposures (2–5 minutes) that achieve a limiting surface brightness of 24 to 25 mag arcsec^{-2} (mostly r-band; Greene et al., 2009). Both of these sets of observations are less sensitive than the other ground-based observations considered here (Ramos Almeida et al., 2011; Bessiere et al., 2012, and the current work), which have a typical limiting surface brightness ∼27 mag arcsec^{-2} that, in line with the general trend, results in higher measured rates of disturbance.

With these differences in limiting sensitivity in mind, it is useful to compare the rates of disturbance with those found for non-active galaxies from the general population, when considering the same surface brightness limits for the detected features (as highlighted by Ramos Almeida et al., 2012). Such comparisons were performed by Bessiere et al. (2012) and Wylezalek et al. (2016), who both found that the fractions of disturbed Type 2 host galaxies show significant excesses relative to those found for non-active early-type galaxies when appropriate ranges of surface brightness were considered: 75^{+7}_{-12} % compared to 37^{+7}_{-6} % (a 2.9 σ difference; Bessiere et al., 2012); and 45^{+11}_{-10} % compared to ∼15 % (Wylezalek et al., 2016). The results from the current analysis, which represents the first focused study of a large sample of the most luminous Type 2 quasars in the low-redshift universe ($z < 0.14$; $L_{[\mathrm{OIII}]} \geq 10^{35}$ W), are consistent with the findings of these two studies, with the Type 2 quasar hosts showing a high rate of disturbance that is an excess at the 3.7 σ level relative to their matched controls.

The high significance of this excess in the current work could be explained by the fact that subtle/low surface brightness features are harder to identify when using the interface method, and so galaxies securely classified as disturbed are more likely to have

Table 5.6: The disturbance rates and host type proportions from studies of the host morphologies of Type 2 quasars, compared with those obtained from the current work. Galaxies with both elliptical and lenticular morphologies are considered for the early-type proportions in all cases. The host type proportions are those determined from visual inspection, except those from Greene et al. (2009) and Wylezalek et al. (2016). These latter classifications are based on detailed modelling of the light profiles, with bulge-dominated profiles and disk-dominated profiles being considered to represent early-type and late-type galaxies, respectively. Note that the disturbance rates and host type proportions are not considered as mutually exclusive categories, except in Urbano-Mayorgas et al. (2019) and Zhao et al. (2019). The current interface classification results are presented both considering just the Type 2 quasar sample alone (Q2 only) and with the addition of the Type 1 and Type 2 quasars in the 3CR sample (Q2 + 3CR quasar). 3C 223 was classed as disturbed and as an elliptical galaxy in both of its sets of classifications, and was only considered once when deriving the listed results. All uncertainties have been converted to those provided by the method of Cameron (2011), where appropriate, for consistency with those in the current work.

	z	N	Disturbance fraction	Early-type	Late-type
HST					
Wylezalek et al. (2016)	0.2–0.6	20	45^{+11}_{-10} %	90^{+3}_{-11} %	10^{+11}_{-3} %
Urbano-Mayorgas et al. (2019)	0.3–0.4	41	22^{+8}_{-5} %	66^{+7}_{-8} %	12^{+7}_{-3} %
Zhao et al. (2019)	0.04–0.4	29	34^{+10}_{-8} %	28^{+10}_{-7} %	38^{+10}_{-8} %
Ground-based					
Greene et al. (2009)	0.1–0.45	15	27^{+14}_{-8} %	60^{+11}_{-13} %	27^{+14}_{-8} %
Ramos Almeida et al. (2011)	0.05–0.7	26	100_{-7} %	–	–
Bessiere et al. (2012)	0.3–0.41	20	75^{+7}_{-12} %	–	–
This work (Q2 only)	0.05–0.14	25	64^{+8}_{-10} %	56^{+9}_{-10} %	8^{+9}_{-3} %
This work (Q2 + 3CR quasar)	0.05–0.30	45	64^{+6}_{-8} %	73^{+6}_{-8} %	4^{+5}_{-1} %

higher surface brightness interaction signatures. Assuming that these brighter features are more common in the Type 2 quasar sample than in its matched control sample, as suggested by the results of the other studies, this would enhance the difference between the two. These results therefore support the idea that galaxy mergers and interactions provide an important triggering mechanism for these powerful AGN.

In addition to the results found for samples of Type 2 quasars selected for their extreme [OIII]λ5007 luminosities, Table 5.6 also provides the results determined considering the quasars in the radio-selected 2Jy and 3CR samples. Note that these results consider both the known Type 1 quasars and the Type 2 quasars with [OIII]λ5007 luminosities above the limit of $L_{[OIII]} \geq 10^{35}$ W, but the Type 1 quasars only comprise 5 out of 21 (24%) of the 3CR objects and 4 out of 26 (15%) of the 2Jy objects with quasar-like

[OIII]λ5007 luminosities. The rates of disturbance for the quasar hosts in these samples are again found to be high, with all 26 of the 2Jy objects and 14 out of 21 of the 3CR objects (67^{+8}_{-11} %) showing signs of disturbance. When the Type 2 quasar sample and 3CR quasar objects are considered together, the rate of disturbance is found to show an excess at the $5.1\,\sigma$ level relative to that found for the corresponding matched controls (64^{+6}_{-8} % and 26 ± 3 %, respectively), greatly strengthening the evidence to suggest that mergers and interactions are highly important for triggering these high-luminosity objects.

While the disturbance rate found for the 3CR quasars is consistent with that found for the Type 2 quasar sample, the rate for the 2Jy sample is found to be significantly in excess of both: differences at the $3.2\,\sigma$ and $3.4\,\sigma$ levels relative to the 3CR quasars and Type 2 quasar sample, respectively. However, it is found that the 2Jy quasars show a preference for higher [OIII]λ5007 luminosities than both of the other groups of objects, lying in the range $35.09 \leq \log(\mathrm{L}_{[\mathrm{OIII}]}) \leq 36.73$ W, with a median of $\log(\mathrm{L}_{[\mathrm{OIII}]}) = 35.43$ W. In particular, a Kolmogorov-Smirnoff test suggests that the null hypothesis that the [OIII]λ5007 luminosities for the 2Jy quasars and the Type 2 quasar sample are drawn from the same underlying distribution can be rejected at the 98.9% level ($D = 0.422$, $p = 0.011$); 95.3% confidence when the 3CR quasars are added to the latter ($D = 0.324$, $p = 0.047$). Given the evidence for a positive correlation between the disturbance enhancement ratio ($f_{\mathrm{AGN}}/f_{\mathrm{cont}}$) and [OIII]$\lambda$5007 luminosity found for the HERGs and Type 2 quasar objects within the current sample (§5.3.1), this supports the idea that merger-based triggering of radiatively-efficient AGN becomes increasingly important towards higher emission line luminosities.

In summary, the results of the interface classification analysis for the Type 2 quasar objects therefore support a scenario in which major galaxy mergers and interactions provide an important triggering mechanism for powerful quasar-like AGN, at least in the local universe. They also serve to demonstrate the necessity of using imaging observations that are sensitive to lower surface brightness interaction signatures, in order to determine the true rates of disturbance.

5.4.3 Host types

As mentioned in previous chapters, traditionally powerful radio AGN ($\mathrm{L}_{1.4\mathrm{GHz}} \gtrsim 10^{25}$ W Hz^{-1}) have a longstanding association with massive elliptical galaxies (e.g. Matthews et al., 1964; Dunlop et al., 2003; Best et al., 2005b). A minority of the objects in the high-flux-density selected 3CR and 2Jy samples do however exhibit disk-like morphologies upon cursory visual inspection, with these typically being found towards the lower end of the radio power range covered (Tadhunter, 2016). Some of these objects, in fact, have intermediate radio powers ($10^{22.5} < \mathrm{L}_{1.4\mathrm{GHz}} < 10^{25}$ W Hz^{-1}), which corroborates previous suggestions that late-type hosts could be more common in this range (e.g. Sadler et al., 2014). Furthermore, the results presented in Chapter 3 showed that HERGs in the intermediate radio power range have a mixture of early-type and late-type morphologies. In combination, these results could suggest a transition towards the predominantly late-type morphologies of Seyfert galaxies (e.g. Adams, 1977) at lower radio powers, at least for radiatively-efficient AGN.

The general trends observed for the morphological type proportions of the active galaxies classified using the interface provide strong support for this picture. Pearson correlation tests revealed evidence for strong positive correlations with radio power for the proportions of active galaxies classified as early-type in both the full active galaxy sample ($r_{\mathrm{full}} = 0.994$, $p_{\mathrm{full}} = 0.006$) and the HERG and Type 2 quasar subset ($r_{\mathrm{HERG}} = 0.998$, $p_{\mathrm{HERG}} = 0.002$). These are coupled with strong decreases in the proportions classified as late-type with increasing radio power, in both cases: $r_{\mathrm{full}} = -0.993$, $p_{\mathrm{full}} = 0.007$ and $r_{\mathrm{HERG}} = -0.997$, $p_{\mathrm{HERG}} = 0.003$, respectively. Both of these sets of trends are clearly demonstrated in Figure 5.8. From bootstrapping analysis, it was also found that these correlations were not sensitive to the uncertainties in the proportions measured in each radio power bin. These results therefore suggest that there is a gradual transition in the dominant host types of radio AGN from early-type galaxies at high radio powers to late-type galaxies at lower radio powers, particularly for radiatively-efficient objects. They are also consistent with the idea that secular triggering mechanisms related to galaxy disks (e.g. Hopkins & Quataert, 2010; Heckman & Best, 2014) become increasingly important towards lower radio powers, as suggested in Chapter 3.

The only significant difference between the morphological type proportions found for the active galaxies and control galaxies is the $3\,\sigma$ excess in the proportion of early-type classifications shown by the 3CR LERGs relative to their matched controls. A high excess of early-type galaxies is also found for the large sample of radio-intermediate LERGs studied by Gordon et al. (2019), for which 91% of the objects with Galaxy Zoo classifications were classed as early-type, compared with 63% of controls matched in stellar mass, redshift, and large-scale environment. Meanwhile, the proportion of 3CR HERGs classified as early-type is similar to that measured for the matched controls, and shows little evidence to suggest they are different (a difference at the $0.05\,\sigma$ level). These results indicate that LERG activity shows a stronger preference for early-type galaxies than HERG activity, at high radio powers.

The few detailed studies of the host galaxies of low to intermediate redshift Type 2 quasars mentioned in §5.4.2 have revealed that, like powerful radio galaxies, they generally show a preference for early-type morphologies relative to disk-dominated/late-type morphologies, as determined from light-profile fitting or visual inspection (see Table 5.6). The only inconsistency in this sense is the study of Zhao et al. (2019), who found a slight preference for late-type galaxies relative to early-types, based on visual inspection, although the difference is not significant ($<1\,\sigma$): 38^{+10}_{-8} % and 28^{+10}_{-7} %, respectively.

Looking at the results for the current Type 2 quasar sample, it is found that the majority of host galaxies are classed as early-type (52^{+9}_{-10} % elliptical, 4^{+8}_{-1} % lenticular) and only 2 out of 25 (8^{+9}_{-3} %) and 3 out of 25 (12^{+10}_{-4} %) are classed as late-type or "merger", respectively; the remaining 24^{+10}_{-6} % have uncertain host types. The preference for early-type hosts is enhanced when the radio-loud quasars in the 3CR sample are also considered, with the proportion rising to 73^{+6}_{-8} %. These results agree well with those of Dunlop et al. (2003), who found both radio-loud and radio-quiet quasars to be predominantly hosted by elliptical galaxies. The host type classifications determined using the interface therefore appear to show good general agreement with those from these previous studies, and lend favour to the idea that powerful quasar-like activity and early-type galaxies are strongly linked.

It is interesting to note that all 6 of the Type 2 quasar hosts that were classified as having an uncertain morphological type were also classed as disturbed based on the responses to the first of the interface questions. In addition, the Type 2 quasar hosts showed a significant excess of the "merger" category relative to their matched controls (at the $3\,\sigma$ level). Coupled with the significant deficit of late-type morphologies in their hosts relative to the matched control galaxies (see Figure 5.7) and their high overall rate of disturbance (64^{+8}_{-10} %), this suggests that Type 2 quasars could preferentially lie in disturbed early-type galaxies, a significant proportion of which are too highly disturbed for the morphological type to be determined accurately. This lends support to the idea that galaxy mergers and interactions are particularly important for triggering this type of AGN, which have the brightest optical emission lines in the general population.

5.5 Chapter summary and conclusions

This chapter has described the analysis of the morphological classifications obtained for the galaxies in the RI-HERG low, RI-HERG high, 3CR, and Type 2 quasar samples using the online interface described in Chapter 4. These classifications were also obtained for large samples of control galaxies matched to the active galaxies in terms of both stellar mass and redshift, to allow the results to be compared with those determined for non-active galaxies in the general population at low to intermediate redshifts.

The broad range of 1.4 GHz radio powers and [OIII]λ5007 emission line luminosities covered by the active galaxy samples has allowed the dependence of AGN triggering by galaxy mergers and interactions on these properties to be investigated in detail. The dependence of host galaxy type on the AGN radio power has also been assessed. The main results are as follows.

- The active galaxies are found to be more frequently disturbed than the matched control galaxies across the full range of stellar masses and redshifts covered by the samples. These excesses are seen with varying levels of significance across the different samples, with the most significant excesses being found for the 3CR ($4.3\,\sigma$) and Type 2 quasar samples ($3.7\,\sigma$). In the former case, this is largely driven by the HERGs in the sample, which show a $4.7\,\sigma$ excess relative to their matched controls. The 3CR LERGs, by comparison, only show a $1.2\,\sigma$ excess in their disturbance fraction. A highly significant excess in the disturbance rate relative to the matched controls is found when all of the objects with quasar-like [OIII]λ5007 emission line luminosities are considered together ($\mathrm{L}_{\mathrm{[OIII]}} \geq 10^{35}$ W; the Type 2 quasar objects and 3CR quasars): $64\,^{-8}_{+6}$ % and 26 ± 3 % for the quasar-like objects and controls, respectively, a difference at the $5.1\,\sigma$ level.

- There is no strong evidence to suggest that the rates of disturbance in the active galaxies are correlated with 1.4 GHz radio power when the rates measured for their matched controls are accounted for. This goes against the conclusions found from the detailed study of the RI-HERG low sample (Chapter 3), although there are suggestions that an underlying correlation between the radio powers and the stellar masses of the objects could have had a significant influence on these results (§5.4.1). In contrast, there is clear evidence to suggest that the enhancement in the rate of disturbance for the HERGs and Type 2 quasars in the sample relative to that found for the matched controls ($f_{\mathrm{AGN}}/f_{\mathrm{cont}}$) increases strongly with [OIII]λ5007 luminosity: $r = 0.972$, $p = 0.028$, from a Pearson correlation test. A significant correlation is not found when the 3CR LERGs are included, suggesting that this relation is most relevant for the hosts of radiatively-efficient AGN.

- The disturbed galaxies in the radio-selected AGN samples show a significant preference for post-coalescence interaction signatures relative to pre-coalescence signatures, suggesting that these objects are more likely to be triggered in the late stages of galaxy mergers. The Type 2 quasars, on the other hand, show the opposite preference, suggesting that they are more likely to be triggered in the early stages of mergers and interactions.

- The AGN in almost all samples show a preference for early-type host galaxies relative to late-types. The exception is the RI-HERG low sample, which exhibits a preference for late-type hosts and a significant deficit ($> 3\sigma$) of early-types relative to its matched control sample. The measured host type proportions also suggest that the fraction of early-type hosts decreases strongly with decreasing radio power, while the fraction of late-type hosts increases. This supports the idea of a transition in the dominant host types of radiatively-efficient radio AGN from early-type galaxies at high radio powers to late-type galaxies at lower radio powers, as suggested in Chapter 3. This could also suggest that triggering via secular processes in galaxy disks holds more importance for these latter objects.

Overall, the measured rates of disturbance imply that the importance of galaxy mergers and interactions for triggering radiatively-efficient AGN (HERGs/Type 2 quasars) is strongly dependent on their optical emission line luminosities (which are correlated with their bolometric luminosities), but not strongly on their radio powers. Moreover, there is particularly strong evidence to suggest that galaxy mergers and interactions provide the dominant triggering mechanism for quasar activity at low to intermediate redshifts. In contrast, these processes appear to be of much lower importance for triggering radiatively-inefficient radio AGN at high radio powers, with the majority of 3CR LERGs being associated with undisturbed elliptical galaxies. The host type fractions are consistent with the picture of a transition in the preferred host types for radiatively-efficient radio AGN from early-type galaxies at high radio powers to the predominantly late-type hosts of Seyfert nuclei at lower radio powers.

Chapter 6

The radio properties of radio-intermediate HERGs

6.1 Declaration

The work described in this chapter was reported in the second of my lead-author publications in Monthly Notices of the Royal Astronomical Society: Pierce et al. (2020), *The radio properties of high-excitation radio galaxies with intermediate radio powers*. Much of the content of this chapter is presented as it was in the publication, but has been adapted for this thesis where appropriate.

6.2 Chapter introduction

As outlined in previous chapters, the jets of radio AGN are often deemed to affect the evolution of their host galaxies through two major feedback processes: i) driving multiphase outflows on the scales of galaxy bulges (e.g. Morganti et al., 2005; Holt et al., 2008; Molyneux et al., 2019); ii) preventing hot gas from cooling to form stars in galaxy haloes, or even the surrounding environment on larger scales (e.g. see McNamara & Nulsen, 2007). There is strong evidence to suggest that AGN with intermediate radio powers ($22.5 < \log(\mathrm{L}_{1.4\mathrm{GHz}}) < 25.0$ $\mathrm{W\,Hz^{-1}}$) and high-excitation optical emission spectra (radio-intermediate HERGs) are particularly important for the former case, since they are seen to be associated with significant kinematic disturbances in both warm-ionised and molecular gas (Mullaney et al., 2013; Tadhunter et al., 2014b; Harrison et al., 2015; Ramos Almeida et al., 2017; Villar-Martín et al., 2017), and are considerably more common than their high-radio-power counterparts (Best & Heckman, 2012). Detailed characterisation of this population could therefore be crucial for providing a better understanding of the role of radio AGN feedback in galaxy evolution.

As a general population, the nuclear activity in HERGs has frequently been linked with the radiatively-efficient accretion of cold gas at relatively high Eddington ratios (e.g. Best & Heckman, 2012; Heckman & Best, 2014; Mingo et al., 2014). At high radio powers, HERGs are also predominantly associated with FRII-like (edge-brightened) radio morphologies, leading to suggestions that such structures could be inherently connected to this mode of accretion (e.g. Lin et al., 2010; Tadhunter, 2016). This is supported by the fact that some Seyfert galaxies, arguably the optically-selected equivalents of HERGs at low radio powers, are also seen to exhibit double-lobed or edge-brightened radio morphologies (Ulvestad & Wilson, 1984; Morganti et al., 1999; Baldi et al., 2018a).

However, the strength and nature of this connection between double-lobed radio structures and radiatively-efficient accretion across the range of radio powers covered by HERGs remains uncertain. For instance, Baldi & Capetti (2010) find that ∼80%

of a sample of 67 local HERGs ($0.03 < z < 0.3$) selected from Best et al. (2005b) have unresolved radio emission structures at the ∼5” limiting angular resolution of the FIRST survey (Becker et al., 1995). This is also found to be true for 97% of the 30 local HERGs with intermediate radio powers ($z < 0.1$; $22.5 < \log(\mathrm{L}_{1.4\mathrm{GHz}}) < 24.0$ W Hz^{-1}) studied for the work presented in Chapter 3. Moreover, several studies in the last decade have shown that the local radio AGN population as a whole is dominated by sources with radio emission that is compact on galaxy scales, given the resolution of typical radio surveys (e.g. Baldi & Capetti, 2010; Sadler et al., 2014; Whittam et al., 2016; Hardcastle et al., 2019). These sources are often collectively termed “FR0s”, in order to separate them from the two traditional classes of extended radio structures: Fanaroff-Riley Type Is (FRIs) and Type IIs (FRIIs, as above; Fanaroff & Riley, 1974).

The majority of FR0s have massive, early-type host galaxies with large central black hole masses (Baldi et al., 2015, 2019a), and typically exhibit low-to-intermediate radio powers ($10^{22} \lesssim \mathrm{L}_{1.4\mathrm{GHz}} \lesssim 10^{24}$ W Hz^{-1}; Baldi et al., 2018b). They are in general identified with LERGs, in which the nuclear activity is thought to be fuelled by a radiatively-inefficient accretion flow at low Eddington ratios (e.g. Best & Heckman, 2012). LERGs at high radio powers are commonly associated with FRI-like (edge-darkened) radio morphologies (Tadhunter, 2016), and have properties that are consistent with the typical host galaxies of FR0 sources: they are also massive; of early-type; and have large black hole masses (Baldi et al., 2015, 2019a; Capetti et al., 2017). In addition, FR0 sources with LERG spectra are found to extend the correlation between core radio luminosity and emission-line luminosity defined by FRIs to lower radio powers (Baldi et al., 2019a).

This has led to suggestions that FRI and FR0 sources are members of a homogeneous LERG population, with the compact emission in FR0s being caused by either short cycles of radio activity or lower jet bulk speeds (e.g. Baldi et al., 2018b, 2019a). It is important to mention, however, that this picture is likely too simplistic, since these latter studies of FR0s are restricted to LERG sources only, and thus exclude known HERG sources with compact radio morphologies. For example, 2 out of the 11 (18^{+16}_{-6} %) compact sources studied by Baldi et al. (2015) have HERG spectra and radio structures that are compact on similar scales to their LERG/FR0s. In addition, a significant minority of high-radio-power LERGs have FRII-like, rather than FRI-like, radio structures (e.g. Baldi et al., 2010; Tadhunter, 2016), which provide a further challenge to the idea of a homogeneous LERG population in terms of radio properties.

Although local LERGs and HERGs with moderate radio powers typically have radio structures that are unresolved on galaxy scales, it is important to note that they could possess extended structures on small (kiloparsec to subkiloparsec) physical scales. Indeed, the double-lobed structures found for some Seyfert galaxies typically manifest on scales of a few 100 pc (Ulvestad & Wilson, 1984), and some sources classified as FR0s in fact exhibit core-jet ("mini-FRI") morphologies on similar scales (e.g. Baldi et al., 2015). In this context, high-resolution radio observations of HERGs with radio powers that are intermediate between those of high-power FRIIs on the one hand, and Seyfert galaxies on the other, could be particularly important for testing how strongly the black hole accretion mode is linked with the two traditional classifications of extended radio emission, i.e. HERGs with FRIIs and LERGs with FRIs, across all radio powers. Given that radio-intermediate HERGs show strong evidence for feedback, such observations could also be important for uncovering the scales on which the radio jets typically interact with the interstellar medium in their host galaxies, and hence help to improve models of galaxy evolution.

Despite their potential importance for understanding both accretion modes and jet-induced feedback, there is a lack knowledge of the detailed radio properties of radio-intermediate HERGs. Therefore, high-resolution VLA radio observations of a sample of 16 local HERGs with intermediate radio powers ($z < 0.1$; $23.0 < \log(\mathrm{L}_{1.4\mathrm{GHz}}) < 24.0$ W Hz^{-1}) were conducted, with the goal of investigating their detailed radio morphologies down to subkiloparsec physical scales. This is in order to test whether they are consistent with the double-lobed structures observed for high-power HERGs and some Seyfert galaxies, or rather the highly-compact or core-jet structures of LERG/FR0 sources. The radio spectra of these objects are also investigated. The chapter is structured as follows. Details on the selection of the sample (a subset of the RI-HERG low sample), the observations, and the reduction, calibration and image production process are outlined in §6.3. The results of the analysis of the images are presented in §6.4, which are discussed and compared to results from the literature in §6.5. A summary of the study is presented in §6.6.

6.3 Sample selection, observations and reduction

6.3.1 Sample selection

The sources studied for this research comprise a 94% complete sample of 16 HERGs with radio powers in the range $23.0 < \log(\mathrm{L}_{1.4\mathrm{GHz}}) < 24.0$ W Hz^{-1}, low redshifts ($z < 0.1$), and right ascension values (α) in the range 07h 15m $< \alpha <$ 16h 45m, as selected from the catalogue of Best & Heckman (2012). These objects represent the subset of the

RI-HERG low sample outlined in Chapter 2 that lie in this range of radio powers, for which the optical r-band images were analysed for the research presented in Chapter 3. The complete sample fulfilling these criteria comprises 17 objects, but one object was not observed due to VLA scheduling constraints (J1622+07).

As outlined in §6.2, all except one of the objects in the RI-HERG low sample (97%) have unresolved emission structures at the $\sim$5 arcsec limiting angular resolution of the FIRST survey. The subsample studied in this chapter includes the one source with clear extended radio emission (J1351+46), and so 15 out of the 16 observed sources (94%) have unresolved radio structures in the FIRST images. The VLA observations hence provided the opportunity to investigate the radio morphologies of the current subsample of 16 radio-intermediate HERGs on much smaller physical scales, to meet the goals of the project. Note that the higher end of the radio power range of the RI-HERG low sample was chosen for the radio observations in order to optimise the signal-to-noise ratio achievable with relatively short on-source integration times (see §6.3.2), and hence improve the observing efficiency.

In addition to the main sample, the two HERGs that have radio powers below the lower end of the range outlined above were also observed with the VLA as part of this project: J0911+45 and J1012+08, with radio powers of $\log(\mathrm{L}_{1.4\mathrm{GHz}}) = 22.62$ and $\log(\mathrm{L}_{1.4\mathrm{GHz}}) = 22.39$, respectively. These are the objects which initially fulfilled the radio power selection criterion based on low resolution NVSS data, which can be subject to source confusion, but were subsequently found to have lower radio powers based on the higher resolution FIRST observations. Observations for these two sources are not included in this chapter, but are presented in Appendix B, for completeness. Some basic information on all of the sources observed with the VLA, including these lower-radio-power sources, is provided in Chapter 2, Table 2.1.

The sample contains a mixture of morphological types, as determined from the visual classifications outlined in Chapter 3, with $31^{+13}_{-9}\,\%$ classified as early-type (elliptical or lenticular), $31^{+13}_{-9}\,\%$ as late-type (spiral or disk), and $38^{+13}_{-10}\,\%$ showing highly disturbed morphologies that are suggestive of galaxy mergers and interactions. The stellar masses of the galaxies lie in the range $10.3 \leq \log(\mathrm{M}_*/\mathrm{M}_\odot) \leq 11.4$, with a median of $10^{10.9}$ $\mathrm{M}_\odot$. The radio powers cover the range $23.01 \leq \log(\mathrm{L}_{1.4\mathrm{GHz}}) \leq 23.98$ $\mathrm{W\,Hz^{-1}}$, but show a preference for lower radio powers within these limits and have a median value of $\mathrm{L}_{1.4\mathrm{GHz}} = 10^{23.31}$ $\mathrm{W\,Hz^{-1}}$.

6.3.2 VLA observations

Continuum L- and C-band observations of the 16 sources in the sample were obtained using the Karl G. Jansky Very Large Array (VLA) in the A-array configuration, taken between 2018 March 25 and 2018 May 17. The use of these two frequency bands allowed for the detection of both diffuse (L-band) and more compact (C-band) emission structures, while also opening up the possibility of determining spectral indices for the sources in the frequency range covered. The L-band observations were conducted using the default configuration of two 8-bit samplers, each with 64 × 1.0 MHz-width channels, yielding a total bandwidth of 1024 MHz centred on a frequency of 1.5 GHz. Two 8-bit samplers were also used for the C-band observations, but were composed of 64 × 2.0 MHz-width channels (i.e. each with total width 1024 MHz) and centred on frequencies of 4.5 GHz and 7.5 GHz. This allowed the C-band to be separated into two distinct subbands, which could be considered separately during subsequent analysis and image production.

On-source integration times for L- and C-band observations were $\sim$5–6 minutes and $\sim$10–12 minutes, respectively. One of the two standard flux density calibrators 3C 147 or 3C 286 was observed at the beginning of each set of observations in both L- and C-bands, and these data were used for flux density and bandpass calibration of the target observations in both bands. The on-source times in the L-band were $\sim$6–7 minutes and $\sim$8–10 minutes for 3C 147 and 3C 286, respectively, with $\sim$2 minute on-source times being used for both calibrators in the C-band. Suitable phase calibrators, selected from the list of standard VLA calibrators[1], were observed before and after each target observation for $\sim$1–3.5 minutes and $\sim$2–4 minutes in the L- and C-bands, respectively. These were used to determine calibration solutions for the complex antenna gains.

---

[1] Available at: https://science.nrao.edu/facilities/vla/observing/callist.

Table 6.1: Basic properties of the final images produced for all targets at all three frequencies. Beam sizes (θ_ν) and position angles (ψ_ν) are provided, with the latter measured with the positive direction from North to East on the sky. Root-mean-square (rms; σ_ν) values, as measured from the residual background variations in boxes placed in suitable regions close to the targets, are also presented. The dates of the target observations are also listed in the final column.

Name	$\theta_{1.5}$ (arcsec)	$\psi_{1.5}$ (deg)	$\sigma_{1.5}$ (μJy)	$\theta_{4.5}$ (arcsec)	$\psi_{4.5}$ (deg)	$\sigma_{4.5}$ (μJy)	$\theta_{7.5}$ (arcsec)	$\psi_{7.5}$ (deg)	$\sigma_{7.5}$ (μJy)	Obs. date
J0725+43	1.76 × 1.40	81.2	86.0	0.71 × 0.50	85.1	16.4	0.41 × 0.28	-82.5	12.0	2018-03-25
J0757+39	1.98 × 1.40	-84.4	58.4	0.74 × 0.54	78.7	20.6	0.42 × 0.29	-88.0	21.9	2018-03-25
J0810+48	1.66 × 1.19	89.2	117.0	0.77 × 0.51	73.1	18.1	0.42 × 0.28	83.4	16.6	2018-03-25
J0836+44	1.80 × 1.28	-81.2	66.5	0.70 × 0.50	85.0	26.8	0.40 × 0.28	-84.7	17.9	2018-03-25
J0902+52	1.62 × 1.24	87.7	71.2	0.88 × 0.50	76.0	18.2	0.45 × 0.28	86.8	23.8	2018-03-28
J0950+37	1.70 × 1.35	37.7	90.6	0.78 × 0.45	-84.1	17.0	0.45 × 0.28	-84.3	16.2	2018-03-28
J1108+51	2.01 × 1.07	82.5	77.2	0.60 × 0.45	76.4	14.0	0.52 × 0.35	28.1	16.1	2018-04-14
J1206+10	2.26 × 1.58	-36.8	182.4	0.83 × 0.45	-52.8	17.5	0.51 × 0.30	-53.7	15.3	2018-04-14
J1236+40	1.63 × 1.16	-85.4	58.3	0.67 × 0.45	-83.0	19.2	0.42 × 0.29	-84.4	13.8	2018-04-14
J1243+37	2.74 × 1.47	78.3	280.0	0.66 × 0.49	88.2	18.0	0.41 × 0.29	-85.0	13.8	2018-04-14
J1257+51	1.54 × 1.22	69.1	50.8	0.57 × 0.45	45.5	13.2	0.34 × 0.27	45.5	13.0	2018-04-12
J1324+17	1.48 × 1.20	-48.8	81.5	0.55 × 0.47	-46.1	12.3	0.33 × 0.28	-45.6	11.5	2018-04-12
J1351+46	1.58 × 1.27	0.9	57.2	0.57 × 0.47	29.3	13.6	0.37 × 0.28	28.1	12.9	2018-04-12
J1358+17	1.58 × 1.30	-86.8	101.9	0.58 × 0.47	-50.7	12.6	0.35 × 0.29	-53.5	15.9	2018-04-12
J1412+24	1.43 × 1.27	42.2	60.4	0.52 × 0.47	7.6	21.8	0.31 × 0.28	5.8	14.3	2018-05-17
J1609+13	1.38 × 1.15	6.8	84.9	0.52 × 0.45	0.6	25.6	0.31 × 0.27	0.6	13.8	2018-05-17

All data reduction, calibration, and image production was performed using standard procedures in the *Common Astronomy Software Applications* (CASA, v. 5.4.1) package, specifically designed for the post-processing of radio-astronomical data (see McMullin et al., 2007). Manual flagging of spurious bad data caused by issues related to individual antenna problems, bad baseline correlations, or radio frequency interference (RFI) was carried out on all calibrator targets prior to calibration of the science target data. Such flagging was also performed on the science target data after the relevant calibration procedures had been applied, where necessary. The poor quality of some of the data resulted in significant losses in some cases; it is estimated that up to ∼50% of the data were lost for the L-band target observations, in particular, but only ∼10–20% for the C-band observations, mainly due to the more significant RFI issues associated with the former dataset.

Following this, iterative self-calibration of the science target data was also performed, firstly using phase-only solutions to remove any residual phase errors that remained after the primary calibration procedures. These were then followed by joint amplitude-phase solutions to correct for residual amplitude errors. This was done until the quality of the subsequent image was not further improved; in some cases, the initial self-calibration provided no improvements, either due to the faintness of the target or to bright sources in the surrounding field negatively affecting the solutions.

All continuum images were produced using the CASA task CLEAN. Images were made for the observations of each target in the L-band and in both of the two sub-bands of the C-band, to provide continuum images centred on frequencies of 1.5 GHz, 4.5 GHz, and 7.5 GHz. Pixel sizes of 0.4 × 0.4 arcsec and 0.1 × 0.1 arcsec were used for the L-band and C-band images, respectively, and natural weighting was used in all cases. The limiting angular resolution achieved in the L-band images for the main sample, estimated by averaging the two beam axes in each case, covered the range 1.27 – 2.11 arcsec, with a median of 1.44 arcsec. Derived in the same way, the values for the C-band were found to cover the range 0.49 – 0.69 arcsec (median = 0.57 arcsec) in the images at 4.5 GHz, and from 0.29 – 0.44 arcsec (median = 0.34 arcsec) in the images at 7.5 GHz. The median root-mean-square (rms) values for residual background variations in the final images, measured in boxes placed in suitable regions close to the targets, are 79.4 μJy beam^{-1}, 17.8 μJy beam^{-1}, and 14.8 μJy beam^{-1} for the images at 1.5 GHz, 4.5 GHz, and 7.5 GHz, respectively. The restoring beam sizes and rms values for all of the final continuum images at each of the three frequencies are listed in Table 6.1, along with dates of the individual target observations.

6.4 Image analysis and Results

The final continuum images produced for all 16 radio-intermediate HERGs at each of the three frequencies (1.5 GHz, 4.5 GHz, and 7.5 GHz) were used to investigate the detailed morphological structure of the radio emission, to meet the main objectives of the project. It is found that there is a mixture of unresolved and extended sources within the sample, which are discussed separately below (in §6.4.1 and §6.4.2, respectively). The flux density and scale of the emission at the three frequencies was determined from all of the target images, derived as described below and presented in Tables 6.2 and 6.3. Radio spectra for the unresolved sources are also presented, which are shown in Figure 6.1. Contour maps of the extended sources at each frequency are provided in Figures 6.4 and 6.5.

6.4.1 Unresolved sources

The first step in characterising the morphology of the radio emission involved separating the sample into resolved and unresolved structures. In order to evaluate whether the radio structures were resolved or unresolved at the resolution of a given image, model Gaussian profiles were fitted to the target emission using the CASA task IMFIT. The measured angular full-width half maximum (FWHM), position angle, and peak flux density provided by the fits were then compared with the restoring beam parameters and total flux density measured for each target, to determine whether the emission was more characteristic of an unresolved or extended source.

From this, it is seen that 9 of the 16 galaxies in the sample ($56\,^{+11}_{-12}\,\%$) have unresolved structures in the VLA observations at all three observing frequencies, meaning that they are compact to an angular resolution of ~0.3 arcsec. In terms of projected physical scale, this is equivalent to ~220–500 pc for these galaxies (median = 420 pc). The limiting angular sizes and corresponding maximum physical diameters of the emission for each of the unresolved sources are reported in Table 6.2, as obtained from the IMFIT fits to the images at 7.5 GHz.

Table 6.2: Flux density measurements and spectral indices for all 9 sources in the sample with unresolved radio structures in the images at all three frequencies, whose basic radio spectra are presented in Figure 6.1. The peak flux density values at each frequency (F_{ν}^{P}) are provided by the double-Gaussian fits of the target emission performed by the CASA task IMFIT. Separate spectral indices for the power law slopes between 1.5 GHz and 4.5 GHz (α_1) and between 4.5 GHz and 7.5 GHz (α_2) are also listed. The maximum angular extents of the structures are provided in the penultimate column (in arcseconds), as estimated using the average of the two beam axes for the images at 7.5 GHz. Estimated physical sizes derived from these values are listed in parsecs in the final column.

Name	F_{NVSS} (mJy)	F_{FIRST} (mJy)	$F_{1.5}^{P}$ (mJy)	$F_{4.5}^{P}$ (mJy)	$F_{7.5}^{P}$ (mJy)	α_1 (1.5-4.5 GHz)	α_2 (4.5-7.5 GHz)	ϕ^{lim} (arcsec)	r_{lim} (pc)
J0725+43	11.0	10.8	9.36 ± 0.48	4.12 ± 0.21	2.02 ± 0.10	-0.746 ± 0.066	-1.40 ± 0.14	0.35	440
J0757+39	99.7	99.2	71.6 ± 3.6	24.1 ± 1.2	12.30 ± 0.62	-0.991 ± 0.064	-1.32 ± 0.14	0.36	430
J0810+48	37.8	49.1	41.1 ± 2.1	17.50 ± 0.88	8.85 ± 0.44	-0.777 ± 0.064	-1.33 ± 0.14	0.35	490
J0950+37	66.6	68.3	61.6 ± 3.1	29.7 ± 1.5	17.12 ± 0.86	-0.665 ± 0.064	-1.08 ± 0.14	0.37	280
J1243+37	13.6	12.6	10.76 ± 0.69	6.40 ± 0.32	4.42 ± 0.22	-0.473 ± 0.074	-0.73 ± 0.14	0.35	540
J1257+51	7.5	7.2	6.91 ± 0.35	3.23 ± 0.16	2.04 ± 0.10	-0.692 ± 0.065	-0.90 ± 0.14	0.31	520
J1324+17	13.6	14.5	12.79 ± 0.65	5.38 ± 0.27	3.24 ± 0.16	-0.789 ± 0.065	-0.99 ± 0.14	0.31	470
J1358+17	17.8	7.9	10.40 ± 0.54	9.84 ± 0.49	8.08 ± 0.40	-0.050 ± 0.066	-0.39 ± 0.14	0.32	540
J1412+24	14.9	13.2	13.34 ± 0.67	5.07 ± 0.26	3.07 ± 0.16	-0.881 ± 0.065	-0.98 ± 0.14	0.30	370

Since the radio structures for these compact sources are unresolved in the images at all three frequencies, it was considered that the peak flux density values determined by the IMFIT task were reasonable estimates for the total flux density values for each target at each frequency. Errors in the peak flux density measurements were estimated by taking into account contributions from the fitting errors provided by IMFIT, the background noise in the image (following Klein et al., 2003), and the uncertainty in the flux density calibration models (considering the upper limit of 5% determined by Perley & Butler, 2017). Based on the assumption that the sources are point-like at all frequencies, it was then possible to produce basic radio spectra for the targets and estimate the slope of the power law (for $F_\nu \propto \nu^\alpha$) between 1.5 GHz and 4.5 GHz (α_1) and between 4.5 GHz and 7.5 GHz (α_2). These spectra are presented in Figure 6.1, and the peak flux density values and estimated power law slopes are also listed in Table 6.2.

From the spectra, it is seen that the majority (7 out of 9) of the unresolved sources show steep power laws between 1.5 GHz and 4.5 GHz ($-0.99 < \alpha_1 < -0.67$), which are characteristic of standard predictions for optically-thin synchrotron emission. The objects J1243+37 and J1358+17, however, have flatter spectra between these frequencies ($\alpha_1 = -0.47$ and -0.05), and J1358+17 remains relatively flat between 4.5 GHz and 7.5 GHz ($\alpha_2 = -0.39$). All of the unresolved objects show steeper spectra between 4.5 GHz and 7.5 GHz (median $\alpha_2 = -0.99$), regardless of their spectral index between 1.5 GHz and 4.5 GHz (median $\alpha_1 = -0.75$), with a median difference in spectral index of $\Delta\alpha = 0.33$ seen between the two ranges. This is shown clearly in Figure 6.2, where α_2 is plotted against α_1 for the unresolved sources and it is seen that all points lie below the line of equality between the two.

Although it is found that these sources are unresolved at the resolution of the VLA observations, it is important to assess whether the sources are truly compact in nature, or rather have extended emission on larger scales that has been resolved out. To investigate this, the 1.5 GHz peak flux densities derived from the VLA observations (here $F_{\rm VLA}$) are here compared with their 1.4 GHz FIRST flux densities ($F_{\rm FIRST}$); these are plotted against each other in Figure 6.3, for both the unresolved and extended sources (see §6.4.2 for discussion of the latter). Here, it is seen that the majority of the unresolved sources lie close to the line of equality between the two, and in fact 6 out of 9 have $F_{\rm FIRST}$ values that lie within $3\,\sigma$ of their $F_{\rm VLA}$ values, suggesting that in most cases the sources have little diffuse emission and are genuinely compact on sub-kpc scales.

However, there is still a tendency for the VLA 1.5 GHz flux densities to lie below the FIRST values, with a median $F_{\rm VLA}/F_{\rm FIRST}$ ratio of 0.88. This could at least partly

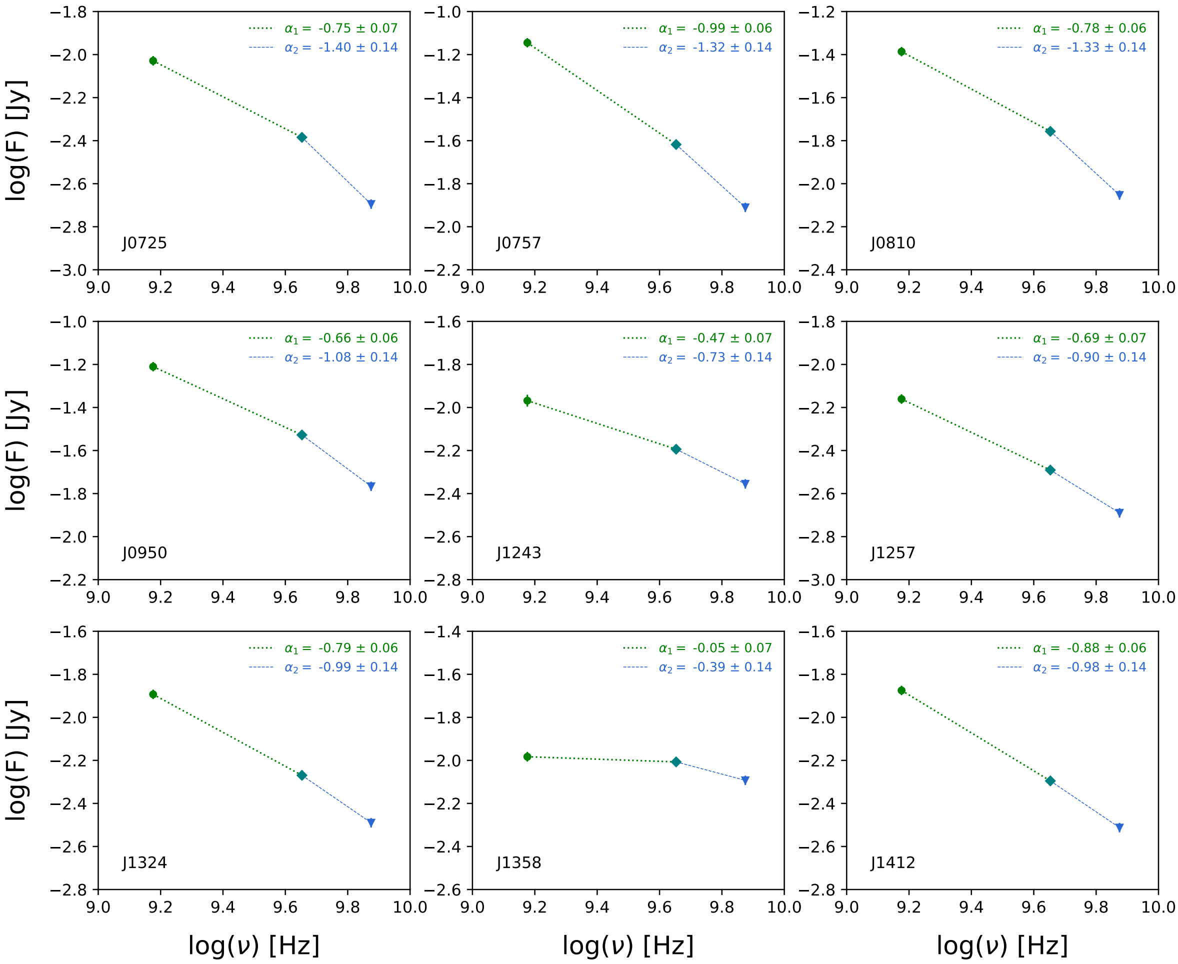

Figure 6.1: Basic radio spectra for the 9 targets that have unresolved structures in the images at all three frequencies, and hence appear as point sources. The flux density measurements were determined using the CASA task IMFIT. The uncertainties associated with these measurements are plotted, but are too small to be visible on the graphs. Estimations of the spectral indices between 1.5 GHz and 4.5 GHz (α_1) and between 4.5 GHz and 7.5 GHz (α_2) are indicated on each graph alongside their associated errors – these are also listed in Table 6.2. These were derived from the measured flux densities at the limits of the aforementioned ranges, as appropriate. Shortened versions of the target names are also indicated in the bottom-left corner of the graphs.

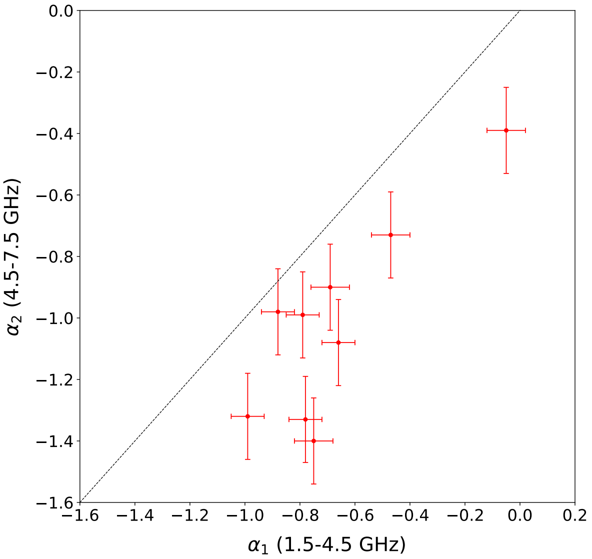

Figure 6.2: The spectral indices from 4.5 GHz to 7.5 GHz (α_2) plotted against those from 1.5 GHz to 4.5 GHz (α_1) for the unresolved sources in the sample. All points are seen to lie below the line of one-to-one correspondence (black), highlighting the systematic spectral steepening that occurs towards higher frequencies. The errors on the points are those listed in Table 6.2.

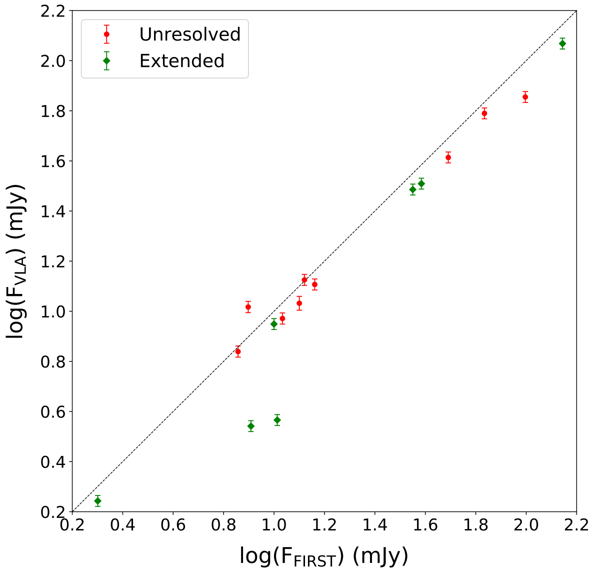

Figure 6.3: The flux densities measured from the VLA images at 1.5 GHz for all unresolved (red points) and extended (green points) sources in the sample, plotted against their FIRST flux densities. Errors are as listed in Tables 6.2 and 6.3.

be explained by the slight difference in the effective frequencies of the two observations: using the median spectral index of the unresolved objects between 1.5 and 4.5 GHz, $\alpha_1 = -0.75$, the expected ratio of the flux densities at 1.5 and 1.4 GHz would be $F_{\rm VLA}/\rm F_{FIRST} = 0.95$. Furthermore, when flagging poor L-band data, more were lost towards the lower frequencies within the band, which would shift the effective frequency to higher values and further lower the expected $F_{\rm VLA}/F_{\rm FIRST}$ ratio; if the effective central frequency was shifted by an additional 0.1 GHz to 1.6 GHz, for example, the expected value would be $F_{\rm VLA}/F_{\rm FIRST} = 0.90$.

However, two of the sources that are unresolved in the VLA observations, J0757+39 and J0810+48, have $F_{\rm VLA}$ values that are significantly lower than their FIRST values (differences at the $7.7\,\sigma$ and $3.9\,\sigma$ levels, respectively). Despite the fact that their emission structures appear to be unresolved in both the FIRST and VLA images, there is still the possibility that the lower flux densities in these cases could be explained by the loss of detection of diffuse emission at the higher angular resolutions achieved.

On the other hand, the final unresolved source (J1358+17) has a VLA 1.5 GHz flux density that lies $4.6\,\sigma$ *above* its FIRST value, and the discrepancy hence cannot be explained in the same way. The flat spectrum observed for J1358+17, however, could suggest that it is a beamed, variable source, which may explain the difference in this case. Further discussion on the unresolved sources is reserved for §6.5.

6.4.2 Extended sources

All of the 7 remaining galaxies in the sample ($44\,^{+12}_{-11}\,\%$) show at least marginally resolved structures in the images at all three frequencies, i.e. even at the typical angular resolution of the L-band images (∼1.4 arcsec). Contour maps at all three frequencies are shown for these galaxies in Figures 6.4 and 6.5, and their contour levels and beam parameters are presented in Table 6.3. A brief description of the emission for each of the extended sources follows here, including comparisons with the optical appearance of the host galaxies in the r-band images presented in Chapter 3.

J0836+44. This source is clearly extended in the images at all three observing frequencies. It exhibits a tail of emission that propagates to ∼4 kpc in projected radial extent from its centre, which is most clearly visible in the two C-band images. The C-band images also reveal a potential double-lobed structure that appears to be symmetric about the optical centre of the galaxy (particularly at 7.5 GHz), with projected diameter ∼2 kpc. The emission is confined to the high-surface-brightness structure of the galaxy that is visible at optical wavelengths.

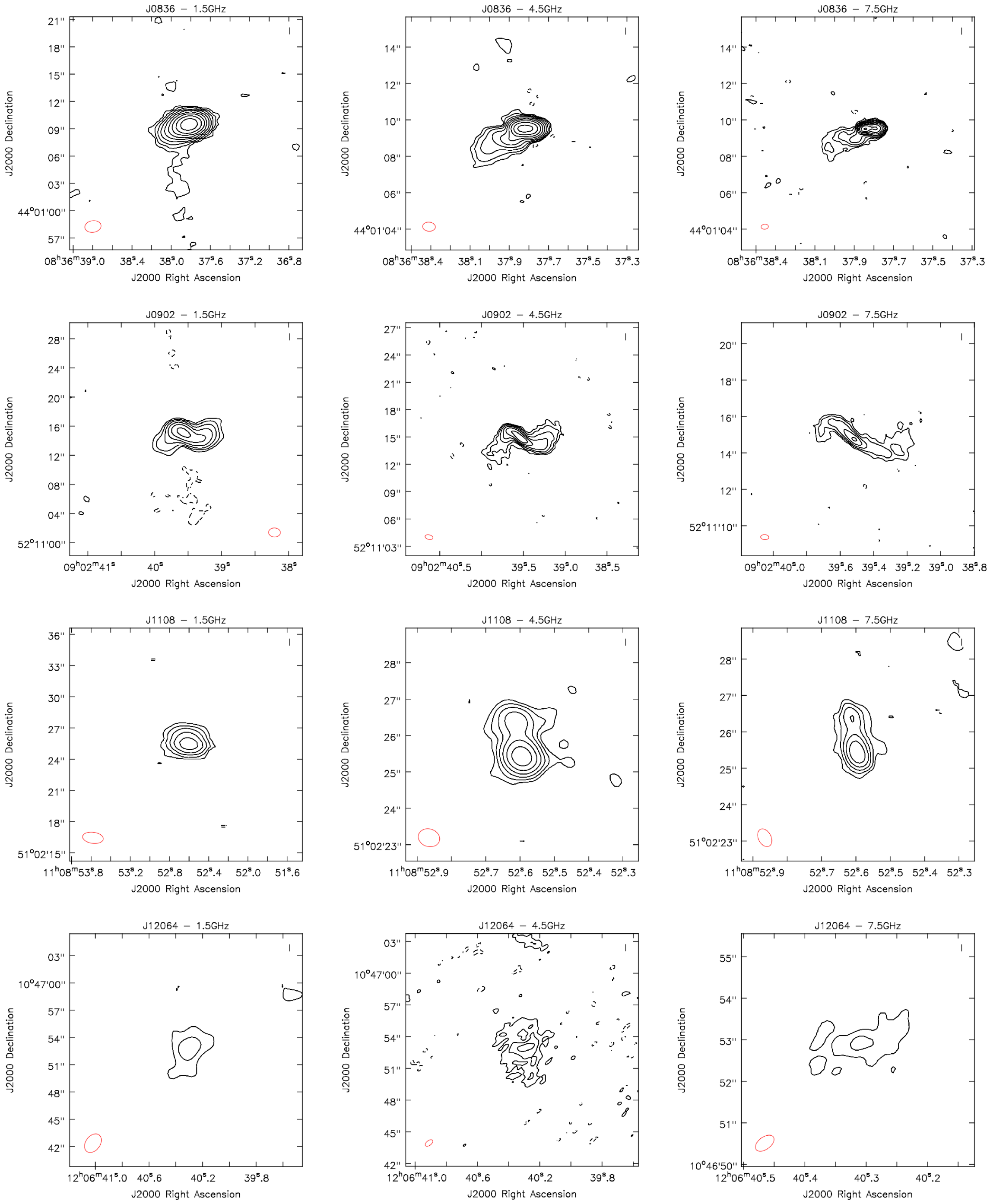

Figure 6.4: Contour plots at 1.5 GHz (left column), 4.5 GHz (middle column), and 7.5 GHz (right column) for the first four targets in the sample that exhibit extended radio emission. Positive contours (solid lines) begin at $3\,\sigma$ and typically increase by subsequent factors of two; exact contour levels are listed in Table 6.3. Negative contours at the $-3\,\sigma$ level are indicated with dashed lines. The red ellipses indicate the approximate beam shape for each image. The images are oriented such that North is up and East is left. The ranges of right ascension and declination covered are indicated in each case. Note that shortened versions of the target names are again used, and J1206+10 is here denoted by J12064.

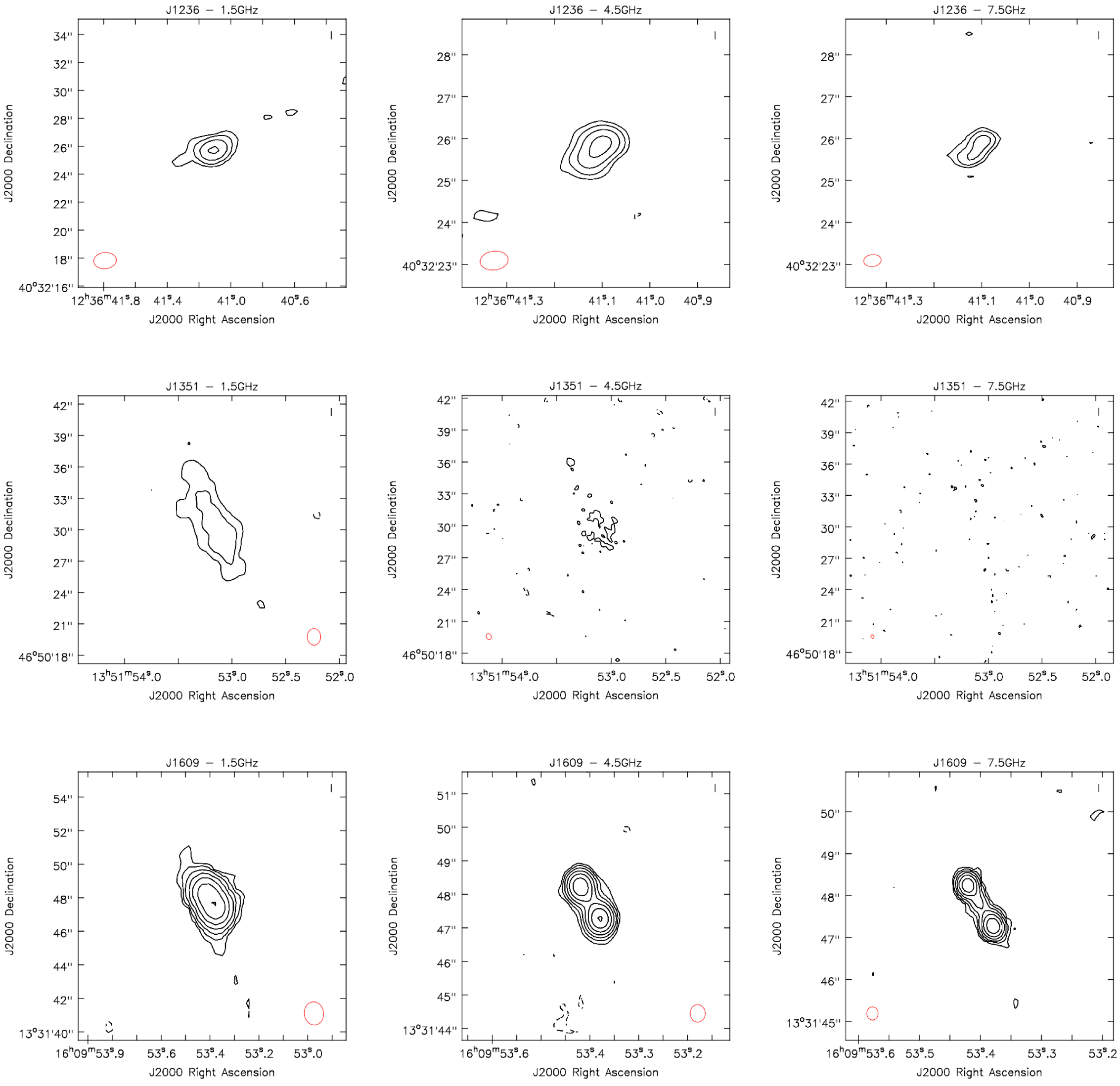

Figure 6.5: Contour plots at 1.5 GHz (left column), 4.5 GHz (middle column), and 7.5 GHz (right column) for the remaining three targets in the sample that exhibit extended radio emission. The image properties are as outlined in Figure 6.4.

J0902+52. This source displays emission that is highly collimated on small scales, but shows a "two-tailed", "S-shape" emission structure at all three frequencies on larger scales. The emission in the outer regions of the tails appears to become diffuse below the detection level when moving towards higher frequencies, due to the increasing resolution. The emission extends over a large proportion of the optical extent of the host galaxy, covering around 16 kpc in maximum projected diameter, with the ends of the tails almost propagating into the optical galaxy halo. Interestingly, its appearance is reminiscent of the innermost kiloparsec of the synthetic radio map produced by Murthy et al. (2019) to explain the features of the low-luminosity radio source B2 0258+35, made by simulating the effects of an inclined jet interacting with an edge-on disk of dense gas (following Mukherjee et al., 2018a,b). Although there are no indications of such a disk at optical wavelengths, this host galaxy appears to have undergone a merger (see Chapter 3), and so it is possible that a higher density of gas could have been supplied to its nuclear regions by this event. Similar structures have also been observed in nearby Seyfert galaxies, with jet precession and/or disruption being the favoured explanations in these instances (Kharb et al., 2006, 2010). Detailed study of optical to infrared emission spectra in these regions could be used to further investigate this possibility, to search for signs of kinematic disturbance in the emission lines that would indicate a strong jet-cloud interaction.

J1108+51. The extended emission for this source is confined to the scales of the galaxy bulge (up to ~6 kpc in diameter), and exhibits a two-component structure in the C-band images that appears to be double-lobed, with a projected diameter of around 3 kpc. Although this source is here considered to be double-lobed in nature, its appearance in the image at 7.5 GHz could also support a core-jet origin. Again, no evidence for alignment of the radio emission with any optical structures is seen.

J1206+10. This target exhibits very diffuse emission at all three frequencies, which is detected on projected scales that propagate to the galaxy halo in the optical image (up to around 8 kpc). Although present on large scales, the emission has no clear overall structure, and lacks the strong central emission that is seen for the majority of the extended sources. The galaxy does not show signs of strong star formation (see Chapter 2, §2.3.4), and so this could indicate that this is remnant emission from a past phase of radio jet activity; see later description for target J1351+46.

Table 6.3: Measurements of the peak flux densities (F_{ν}^{p}), total flux densities (F_{ν}^{T}), maximum angular sizes ($\phi_{\nu}^{\mathrm{max}}$), and projected physical diameters (d_{ν}^{max}) of the radio emission for the extended sources in the sample. Contour levels for the continuum maps displayed in Figure 6.4 are also presented, as multiples of the background rms measurements in the images (σ_{rms}; μJy, final column). The NVSS (Condon et al., 1998) and FIRST (Becker et al., 1995) flux densities, measured at 1.4 GHz, are also presented for comparison. All flux density measurements are given in mJy. The maximum angular sizes of the structures are listed in arcseconds and their corresponding maximum physical extents in kiloparsecs. The three rows for each target indicate the values for the 1.5 GHz, 4.5 GHz, and 7.5 GHz maps, respectively.

Name	F_{NVSS} (mJy)	F_{FIRST} (mJy)	F_{ν}^{P} (mJy)	F_{ν}^{T} (mJy)	$\phi_{\nu}^{\mathrm{max}}$ (arcsec)	d_{ν}^{max} (kpc)	Contour levels ($n\sigma_{\mathrm{rms}}$)	σ_{rms} (μJy)
J0836+44	130.8	139.3	93.6 ± 4.7	117.0 ± 5.9	7.0	7.2	[−3, 3, 6, 12, 24, 48, 96, 192, 384, 768]	66.5
			29.3 ± 1.5	55.7 ± 2.8	4.5	4.7	[−3, 3, 6, 12, 24, 48, 96, 192, 384, 768]	26.8
			15.18 ± 0.76	35.3 ± 1.8	3.6	3.7	[−3, 3, 6, 12, 24, 48, 96, 192, 384, 768]	17.9
J0902+52	39.5	38.4	9.96 ± 0.50	32.3 ± 1.6	9.4	16.4	[−3, 3, 6, 12, 24, 48, 96]	71.2
			3.15 ± 0.16	16.47 ± 0.83	8.7	15.2	[−3, 3, 6, 12, 24, 48, 96, 192, 384, 768]	18.2
			1.386 ± 0.073	8.32 ± 0.44	5.1	8.9	[−3, 3, 6, 12, 24, 48, 96, 192, 384, 768]	23.8
J1108+51	10.9	10.0	6.33 ± 0.33	8.89 ± 0.47	4.8	6.1	[−3, 3, 6, 12, 24, 48]	77.2
			2.28 ± 0.11	2.07 ± 0.11	2.2	2.8	[−3, 3, 6, 12, 24, 48, 96]	14.0
			1.533 ± 0.078	2.58 ± 0.14	2.0	2.6	[−3, 3, 6, 12, 24, 48]	16.1
J1206+10	14.2	10.3	2.04 ± 0.21	3.68 ± 0.32	3.8	6.1	[−3, 3, 6]	182.4
			0.321 ± 0.024	2.16 ± 0.13	5.0	8.0	[−3, 3, 6, 12]	17.5
			0.170 ± 0.018	0.316 ± 0.030	1.2	1.9	[−3, 3, 6]	15.3
J1236+40	5.7	2.0	1.67 ± 0.10	1.75 ± 0.12	3.1	5.3	[−3, 3, 6, 12, 24]	58.3
			0.552 ± 0.034	0.866 ± 0.056	1.5	2.6	[−3, 3, 6, 12, 24]	19.2
			0.265 ± 0.019	0.564 ± 0.040	1.1	1.9	[−3, 3, 6, 12]	13.8
J1351+46	8.6	8.1	0.545 ± 0.063	3.48 ± 0.25	11.1	19.0	[−3, 3, 6]	57.2
			–	–	–	–	–	13.6
			–	–	–	–	–	12.9
J1609+13	37.6	35.5	17.31 ± 0.87	30.6 ± 1.5	6.1	4.2	[−3, 3, 6, 12, 24, 48, 96, 192]	84.9
			5.31 ± 0.27	11.69 ± 0.59	2.4	1.6	[−3, 3, 6, 12, 24, 48, 96, 192]	25.6
			2.70 ± 0.14	7.27 ± 0.37	2.0	1.4	[−3, 3, 6, 12, 24, 48, 96, 192]	13.8

J1236+40. This source has only marginally extended emission at 1.5 GHz, the structure of which is only slightly resolved in the C-band images; this is perhaps in part due to its relatively high redshift within the sample. Although it shows signs of symmetric structure in the North-West to South-East direction at 4.5 and 7.5 GHz that could be lobed, it is not possible to determine the true morphology with certainty from the current observations. Again, the radio emission appears to be confined to the projected scale of the host galaxy bulge (∼5 kpc); the slight tail to the North-West in the L-band image is aligned with the appearance of the beam structure and is likely an artefact.

J1351+46. This target exhibits very diffuse emission with structure that is only clearly detected in its L-band image, but is not detected at the higher frequencies due to the increased resolution. The structure at 1.5 GHz is the largest seen for the extended sources in the sample (diameter ∼19 kpc), and it is the only target for which the emission is clearly resolved in its FIRST image. Interestingly, the emission structure is not centred on its host galaxy, and it in fact appears to propagate from its optical centre out into the surrounding galaxy environment to the North-East; the Southern edge of the VLA structure is centred on the optical nucleus of the galaxy, but there is no evidence for a compact radio core. This can be seen in Figure 6.6, in which the 1.5 GHz contours from the VLA observations are overlaid on the optical image of the host galaxy.

This target is also strongly detected at 144 MHz, with flux density $F_{144\mathrm{MHz}} \sim 41$ mJy beam^{-1}, as determined from the first data release of the LOFAR Two-metre Sky Survey (LoTSS; Shimwell et al., 2019). LoTSS contours are also overlaid on the optical image in Figure 6.6 (limiting resolution ∼6 arcsec), appearing to share a common centre with the VLA contours and also showing evidence for additional emission on the opposing side of the galaxy; the same morphology is also seen when the FIRST contours are overlaid.

In combination, these results could suggest that the radio jets have temporarily switched off in this object, leaving only remnant radio emission from a previous phase of radio AGN activity – see Morganti (2017) for a review of radio AGN life cycles. Although this interpretation is favoured here, the idea that the emission structure belongs to a larger, more distant radio source cannot be ruled out; indeed, both sets of radio contours appear to centre on a patch of optical emission to the North-East, which could in fact be a background galaxy.

J1609+13. This source shows a clear double-lobed structure in its 4.5 and 7.5 GHz images, with projected physical diameter ∼1–2 kpc. The emission is only extended on

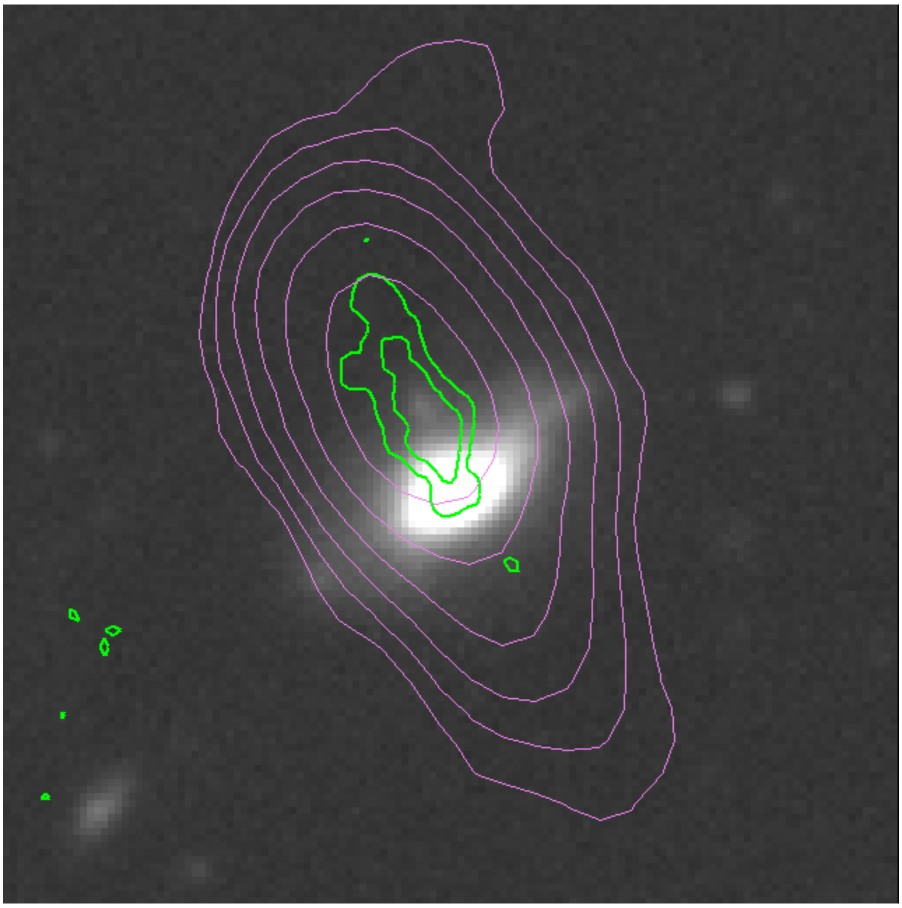

Figure 6.6: 1.5 GHz contours from the VLA observations (green) and 144 MHz contours from LoTSS DR1 (purple; Shimwell et al., 2019) for the target J1351+46, overlaid on its optical (r-band) image (as presented in Chapter 3). LoTSS contour levels begin at $5\,\sigma_{\rm rms}$ and increase in factors of two up to $160\,\sigma_{\rm rms}$, for $\sigma_{\rm rms} = 54.5$ μJy beam^{-1}. This target shows a diffuse, roughly linear radio emission structure at 1.5 GHz that propagates outwards from the optical centre on one side of the host galaxy. This structure appears to share a common centre with the LoTSS contours (limiting resolution ∼6”), which also provide evidence for additional emission on the opposite side of the galaxy. In combination, these features could be suggestive of remnant emission from a past phase of radio AGN activity.

the scale of the bulge of its host galaxy (maximum diameter ∼4 kpc), although the lobes are aligned with the plane of its large, edge-on disk.

Looking at these sources as a whole, there is therefore no favoured morphological structure amongst the objects that exhibit extended radio emission. Two galaxies, J1206+10 and J1351+46, display notably diffuse emission structures at all three frequencies and appear to lack prominent emission on small scales (e.g. compact radio cores). Although this type of emission structure is more typical of star forming regions than AGN jets, all targets in the sample were found to lack the far-infrared emission that would be expected if star formation contributed significantly to the radio emission (see Chapter 2, §2.3.4). These structures, however, could also be indicative of remnant radio emission from a past phase of activity (Morganti, 2017). As discussed above, J1351+46, in particular, shows strong evidence for this latter interpretation.

The remaining 5 extended sources have collimated morphologies that are more representative of those expected to be produced by AGN jets. Of these, three show evidence for double-lobed morphologies with projected diameters ($5\,\sigma$ boundaries; see below) of ∼1–3 kpc: J0836+44 (at 7.5GHz); J1108+51 (at 4.5 GHz and 7.5 GHz); and J1609+13 (at 4.5 GHz at 7.5 GHz) – these sizes do not account for the effects of beam smearing, however, so it is also noted that the distances between the peak flux densities of the two lobes in these cases are of order 0.5, 0.8, and 1.3 kpc, respectively. J1236+40 also exhibits a roughly symmetric structure that shows hints of being lobed, although this is not resolved well enough to be characterised with certainty. The other galaxy in this group, J0902+52, shows a morphology that is more reminiscent of FRI radio sources, with a highly collimated, jetted structure close to the nucleus (central ∼2 kpc) and a more diffuse lobes on larger scales that contribute to an overall “S-shaped” structure (∼9–16 kpc).

The maximum angular extent of the emission structures for the extended sources were measured using $5\,\sigma$ contours as limiting boundaries for the emission, which were subsequently converted to estimates of their maximum projected physical diameters. The emission structures range from 1.4 to 19.0 kpc in their maximum projected extents, with median values of 6.1 kpc, 3.7 kpc, and 2.2 kpc at 1.5 GHz, 4.5 GHz, and 7.5 GHz, respectively. Note that caution should be taken when interpreting these measurements, however, since the diameter estimates have not been corrected for beam-smearing effects, and the median physical scales of the beams at the three frequencies are 2.4 kpc (1.5 GHz), 0.89 kpc (4.5 GHz), and 0.55 kpc (7.5 GHz; from averaging the two beam axes). Certainly, beam smearing could at least partially explain why the maximum diameters are larger at 1.5 GHz in all cases. The largest angular and projected physical scales of the emission structures for the extended targets are listed in Table 6.3.

The $5\,\sigma$ contours were also used to measure the total flux density values for the extended sources, with the peak flux density values representing the maximum flux density per beam detected within these regions; these results are also presented in Table 6.3. The errors on these measurements were calculated in the same way as described for the unresolved sources in §6.4.1, although fitting errors were not relevant in these cases. The 1.5 GHz total flux densities are compared to the FIRST flux densities in Figure 6.3. All values are seen to lie below the line of equality, and in this instance it is found that only 2 out of 7 of the sources lie within $3\,\sigma$ of their FIRST values. Unsurprisingly, the discrepancy is notably larger for J1206+10 and J1351+46 (both $>18\,\sigma$), the two targets that show the most diffuse emission structures in the contour maps; only ∼40% of the FIRST flux densities are recovered in each case. This suggests that a significant amount of flux has been resolved out due to the higher resolution of the VLA observations, and confirms that these sources are typically much less compact than the unresolved objects.

6.5 Discussion

High-resolution VLA observations of a sample of 16 radio-intermediate HERGs have revealed a variety of morphologies in their emission structures. For the majority of galaxies in the sample (9 out of 16; $56\,^{+11}_{-12}\,\%$) the morphology of the emission is unresolved at a limiting angular resolution of ∼0.3 arcsec, corresponding to maximum projected physical diameters of ∼280–540 pc for these sources. For the remaining galaxies (7 out of 16; $44\,^{+12}_{-11}\,\%$), the emission is extended in the images at all three frequencies, with projected maximum physical extents ranging from 1.4–19.0 kpc. There is no favoured morphological type within this group, and only $19\,^{+13}_{-6}\,\%$ of the sample (3 out of 16) show clear evidence for double-lobed emission structures at the frequencies considered. In this section, these results are discussed and compared with those found for FR0s (§6.5.1), radio-intermediate Type 2 quasars (§6.5.2), and radio-powerful HERGs and Seyfert galaxies (§6.5.3).

6.5.1 Relation to FR0s

Several studies have now shown that the majority of local radio AGN have unresolved radio structures at the resolution limits of typical radio surveys (e.g. Baldi et al., 2010; Sadler et al., 2014; Whittam et al., 2016). These sources are often collectively named

“FR0s”, to distinguish them from the two traditional Fanaroff & Riley (1974) classes of extended radio structures: FRIs (edge-darkened) and FRIIs (edge-brightened). High-resolution VLA observations of these compact AGN radio sources at frequencies of 1.5 GHz, 4.5 GHz, and 7.5 GHz have revealed that the majority (22 out of 29; $76\,^{+6}_{-9}\,\%$) remain unresolved or marginally resolved at limiting angular resolutions of order 0.3 arcsec, corresponding to projected physical scales of ∼100–400 pc (Baldi et al., 2015, 2019a). Given that $56\,^{+11}_{-12}\,\%$ of the sample have unresolved radio emission structures at the same limiting angular resolution and similar projected physical scales (∼280–540 pc) when using an identical observing strategy, it is natural to compare the properties of these objects with those of FR0 sources.

Firstly, it is noted that although FR0s are largely associated with low-excitation optical emission – recent studies even restrict their definitions of FR0s to only those with LERG spectra (e.g. Baldi et al., 2015, 2018a, 2019a), which are denoted as LERG/FR0s from this point forward – many HERG sources also have compact radio morphologies (e.g. Baldi et al., 2010). However, the only compact HERG source that has previously been observed at high-resolution at 1.5 GHz, 4.5 GHz, and 7.5 GHz exhibits extended radio emission in its C-band images (4.5 and 7.5 GHz; Baldi et al., 2015). This source has intermediate radio power ($\log(\mathrm{L_{1.4GHz}}) = 23.35$ W Hz^{-1}), and shows a clear double-lobed/edge-brightened structure of ∼0.8 kpc in diameter[2].

The remaining sources in the Baldi et al. (2015, 2019a) samples are compact LERGs, and only a minority show extended radio structures in the VLA images. Most of these (5 out of 6) have strong and clearly visible core components at high resolution and, as a result, these radio structures tend to be edge-darkened. No clearly detected cores are seen for any of the radio-intermediate HERGs in the current sample with extended radio structures, which also show a preference for edge-brightened or diffuse emission (see Figure 6.4). The detection of strong core components for the LERG/FR0s also enabled their central radio spectra to be easily determined, regardless of whether or not the sources showed extended emission, and these spectra are now compared with those obtained for the unresolved sources in the current sample. The Baldi et al. (2019a) sample is considered for this comparison, since these objects were selected from the same Best & Heckman (2012) parent sample as the radio-intermediate HERGs.

Although the unresolved objects in the current HERG sample ($10^{23} < \mathrm{L_{1.4GHz}} < 10^{24}$ W Hz^{-1}) have similar radio powers to LERG/FR0s ($10^{22} \lesssim \mathrm{L_{1.4GHz}} \lesssim 10^{24}$ W Hz^{-1};

---

[2] Another higher radio power ($\log(\mathrm{L_{1.4GHz}}) = 25.03$ W Hz^{-1}) HERG source was also observed by Baldi et al. (2015), but this is is clearly extended in its FIRST image and shows a complex, potentially multiple-lobed morphology on large scales (up to ∼40 kpc).

Baldi et al., 2018b), the typical radio spectra in the range 1.5 to 7.5 GHz appear to differ between the two populations. Baldi et al. (2019a) found that 11 of the 18 LERG/FR0s they observed have flat spectra between 1.5 GHz and 4.5 GHz (61^{+10}_{-12}%), defined as having spectral indices (for $F_\nu \propto \nu^\alpha$) in the range $-0.4 < \alpha < 0.2$; the median value for the sample as a whole is $\alpha = -0.29$. Only one out of the 9 unresolved HERG objects studied here (11^{+18}_{-4}%), the source J1358+17, has a spectral index that lies within this range when measured in the same way, with the other sources displaying steep spectra ($-0.99 < \alpha_1 < -0.47$); median $\alpha_1 = -0.75$. A two-sample Kolmogorov-Smirnov test highlights the difference, indicating that the null hypothesis that the 9 unresolved radio-intermediate HERG sources and 18 Baldi et al. LERG/FR0s are drawn from the same underlying distribution can be rejected at a confidence level of 98.3% ($p = 0.017$). The distributions of the spectral indices between 1.5 and 4.5 GHz of these two samples is presented in Figure 6.7, which illustrates this difference.

Interestingly, Baldi et al. (2019a) observed a spectral steepening for their objects between 4.5 GHz and 7.5 GHz, which is also observed for the unresolved sources in the current analysis (see Figure 6.2). It is found that the steepening is in fact stronger, however, for the unresolved radio-intermediate HERGs; the median difference in spectral index is determined to be $\Delta\alpha = 0.33$, compared with the value of $\Delta\alpha = 0.16$ measured by Baldi et al. (2019a). One caveat that could affect this result, as well as those above, is that the LERG/FR0s in the Baldi et al. (2019a) sample typically have lower redshifts (all $z < 0.05$) than those of the radio-intermediate HERGs studied here ($0.03 < z < 0.1$, median $z = 0.082$), meaning that the measured flux densities probe the spectra at higher rest-frame frequencies in most cases. However, this is likely to be a relatively minor effect.

Further differences between the two samples become apparent when considering their general host galaxy properties. LERG/FR0s are typically characterised by luminous, red early-type host galaxies, large black hole masses (typically $10^8 \lesssim \mathrm{M_{BH}} \lesssim 10^9$ $\mathrm{M_\odot}$), and, of course, low-excitation optical emission (Baldi et al., 2018b). They share most of these properties with the hosts of traditional FRI sources that generally exist at higher radio powers (e.g. $10^{23} \lesssim \mathrm{L_{1.4GHz}} \lesssim 10^{25}$ W Hz^{-1} in the FRI*CAT* of Capetti et al., 2017), with the only other clear difference lying in the compactness of the FR0 radio structures.

In contrast, the unresolved objects in the current HERG sample have black hole masses[3] that show a preference for lower values, lying in the range $10^{7.4} \lesssim \mathrm{M_{BH}} \lesssim 10^{8.3}$

---

[3] These were estimated from the velocity dispersion measurements (σ_*) provided by the MPA/JHU value-added catalogue for SDSS DR7 galaxies (available at: `https://wwwmpa.mpa-garching.mpg.de/SDSS/DR7/`), using the formulation of $\log(\mathrm{M_{BH}/M_\odot}) = 8.13 + 4.02\ \log(\sigma_*/200\,\mathrm{km\,s^{-1}})$ from Tremaine et al. (2002).

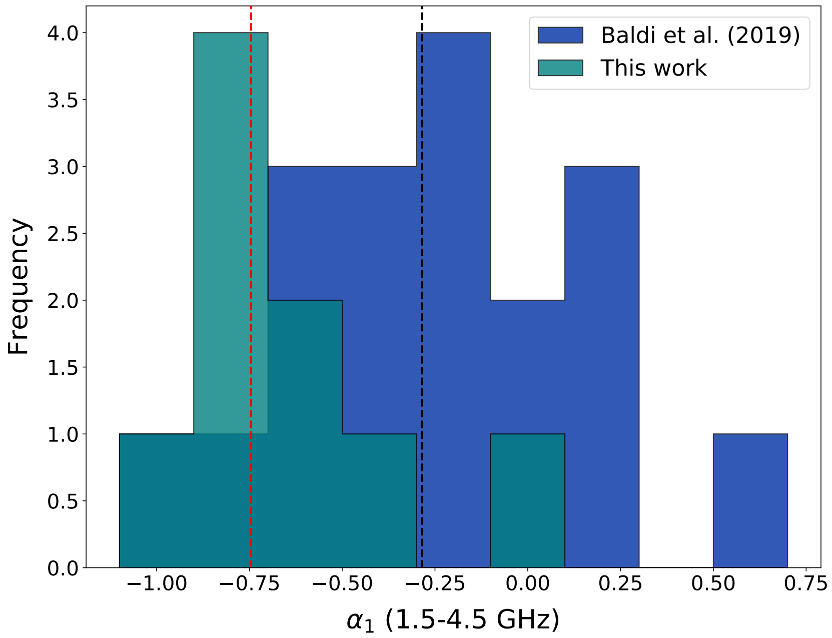

Figure 6.7: The distributions of the spectral indices between 1.5 and 4.5 GHz for the unresolved sources in the current radio-intermediate HERG sample (teal) and all 18 LERG/FR0s studied by Baldi et al. (2019a; blue). The median values for the two samples are indicated by the red and black dashed lines, respectively.

$M_\odot$, with a median of $M_{BH} = 10^{7.8}$ $M_\odot$. Furthermore, in Chapter 3 it was shown that the host galaxies of radio-intermediate HERGs have a variety of optical morphologies, from late-types through to early-types, as identified using both visual inspection and light profile modelling. This is reflected by the unresolved HERG sources within the current subsample, but with a slight preference for early-type galaxies relative to late-types; a ratio of 2:4:3 is seen for late-type : early-type : mergers. However, the contrast between the host properties and black hole masses of the unresolved HERGs and the Baldi et al. LERG/FR0s is perhaps unsurprising, since these differences are apparent for the general populations of LERGs and HERGs from which these samples have both been drawn (Best & Heckman, 2012).

In summary, the sources in the current radio-intermediate HERG sample therefore have radio morphologies, radio spectra (for the unresolved objects), and host/nuclear properties that are significantly different from those of LERG/FR0 sources, and consequently also those of FRI sources at higher radio powers. Hence, it appears that they are representative of an important population of compact radio AGN sources that is distinct from those typically classified as FR0s, and that has not yet been explored in detail.

6.5.2 Comparison with radio-intermediate Type 2 quasars

Recently, Jarvis et al. (2019) studied a sample of 10 local Type 2 quasars with intermediate radio powers ($z < 0.2$; $23.3 < \log(\mathrm{L}_{1.4\mathrm{GHz}}) < 24.4$ $\mathrm{W\,Hz^{-1}}$), which were also observed with the VLA in the L- and C-bands at a similar limiting angular resolution to the current observations (∼0.2–0.3 arcsec). These objects are comparable in radio power to the radio-intermediate HERGs studied here, but differ mainly in their much higher optical luminosities – all of the HERGs from Chapter 3 have [OIII] λ5007 luminosities below the 10^{42} $\mathrm{erg\,s^{-1}}$ lower limit for the Jarvis et al. (2019) sample. The Type 2 quasars were also originally selected to have luminous, broad [OIII] λ5007 line components, i.e. which contribute $\geq 30\%$ of the total line flux and have a FWHM exceeding 700 $\mathrm{km\,s^{-1}}$.

While it has been suggested that the radio emission in bright radiatively-efficient AGN could also originate from shocks in high-velocity, radiatively-driven winds (e.g. Stocke et al., 1992; Zakamska & Greene, 2014), Jarvis et al. (2019) conclude that the morphologies, spectra and size-luminosity relationship for the Type 2 quasar radio structures lend favour to a jet-based origin. In particular, it is thought that radio emission caused by shocks would be at most loosely collimated by galactic discs (Alexandroff et al., 2016), contrasting with the highly-collimated structures observed for their objects. Due to the similar appearance of the radio-intermediate HERG radio structures, this interpretation is also favoured for the sources in the current sample. The radio-intermediate HERGs also have lower [OIII] λ5007 luminosities than the Type 2 quasars, which makes the feasibility of producing the observed radio luminosities through radiatively-driven wind shocks more questionable.

For the 9 Jarvis et al. objects for which radio AGN jet activity is found to dominate the total radio emission, it is seen that a much higher proportion (8 out of 9; $89^{+4}_{-18}\,\%$) exhibit extended emission structures than for the radio-intermediate HERGs ($44^{+12}_{-11}\,\%$). Like the extended objects in the current sample, the morphologies of the radio structures for the Type 2 quasars are varied, although the latter are typically extended on larger scales. For instance, the median largest linear scale for the radio structures of the Type 2 quasars is 8.3 kpc, while the median maximum projected extent (in the L-band images) for the extended radio-intermediate HERG sources is 6.1 kpc. One caveat with this comparison is that the maximum projected diameters in the current analysis were measured using $5\,\sigma$ contours as the boundaries for the emission (see §6.4.2), while the largest linear scales for the Jarvis et al. (2019) objects were measured between the peaks of the two furthest separated radio structures; the radio structures seen for the extended HERG sources typically do not allow for this latter technique. However, since this means that the current measurements are more susceptible to beam smearing, it is stressed that this only serves to increase the discrepancy in the extension of the emission between the two samples.

Although the Jarvis et al. (2019) sources display a variety of radio morphologies, two show clear edge-brightened/double-lobed structures in their high-resolution C-band images (median resolution ∼0.2 arcsec), with largest linear scales of ∼0.9 and 1.4 kpc. This is comparable with the scale of the similar structures found for both the compact HERG source discussed in §6.5.1 (∼0.8 kpc) and for the examples in the current sample (∼0.5–1.3 kpc in peak-to-peak distance). Interestingly, these sizes are intermediate between those of similar structures in Seyfert galaxies (typically few 100 pc; Ulvestad & Wilson, 1984) and in radio-powerful HERG/FRII sources (few 10s kpc, up to Mpc scales). The results for the extended sources in the current sample are compared with these populations in the following section.

6.5.3 Comparison with radio-powerful HERGs and Seyferts

As mentioned in §6.2, many studies have suggested that high-excitation optical emission from AGN is linked with a radiatively efficient black hole accretion mode, regardless of the strength of the associated radio emission (e.g. Best & Heckman, 2012; Heckman & Best, 2014; Mingo et al., 2014). At high radio powers, it is seen that the vast majority of SLRGs are associated with classical FRII radio morphologies (Tadhunter, 2016). At low radio powers, high-resolution radio observations of nearby Seyfert galaxies have revealed that many also display double-/triple-lobed or edge-brightened radio structures (Ulvestad & Wilson, 1984; Morganti et al., 1999; Baldi et al., 2018a), although on much smaller scales (typically $\lesssim$400 pc).

This could suggest that HERGs and Seyfert galaxies in fact compose a continuous AGN population with a common black hole accretion mode that leads to edge-brightened, double-lobed radio structures, with the jet-launching mechanism perhaps providing the link between the two. In this picture, radio-intermediate HERGs would represent the missing population between radio-powerful HERGs at high radio powers and Seyfert galaxies at low radio powers, and should therefore also preferentially display multiple-lobed or edge-brightened extended radio structures.

From the current analysis, however, it is found that only 3 out of the 16 galaxies in the sample ($19\,^{+13}_{-6}\,\%$) appear to show evidence for possible edge-brightened, double-lobed structures in at least one of the images at the three observation frequencies. On the other hand, it is important to consider that 9 out of the 16 galaxies in the sample have unresolved radio structures at all three frequencies, for which the upper limits on the projected physical diameters ($d_{\max}$ in Table 6.2) range from ∼280–540 pc, with a median of 470 pc. Given that the edge-brightened structures seen for some Seyfert galaxies typically manifest on scales below ∼400 pc, and can even appear on sub-100 pc scales (e.g. as seen for Mrk 348; Neff & de Bruyn, 1983), it cannot definitively be ruled out that such radio structures still exist within these galaxies.

Looking at the extended sources alone, it is found that a slight minority (3 out of 7; $43^{+18}_{-15}\,\%$) show some suggestion of double-lobed structures. Two of the remaining galaxies (J1206+10 and J1351+46), however, display diffuse emission structures in the images and lack strong emission on small scales. Although this could suggest that star formation provides the main contribution to their radio emission, this was deemed to be unlikely for both galaxies based on the properties of their optical and far-infrared emission (see Chapter 2, §2.3.4). As discussed in §6.4.2, this lends favour to the explanation that the radio jets have temporarily switched off in these objects to leave only remnant radio emission from a previous phase of radio AGN activity (e.g. see Morganti, 2017); the case is particularly strong for J1351+46, which also has a strong detection at 144 MHz in LoTSS DR1 (Shimwell et al., 2019).

Of the remainder, it is found that J1236+40 shows a roughly symmetric emission structure on scales of up to ∼5 kpc that could also be lobed, although it is not resolved well enough to determine this with certainty. J0902+52 also shows clear jet-related structure on small scales, but which appears in an "S-shape", with "tails" of emission that diverge from the main axis of the jet around 2–3 kpc from the centre. Therefore, considering the sources that show strong evidence of currently being in a phase of activity in which the radio jets are switched on, it is found that the majority (3 out of 5; $60^{+16}_{-22}\,\%$) exhibit double-lobed structures.

Given that the unresolved sources in the sample show differences from the properties of typical LERG/FR0 sources and could still show double-lobed/edge-brightened structures on smaller physical scales than those probed here, the results could therefore still be consistent with the picture of a continuous connection between radiatively-efficient accretion and edge-brightened radio emission structures along the HERG sequence, for currently active jets. Clearly, high-resolution radio observations of greater numbers of radio-intermediate HERGs are required to test this idea further. Ideally, such observations would be done at higher resolution than those used here, in order to ensure that the structures are investigated in appropriate detail, including the unresolved HERG sources in the current sample.

6.6 Chapter summary and conclusions

In the past decade, high sensitivity radio surveys with large-scale sky coverage have revealed that compact sources with low-to-moderate radio powers dominate the local radio AGN population. Local HERGs with intermediate radio powers ($z < 0.15$; $22.5 < \log(\mathrm{L}_{1.4\mathrm{GHz}}) < 25.0\ \mathrm{W\,Hz^{-1}}$) form an important sub-population that also shows strong evidence for driving outflows on the scale of galaxy bulges. Here, high-resolution radio observations of a sample of 16 radio-intermediate HERGs at 1.5 GHz, 4.5 GHz, and 7.5 GHz have been used to characterise the morphologies and extents of their radio structures down to subkiloparsec scales. The main results are as follows.

- The majority of targets in the sample (9 out of 16; 56^{+11}_{-12} %) are unresolved at an angular resolution of ∼0.3 arcsec, placing an upper limit on their projected physical diameters of ∼280–540 pc. All of these sources show steep radio spectra between 1.5 GHz and 4.5 GHz ($-0.99 < \alpha < -0.47$, for $F_\nu \propto \nu^\alpha$), except one (J1358+17), which has a flat spectrum ($\alpha_1 = -0.05 \pm 0.01$). The latter also has a 1.5 GHz flux density that is greatly discrepant from its FIRST value, which could suggest it is a beamed, variable source. All of this group, including J1358+17, show a systematic spectral steepening between 4.5 GHz and 7.5 GHz (median $\Delta\alpha = 0.33$).

- 7 sources in the sample display extended emission structures with projected diameters of 1.4–19.0 kpc. Of these, it is found that three (43^{+18}_{-15} %) show suggestions of double-lobed emission structures in at least one of the images at the three frequencies used. One other extended source shows signs of a symmetric emission structure that could be lobed, but it is not resolved well enough to classify with certainty. Of the remainder, two sources (J1206+10 and J1351+46) show diffuse emission structures in the images that could be suggestive of remnant emission from past phases of jet activity. The remaining source (J0902+52) shows an "S-shaped" morphology that could be suggestive of either an interaction between an inclined jet and a disk of dense gas, or jet precession. The majority of the sources with clear evidence for currently active radio jets therefore exhibit double-lobed structures (3 out of 5; 60^{+16}_{-22} %).

- Although compact on similar scales, the radio-intermediate HERG sources are found to differ from LERG/FR0s in their radio morphologies, radio spectra (for the unresolved objects), and, as found in previous studies of larger HERG and LERG samples, their host properties and black hole masses.

These results provide some evidence to suggest that there is a link between double-lobed/edge-brightened radio structures and the radiatively-efficient accretion mode often associated with HERGs, although the strength of this connection remains uncertain. However, they also reveal that a significant population of compact AGN radio sources with high-excitation optical emission exists, which up until now has not been explored in detail. Additional high-resolution radio observations of HERGs with low-to-intermediate radio powers are therefore required to improve our understanding of this population, and further investigate the link between AGN accretion mode and radio morphology. This includes follow-up radio observations of the unresolved sources in the current sample at higher angular resolutions, to rule out the possibility that double-lobed structures exist on the scales at which they can manifest in Seyfert galaxies.

Chapter 7

Conclusions and future prospects

7.1 Summary and conclusions

The strong correlation between the masses of supermassive black holes (SMBHs) and the stellar velocity dispersions and luminosities of the surrounding galaxy bulges has led to the conventional idea that SMBHs and their host galaxies coevolve. In our current models of galaxy evolution, strong outflows of material driven by the jets and intense radiation fields of active galactic nuclei (AGN) are thought to play an important role in regulating this connection – so-called *AGN feedback* (Fabian, 2012). The jets of radio AGN are thought to be especially important in this context, given their association with two distinct sources of AGN feedback: (i) driving strong multiphase gas outflows in galaxy nuclei (typically $\lesssim$10 kpc); (ii) preventing the hot gas in galaxy haloes and the surrounding large-scale environments from cooling to form stars (10 kpc – 1 Mpc). In particular, this latter mode is thought to explain the lack of galaxies at the high-mass end of the observed galaxy luminosity function, relative to theoretical predictions (Croton et al., 2006; Bower et al., 2006).

While much previous research concerning radio AGN has focused on those with high radio powers ($L_{1.4GHz} \gtrsim 10^{25}$ W Hz^{-1}), the advent of deep radio surveys with broad sky coverage has revealed that the local radio luminosity function rises steeply towards lower radio powers, such that the population is overwhelmingly dominated by these lower-power sources (Best et al., 2005b; Mauch & Sadler, 2007; Best & Heckman, 2012; Sadler et al., 2014; Sabater et al., 2019). There is also strong evidence to suggest that the subpopulation that have intermediate radio powers ($10^{22.5} < L_{1.4GHz} < 10^{25}$ W Hz^{-1}) and strong optical emission lines (high-excitation radio galaxies, or HERGs) are capable of causing kinematic disturbances in the multiphase gas content of their host galaxies (e.g. Morganti et al., 2005; Tadhunter et al., 2014a; Harrison et al., 2015; Ramos Almeida et al., 2017; Villar-Martín et al., 2017), perhaps even having a more significant effect than AGN with higher radio powers (Mullaney et al., 2013). Investigation of the properties of these important, yet relatively unexplored members of the local radio AGN population is therefore critical for improving our understanding of the role of AGN feedback in galaxy evolution.

Using deep optical imaging data, this thesis has provided the first focused study of the detailed morphologies of local radio-intermediate HERGs, with the goal of determining their dominant morphological types and the importance of triggering of the nuclear activity by galaxy mergers and interactions. This has been supplemented by similar analysis of the optical morphologies of powerful 3CR radio galaxies and the hosts of Type 2 quasars, as well as a large sample of non-active control galaxies from the general population, in order to investigate how these properties depend on the radio power and optical emission line luminosity of the AGN. In addition, high-resolution radio observations of these radio-intermediate HERGs have been used to characterise their radio properties for the first time, with the aim of investigating the apparent connection between radiatively-efficient AGN accretion and double-lobed, edge-brightened radio structures. The main results of this research are summarised here, with reference to the key open questions outlined in the thesis introduction.

Does the apparent relationship between high-radio-power AGN and galaxy mergers, which is particularly apparent for radiatively-efficient objects, continue for those with intermediate radio powers? (Chapters 3 and 5)

Previous study of the detailed optical morphologies of powerful radio galaxies has revealed frequent signatures of past or ongoing galaxy mergers and interactions, a connection that is particularly strong for those hosting AGN with strong optical emission lines (Heckman et al., 1986; Smith & Heckman, 1989b; Ramos Almeida et al., 2011). For the objects in the 2Jy sample in particular, it is found that $94^{+4}_{-7}\,\%$ of the strong-line radio galaxies (SLRGs; [OIII]λ5007 equivalent width > 10 Å) show morphological signatures of these events, which typically have higher surface brightnesses than those found for non-active elliptical galaxies from the general population (Ramos Almeida et al., 2012). The 2Jy SLRGs also show a significant preference for group-like large-scale environments relative to these non-active galaxies (Ramos Almeida et al., 2013), in which galaxy mergers can occur frequently.

In contrast, the 2Jy weak-line radio galaxies (WLRGs; [OIII]λ5007 equivalent width < 10 Å) exhibit a much lower rate of disturbance ($27^{+16}_{-9}\,\%$; Ramos Almeida et al., 2011) and show a preference for dense cluster environments (Ramos Almeida et al., 2013), where the merger rate is thought to be lowered by the typically higher relative galaxy velocities (Popesso & Biviano, 2006). These results are consistent with the idea that galaxy mergers and interactions provide the dominant triggering mechanism for radio AGN fuelled by radiatively-efficient SMBH accretion (i.e. those with strong optical emission lines), but suggest that other mechanisms must be important for fuelling radiatively-efficient radio AGN (the weak-line objects).

In order to investigate whether the connection between galaxy mergers and radio AGN with strong optical emission lines is preserved at lower radio powers, the optical morphologies of a sample of 30 local radio-intermediate HERGs ($z < 0.1$, $22.5 < \log(\mathrm{L}_{1.4\mathrm{GHz}}) < 24.0$ W Hz^{-1}; the RI-HERG low sample) were characterised using deep

INT/WFC optical imaging observations (Chapter 3). Detailed visual inspection by several independent classifiers revealed interaction signatures in 53 ± 9 % (16 out of 30) of the galaxies in the sample, a deficit at the $3.8\,\sigma$ level compared to the rate found for the 2Jy SLRGs. A higher proportion of disturbed galaxies was found in the higher-radio-power half of the sample (10 out of 15; $67^{+10}_{-14}\,\%$) than in the lower-radio-power half (6 out of 15; $40^{+13}_{-11}\,\%$), with the former also being found to contain all eight of the galaxies identified as highly disturbed from cursory visual inspection (a $3.8\,\sigma$ result). While the same proportions were measured when the sample was divided in two by [OIII]λ5007 emission line luminosity, it was found that the high-luminosity half and low-luminosity half contained 5 out of 8 and 3 out of 8 of the highly disturbed objects, respectively, a difference at the $0.8\,\sigma$ level. These results therefore suggested that triggering of radiatively-efficient radio AGN by mergers and interactions is generally less important in the radio-intermediate population. They were also consistent with the idea that the importance of merger-based triggering was strongly dependent on the 1.4 GHz radio power of the AGN, but not strongly dependent on the [OIII]λ5007 emission line luminosity.

In Chapter 5, the morphologies of a much larger sample of active galaxies that covered a broad range of both 1.4 GHz radio power and [OIII]λ5007 emission line luminosity were investigated, allowing the relationships between these properties and the rate of disturbance to be explored in more detail. This sample comprised a total of 155 active galaxies with low-to-intermediate redshifts: 58 radio-intermediate HERGs[1] ($z < 0.15$, $22.5 < \log(\mathrm{L_{1.4GHz}}) < 25.0$ W Hz^{-1}); 72 powerful radio galaxies from the 3CR sample ($0.05 < z < 0.3$, $24.7 < \log(\mathrm{L_{1.4GHz}}) < 28.2$ W Hz^{-1}); and 25 Type 2 quasar objects ($z < 0.1$, $\mathrm{L_{[OIII]}} \gtrsim 10^{35}$ W) – details on the selection of the individual samples was provided in Chapter 2. While this sample was largely composed of radiatively-efficient objects (HERGs/Type 2 quasars), the 3CR sample also contained 30 radiatively-inefficient low-excitation radio galaxies (LERGs). This allowed the picture of a reduced importance of merger-based triggering in this latter population, as suggested by the findings of the 2Jy studies (Ramos Almeida et al., 2011, 2012, 2013), to be tested.

Morphological classifications of these galaxies were obtained from several independent researchers using an online classification interface. This also allowed a large number of non-active control galaxies, selected to lie in the wide INT image fields and matched to the targets in terms of their stellar masses and redshifts, to be classified alongside the active galaxies – the interface methodology and the selection of the matched con-

---

[1] Note that this included the 30 radio-intermediate HERGs that were studied with the more detailed analysis presented in Chapter 3.

trols was outlined in Chapter 4. The standardised image appearance, matching image quality/observing conditions, and the randomised and blind classification of the active and non-active galaxies provided substantial improvements on the analysis performed in Chapter 3, and for similar previous studies in this area (e.g. the 2Jy studies; Ramos Almeida et al., 2011, 2012). Using the interface, classifiers were required to indicate whether or not an object was disturbed, and also identify the types of interaction signatures associated with disturbed objects. The key results derived from the analysis of these interface classifications are as follows.

- In contrast with the results presented in Chapter 3, there was no strong evidence to suggest that the rates of disturbance in the active galaxies were correlated with 1.4 GHz radio power, after the rates measured for their matched controls from the general population are accounted for. It was found that an underlying correlation between the radio powers and stellar masses of the objects could have had a significant influence on the results found for the RI-HERG low sample (in Chapter 5).

- On the other hand, the analysis in Chapter 5 revealed clear evidence that the enhancement in the rate of disturbance for the radiatively-efficient objects in the sample (HERGs/Type 2 quasars) relative to the matched controls ($f_{\mathrm{AGN}}/f_{\mathrm{cont}}$) increases strongly with [OIII]λ5007 luminosity. A highly significant excess in the disturbance rate relative to the matched controls was also found when all objects in the Type 2 quasar and 3CR samples with quasar-like [OIII]λ5007 emission line luminosities ($L_{[\mathrm{OIII}]} \geq 10^{35}$ W) are considered together (at the 5.1 σ level), providing strong supporting evidence for this connection. A significant correlation was not found when the 3CR LERGs were included, suggesting that this relationship is specific to radiatively-efficient AGN.

- Interaction signatures that suggested both post-coalescence and pre-coalescence interactions were identified for all active galaxy samples. However, the radio-selected samples showed a preference for post-coalescence relative to pre-coalescence interactions, with the Type 2 quasar hosts exhibiting the opposite preference. This suggests that radio AGN are more likely to be triggered in the late stages of galaxy mergers and interactions, while Type 2 quasars are more likely to be triggered in their early stages.

These results are consistent with a picture in which the importance of galaxy mergers and interactions for triggering radiatively-efficient AGN is strongly dependent on their optical emission line luminosities, but not strongly dependent on their radio powers. Since the optical emission line luminosities of AGN are thought to be correlated with their bolometric luminosities (e.g. Heckman et al., 2004), this is also consistent with a trend with the total power output of the AGN, as suggested by some previous studies (e.g. Treister et al., 2012). The results also agree with the idea that mergers and interactions are relatively less important for triggering radiatively-inefficient AGN at high radio powers, in line with the findings of the 2Jy studies.

Are lower-radio-power AGN predominantly associated with elliptical host galaxies, like their high-radio-power counterparts, or late-type (spiral/disk) hosts, as found for Seyfert galaxies? (Chapters 3 and 5)

Previous studies of powerful radio AGN have found them to be predominantly associated with massive elliptical host galaxies (Matthews et al., 1964; Dunlop et al., 2003; Best et al., 2005b). However, in the 3CR and 2Jy samples, which contain low-to-intermediate redshift radio galaxies selected for their high flux densities, it is found that the few that show evidence for clear disk-like structures on inspection of their optical images are typically found towards the lower-radio-power ends, with half lying in the radio-intermediate regime (Tadhunter, 2016). An increased frequency of late-type hosts towards lower radio powers has also been found for low redshift radio AGN from the Australia Telescope 20 GHz survey (mostly $L_{1.4\mathrm{GHz}} \sim 10^{22-23}$ W Hz^{-1}; Sadler et al., 2014). Seyfert galaxies, which are also linked with radiatively-efficient accretion and are arguably the counterparts of HERGs at low radio powers, are predominantly associated with late-type morphologies (Adams, 1977). In combination, these results suggest a possible transition in the dominant hosts of radio AGN from early-type galaxies at high radio powers to late-type galaxies at low radio powers.

In Chapter 3, the morphological types of 30 objects in the RI-HERG low sample were classified using both visual inspection and light profile fitting (with the `GALFIT` package; Peng et al., 2002, 2010). The visual inspection revealed that the sample contained a mixture of early-type (elliptical or lenticular) and late-type (spiral/disk) hosts, with a slight preference for the latter: 11 out of 30 (37^{+9}_{-8} %) and 13 out of 30 (43^{+9}_{-8} %), respectively. The remaining objects (6 out of 30; 20^{+9}_{-5} %) were found to have highly disturbed morphologies, such that the morphological types could not be classified with certainty. These visual classifications showed good agreement with those obtained from the Galaxy Zoo project (Lintott et al., 2008, 2011), which also suggested a mixed population with a slight preference for late-type morphologies. The `GALFIT` modelling further indicated the presence of a mixture of morphological types, but with a preference for early-type morphologies being exhibited, in this case: bulge-like Sérsic profiles were found to fit or dominate the light profiles from 14 out of 30 (47 ± 9 %) objects, with exponential disk profiles only found to be dominant for 8 out of 30 (27^{+9}_{-6} %) of the objects. However, many of the objects showed signs of strong disk components (15 out of 30; 50 ± 9 %) in the models, and the majority of fits requiring both bulge and disk components were seen to be disk dominated – 8 out of 15 (53^{+12}_{-13} %), with a median bulge-to-disk ratio of $B/D \sim 0.8$.

In addition to the classifications relating to morphological disturbance, the online interface was also used to classify the morphological types of all of the samples of active galaxies and matched control galaxies considered (Chapter 5). From these classifications, it was found that almost all of the AGN populations showed a preference for early-type relative to late-type morphologies. The exception was the RI-HERG low sample, which showed a preference for late-type morphologies in the interface classifications, in agreement with the results outlined above. However, the dominant host types for the AGN were found to depend strongly on their radio powers, with the proportion of early-type hosts being observed to increase significantly towards higher radio powers, while the proportion of late-type hosts showed the opposite trend. These results provide strong support for the picture of a transition in the dominant host types of radiatively-efficient AGN from early-type galaxies at high radio powers to late-type galaxies at lower radio powers (i.e. like Seyfert galaxies), as outlined above.

How do radio galaxies compare to the general galaxy population in these two aspects? (Chapter 5)

The use of an online classification interface, which greatly improved the time efficiency of the classification process, allowed the morphologies of a large number of non-active control galaxies from the general population to be classified alongside the active galaxies. From these classifications, it was found that the active galaxies were more frequently disturbed than their corresponding matched control galaxies across the full ranges of stellar mass and redshift covered by the samples. The most significant excesses in the rates of disturbance were found for the 3CR HERGs ($4.7\,\sigma$) and Type 2 quasars ($3.7\,\sigma$), while the least significant excess was found for the 3CR LERGs (at the $1.2\,\sigma$ level). This is again consistent with the idea that merger based triggering is relatively less important for triggering radiatively-inefficient radio AGN compared to radiatively-efficient objects.

On the other hand, the morphological type classifications for the active galaxies and the control galaxies were found to be largely consistent across the full ranges of stellar mass and redshift covered. The only significant differences were the excess of early-type morphologies found for the 3CR LERGs relative to their matched controls, and the deficit of early-type morphologies found for the RI-HERG low sample (both at the $3\,\sigma$ level).

How do the radio properties of radio AGN vary towards lower radio powers? Is the apparent connection between double-lobed (FRII-like) radio structures and radiatively-efficient accretion seen for radio-powerful SLRGs/HERGs preserved in the radio-intermediate population? (Chapter 6)

At high radio powers, HERGs are found to be predominantly associated with FRII-like (double-lobed, edge-brightened) radio morphologies, leading to suggestions that such structures could be inherently connected to the radiatively-efficient accretion mode (e.g. Tadhunter, 2016). This is supported by the fact that some Seyfert galaxies, arguably the optically-selected equivalents of HERGs at low radio powers, are also seen to exhibit double-lobed or edge-brightened radio morphologies (Ulvestad & Wilson, 1984; Morganti et al., 1999; Baldi et al., 2018b). However, several studies in the last decade have shown that the lower-power sources that dominate the local radio AGN population often have radio emission structures that are compact on galaxy scales, based on the limiting angular resolutions of typical radio surveys (e.g. Baldi & Capetti, 2010; Sadler et al., 2014; Whittam et al., 2016; Baldi et al., 2018a). These sources are often collectively termed "FR0s", in order to separate them from the two traditional classes of extended radio structures: Fanaroff-Riley Type Is (FRIs) and Type IIs (FRIIs; Fanaroff & Riley, 1974).

While the majority of objects identified as FR0s have been associated with LERGs with intermediate and lower radio powers ($L_{1.4\mathrm{GHz}} \lesssim 10^{25}\,\mathrm{W\,Hz^{-1}}$), there is some previous evidence to suggest that HERGs with these radio powers could also be linked with compact radio structures (e.g. as found for ~80% of the 67 objects studied by Baldi & Capetti, 2010). In support of this idea, inspection of the FIRST survey (Becker et al., 1995) images of the sources in the RI-HERG low sample revealed that 29 out of 30 (97%) had radio emission structures that were compact at the ~5 arcsec limiting angular resolution of the observations.

However, the FIRST observations do not probe the kiloparsec to subkiloparsec physical scales on which some Seyfert galaxies exhibit extended emission structures (e.g. Ulvestad & Wilson, 1984), and so the idea that radiatively-efficient accretion and double-lobed, edge-brightened radio morphologies are connected in the intermediate radio power regime could not be ruled out based on these results. In order to investigate this connection in more detail, high-resolution VLA observations were obtained for a 94% complete sample of 16 of the RI-HERG low objects with radio powers in the range $23.0 < \log(\mathrm{L}_{1.4\mathrm{GHz}}) < 24.0\ \mathrm{W\,Hz^{-1}}$. The results obtained from analysis of these observations are as follows.

- The majority of targets in the sample (9 out of 16; $56^{+11}_{-12}\,\%$) were found to remain unresolved at the highest angular resolution achieved (~0.3 arcsec), placing an upper limit on their projected physical diameters of ~280–540 pc. However, the steep radio spectra found for 8 out of 9 these objects suggests that they exhibit extended emission on smaller physical scales, and so the existence of double-lobed radio structures on such scales can still not be ruled out.
- 7 sources in the sample displayed extended emission structures with projected diameters of 1.4–19.0 kpc. Of these sources, three ($43^{+18}_{-15}\,\%$) showed suggestions of double-lobed emission structures. One other extended source showed signs of a symmetric emission structure that could be double-lobed, but it is not resolved well enough to classify with certainty. Of the remainder, two sources showed diffuse emission structures in the images that could be suggestive of remnant emission from past phases of jet activity, and the final source exhibited an "S-shaped" morphology that was suggestive of either jet precession or a jet interacting with a dense gaseous disk. The majority of the sources with clear evidence for currently active radio jets were therefore found to exhibit clear double-lobed structures (3 out of 5; $60^{+16}_{-22}\,\%$).
- When compared with LERG/FR0s with low-to-intermediate radio powers and radio structures that are compact on similar physical scales (Baldi et al., 2015, 2019b), the radio-intermediate HERG sources were found to differ in terms of the morphologies of their extended emission structures and their typically steeper radio spectra (measured for the unresolved objects). Furthermore, as found in previous studies of larger HERG and LERG samples (e.g. Best & Heckman, 2012), while the LERGs predominantly have early-type morphologies and host SMBHs with large masses, the HERGs were associated with a mixture of morphological types (see Chapter 3) and lower-mass SMBHs.

These results therefore provide some evidence to suggest that there is a continuity in the connection between double-lobed/edge-brightened radio structures and the radiatively-efficient AGN accretion mode along the HERG sequence, although its strength remains uncertain. Regardless of this, they have served to reveal the existence of a significant population of compact AGN radio sources with strong optical emission lines, which had not been explored in detail before this thesis.

Overall, the results presented in this thesis have served to improve our understanding of the host morphologies and radio properties of radio-intermediate HERGs, which represent an important subgroup of the lower-power radio sources that dominate the local radio AGN population. They have provided strong evidence to suggest that the importance of merger-based triggering for radiatively-efficient AGN is strongly dependent on their optical emission line luminosities, but more weakly dependent on their radio powers. Clear evidence for a transition in the dominant host types of these AGN, from early-type galaxies at high radio powers to late-type galaxies at low radio powers, has also been presented.

7.2 Future prospects

This thesis has helped to address several open questions concerning the properties of HERGs with intermediate radio powers and how they relate to those of their counterparts at higher and lower radio powers (quasars, Seyfert galaxies, and high-radio-power HERGs). However, it has also highlighted several topics that warrant further investigation, and which represent promising future directions in this area of research. The following projects would help to address these open issues.

Further investigation of radio AGN and Type 2 quasar host morphologies

One of the key outcomes of the morphological analysis performed for the active galaxies studied in this thesis (radio-intermediate HERGs, 3CR radio galaxies, and Type 2 quasars) is the evidence for an increasing rate of disturbance towards higher [OIII]$\lambda5007$ luminosities, which is particularly strong when only radiatively-efficient AGN are considered. Alongside this, it was found that while the radiatively-inefficient LERGs in the 3CR sample showed a slight excess in their rate of disturbance relative to their matched non-active control galaxies (at the $1.2\,\sigma$ level), they exhibited a deficit relative to the 3CR HERGs (at the $2.4\,\sigma$ level).

Although these results are consistent with the idea that galaxy mergers and interactions are important for triggering radiatively-efficient AGN but not radiatively-inefficient

AGN at high radio powers, the extent of this difference is not yet fully determined. The strength of the dependence of merger-based triggering on optical emission line luminosity in radiatively-efficient objects is also uncertain. Similar analysis of deep, wide-field imaging observations for additional samples of HERGs, LERGs, and Type 2 quasars would help to better characterise these relationships. The greatly improved sky coverage provided by such wide-field imaging observations would also increase the chance of finding suitable non-active control galaxy matches for the highest mass objects in the 3CR sample within the image fields, which would improve the analysis of their rates of disturbance and typical host types.

In addition to the acquisition of further optical imaging data, more detailed analysis of the existing observations would also be useful. As shown by Ramos Almeida et al. (2012) and Bessiere et al. (2012), and by the analysis of the radio-intermediate HERGs performed in Chapter 3 (the RI-HERG low sample), an important factor to consider when comparing the levels of morphological disturbance in different samples of objects is the surface brightness of the identified interaction signatures. In addition to the higher rates of disturbance found for the 2Jy SLRGs relative to non-active elliptical control galaxies, Ramos Almeida et al. (2012) found that the tidal features associated with the active galaxies were of typically higher surface brightness than those associated with the controls. While the rates of disturbance for the Type 2 quasar hosts and matched non-active control galaxies studied by Bessiere et al. (2012) were seen to be similar, it was found that the active galaxies again showed typically higher-surface-brightness interaction signatures.

In Chapter 3, it was found that the tidal features associated with the RI-HERG low objects had typically lower surface brightnesses than the SLRGs in the 2Jy sample. This is consistent with the idea that more disruptive merger events are required to trigger more powerful AGN, while weaker AGN can be triggered by less disruptive interactions. Measurements of the interaction signature surface brightnesses for the large sample of galaxies studied in Chapter 5, which encompasses AGN with a broad range of powers, as well as non-active control galaxies, would be useful for investigating this picture.

The influence of star-forming activity

One factor not considered in this thesis is the influence that the level of star-forming activity may have on the measured merger rates for the galaxies studied. Many results from numerical simulations of major galaxy-galaxy interactions suggest that they can notably enhance overall star formation rates (e.g. Barnes & Hernquist, 1991; Mihos &

Hernquist, 1996; Di Matteo et al., 2005; Moreno et al., 2015), a picture that is largely supported by observational studies of galaxies in various stages of merging events (e.g. Li et al., 2008a; Ellison et al., 2013; Patton et al., 2013; Knapen et al., 2015). Reanalysis of the merger rates in the active and non-active galaxies studied here, with additional matching in terms of star formation rate, could be useful for ensuring that the observed results are not linked with an underlying association with star-forming activity (e.g. see Li et al., 2008b; Sabater et al., 2015). Of all of the comparisons made in this thesis, it is thought that this could be most important for the differences found between the radiatively-efficient (HERG/SLRG) and radiatively-inefficient (LERG/WLRG) radio galaxies, since the former subgroup is more typically associated with both bluer colours and higher star formation rates than the latter (e.g. Best & Heckman, 2012; Janssen et al., 2012; Tadhunter, 2016).

The large-scale environments of active radio galaxies

Another factor that is important to consider when investigating AGN triggering mechanisms is the large-scale environments of the host galaxies, which have not yet been determined for the objects studied in this thesis. It has previously been suggested that the high relative galaxy velocities present in cluster environments can reduce the rate of mergers within them, while this would not provide a significant issue in group-like environments, where the relative galaxy velocities are lower (Popesso & Biviano, 2006). Furthermore, alternative AGN fuelling mechanisms are thought to be important in clusters that are not as feasible in group-like environments, due to the large reservoirs of hot gas that are only available in the former: direct Bondi accretion (e.g. Allen et al., 2006; Hardcastle et al., 2007); chaotic cold accretion (Gaspari et al., 2013, 2015); or cooling flows (e.g. Tadhunter et al., 1989; Baum et al., 1992; Best et al., 2005b). The large-scale environments of the AGN host galaxies could therefore have a strong influence on the dominant triggering mechanisms for the activity, and so characterising them is key for such investigations.

Study of the large-scale environments of the powerful radio galaxies in the 2Jy sample, by Ramos Almeida et al. (2013), revealed that these objects showed a significant preference for denser environments than early-type galaxies from the general population, but no significant difference was found between the environments of early-type galaxies and Type 2 quasar hosts. In addition, the radiatively-inefficient objects in the 2Jy sample (WLRGs) showed a significant preference for denser (cluster-like) environments than the radiatively-efficient objects (SLRGs), which exhibited a preference for group-like environments. In combination with the low rate of disturbance found for the 2Jy WLRGs, this is consistent with the idea that the alternative triggering mechanisms available in dense cluster environments are dominant for these sources. On the other hand, the group-like environments in which the 2Jy SLRGs are typically found are suitable for frequent galaxy mergers and interactions. Along with their high rates of disturbance (Ramos Almeida et al., 2011), this is consistent with the idea that these objects are predominantly triggered by these events.

Analysis of the large-scale environments of the large number of active galaxies studied in this thesis would therefore be useful for determining the likely triggering mechanisms for the different types of AGN included. This would be particularly useful for testing the picture of an apparent dichotomy in the dominant triggering mechanisms for radiatively-efficient and radiatively-inefficient radio AGN (galaxy mergers/interactions and cluster-based processes, respectively). Performing this analysis for the non-active control galaxies is also important for testing whether or not differences between the large-scale environments of the active and non-active galaxies have had an influence on the results obtained in Chapter 5. This research would ideally be performed using an identical number counting technique to that used by Ramos Almeida et al. (2013), to allow for direct comparison with their results.

Further investigation of the radio properties of radio-intermediate AGN

The results from the analysis of the radio properties of radio-intermediate HERGs presented in Chapter 6 provided some suggestion that there is a continuity in the connection between double-lobed, edge-brightened radio structures and radiatively-efficient AGN accretion in the intermediate radio power regime, although the strength of this association remains unclear. The steep radio spectra found for the sources with unresolved radio structures suggests that these objects exhibit extended emission on smaller physical scales than those probed by the VLA observations (i.e. $\lesssim$ 280–540 pc), scales on which some Seyfert galaxies have been found to show extended structures (e.g. Neff & de Bruyn, 1983). Higher resolution radio observations (e.g. e-MERLIN or VLBI) of these sources would be useful for providing a more definitive test of the idea that double-lobed, edge-brightened radio structures are connected with these radiatively-efficient objects along the HERG sequence. Additional VLA observations of further samples of radio-intermediate HERGs would also be useful for investigating this picture.

Bibliography

Abazajian K. N., et al., 2009, ApJS, 182, 543

Adams T. F., 1977, ApJS, 33, 19

Adelman-McCarthy J. K., et al., 2008, ApJS, 175, 297

Aird J., Coil A. L., Georgakakis A., Nandra K., Barro G., Pérez-González P. G., 2015, MNRAS, 451, 1892

Alatalo K., et al., 2011, ApJ, 735, 88

Alexandroff R. M., Zakamska N. L., van Velzen S., Greene J. E., Strauss M. A., 2016, MNRAS, 463, 3056

Allen S. W., Dunn R. J. H., Fabian A. C., Taylor G. B., Reynolds C. S., 2006, MNRAS, 372, 21

Antonucci R., 1993, ARAA, 31, 473

Antonucci R. R. J., Miller J. S., 1985, ApJ, 297, 621

Atkinson A. M., Abraham R. G., Ferguson A. M. N., 2013, ApJ, 765, 28

Baade W., Minkowski R., 1954a, ApJ, 119, 206

Baade W., Minkowski R., 1954b, ApJ, 119, 215

Bahcall N. A., 1977, ARAA, 15, 505

Baldi R. D., Capetti A., 2008, A&A, 489, 989

Baldi R. D., Capetti A., 2009, A&A, 508, 603

Baldi R. D., Capetti A., 2010, A&A, 519, A48

Baldi R. D., et al., 2010, ApJ, 725, 2426

Baldi R. D., Capetti A., Giovannini G., 2015, A&A, 576, A38

Baldi R. D., et al., 2018a, MNRAS, 476, 3478

Baldi R. D., Capetti A., Massaro F., 2018b, A&A, 609, A1

Baldi R. D., Capetti A., Giovannini G., 2019a, MNRAS, 482, 2294

Baldi R. D., Capetti A., Giovannini G., 2019b, MNRAS, 482, 2294

Baldwin J. A., Phillips M. M., Terlevich R., 1981, PASP, 93, 5

Bamford S. P., et al., 2009, MNRAS, 393, 1324

Bardeen J. M., 1970, Nature, 226, 64

Barnes J. E., Hernquist L. E., 1991, ApJL, 370, L65

Barnes J. E., Hernquist L., 1996, ApJ, 471, 115

Baum S. A., Heckman T. M., van Breugel W., 1992, ApJ, 389, 208

Becker R. H., White R. L., Helfand D. J., 1995, ApJ, 450, 559

Begelman M. C., Blandford R. D., Rees M. J., 1984, Reviews of Modern Physics, 56, 255

Bell E. F., de Jong R. S., 2001, ApJ, 550, 212

Bell E. F., McIntosh D. H., Katz N., Weinberg M. D., 2003, ApJS, 149, 289

Bennert N., Canalizo G., Jungwiert B., Stockton A., Schweizer F., Peng C. Y., Lacy M., 2008, ApJ, 677, 846

Bennett A. S., 1962, Mem. R. Astron. Soc., 68, 163

Bentz M. C., et al., 2009, ApJ, 705, 199

Bertin E., 2006, in Gabriel C., Arviset C., Ponz D., Enrique S., eds, Astronomical Society of the Pacific Conference Series Vol. 351, Astronomical Data Analysis Software and Systems XV. p. 112

Bertin E., Arnouts S., 1996, A&A Suppl., 117, 393

Bessiere P. S., Tadhunter C. N., Ramos Almeida C., Villar Martín M., 2012, MNRAS, 426, 276

Best P. N., 2009, Astronomische Nachrichten, 330, 184

Best P. N., Heckman T. M., 2012, MNRAS, 421, 1569

Best P. N., Kauffmann G., Heckman T. M., Ivezić Ž., 2005a, MNRAS, 362, 9

Best P. N., Kauffmann G., Heckman T. M., Brinchmann J., Charlot S., Ivezić Ž., White S. D. M., 2005b, MNRAS, 362, 25

Best P. N., Kaiser C. R., Heckman T. M., Kauffmann G., 2006, MNRAS, 368, L67

Best P. N., von der Linden A., Kauffmann G., Heckman T. M., Kaiser C. R., 2007, MNRAS, 379, 894

Bicknell G. V., 1995, ApJS, 101, 29

Bîrzan L., McNamara B. R., Nulsen P. E. J., Carilli C. L., Wise M. W., 2008, ApJ, 686, 859

Blandford R. D., Znajek R. L., 1977, MNRAS, 179, 433

Bolton J. G., 1948, Nature, 162, 141

Bolton J. G., Stanley G. J., Slee O. B., 1949, Nature, 164, 101

Bournaud F., et al., 2012, ApJ, 757, 81

Bower R. G., Benson A. J., Malbon R., Helly J. C., Frenk C. S., Baugh C. M., Cole S., Lacey C. G., 2006, MNRAS, 370, 645

Bower R. G., Benson A. J., Crain R. A., 2012, MNRAS, 422, 2816

Bruzual G., Charlot S., 2003, MNRAS, 344, 1000

Burbidge G. R., 1961, Nature, 190, 1053

Burbidge E. M., 1967, ApJL, 149, L51

Burbidge G. R., Burbidge E. M., Sandage A. R., 1963a, Reviews of Modern Physics, 35, 947

Burbidge E. M., Burbidge G. R., Prendergast K. H., 1963b, ApJ, 137, 1022

Burns J. O., 1990, AJ, 99, 14

Buttiglione S., Capetti A., Celotti A., Axon D. J., Chiaberge M., Macchetto F. D., Sparks W. B., 2009, A&A, 495, 1033

Buttiglione S., Capetti A., Celotti A., Axon D. J., Chiaberge M., Macchetto F. D., Sparks W. B., 2010, A&A, 509, A6

Buttiglione S., Capetti A., Celotti A., Axon D. J., Chiaberge M., Macchetto F. D., Sparks W. B., 2011, A&A, 525, A28

Cabrera-Vives G., Miller C. J., Schneider J., 2018, preprint, (`arXiv:1811.03577`)

Callingham J. R., et al., 2015, ApJ, 809, 168

Calzetti D., et al., 2010, ApJ, 714, 1256

Cameron E., 2011, PASA, 28, 128

Campbell W. W., Moore J. H., 1918, Publications of Lick Observatory, 13, 75

Capetti A., Massaro F., Baldi R. D., 2017, A&A, 601, A81

Cattaneo A., et al., 2009, Nature, 460, 213

Cavagnolo K. W., McNamara B. R., Nulsen P. E. J., Carilli C. L., Jones C., Bîrzan L., 2010, ApJ, 720, 1066

Chabrier G., 2003, PASP, 115, 763

Chambers K. C., et al., 2016, arXiv e-prints, p. arXiv:1612.05560

Chiaberge M., Marconi A., 2011, MNRAS, 416, 917

Chiaberge M., Gilli R., Lotz J. M., Norman C., 2015, ApJ, 806, 147

Chilingarian I. V., Melchior A.-L., Zolotukhin I. Y., 2010, MNRAS, 405, 1409

Cid Fernandes R., Stasińska G., Schlickmann M. S., Mateus A., Vale Asari N., Schoenell W., Sodré L., 2010, MNRAS, 403, 1036

Cid Fernandes R., Stasińska G., Mateus A., Vale Asari N., 2011, MNRAS, 413, 1687

Cielo S., Bieri R., Volonteri M., Wagner A. Y., Dubois Y., 2018, MNRAS, 477, 1336

Ciotti L., Ostriker J. P., Proga D., 2010, ApJ, 717, 708

Cisternas M., et al., 2011, ApJ, 726, 57

Coldwell G. V., Alonso S., Duplancic F., Mesa V., 2018, MNRAS, 476, 2457

Colgate S. A., 1967, ApJ, 150, 163

Colgate S. A., 1968, AJ, 73, 905

Condon J. J., 1992, ARAA, 30, 575

Condon J. J., Cotton W. D., Greisen E. W., Yin Q. F., Perley R. A., Taylor G. B., Broderick J. J., 1998, AJ, 115, 1693

Conselice C. J., Wilkinson A., Duncan K., Mortlock A., 2016, ApJ, 830, 83

Costero R., Osterbrock D. E., 1977, ApJ, 211, 675

Croton D. J., et al., 2006, MNRAS, 365, 11

Croton D. J., et al., 2016, ApJS, 222, 22

Dasyra K. M., Combes F., 2012, A&A, 541, L7

Dey A., et al., 2019, AJ, 157, 168

Di Matteo T., Springel V., Hernquist L., 2005, Nature, 433, 604

Dicken D., Tadhunter C., Axon D., Morganti R., Inskip K. J., Holt J., González Delgado R., Groves B., 2009, ApJ, 694, 268

Dicken D., Tadhunter C., Axon D., Robinson A., Morganti R., Kharb P., 2010, ApJ, 722, 1333

Dicken D., et al., 2012, ApJ, 745, 172

Donley J. L., et al., 2018, ApJ, 853, 63

Donzelli C. J., Chiaberge M., Macchetto F. D., Madrid J. P., Capetti A., Marchesini D., 2007, ApJ, 667, 780

Driver S. P., et al., 2016, MNRAS, 455, 3911

Duc P.-A., et al., 2015, MNRAS, 446, 120

Dunlop J. S., McLure R. J., Kukula M. J., Baum S. A., O'Dea C. P., Hughes D. H., 2003, MNRAS, 340, 1095

Edge D. O., Shakeshaft J. R., McAdam W. B., Baldwin J. E., Archer S., 1959, Mem. R. Astron. Soc., 68, 37

Elbaz D., et al., 2007, A&A, 468, 33

Ellison S. L., Mendel J. T., Patton D. R., Scudder J. M., 2013, MNRAS, 435, 3627

Elvis M., Maccacaro T., Wilson A. S., Ward M. J., Penston M. V., Fosbury R. A. E., Perola G. C., 1978, MNRAS, 183, 129

Emonts B. H. C., Morganti R., Tadhunter C. N., Oosterloo T. A., Holt J., van der Hulst J. M., 2005, MNRAS, 362, 931

Evans I. N., et al., 2010, ApJS, 189, 37

Event Horizon Telescope Collaboration et al., 2019a, ApJL, 875, L1

Event Horizon Telescope Collaboration et al., 2019b, ApJL, 875, L5

Fabbiano G., Miller L., Trinchieri G., Longair M., Elvis M., 1984, ApJ, 277, 115

Fabian A. C., 1994, ARAA, 32, 277

Fabian A. C., 2012, ARAA, 50, 455

Falomo R., Bettoni D., Karhunen K., Kotilainen J. K., Uslenghi M., 2014, MNRAS, 440, 476

Fanaroff B. L., Riley J. M., 1974, MNRAS, 167, 31P

Fath E. A., 1909, Lick Observatory Bulletin, 149, 71

Ferrarese L., Ford H., 2005, Space Science Reviews, 116, 523

Floyd D. J. E., Kukula M. J., Dunlop J. S., McLure R. J., Miller L., Percival W. J., Baum S. A., O'Dea C. P., 2004, MNRAS, 355, 196

Fragile P. C., Anninos P., Croft S., Lacy M., Witry J. W. L., 2017, ApJ, 850, 171

Frederick S., et al., 2019, ApJ, 883, 31

Fukugita M., Ichikawa T., Gunn J. E., Doi M., Shimasaku K., Schneider D. P., 1996, AJ, 111, 1748

Gaia Collaboration et al., 2018, A&A, 616, A1

Gaibler V., Khochfar S., Krause M., Silk J., 2012, MNRAS, 425, 438

Galloway M. A., et al., 2015, MNRAS, 448, 3442

Gao H., Ho L. C., 2017, ApJ, 845, 114

Gaspari M., Ruszkowski M., Oh S. P., 2013, MNRAS, 432, 3401

Gaspari M., Brighenti F., Temi P., 2015, A&A, 579, A62

Genzel R., Eisenhauer F., Gillessen S., 2010, Reviews of Modern Physics, 82, 3121

Ghisellini G., 2011, in Aharonian F. A., Hofmann W., Rieger F. M., eds, American Institute of Physics Conference Series Vol. 1381, American Institute of Physics Conference Series. pp 180–198 (`arXiv:1104.0006`), doi:10.1063/1.3635832

Gordon Y. A., et al., 2019, ApJ, 878, 88

Grandi S. A., Osterbrock D. E., 1978, ApJ, 220, 783

Greene J. E., Zakamska N. L., Liu X., Barth A. J., Ho L. C., 2009, ApJ, 702, 441

Greenstein J. L., Matthews T. A., 1963, Nature, 197, 1041

Greenstein J. L., Schmidt M., 1964, ApJ, 140, 1

Gürkan G., et al., 2015, MNRAS, 452, 3776

Hardcastle M. J., 2018, MNRAS, 475, 2768

Hardcastle M. J., Evans D. A., Croston J. H., 2007, MNRAS, 376, 1849

Hardcastle M. J., et al., 2013, MNRAS, 429, 2407

Hardcastle M. J., et al., 2019, A&A, 622, A12

Harrison C. M., Thomson A. P., Alexander D. M., Bauer F. E., Edge A. C., Hogan M. T., Mullaney J. R., Swinbank A. M., 2015, ApJ, 800, 45

Heckman T. M., 1980, A&A, 500, 187

Heckman T. M., Best P. N., 2014, ARAA, 52, 589

Heckman T. M., Smith E. P., Baum S. A., van Breugel W. J. M., Miley G. K., Illingworth G. D., Bothun G. D., Balick B., 1986, ApJ, 311, 526

Heckman T. M., Kauffmann G., Brinchmann J., Charlot S., Tremonti C., White S. D. M., 2004, ApJ, 613, 109

Herschel W., 1785, Philosophical Transactions of the Royal Society of London Series I, 75, 213

Hickox R. C., Alexander D. M., 2018, ARAA, 56, 625

Hickox R. C., et al., 2009, ApJ, 696, 891

Hine R. G., Longair M. S., 1979, MNRAS, 188, 111

Ho L. C., 2008, ARAA, 46, 475

Ho L. C., Filippenko A. V., Sargent W. L. W., 1997, ApJ, 487, 568

Hoessel J. G., 1980, ApJ, 241, 493

Holt J., Tadhunter C. N., Morganti R., 2008, MNRAS, 387, 639

Hong J., Im M., Kim M., Ho L. C., 2015, ApJ, 804, 34

Hood C. E., Kannappan S. J., Stark D. V., Dell'Antonio I. P., Moffett A. J., Eckert K. D., Norris M. A., Hendel D., 2018, ApJ, 857, 144

Hopkins P. F., Quataert E., 2010, MNRAS, 407, 1529

Hopkins P. F., Hernquist L., Cox T. J., Kereš D., 2008, ApJS, 175, 356

Hoyle F., Fowler W. A., 1963a, MNRAS, 125, 169

Hoyle F., Fowler W. A., 1963b, Nature, 197, 533

Hubble E., 1925, ApJ, 62, 409

Hubble E., 1926a, ApJ, 63, 236

Hubble E., 1926b, ApJ, 64, 321

Hubble E., 1929a, Proceedings of the National Academy of Science, 15, 168

Hubble E., 1929b, ApJ, 69, 103

Huggins S. W., Huggins L., 1899, An atlas of representative stellar spectra from λ 4870 to λ 3300. William Wesley and Son, London, doi:10.3931/e-rara-58789, `https://www.e-rara.ch/zut/content/titleinfo/15851436`

Ineson J., Croston J. H., Hardcastle M. J., Kraft R. P., Evans D. A., Jarvis M., 2013, ApJ, 770, 136

Ineson J., Croston J. H., Hardcastle M. J., Kraft R. P., Evans D. A., Jarvis M., 2015, MNRAS, 453, 2682

Inskip K. J., Tadhunter C. N., Morganti R., Holt J., Ramos Almeida C., Dicken D., 2010, MNRAS, 407, 1739

Jansky K. G., 1935, Proceedings of the Institute of Radio Engineers, 23, 1158

Janssen R. M. J., Röttgering H. J. A., Best P. N., Brinchmann J., 2012, A&A, 541, A62

Jarrett T. H., Chester T., Cutri R., Schneider S., Skrutskie M., Huchra J. P., 2000, AJ, 119, 2498

Jarvis M. E., et al., 2019, MNRAS, 485, 2710

Kaiser C. R., Best P. N., 2007, MNRAS, 381, 1548

Kaiser C. R., Dennett-Thorpe J., Alexander P., 1997, MNRAS, 292, 723

Kant I., 1755, Allgemeine Naturgeschichte und Theorie des Himmels

Kauffmann G., et al., 2003, MNRAS, 346, 1055

Kauffmann G., Heckman T. M., Best P. N., 2008, MNRAS, 384, 953

Keeler J. E., 1899, Astronomische Nachrichten, 151, 1

Kellermann K. I., Pauliny-Toth I. I. K., 1968, ARAA, 6, 417

Kellermann K. I., Pauliny-Toth I. I. K., 1981, ARAA, 19, 373

Kellermann K. I., Sramek R., Schmidt M., Shaffer D. B., Green R., 1989, AJ, 98, 1195

Kennicutt Robert C. J., 1998, ARAA, 36, 189

Kewley L. J., Dopita M. A., Sutherland R. S., Heisler C. A., Trevena J., 2001, ApJ, 556, 121

Kewley L. J., Groves B., Kauffmann G., Heckman T., 2006, MNRAS, 372, 961

Khachikian E. Y., Weedman D. W., 1974, ApJ, 192, 581

Kharb P., O'Dea C. P., Baum S. A., Colbert E. J. M., Xu C., 2006, ApJ, 652, 177

Kharb P., Hota A., Croston J. H., Hardcastle M. J., O'Dea C. P., Kraft R. P., Axon D. J., Robinson A., 2010, ApJ, 723, 580

Klein U., Mack K. H., Gregorini L., Vigotti M., 2003, A&A, 406, 579

Knapen J. H., Cisternas M., Querejeta M., 2015, MNRAS, 454, 1742

Kocevski D. D., et al., 2012, ApJ, 744, 148

Kormendy J., Ho L. C., 2013, ARAA, 51, 511

Kormendy J., Kennicutt Jr. R. C., 2004, ARAA, 42, 603

Kormendy J., Richstone D., 1995, ARAA, 33, 581

Kroupa P., 2001, MNRAS, 322, 231

Kuo C. Y., et al., 2011, ApJ, 727, 20

Laing R. A., Jenkins C. R., Wall J. V., Unger S. W., 1994, in Bicknell G. V., Dopita M. A., Quinn P. J., eds, Astronomical Society of the Pacific Conference Series Vol. 54, The Physics of Active Galaxies. p. 201

Lansbury G. B., Jarvis M. E., Harrison C. M., Alexander D. M., Del Moro A., Edge A. C., Mullaney J. R., Thomson A. P., 2018, ApJL, 856, L1

Läsker R., Ferrarese L., van de Ven G., Shankar F., 2014, ApJ, 780, 70

Leavitt H. S., 1908, Annals of Harvard College Observatory, 60, 87

Leavitt H. S., Pickering E. C., 1912, Harvard College Observatory Circular, 173, 1

Ledlow M. J., Owen F. N., 1996, AJ, 112, 9

Li C., Kauffmann G., Heckman T. M., Jing Y. P., White S. D. M., 2008a, MNRAS, 385, 1903

Li C., Kauffmann G., Heckman T. M., White S. D. M., Jing Y. P., 2008b, MNRAS, 385, 1915

Lin Y.-T., Shen Y., Strauss M. A., Richards G. T., Lunnan R., 2010, ApJ, 723, 1119

Lintott C. J., et al., 2008, MNRAS, 389, 1179

Lintott C., et al., 2011, MNRAS, 410, 166

Lynden-Bell D., 1969, Nature, 223, 690

Lynden-Bell D., 1971, MNRAS, 155, 95

Lynden-Bell D., 1978, Physica Scripta, 17, 185

Maccagni F. M., Morganti R., Oosterloo T. A., Geréb K., Maddox N., 2017, A&A, 604, A43

Magorrian J., et al., 1998, AJ, 115, 2285

Marconi A., Hunt L. K., 2003, ApJL, 589, L21

Marconi A., Risaliti G., Gilli R., Hunt L. K., Maiolino R., Salvati M., 2004, MNRAS, 351, 169

Marian V., et al., 2019, ApJ, 882, 141

Massaro F., et al., 2010, ApJ, 714, 589

Massaro F., et al., 2012, ApJS, 203, 31

Matthews T. A., Morgan W. W., Schmidt M., 1964, ApJ, 140, 35

Mauch T., Sadler E. M., 2007, MNRAS, 375, 931

McConnell N. J., Ma C.-P., 2013, ApJ, 764, 184

McLure R. J., Dunlop J. S., 2002, MNRAS, 331, 795

McMullin J. P., Waters B., Schiebel D., Young W., Golap K., 2007, in Shaw R. A., Hill F., Bell D. J., eds, Astronomical Society of the Pacific Conference Series Vol. 376, Astronomical Data Analysis Software and Systems XVI. p. 127

McNamara B. R., Nulsen P. E. J., 2007, ARAA, 45, 117

McNamara B. R., Rohanizadegan M., Nulsen P. E. J., 2011, ApJ, 727, 39

McNamara B. R., et al., 2014, ApJ, 785, 44

Mechtley M., et al., 2016, ApJ, 830, 156

Menci N., Gatti M., Fiore F., Lamastra A., 2014, A&A, 569, A37

Merloni A., Heinz S., 2008, MNRAS, 388, 1011

Meurs E. J. A., Wilson A. S., 1984, A&A, 136, 206

Mihos J. C., Hernquist L., 1996, ApJ, 464, 641

Mingo B., Hardcastle M. J., Croston J. H., Dicken D., Evans D. A., Morganti R., Tadhunter C., 2014, MNRAS, 440, 269

Mingo B., et al., 2019, MNRAS, 488, 2701

Minkowski R., 1960, ApJ, 132, 908

Molyneux S. J., Harrison C. M., Jarvis M. E., 2019, A&A, 631, A132

Monet D. G., et al., 2003, AJ, 125, 984

Moran E. C., Barth A. J., Eracleous M., Kay L. E., 2007, ApJL, 668, L31

Moreno J., Torrey P., Ellison S. L., Patton D. R., Bluck A. F. L., Bansal G., Hernquist L., 2015, MNRAS, 448, 1107

Morganti R., 2017, Nature Astronomy, 1, 596

Morganti R., Oosterloo T., Tsvetanov Z., 1998, AJ, 115, 915

Morganti R., Tsvetanov Z. I., Gallimore J., Allen M. G., 1999, A&A Suppl., 137, 457

Morganti R., Tadhunter C. N., Oosterloo T. A., 2005, A&A, 444, L9

Morganti R., Fogasy J., Paragi Z., Oosterloo T., Orienti M., 2013, Science, 341, 1082

Morganti R., Oosterloo T., Oonk J. B. R., Frieswijk W., Tadhunter C., 2015, A&A, 580, A1

Morrison P., 1969, ApJL, 157, L73

Morrison P., Cavaliere A., 1971, in O'Connell D. J. K., ed., Study Week on Nuclei of Galaxies. p. 485

Moshir M., Kopman G., Conrow T. A. O., 1992, IRAS Faint Source Survey, Explanatory supplement version 2

Mukherjee D., Bicknell G. V., Sutherland R., Wagner A., 2016, MNRAS, 461, 967

Mukherjee D., Wagner A. Y., Bicknell G. V., Morganti R., Oosterloo T., Nesvadba N., Sutherland R. S., 2018a, MNRAS, 476, 80

Mukherjee D., Bicknell G. V., Wagner A. e. Y., Sutherland R. S., Silk J., 2018b, MNRAS, 479, 5544

Mullaney J. R., Alexander D. M., Goulding A. D., Hickox R. C., 2011, MNRAS, 414, 1082

Mullaney J. R., Alexander D. M., Fine S., Goulding A. D., Harrison C. M., Hickox R. C., 2013, MNRAS, 433, 622

Murphy E. J., et al., 2011, ApJ, 737, 67

Murthy S., et al., 2019, A&A, 629, A58

Narayan R., 2005, Ap&SS, 300, 177

Narayan R., Yi I., 1994, ApJL, 428, L13

Narayan R., Yi I., 1995, ApJ, 452, 710

Neff S. G., de Bruyn A. G., 1983, A&A, 128, 318

Nesvadba N. P. H., et al., 2010, A&A, 521, A65

O'Dea C. P., 1998, PASP, 110, 493

Oosterloo T. A., Morganti R., Tzioumis A., Reynolds J., King E., McCulloch P., Tsvetanov Z., 2000, AJ, 119, 2085

Orienti M., 2016, Astronomische Nachrichten, 337, 9

Osterbrock D. E., 1989, Astrophysics of gaseous nebulae and active galactic nuclei

Osterbrock D. E., Miller J. S., 1975, ApJ, 197, 535

Osterbrock D. E., Koski A. T., Phillips M. M., 1976, ApJ, 206, 898

Owen F. N., 1993, Steps Toward a Radio H-R Diagram. p. 273, doi:10.1007/3-540-57164-7˙104

Ozernoi L. M., 1966, Soviet Astronomy, 10, 241

Padovani P., et al., 2017, Astronomy and Astrophysics Review, 25, 2

Patton D. R., Torrey P., Ellison S. L., Mendel J. T., Scudder J. M., 2013, MNRAS, 433, L59

Peacock J. A., Miller L., Longair M. S., 1986, MNRAS, 218, 265

Peng C. Y., Ho L. C., Impey C. D., Rix H.-W., 2002, AJ, 124, 266

Peng C. Y., Ho L. C., Impey C. D., Rix H.-W., 2010, AJ, 139, 2097

Perley R. A., Butler B. J., 2017, ApJS, 230, 7

Peterson B. M., et al., 2004, ApJ, 613, 682

Piddington J. H., 1970, MNRAS, 148, 131

Pierce J. C. S., Tadhunter C. N., Ramos Almeida C., Bessiere P. S., Rose M., 2019, MNRAS, 487, 5490

Pierce J. C. S., Tadhunter C. N., Morganti R., 2020, MNRAS, 494, 2053

Polatidis A. G., Conway J. E., 2003, PASA, 20, 69

Popesso P., Biviano A., 2006, A&A, 460, L23

Quinn P. J., 1984, ApJ, 279, 596

Rafferty D. A., McNamara B. R., Nulsen P. E. J., 2008, ApJ, 687, 899

Ramos Almeida C., Ricci C., 2017, Nature Astronomy, 1, 679

Ramos Almeida C., Tadhunter C. N., Inskip K. J., Morganti R., Holt J., Dicken D., 2011, MNRAS, 410, 1550

Ramos Almeida C., et al., 2012, MNRAS, 419, 687

Ramos Almeida C., Bessiere P. S., Tadhunter C. N., Inskip K. J., Morganti R., Dicken D., González-Serrano J. I., Holt J., 2013, MNRAS, 436, 997

Ramos Almeida C., Martínez González M. J., Asensio Ramos A., Acosta-Pulido J. A., Hönig S. F., Alonso-Herrero A., Tadhunter C. N., González-Martín O., 2016, MNRAS, 461, 1387

Ramos Almeida C., Piqueras López J., Villar-Martín M., Bessiere P. S., 2017, MNRAS, 470, 964

Rawlings S., Saunders R., 1991, Nature, 349, 138

Reber G., 1944, ApJ, 100, 279

Rees M. J., 1978a, Physica Scripta, 17, 193

Rees M. J., 1978b, Nature, 275, 516

Rees M. J., 1984, ARAA, 22, 471

Reyes R., et al., 2008, AJ, 136, 2373

Rosse T. E. O., 1850, Philosophical Transactions of the Royal Society of London Series I, 140, 499

Russell H. R., McNamara B. R., Edge A. C., Hogan M. T., Main R. A., Vantyghem A. N., 2013, MNRAS, 432, 530

Russell H. R., et al., 2017, MNRAS, 472, 4024

Russell H. R., et al., 2019, MNRAS, 490, 3025

Ryle M., Smith F. G., 1948, Nature, 162, 462

Ryle M., Smith F. G., Elsmore B., 1950, MNRAS, 110, 508

Sabater J., Best P. N., Argudo-Fernández M., 2013, MNRAS, 430, 638

Sabater J., Best P. N., Heckman T. M., 2015, MNRAS, 447, 110

Sabater J., et al., 2019, A&A, 622, A17

Sadler E. M., et al., 2002, MNRAS, 329, 227

Sadler E. M., Ekers R. D., Mahony E. K., Mauch T., Murphy T., 2014, MNRAS, 438, 796

Salpeter E. E., 1964, ApJ, 140, 796

Sandage A., 1965, ApJ, 141, 1560

Sandage A., 1966, ApJ, 145, 1

Sandage A., Luyten W. J., 1967, ApJ, 148, 767

Sanders D. B., Soifer B. T., Elias J. H., Madore B. F., Matthews K., Neugebauer G., Scoville N. Z., 1988, ApJ, 325, 74

Scheiner J., 1899, ApJ, 9, 149

Schirmer M., 2013, ApJS, 209, 21

Schlafly E. F., Finkbeiner D. P., 2011, ApJ, 737, 103

Schlegel D. J., Finkbeiner D. P., Davis M., 1998, ApJ, 500, 525

Schmidt M., 1963, Nature, 197, 1040

Schmidt M., 1965a, ApJ, 141, 1

Schmidt M., 1965b, ApJ, 141, 1295

Schmidt M., 1970, ApJ, 162, 371

Schreiber C., et al., 2015, A&A, 575, A74

Seyfert C. K., 1943, ApJ, 97, 28

Shah E. A., et al., 2020, ApJ, 904, 107

Shakura N. I., Sunyaev R. A., 1973, A&A, 24, 337

Shapley H., Curtis H. D., 1921, Bulletin of the National Research Council, 2, 171

Shimwell T. W., et al., 2019, A&A, 622, A1

Silk J., Rees M. J., 1998, A&A, 331, L1

Singh R., et al., 2013, A&A, 558, A43

Skrutskie M. F., et al., 2006, AJ, 131, 1163

Slipher V. M., 1915, Popular Astronomy, 23, 21

Slipher V. M., 1917a, Lowell Observatory Bulletin, 3, 59

Slipher V. M., 1917b, Proceedings of the American Philosophical Society, 56, 403

Smith E. P., Heckman T. M., 1989a, ApJS, 69, 365

Smith E. P., Heckman T. M., 1989b, ApJ, 341, 658

Soltan A., 1982, MNRAS, 200, 115

Spinrad H., Djorgovski S., Marr J., Aguilar L., 1985, PASP, 97, 932

Spitzer Lyman J., Saslaw W. C., 1966, ApJ, 143, 400

Springel V., Di Matteo T., Hernquist L., 2005, MNRAS, 361, 776

Stocke J. T., Morris S. L., Weymann R. J., Foltz C. B., 1992, ApJ, 396, 487

Strittmatter P. A., Hill P., Pauliny-Toth I. I. K., Steppe H., Witzel A., 1980, A&A, 88, L12

Tadhunter C. N., 1991, MNRAS, 251, 46P

Tadhunter C., 2016, Astronomy and Astrophysics Review, 24, 10

Tadhunter C. N., Fosbury R. A. E., Quinn P. J., 1989, MNRAS, 240, 225

Tadhunter C. N., Morganti R., di Serego Alighieri S., Fosbury R. A. E., Danziger I. J., 1993, MNRAS, 263, 999

Tadhunter C. N., Morganti R., Robinson A., Dickson R., Villar-Martin M., Fosbury R. A. E., 1998, MNRAS, 298, 1035

Tadhunter C., et al., 2011, MNRAS, 412, 960

Tadhunter C., Dicken D., Morganti R., Konyves V., Ysard N., Nesvadba N., Almeida C. R., 2014a, MNRAS, 445, L51

Tadhunter C., Morganti R., Rose M., Oonk J. B. R., Oosterloo T., 2014b, Nature, 511, 440

Tal T., van Dokkum P. G., Nelan J., Bezanson R., 2009, AJ, 138, 1417

Tananbaum H., et al., 1979, ApJL, 234, L9

Taylor M. D., Tadhunter C. N., Robinson T. G., 2003, MNRAS, 342, 995

Tchekhovskoy A., Bromberg O., 2016, MNRAS, 461, L46

Thorne K. S., 1974, ApJ, 191, 507

Tonry J. L., et al., 2012, ApJ, 750, 99

Toomre A., Toomre J., 1972, ApJ, 178, 623

Tortora C., Antonuccio-Delogu V., Kaviraj S., Silk J., Romeo A. D., Becciani U., 2009, MNRAS, 396, 61

Treister E., Schawinski K., Urry C. M., Simmons B. D., 2012, ApJL, 758, L39

Tremaine S., et al., 2002, ApJ, 574, 740

Tzioumis A., et al., 2002, A&A, 392, 841

Ulvestad J. S., Wilson A. S., 1984, ApJ, 285, 439

Urbano-Mayorgas J. J., et al., 2019, MNRAS, 483, 1829

Urry C. M., Padovani P., 1995, PASP, 107, 803

Veilleux S., et al., 2009, ApJ, 701, 587

Veilleux S., Maiolino R., Bolatto A. D., Aalto S., 2020, Astronomy and Astrophysics Review, 28, 2

Villar-Martín M., et al., 2017, MNRAS, 472, 4659

Villforth C., et al., 2014, MNRAS, 439, 3342

Villforth C., et al., 2017, MNRAS, 466, 812

Wagner A. Y., Bicknell G. V., 2011, ApJ, 728, 29

Wagner A. Y., Bicknell G. V., Umemura M., 2012, ApJ, 757, 136

Weedman D. W., 1976a, Quarterly Journal of the Royal Astronomical Society, 17, 227

Weedman D. W., 1976b, ApJ, 208, 30

Weedman D. W., 1977, ARAA, 15, 69

Whittam I. H., Riley J. M., Green D. A., Jarvis M. J., 2016, MNRAS, 462, 2122

Willett K. W., et al., 2013, MNRAS, 435, 2835

Willmer C. N. A., 2018, ApJS, 236, 47

Woltjer L., 1964, Nature, 201, 803

Wright T., 1750, An Original Theory Or New Hypothesis Of The Universe, Founded Upon The Laws Of Nature, And Solving By Mathematical Principles the General Phænomena Of The Visible Creation And Particularly The Via Lactea. Chapelle, London, `https://books.google.co.uk/books?id=80VZAAAAcAAJ`

Wylezalek D., Zakamska N. L., Liu G., Obied G., 2016, MNRAS, 457, 745

Yu Q., Tremaine S., 2002, MNRAS, 335, 965

Yuan F., Narayan R., 2014, ARAA, 52, 529

Zakamska N. L., Greene J. E., 2014, MNRAS, 442, 784

Zakamska N. L., et al., 2003, AJ, 126, 2125

Zakamska N. L., et al., 2006, AJ, 132, 1496

Zamorani G., et al., 1981, ApJ, 245, 357

Zeldovich Y. B., Novikov I. D., 1964, Dokl. Acad. Nauk. SSSR, 158, 811

Zhao Y.-H., Huang J.-S., Ashby M., Fazio G., Miyazaki S., 2009, Research in Astronomy and Astrophysics, 9, 1061

Zhao D., Ho L. C., Zhao Y., Shangguan J., Kim M., 2019, ApJ, 877, 52

Zirbel E. L., Baum S. A., 1995, ApJ, 448, 521

de Nicola S., Marconi A., Longo G., 2019, MNRAS, 490, 600

van den Bosch R. C. E., Gebhardt K., Gültekin K., Yıldırım A., Walsh J. L., 2015, ApJS, 218, 10

Appendix A

Raw morphological classification results from the online interface

For the second optical morphological classification project outlined in Chapters 4 and 5, the morphologies of the active galaxies and control galaxies (matched to the active galaxies in terms of stellar mass and redshift) were classified using an online interface. The following questions and corresponding responses were used for the classifications (see Chapter 4, §4.3.2, for more details):

1. **Does this galaxy show at least one clear interaction signature?**
    - Yes
    - No
    - Not classifiable (e.g. image defect, bad region/spike from saturated star);
2. **What types of interaction signature are visible?**
    - Tail (T)
    - Fan (F)
    - Shell (S)
    - Bridge (B)
    - Amorphous halo (A)
    - Irregular (I)
    - Multiple nuclei (2N, 3N...)
    - Dust lane (D)

  - Tidally interacting companion (TIC);

3. **On first impression, what is the morphological type of the galaxy?**
  - Spiral/disk
  - Elliptical
  - Lenticular
  - Merger (too disturbed to classify)
  - Unclassifiable (due to image defects, *not* merger) .

While the general results for the active galaxy samples were discussed in Chapter 5, information on the classifications for individual active galaxies was not provided. As a result, the raw classification data obtained for all of the active galaxies using the online interface is included here, for completeness.

Tables A.1–A.4 display the number of "votes" recorded for each of the possible responses to the questions above, for the galaxies in the Type 2 quasar, RI-HERG low, RI-HERG high, and 3CR samples, respectively. Eight researchers carried out the classifications (myself, Clive Tadhunter, Yjan Gordon, Sara Ellison, Cristina Ramos Almeida, Chris O'Dea, Liam Grimmett, and Lydia Makrygianni) and responses could not be selected multiple times by the same classifier. Eight was therefore the maximum number of votes possible for any given category. Note that 3C 223 was observed twice and classified twice, due to its membership in both the 3CR and Type 2 quasar samples.

Table A.1: The raw classification results for the galaxies in the Type 2 quasar sample. The columns list the vote numbers for all possible responses to the three questions asked in the online interface, which are outlined in detail §4.3.2. Note that totals listed in the "Disturbed" column do not include cases where dust was the only interaction signature identified by the classifier. These votes were instead added to the total recorded for "Not disturbed".

	Question 1			Question 2									Question 3				
	Disturbed	Not disturbed	Image issues	T	B	I	MN	S	TIC	A	F	D	Ell.	Spiral/ disk	Len.	Merger	Image issues
J0052−01	0	8	0	0	0	0	0	0	0	0	0	0	1	1	6	0	0
J0232−08	2	6	0	0	0	0	0	2	0	0	0	0	7	0	1	0	0
J0731+39	0	8	0	0	0	0	0	0	0	0	0	0	7	0	1	0	0
J0759+50	1	7	0	0	0	0	0	0	1	0	1	0	6	1	1	0	0
J0802+25	8	0	0	7	0	4	1	1	0	5	3	0	1	1	0	6	0
J0802+46	1	7	0	0	0	0	0	0	0	0	1	0	6	0	2	0	0
J0805+28	7	1	0	6	0	0	5	1	1	3	0	0	0	4	1	3	0
J0818+36	8	0	0	6	6	0	0	1	6	0	1	0	4	1	3	0	0
J0841+01	8	0	0	2	2	0	6	0	5	2	0	1	7	0	0	1	0
J0858+31	7	1	0	1	2	0	2	0	7	0	0	0	8	0	0	0	0
J0915+30	8	0	0	5	8	2	0	0	7	0	1	0	0	1	1	6	0
3C 223	8	0	0	7	4	0	0	0	6	4	2	1	7	0	0	1	0
J0945+17	8	0	0	8	0	0	1	1	0	3	4	0	4	1	1	2	0
J1010+06	8	0	0	6	2	0	2	1	7	2	0	0	7	0	1	0	0
J1015+00	8	0	0	7	1	0	8	0	1	2	0	0	4	1	2	1	0

Table A.1 – continued.

J1016+00	8	0	0	5	0	1	7	0	1	3	3	0	6	0	0	2	0
J1034+60	8	0	0	2	0	1	0	4	1	5	1	0	1	4	1	2	0
J1036+01	8	0	0	2	4	0	1	0	8	1	2	0	0	7	0	1	0
J1100+08	0	8	0	0	0	0	0	0	0	0	0	0	0	8	0	0	0
J1137+61	1	7	0	0	0	0	0	1	0	0	1	0	8	0	0	0	0
J1152+10	8	0	0	8	0	2	0	5	0	2	5	0	4	0	1	3	0
J1157+37	3	5	0	0	0	0	0	2	0	1	0	0	8	0	0	0	0
J1200+31	8	0	0	4	3	0	3	1	6	3	2	0	5	0	1	2	0
J1218+47	8	0	0	4	0	2	1	5	1	6	0	0	1	2	0	5	0
J1223+08	0	8	0	0	0	0	0	0	0	0	0	0	8	0	0	0	0

Table A.2: The raw classification results for the galaxies in the RI-HERG low sample. The columns list the vote numbers for all possible responses to the three questions asked in the online interface, which are outlined in detail §4.3.2. Note that totals listed in the "Disturbed" column do not include cases where dust was the only interaction signature identified by the classifier. These votes were instead added to the total recorded for "Not disturbed".

	Question 1			Question 2									Question 3				
	Disturbed	Not disturbed	Image issues	T	B	I	MN	S	TIC	A	F	D	Ell.	Spiral/ disk	Len.	Merger	Image issues
J0725+43	1	7	0	1	0	0	0	0	0	0	0	0	0	5	3	0	0
J0757+39	8	0	0	7	0	1	0	5	0	3	0	0	0	7	0	1	0
J0810+48	1	7	0	0	0	0	1	0	0	0	0	0	0	3	5	0	0
J0827+12	4	4	0	4	0	1	0	0	0	1	0	0	0	6	0	2	0
J0836+44	8	0	0	3	0	0	1	8	2	3	2	0	4	1	0	3	0
J0838+26	2	5	1	0	0	0	0	0	0	1	1	3	1	6	1	0	0
J0902+52	8	0	0	6	0	1	0	4	0	5	4	0	3	1	0	4	0
J0911+45	2	6	0	0	0	2	0	0	0	0	1	0	0	5	3	0	0
J0931+47	0	8	0	0	0	0	0	0	0	0	0	0	8	0	0	0	0
J0950+37	0	8	0	0	0	0	0	0	0	0	0	1	0	7	1	0	0
J1036+38	6	2	0	1	1	0	0	2	5	1	0	0	0	8	0	0	0
J1100+10	0	8	0	0	0	0	0	0	0	0	0	0	0	4	4	0	0
J1108+51	0	8	0	0	0	0	0	0	0	0	0	0	0	3	5	0	0
J1147+33	0	8	0	0	0	0	0	0	0	0	0	0	0	6	2	0	0
J1150+01	1	7	0	1	0	0	0	0	0	0	0	0	0	2	5	1	0

Table A.2 – continued.

J1206+35	0	8	0	0	0	0	0	0	0	0	0	0	2	3	3	0	0
J1206+10	2	6	0	0	0	0	0	0	2	0	0	1	1	5	2	0	0
J1236+40	0	8	0	0	0	0	0	0	0	0	0	0	0	5	3	0	0
J1243+37	8	0	0	2	4	2	5	1	5	1	0	1	4	1	0	3	0
J1257+51	8	0	0	6	0	3	0	0	0	4	3	0	1	2	1	3	1
J1324+17	5	3	0	1	0	4	0	1	0	0	0	0	0	8	0	0	0
J1351+46	7	1	0	3	0	2	2	2	0	3	1	2	1	2	2	3	0
J1358+17	7	1	0	3	5	0	0	0	6	2	1	0	5	1	1	1	0
J1412+24	8	0	0	3	8	0	0	0	7	1	0	0	8	0	0	0	0
J1529+02	0	8	0	0	0	0	0	0	0	0	0	0	0	6	2	0	0
J1555+27	0	8	0	0	0	0	0	0	0	0	0	0	2	2	4	0	0
J1601+43	4	4	0	0	0	0	0	1	0	3	2	0	7	0	1	0	0
J1609+13	4	4	0	4	0	0	0	0	1	0	1	3	0	8	0	0	0
J1622+07	6	2	0	2	0	0	0	4	0	2	0	0	0	7	1	0	0
J1630+12	2	6	0	0	0	0	2	0	0	0	1	0	8	0	0	0	0

Table A.3: The raw classification results for the galaxies in the RI-HERG high sample. The columns list the vote numbers for all possible responses to the three questions asked in the online interface, which are outlined in detail §4.3.2. Note that totals listed in the "Disturbed" column do not include cases where dust was the only interaction signature identified by the classifier. These votes were instead added to the total recorded for "Not disturbed".

	Question 1			Question 2									Question 3				
	Disturbed	Not disturbed	Image issues	T	B	I	MN	S	TIC	A	F	D	Ell.	Spiral/ disk	Len.	Merger	Image issues
J0752+45	3	5	0	1	0	0	0	3	0	1	0	0	8	0	0	0	0
J0806+19	8	0	0	2	4	1	0	2	5	5	4	0	3	1	0	4	0
J0817+31	8	0	0	4	0	1	3	0	1	2	6	0	2	0	0	6	0
J0836+05	3	5	0	1	0	1	0	1	0	1	0	0	0	8	0	0	0
J0840+29	8	0	0	1	0	3	2	7	0	4	0	0	1	5	1	1	0
J0853+09	0	8	0	0	0	0	0	0	0	0	0	0	7	0	1	0	0
J0854+42	2	6	0	0	0	0	2	0	0	0	0	0	7	0	1	0	0
J0909+34	3	5	0	0	0	0	1	0	1	0	1	0	8	0	0	0	0
J0912+53	8	0	0	3	0	0	8	0	3	4	1	0	8	0	0	0	0
J1036+32	4	4	0	0	1	0	0	1	1	3	0	0	8	0	0	0	0
J1102+59	8	0	0	1	0	3	0	5	0	4	0	0	2	6	0	0	0
J1123+20	8	0	0	8	1	0	0	1	4	3	4	0	3	2	0	3	0
J1147+35	7	1	0	4	0	0	2	1	0	4	2	0	6	1	0	1	0
J1207+33	8	0	0	2	0	2	0	1	0	5	1	0	3	4	0	1	0
J1247+32	0	8	0	0	0	0	0	0	0	0	0	0	8	0	0	0	0

Table A.3 – continued.

J1314+28	7	1	0	4	0	0	1	1	3	6	2	0	7	0	0	1	0
J1328+27	3	5	0	0	0	0	0	2	0	1	0	0	8	0	0	0	0
J1334+38	2	6	0	0	0	0	1	1	0	0	0	0	8	0	0	0	0
J1409+36	8	0	0	5	7	0	0	0	5	1	1	0	7	0	0	1	0
J1425+39	8	0	0	8	0	0	0	2	0	3	5	0	5	1	1	1	0
J1436+08	8	0	0	2	0	0	0	7	0	2	2	0	0	8	0	0	0
J1450−01	8	0	0	3	0	0	0	2	1	4	5	0	4	2	0	2	0
J1512−01	0	8	0	0	0	0	0	0	0	0	0	0	8	0	0	0	0
J1516+05	1	7	0	0	0	0	0	0	0	0	1	1	3	1	4	0	0
J1523+32	7	1	0	1	0	1	0	1	0	5	0	0	4	3	1	0	0
J1529+36	8	0	0	0	0	1	0	4	0	5	3	0	6	0	1	1	0
J1537−00	8	0	0	0	0	0	0	2	0	5	5	0	8	0	0	0	0
J1541+47	3	5	0	0	1	0	1	0	1	2	0	0	8	0	0	0	0

Table A.4: The raw classification results for the galaxies in the 3CR sample. The columns list the vote numbers for all possible responses to the three questions asked in the online interface, which are outlined in detail in §4.3.2. Note that totals listed in the "Disturbed" column do not include cases where dust was the only interaction signature identified by the classifier. These votes were instead added to the total recorded for "Not disturbed".

	Question 1			Question 2									Question 3				
	Disturbed	Not disturbed	Image issues	T	B	I	MN	S	TIC	A	F	D	Ell.	Spiral/ disk	Len.	Merger	Image issues
3C 20	1	7	0	0	0	0	0	0	0	1	0	0	8	0	0	0	0
3C 28	2	6	0	0	1	0	0	1	0	1	0	0	8	0	0	0	0
3C 33	6	1	1	1	0	0	0	4	1	3	4	1	6	0	1	1	0
3C 33.1	5	2	1	0	1	0	3	0	1	0	0	0	7	0	0	0	1
3C 35	5	3	0	1	0	0	0	1	4	0	1	0	8	0	0	0	0
3C 52	2	6	0	2	0	0	0	0	0	0	2	0	8	0	0	0	0
3C 61.1	4	4	0	0	0	0	0	0	0	2	3	0	8	0	0	0	0
3C 63	0	8	0	0	0	0	0	0	0	0	0	0	8	0	0	0	0
3C 79	8	0	0	7	0	0	0	0	0	4	0	0	7	0	1	0	0
3C 89	3	5	0	0	0	0	0	0	0	2	1	0	7	0	1	0	0
3C 93.1	6	2	0	2	2	0	0	0	0	3	1	0	7	1	0	0	0
3C 123	0	5	3	0	0	0	0	0	0	0	0	0	6	0	0	0	2
3C 130	0	8	0	0	0	0	0	0	0	0	0	0	8	0	0	0	0
3C 132	6	0	2	1	1	0	2	0	1	1	2	0	6	0	0	1	1
3C 133	3	5	0	2	0	0	0	0	1	1	0	0	8	0	0	0	0

Table A.4 – continued.

3C 135	7	1	0	0	0	0	6	0	2	0	0	0	8	0	0	0	0
3C 136.1	8	0	0	3	0	4	0	0	0	3	3	0	0	2	2	4	0
3C 153	0	8	0	0	0	0	0	0	0	0	0	0	8	0	0	0	0
3C 165	3	5	0	0	0	0	2	0	0	0	1	0	8	0	0	0	0
3C 166	0	8	0	0	0	0	0	0	0	0	0	0	8	0	0	0	0
3C 171	8	0	0	4	0	1	0	0	1	2	6	0	4	0	0	4	0
3C 173.1	8	0	0	3	1	0	2	2	0	4	3	0	8	0	0	0	0
3C 180	7	1	0	1	0	0	0	0	0	7	3	1	5	1	1	1	0
3C 184.1	6	2	0	4	2	0	1	0	3	1	1	0	7	0	1	0	0
3C 192	0	8	0	0	0	0	0	0	0	0	0	0	8	0	0	0	0
3C 196.1	2	6	0	0	0	0	1	0	0	1	0	0	8	0	0	0	0
3C 197.1	0	8	0	0	0	0	0	0	0	0	0	0	8	0	0	0	0
3C 198	3	5	0	0	0	0	0	1	0	2	0	0	8	0	0	0	0
3C 213.1	8	0	0	2	1	0	0	2	0	6	4	0	7	0	0	1	0
3C 219	7	1	0	0	3	0	0	0	7	2	0	0	8	0	0	0	0
3C 223	6	2	0	3	3	0	0	0	3	3	3	0	8	0	0	0	0
3C 223.1	8	0	0	5	0	0	0	0	0	3	3	0	0	5	3	0	0
3C 234	6	2	0	0	1	0	1	0	1	2	2	0	8	0	0	0	0
3C 236	8	0	0	0	0	0	0	8	0	1	2	1	7	1	0	0	0
3C 258	4	4	0	0	0	0	0	0	0	2	2	0	8	0	0	0	0
3C 277.3	5	3	0	2	0	0	1	4	0	1	1	0	8	0	0	0	0

Table A.4 – continued.

3C 284	6	2	0	3	1	0	0	2	0	2	1	0	8	0	0	0	0
3C 285	8	0	0	4	0	3	0	0	1	3	2	3	0	4	0	4	0
3C 287.1	5	3	0	0	1	0	0	0	1	2	2	0	8	0	0	0	0
3C 288	1	5	2	0	0	0	0	0	0	1	0	0	8	0	0	0	0
3C 300	7	1	0	3	0	1	0	0	0	4	2	0	5	2	1	0	0
3C 303	4	4	0	1	0	0	0	0	0	3	1	0	8	0	0	0	0
3C 303.1	2	6	0	0	0	0	0	0	1	1	1	0	8	0	0	0	0
3C 310	8	0	0	0	3	0	0	0	7	3	0	0	8	0	0	0	0
3C 314.1	1	6	1	0	0	0	0	0	0	0	1	0	8	0	0	0	0
3C 315	8	0	0	2	3	0	2	2	3	4	0	0	7	0	0	1	0
3C 319	0	8	0	0	0	0	0	0	0	0	0	0	4	1	3	0	0
3C 321	7	0	0	7	2	0	7	0	3	2	1	0	2	0	0	5	0
3C 323.1	7	1	0	1	0	0	3	0	2	1	3	0	8	0	0	0	0
3C 326	6	2	0	0	3	0	0	1	0	3	2	0	8	0	0	0	0
3C 332	6	2	0	0	1	0	4	0	2	1	0	0	8	0	0	0	0
3C 346	8	0	0	1	2	0	6	0	4	4	3	0	4	0	0	4	0
3C 349	4	4	0	1	0	0	0	1	1	3	0	0	7	0	1	0	0
3C 357	2	6	0	0	0	0	0	0	0	1	1	0	8	0	0	0	0
3C 371	7	1	0	1	3	0	0	1	2	3	0	0	8	0	0	0	0
3C 379.1	2	6	0	0	0	0	0	1	0	1	0	0	8	0	0	0	0
3C 381	6	2	0	2	1	0	1	1	3	2	1	0	8	0	0	0	0

Table A.4 – continued.

3C 382	8	0	0	7	0	1	0	3	0	7	4	0	4	1	1	2	0
3C 388	2	6	0	0	0	0	2	0	0	0	0	0	8	0	0	0	0
3C 390.3	4	3	1	0	0	0	0	0	0	3	1	0	8	0	0	0	0
3C 401	1	7	0	0	0	0	1	0	0	0	0	0	8	0	0	0	0
3C 403.1	3	4	1	0	0	0	0	1	1	1	0	0	7	0	0	0	1
3C 405	2	5	1	0	0	0	2	0	0	1	0	1	7	1	0	0	0
3C 410	0	8	0	0	0	0	0	0	0	0	0	0	8	0	0	0	0
3C 424	6	2	0	0	0	0	0	1	1	6	1	0	8	0	0	0	0
3C 430	2	6	0	0	0	0	0	1	0	1	0	0	8	0	0	0	0
3C 433	8	0	0	4	1	2	2	8	4	3	0	0	1	1	1	5	0
3C 436	8	0	0	8	0	0	0	2	0	6	2	1	4	3	0	1	0
3C 438	3	5	0	0	0	1	1	1	0	1	0	0	8	0	0	0	0
3C 456	0	8	0	0	0	0	0	0	0	0	0	0	8	0	0	0	0
3C 458	8	0	0	7	1	0	0	0	1	1	1	0	7	0	0	1	0
3C 460	7	1	0	3	1	1	2	1	2	2	0	1	6	0	0	2	0

Appendix B

Radio observations of HERGs with lower radio powers

In addition to the results presented for the sample of 16 radio-intermediate HERGs presented in Chapter 6 ($23.0 < \log(\mathrm{L}_{1.4\mathrm{GHz}}) < 24.0$ W Hz^{-1}), two other HERG sources with lower radio powers ($\log(\mathrm{L}_{1.4\mathrm{GHz}}) = 22.39$ and 22.62 W Hz^{-1}) were also observed with the VLA in the same period, using the same observing strategy. Both of these objects were observed on the date 2018-03-28. The data reduction and image production were performed in an identical manner to that carried out for the targets in the main sample (Chapter 6, §6.3). Basic properties for these targets are presented alongside those of the other objects in the sample in Chapter 2, Table 2.1. The contour maps for these sources are presented in Figure B.1, and the contour levels are presented in Table B.1. The nature of the emission for these targets and their relation to the optical appearance of the host galaxies is briefly described below.

J0911+45. This target has slightly extended structure in the images at 4.5 GHz and 7.5 GHz, although this is only just resolved at 1.5 GHz; there is a patch of emission above the $3\,\sigma$ threshold in the 1.5 GHz image, but there is little difference between the peak and total flux values for this source (see Table B.1). The emission is confined to the scales of the bulge of its host galaxy and does not align with any optical features. Given that the emission structure is only just resolved, it is not possible to characterise its appearance further.

J1012+08. This source only has clearly resolved emission in its image at 7.5 GHz, although it appears to be marginally extended along the same position angle in its 4.5 GHz image. As with J0911+45, the emission is confined to the host galaxy bulge and shows no alignment with optical features.

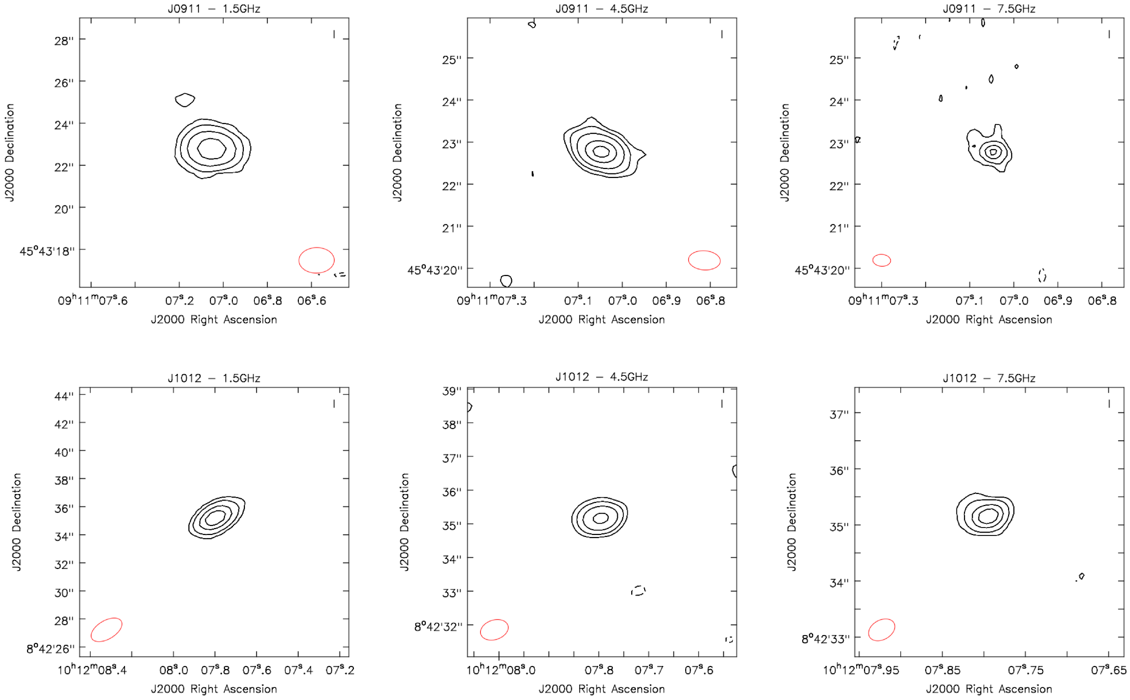

Figure B.1: Contour plots for the two lower-radio-power HERGs observed with the VLA at 1.5 GHz (left column), 4.5 GHz (middle column), and 7.5 GHz (right column). Positive contours (solid lines) begin at $3\,\sigma$ and typically increase by subsequent factors of two; exact contour levels are listed in Table B.1. Negative contours at the $-3\,\sigma$ level are indicated with dashed lines. The red ellipses indicate the approximate beam shape for each image.

Flux measurements and error calculations for the sources were conducted using the same methods as outlined in Chapter 6, §6.3, and are listed in Table B.1. Both sources are found to have fluxes at 1.5 GHz that exceed their FIRST values, although for J0911+45 the fluxes are consistent when considering the errors on the VLA measurements. For J1012+08, however, the difference appears to be more significant (at the $4.9\,\sigma$ level). The fact that the VLA flux is higher than the FIRST value means that this cannot be caused by flux losses introduced by the improved resolution of the VLA observations, and the ~30% discrepancy appears to be too large to be explained by variability. The cause of this difference therefore remains uncertain.

Given their relatively high redshifts within the sample, higher-resolution observations are important for determining the radio structures of these sources in more detail, particularly because both galaxies show signs of extended emission, at some level.

Table B.1: Emission properties and contour levels for the continuum maps displayed in Figure B.1. The three rows for each target indicate the values for the 1.5 GHz, 4.5 GHz, and 7.5 GHz maps, respectively. The beam parameters are presented as in Table 6.1, and the peak fluxes (f_ν^P) and total fluxes (f_ν^T) as in Table 6.3. FIRST and NVSS fluxes for the targets are also listed for comparison. The maximum angular ($\theta_\nu^{\max}$) and projected physical extents ($d_\nu^{\max}$) are also as presented in Table 6.3, although the bracketed values for J1012+08 at 1.5 GHz are calculated from the average of the two beam axis lengths, as in Table 6.2. Contour levels are presented as multiples of the background rms measurements in the images ($\sigma_{\rm rms}$), the values of which are also listed in the final column. The units are presented in brackets beneath their associated measurements, where appropriate.

Name	$F_{\rm NVSS}$ (mJy)	$F_{\rm FIRST}$ (mJy)	f_ν^P (mJy)	f_ν^T (mJy)	$\phi_\nu^{\max}$ (arcsec)	$d_\nu^{\max}$ (kpc)	$\theta_{1.5}$ (arcsec)	$\psi_{1.5}$ (deg)	Contour levels ($n\sigma_{\rm rms}$)	$\sigma_{\rm rms}$ (μJy)
J0911+45	8.6	1.9	1.92 ± 0.11	1.98 ± 0.13	3.2	5.5	1.68 × 1.21	-88.8	[-3,3,6,12,24]	54.5
			0.670 ± 0.037	0.882 ± 0.053	1.5	2.6	0.76 × 0.45	86.2	[-3,3,6,12,24,36]	15.7
			0.346 ± 0.025	0.448 ± 0.036	0.7	1.3	0.42 × 0.28	86.5	[-3,3,6,12,18]	18.0
J1012+08	11.1	1.2	1.83 ± 0.12	-	(1.9)	(3.2)	2.43 × 1.31	-59.2	[-3,3,6,12,18]	74.8
			0.761 ± 0.046	0.779 ± 0.055	1.5	2.5	0.84 × 0.58	-71.1	[-3,3,6,12,24]	26.5
			0.375 ± 0.025	0.428 ± 0.032	0.9	1.5	0.50 × 0.35	-60.9	[-3,3,6,12,18]	15.8